THE UNIVERSITY OF WARWICK

Library Declaration and Deposit Agreement

1. STUDENT DETAILS

Please complete the following:

Full name: ……

University ID number: ……

2. THESIS DEPOSIT

2.1 I understand that under my registration at the University, I am required to deposit my thesis with the University in BOTH hard copy and in digital format. The digital version should normally be saved as a single pdf file.

2.2 The hard copy will be housed in the University Library. The digital version will be deposited in the University's Institutional Repository (WRAP). Unless otherwise indicated (see 2.3 below) this will be made openly accessible on the Internet and will be supplied to the British Library to be made available online via its Electronic Theses Online Service (EThOS) service.
[At present, theses submitted for a Master's degree by Research (MA, MSc, LLM, MS or MMedSci) are not being deposited in WRAP and not being made available via EthOS. This may change in future.]

2.3 In exceptional circumstances, the Chair of the Board of Graduate Studies may grant permission for an embargo to be placed on public access to the hard copy thesis for a limited period. It is also possible to apply separately for an embargo on the digital version. (Further information is available in the *Guide to Examinations for Higher Degrees by Research*.)

2.4 *If you are depositing a thesis for a Master's degree by Research, please complete section (a) below. For all other research degrees, please complete both sections (a) and (b) below:*

(a) Hard Copy

I hereby deposit a hard copy of my thesis in the University Library to be made publicly available to readers (please delete as appropriate) EITHER immediately OR after an embargo period of ……..... months/years as agreed by the Chair of the Board of Graduate Studies.

I agree that my thesis may be photocopied. YES / NO (*Please delete as appropriate*)

(b) Digital Copy

I hereby deposit a digital copy of my thesis to be held in WRAP and made available via EThOS.

Please choose one of the following options:

EITHER My thesis can be made publicly available online. YES / NO (*Please delete as appropriate*)

OR My thesis can be made publicly available only after…..[date] (Please give date)
YES / NO (*Please delete as appropriate*)

OR My full thesis cannot be made publicly available online but I am submitting a separately identified additional, abridged version that can be made available online.
YES / NO (*Please delete as appropriate*)

OR My thesis cannot be made publicly available online. YES / NO (*Please delete as appropriate*)

3. GRANTING OF NON-EXCLUSIVE RIGHTS

Whether I deposit my Work personally or through an assistant or other agent, I agree to the following:

Rights granted to the University of Warwick and the British Library and the user of the thesis through this agreement are non-exclusive. I retain all rights in the thesis in its present version or future versions. I agree that the institutional repository administrators and the British Library or their agents may, without changing content, digitise and migrate the thesis to any medium or format for the purpose of future preservation and accessibility.

4. DECLARATIONS

(a) I DECLARE THAT:

- I am the author and owner of the copyright in the thesis and/or I have the authority of the authors and owners of the copyright in the thesis to make this agreement. Reproduction of any part of this thesis for teaching or in academic or other forms of publication is subject to the normal limitations on the use of copyrighted materials and to the proper and full acknowledgement of its source.

- The digital version of the thesis I am supplying is the same version as the final, hard-bound copy submitted in completion of my degree, once any minor corrections have been completed.

- I have exercised reasonable care to ensure that the thesis is original, and does not to the best of my knowledge break any UK law or other Intellectual Property Right, or contain any confidential material.

- I understand that, through the medium of the Internet, files will be available to automated agents, and may be searched and copied by, for example, text mining and plagiarism detection software.

(b) IF I HAVE AGREED (in Section 2 above) TO MAKE MY THESIS PUBLICLY AVAILABLE DIGITALLY, I ALSO DECLARE THAT:

- I grant the University of Warwick and the British Library a licence to make available on the Internet the thesis in digitised format through the Institutional Repository and through the British Library via the EThOS service.

- If my thesis does include any substantial subsidiary material owned by third-party copyright holders, I have sought and obtained permission to include it in any version of my thesis available in digital format and that this permission encompasses the rights that I have granted to the University of Warwick and to the British Library.

5. LEGAL INFRINGEMENTS

I understand that neither the University of Warwick nor the British Library have any obligation to take legal action on behalf of myself, or other rights holders, in the event of infringement of intellectual property rights, breach of contract or of any other right, in the thesis.

Please sign this agreement and return it to the Graduate School Office when you submit your thesis.

Student's signature: .....…… Date: .....

Birefringent Properties of the Human Cornea *in vivo*: Towards a New Model of Corneal Structure

Gary P Misson

A thesis submitted in fulfilment of the requirements for the degree of

Doctor of Philosophy

University of Warwick

School of Engineering

September 2012

TO

AEJM, MM & GPM

Abstract

The fundamental corneal properties of mechanical rigidity, maintenance of curvature and optical transparency result from the specific organisation of collagen fibrils in the corneal stroma. The exact arrangement of stromal collagen is currently unknown but several structural models have been proposed. The purpose of the present study is to investigate inconsistencies between current x-ray derived structural models of the cornea and optically derived birefringence data.

Firstly, the thesis reviews the current understanding of corneal structure, particularly in relation to corneal birefringence. It also reviews and develops the different analytical approaches used to model optical biaxial behaviour, particularly as applied to predict corneal optical phase retardation.

The second part develops a novel technique of elliptic polarization biomicroscopy (EPB), enabling study of corneal birefringence *in vivo*. Using EPB, the pattern of corneal retardation is recorded for a range of human subjects. This dataset is then used to investigate both central and peripheral corneal birefringence as well as the corneal microstructure.

A key finding is that the central parts of the cornea exhibit a retardation pattern compatible with a negative biaxial crystal, whereas the peripheral corneal regions do not. Furthermore, within the central regions of the cornea, orthogonal confocal conic fibrillar structures are identified which resemble the analytically derived contours of equal refractive index of an ideal negative biaxial crystal.

The third part of this work presents a synthesis of previous published experimental, anatomical and theoretical findings and the experimental results presented in this thesis. Based on these findings, a novel corneal structural model is proposed that comprises overlapping spherical elliptic structural units.

Finally, ensuing biomechanical and clinical consequences of the spherical elliptic structural model and of the EPB technique are discussed including their potential diagnostic and surgical applications.

Table of Contents

Abstract ... **ii**

Table of Contents ... **iii**

List of Tables ... **viii**

List of Figures ... **ix**

Acknowledgments ... **xii**

Declaration ... **xiii**

Symbols used in text ... **xiv**

1 Introduction ... **1-1**

1.1 Background ... *1-2*

1.2 Thesis Outline ... *1-4*

2 The Cornea ... **2-7**

2.1.1 Corneal zones and orientations ... 2-8
2.1.2 Corneal thickness ... 2-10

2.2 Microscopic Structure of the Cornea ... *2-10*
2.2.1 The corneal stroma ... 2-12
2.2.2 Lamellar organization: transverse section ... 2-13
2.2.3 Lamellar organization: Stromal architecture ... 2-15

2.3 Biomechanical properties ... *2-18*

2.4 Corneal optics ... *2-20*
2.4.1 Birefringence ... 2-22

2.5 Chapter Summary ... *2-26*

3 A Theoretical review of refractive index, birefringence and retardation ... **3-29**

3.1 Isotropic materials ... *3-29*

3.2 Anisotropic materials ... *3-31*

3.3 Uniaxial optical anisotropy ... *3-32*

3.4 Biaxial optical anisotropy ... *3-33*
3.4.1 Refractive index ... 3-36
3.4.2 Projection onto a spherical surface ... 3-38
3.4.3 Birefringence ... 3-40
3.4.4 Retardation ... 3-41

3.5 Chapter Summary ... *3-42*

4 Retardation and Birefringence of the Human Eye ... **4-43**

4.1 Literature review ... *4-43*

4.2 Methods ... *4-46*

4.3 Results 1: Refractive index 4-48

4.4 Results 2: Birefringence 4-53

4.5 Results 3: Thickness, Retardation and Isochromes 4-54
4.5.1 Thickness models 4-55
4.5.1.1 Spherical model 4-56
4.5.1.2 Conic model 4-56
4.5.2 Retardation: Spherical model 4-61
4.5.3 Retardation: Astigmatic model 4-62

4.6 A physical analogue of corneal birefringence 4-64

4.7 Discussion 4-67
4.7.1 A biaxial model of corneal structure 4-67

4.8 Chapter summary 4-71

5 Polariscopy 5-73

5.1 Polariscopy 5-73
5.1.1 Ophthalmic polariscopy 5-75

5.2 Polariscopy with monochromatic light 5-79
5.2.1 Transmitted polarized light 5-80
5.2.2 Retarder train, transmitted linear polarized light 5-82
5.2.3 'Circular' polariscope 5-84
5.2.4 Reflected linear polarized light 5-84
5.2.5 Retarder train, reflected linear polarized light 5-87
5.2.6 Synopsis 5-90

5.3 Transmission and reflection polariscopy with white light 5-91
5.3.1 Transmission through one or more retarders 5-92
5.3.2 Reflected double-pass through a single retarder 5-94
5.3.3 Reflected double-pass through two retarders 5-94

5.4 Experimental validation of theory 5-98
5.4.1 Methods 5-98
5.4.2 Results: Transmitted light 5-101
5.4.3 Results: Reflected light 5-101

5.5 Discussion 5-106

5.6 Chapter Summary 5-109

6 Experimental basis for a clinical method 6-110

6.1 Chromatic effects of retardation 6-110
6.1.1 The quartz wedge 6-110
6.1.2 Method 6-111
6.1.2.1 Transmitted monochromatic light 6-112
6.1.2.2 Transmitted white light 6-113
6.1.3 Reflected light 6-115
6.1.3.1 Monochromatic light, wedge only 6-115
6.1.3.2 White light: wedge 6-115
6.1.3.3 White light: wedge, retarders and parallel polarizers 6-116

6.2 'Circular' polarizers 6-120
6.2.1 Methods 6-121
6.2.2 Results: graduated wedge 6-123

6.3 Conclusion/ synthesis 6-124

6.4 Chapter Summary *6-126*

7 Corneal elliptic polarization biomicroscopy: preliminary and macroscopic findings. Normal Human corneas *in vivo* **7-129**

7.1 Method *7-129*

7.2 A pilot study *7-131*
7.2.1 140P 7-131
7.2.2 550P 7-134

7.3 Chapter Summary *7-137*

8 Microscopic Findings: Corneal fine structure **8-139**

8.1 Methods *8-140*

8.2 Results *8-142*

8.3 Discussion *8-147*

8.4 Chapter Summary *8-148*

9 Corneal Isotropes and Isochromes **9-149**

9.1 Subjects and Methods *9-149*

9.2 Quantification and parameters *9-150*

9.3 Results *9-152*
9.3.1 Isotropes 9-152
9.3.2 Isochromes 9-153
9.3.3 Right/Left eye comparison 9-156
9.3.4 Correlation between parameters 9-157

9.4 Discussion *9-158*

9.5 Chapter Summary *9-161*

10 Isochromes, Corneal Topography and Pachymetry **10-163**

10.1 Methods *10-163*
10.1.1 Estimation of birefringence 10-166

10.2 Results 1: isochrome distribution and topographic pachymetry *10-168*
10.2.1 Relationship of r_a to topographic pachymetry 10-172
10.2.2 4mm radius data 10-174

10.3 Results 2: Birefringence *10-176*

10.4 Discussion *10-179*

10.5 Chapter Summary *10-182*

11 The biaxial model of corneal birefringence **11-183**

11.1 Comparison of birefringence: cornea v negative biaxial crystal *11-183*
11.1.1 Theoretically derived equirefringence contours. 11-187

11.2 Transformation of the biaxial model *11-189*
11.2.1 Astigmatic model 11-189
11.2.2 Quadrangular isochromes 11-190

11.3 Discussion *11-193*

11.4 Chapter Summary *11-195*

12 Corneal Polarization Biomicroscopy of the abnormal cornea **12-197**

12.1.1 Corneal disease / trauma 12-197
12.1.1.1 Calcific band keratopathy 12-197
12.1.1.2 Corneal scarring 12-199
12.1.1.3 Keratoconus 12-200
12.1.2 Corneal Surgery 12-200
12.1.2.1 Penetrating keratoplasty 12-201
12.1.2.2 Post-refractive surgical cornea 12-203

13 A model of corneal structure **13-206**

13.1 Historical Review *13-206*

13.2 Current models *13-210*
13.2.1 X-ray scatter models 13-210
13.2.2 Stacked lamellar models 13-213
13.2.3 Biaxial model 13-214

13.3 Synthesis *13-216*
13.3.1 Central retardation: 13-216
13.3.2 Isotropes 13-217
13.3.3 Isochromes 13-218

13.4 The spherical elliptic model of corneal structure *13-222*
13.4.1 Composite structures 13-224

13.5 Discussion *13-228*

13.6 Chapter Summary *13-231*

14 Summary, Implications and Future Study **14-233**

14.1 EPB and its interpretation *14-234*
14.1.1 EPB technique 14-234
14.1.2 EPB results, interpretation and application 14-235

14.2 The unified model of corneal structure *14-236*

14.3 Clinical application *14-237*
14.3.1 EPB as a diagnostic instrument 14-238
14.3.2 Understanding biomechanical pathology: Keratoconus and iatrogenic ectasia 14-239
14.3.3 Biomechanical intervention: predicting surgery 14-240
14.3.3.1 Corneorefractive surgery 14-240
14.3.3.2 Surgically induced refractive errors and astigmatism 14-241
14.3.3.3 Keratoplasty 14-243
14.3.3.4 Artificial corneas 14-244
14.3.4 Clinical polarimetry 14-244

15 Appendices **15-245**

15.1 The Eye *15-245*

15.2 Geometric models: corneal topography and peripheral thickness *15-250*
15.2.1 Mathematical models of corneal shape 15-250
15.2.2 Models of corneal thickness 15-252
15.2.3 Spherical model 15-252
15.2.4 Conic model 15-256
15.2.4.1 Anastigmatic (E0) 15-257

15.2.4.2 'Physiological' astigmatic (Ea). 15-258
15.2.4.3 Extreme astigmatic (Ex) 15-259

15.3 Light, polarization and birefringence 15-260
15.3.1 Polarized light 15-261
15.3.2 Polarization Theory: retardation, retardance and birefringence 15-264
15.3.2.1 Interference 15-266
15.3.3 Mueller Matrices 15-267

15.4 Retarders and their calibration 15-268
15.4.1 The Berek compensator 15-269
15.4.2 The quartz wedge 15-269
15.4.3 Graduated wedge calibration 15-270

15.5 Examining and Measuring the Cornea 15-272
15.5.1 Topographic measurements 15-272
15.5.1.1 Discrete measurements 15-272
15.5.1.2 Mapping Techniques: Corneal Topography 15-274
15.5.1.3 Pentacam (Oculus, Berlin) 15-274
15.5.2 Slit-lamp biomicroscopy and photography 15-275

15.6 Miscellaneous Experimental Results 15-278

15.7 Bézier curves 15-280

15.8 Miscellaneous areas of further study 15-282

16 References 16-283

List of Tables

Table 4.1 Parameters for corneal model 4-46
Table 4.2 Coordinate system conventions 4-48
Table 5.1 Solutions to Eq 5.1 as, function of δ_1, θ_1, α 5-81
Table 5.2 Solutions to Eq 5.4 as function of δ_1, δ_2, θ_1, θ_2, α....5-82
Table 5.3 Solutions to Eq 5.14 as function of δ_1, θ_1, α 5-86
Table 5.4 Solutions to Eq 5.18 as function of δ_1, δ_2, θ_1, θ_2, α....5-88
Table 8.1 Summary statistics for the 38 phakic subjects 8-145
Table 8.2 Right/Left interfocal distance, interfocal azimuth and corneal radius of the ten pseudophakic subjects 8-145
Table 9.1 Definitions of isochrome / isotrope parameters 9-152
Table 9.2 Summary data for the right eyes of 25 normal subjects....9-153
Table 10.1 Topographic parameters: summary results 10-168
Table 10.2 Mean, maximum and minimum estimated birefringence 10-177
Table 13.1 Biaxial model vs. Experimental findings....13-215
Table 13.2 Comparison of corneal models 13-230
Table 15.1 Comparison of thickness models Ea and Ex with measured data....15-258
Table 15.2 Correlation data for all parameters....15-279

List of Figures

Figure 1.1 The eye. Adapted from Bron (1997).....1-1
Figure 2.1 The eye and cornea.....2-8
Figure 2.2 Anatomical definitions and orientations.....2-9
Figure 2.3 Transverse section through a typical human cornea.....2-12
Figure 2.4 Models of corneal fibril orientation.....2-17
Figure 2.5 Light transmittance of (a) cornea, (b) aqueous humour.....2-21
Figure 3.1 The isotropic indicatrix.....3-30
Figure 3.2 The uniaxial indicatrix.....3-32
Figure 3.3 The biaxial index ellipsoid.....3-35
Figure 3.4 The negative biaxial index ellipsoid.....3-36
Figure 3.5 Cone of normals to cone radius ρ.....3-38
Figure 3.6 Generation of spherical ellipses (spheroconics).....3-39
Figure 4.1 The cornea and a biaxial crystal observed between crossed polarizers....4-44
Figure 4.2 Three-dimensional representation of spheroconics ρ with parameters α, β, γ as defined in Table 4.1.....4-51
Figure 4.3 Orthographic projection of lines of equal refractive index of model cornea with principle/partial refractive indices α<α'<β<γ'<γ.....4-52
Figure 4.4 Distribution of birefringence according to Eq. 3.11 for unit sphere.....4-54
Figure 4.5 Anastigmatic corneal thickness model: radially symmetric surfaces (E0).....4-58
Figure 4.6 Astigmatic corneal models.....4-59
Figure 4.7 Elliptic corneal model: section functions.....4-60
Figure 4.8 Equiretardation contours for spherical model.....4-61
Figure 4.9 Equiretardation contours of astigmatic corneal thickness model Ea.....4-63
Figure 4.10 Muscovite (a, c) and aragonite (b, d) 30μm sections.....4-66
Figure 5.1 Polariscope configurations.....5-79
Figure 5.2 Spectral transmission curves from 360 – 780nm for retarder (Λ).....5-93
Figure 5.3 Spectral transmission curves for white light λ = 360 – 780nm reflected through linear polarizer and two superimposed retarders as determined by the STF.....5-97
Figure 5.4 Polarizing microscope (Zetopan Pol, Reichert Berlin) adapted for transmission and reflection.....5-99
Figure 5.5 Schematic of experimental setup for reflected polarimetry.....5-99
Figure 5.6 Definition of variables.....5-100
Figure 5.7 Experimental and theoretical (red) transmission spectra.....5-101
Figure 5.8 Experimental combinations of retarders.....5-102
Figure 5.9 Experimental and theoretical (red) transmission spectra for the two sets of retarders: coaxial (normal-incidence) reflected illumination.....5-103
Figure 5.10 Experimental and theoretical (red) transmission spectra for light reflected through retarder pairs.....5-105
Figure 6.1 Schematic experimental setup:.....6-111
Figure 6.2 Wedge in monochromatic light.....6-112

Figure 6.3 Quartz wedge (central two images, thin end below) observed in white light between crossed polarizers (left) and parallel polarizers (right) 6-114
Figure 6.4 Quartz wedge orientated $-45° \le \theta_2 \le 45°$ 6-116
Figure 6.5 Quartz wedge and fixed retarder 6-117
Figure 6.6 Experimental setup 6-122
Figure 6.7 Graduated quartz wedge: coaxial reflected white light illumination/observation with/without 140P and 550P 6-122
Figure 7.1 Schematic configuration of corneal examination with 140P/550P 7-130
Figure 7.2 A typical image with 140P 7-132
Figure 7.3 Addition and subtraction phenomena and correspondence of observed isochromes with quartz wedge interference colours. 7-133
Figure 7.4 Right/Left eye pair of subject IL01. 140P upper, 550P lower. 7-135
Figure 8.1 Schematic diagram of phakic (a) and pseudophakic (b) eyes with near-normal illumination/reflection 8-140
Figure 8.2 Pseudophakic eyes showing typical appearance 8-143
Figure 8.3 Right (a) left (b) eye pair showing approximate mirror symmetry 8-144
Figure 8.4 Comparison of Right v Left eyes of the 38 phakic subjects 8-145
Figure 8.5 Detail at isotrope 8-146
Figure 9.1 Definition of isochrome and isotrope parameters: right eye. subject IO29 9-151
Figure 9.2 Isochromes and isotropes of nine right eyes 9-154
Figure 9.3 Raw 280nm isochrome r_a data 9-155
Figure 9.4 Mean ±sd of 280nm isochrome distribution as in Figure 9.3 n = 25 9-155
Figure 9.5 Right/left eye isotrope comparison 9-156
Figure 9.6 Mean r_a of 11 Right/Left eye pairs 9-157
Figure 10.1 The Pentacam corneal topography system (Oculus, Inc., Wetzlar, Germany) 10-164
Figure 10.2 Calculation of path distance (τ) 10-167
Figure 10.3 A typical data set Left eye of subject P11 10-169
Figure 10.4 Corneal thickness profile and isochromes 10-170
Figure 10.5 Topographic comparison of isochrome maxima and minima 10-171
Figure 10.6 Comparison of r_a and $p740_a$ 10-172
Figure 10.7 Isochromes and isopachs. 10-173
Figure 10.8 Comparison of r_a with 4mm radius pachymetry and corneal curvatures (mean ±sd) 10-175
Figure 10.9 Graph of mean(±sd) r_a, mean(±sd) pr_a and calculated mean(±sd) birefringence 10-176
Figure 10.10 Graphs of r_a and calculated birefringence at r_a .(right) for right eyes of all five cases 10-178
Figure 11.1 Experimental configuration 11-184
Figure 11.2 Aragonite plate and cornea 11-186
Figure 11.3 Overlay of theoretically calculated biaxial equirefringence contours onto (a) aragonite model, (b) cornea 11-188
Figure 11.4 Corneal mean (±sd) 280nm isochrome distribution and calculated biaxial isochromes 11-188
Figure 11.5 Height and thickness profiles of corneal model Ex 11-191
Figure 11.6 Simulation of quadrangular isochromes 11-192

Figure 11.7 Thickness at 4mm radius from corneal centre of predicted (upper graph, filled circles) vs. mean (±sd) Pentacam values 11-192
Figure 12.1 Calcific band keratopathy 12-198
Figure 12.2 Calcific band keratopathy 12-198
Figure 12.3 Corneal scarring 12-199
Figure 12.4 Keratoconus 12-200
Figure 12.5 Penetrating keratoplasty 12-202
Figure 12.6 Penetrating keratoplasty 12-203
Figure 12.7 Radial keratotomy 12-204
Figure 12.8 Subepithelial ablation 12-204
Figure 12.9 LASIK 12-205
Figure 13.1 Schiötz model of lamellar distribution 13-207
Figure 13.2 Stanworth and Naylor's vibration directions. a uniaxial; b biaxial 13-209
Figure 13.3 Comparison of aligned collagen scatter maps with isochromes 13-221
Figure 13.4 The spherical elliptic model of corneal stromal organization 13-223
Figure 13.5 Transformed spherical elliptic model of corneal stromal structure 13-224
Figure 13.6 Bézier curves 13-226
Figure 13.7 Hyperbolic and elliptic moiré fringes 13-227
Figure 15.1 The Eye 15-247
Figure 15.2 Simple models of corneal curvature 15-250
Figure 15.3 Schematic of corneal thickness models 15-253
Figure 15.4 Calculation of path distance: simplified model 15-254
Figure 15.5 Corneal thickness (t and t_s) and path difference (τ) 15-256
Figure 15.6 Extreme astigmatic model: section profiles 15-259
Figure 15.7 Conventional representation of a plane polarized light wave 15-260
Figure 15.8 Calibration of quartz wedge 15-270
Figure 15.9 Graduated wedge calibration curve at 560nm 15-271
Figure 15.10 Modes of slit-lamp examination 15-276
Figure 15.11 Raw 280nm isochrome data (b) 15-278

Acknowledgments

I wish to thank Prof Peter Bryanston-Cross for allowing me the opportunity to pursue a PhD under his guidance. I am most grateful to him and also to Dr Brenda Timmerman for their kindness, continued support, advice, and constructive criticism. I also wish to thank Dr John Harry, Emeritus Ophthalmic Pathologist, Birmingham and Midland Eye Hospital, for invaluable advice and assistance with microscopy and microscopic techniques. Early experiments were performed with my friend and colleague Mr Julian Stevens during our residency at the Oxford Eye Hospital.

Special thanks go to the enduring patience, tolerance, and support of my family.

The seeds of the study were sown during many hours of discussions and long walks with my friend and mentor, the late Dr Arthur E. Mourant FRS. I learnt from Arthur that there are no boundaries between scientific disciplines and that depth of understanding can only be achieved by an open and receptive mind. It is to the memories of Arthur and my late parents that this work is dedicated.

Declaration

This thesis is presented in accordance with the regulations of the degree of Doctor of Philosophy. It has been written by myself and has not been submitted for a degree at another university. The work described in the thesis is the result of my own investigations except where otherwise stated.

Symbols used in text

α	First (fast) principle refractive index (biaxial index ellipsoid) Angle of polarizer clockwise from horizontal
β	second (intermediate) principle refractive index (biaxial index ellipsoid)
γ	third (slow) principle refractive index (biaxial index ellipsoid)
Δ	Total retardance of a system
ΔT	Total retardance of a system
Δw	wedge retardance (ref quartz wedge)
δ	Retardance, phase difference, relative phase shift: generally of a retarding component of a system. Used as subscripts in Mueller matrices. (angular units or fractions of wavelength)
ε	Smallest (fast) principle refractive index (uniaxial index ellipsoid)
θ	Angle of principle axis (e.g. of polarizer/retarder Mueller matrix) from horizontal. Depends on context and subscript
Λ	Optical path length, retardation (measured as a length in nm)
λ	wavelength
μ	Micro- (10^{-6})
ν	Frequency
π	3.14159 etc
ρ	Arbitrary refractive index (index ellipsoid)
τ	Angle between polarizer principle axis and retarder principle axis (any)
ϕ	Phase of a wave, cf δ, phase difference
ψ	Angle between privileged directions of polarizer and analyzer (or between two polarizers)
ω	Highest principle refractive index (uniaxial index ellipsoid)
B	Magnetic vector of electromagnetic wave
b	birefringence
c	Speed of light *in vacuo*
d	Thickness of a plate of refractile material

E	Electric vector of electromagnetic wave
EPB	elliptical polarization biomicroscopy
f	frequency
i	the row designation of an element of a matrix
j	the column designation of an element of a matrix
Mx	Mueller matrix (characterised by subscript x)
Mp θ	Mueller matrix of a polarizer with axis θ
Mrδ, θ	Mueller matrix of a retarder with retardation δ, axis θ
$m_{i,j}$	the i th row, j th column element of the Mueller matrix M
n	An integer such that n∈ Z
S	Stokes vector (characterised by subscript)
S_n	n th component of Stokes vector S
STF	Spectral transmission function
$T_{\parallel}$	Light transmission through an optical system with parallel polarizers
$T_{\perp}$	Light transmission through an optical system with crossed polarizers
x	x-axis of index ellipsoid
y	y-axis of index ellipsoid
Z, ℤ	The set of integers { 0, ±1, ±2, … }
z	z-axis of index ellipsoid

1 Introduction

The cornea is the transparent window at the front of the eye and part of the eye's imaging system (Figure 1.1). Changes in the cornea due to disease or injury have profound effects on vision and can result in blindness with its consequent disability, loss of quality of life and social isolation. It is estimated that 10 million people are blind as a result of potentially preventable or treatable corneal damage or disease. Conversely, deliberate surgical manipulation can cure corneal blindness and laser treatments can improve the performance of otherwise normal eyes with significant refractive errors.

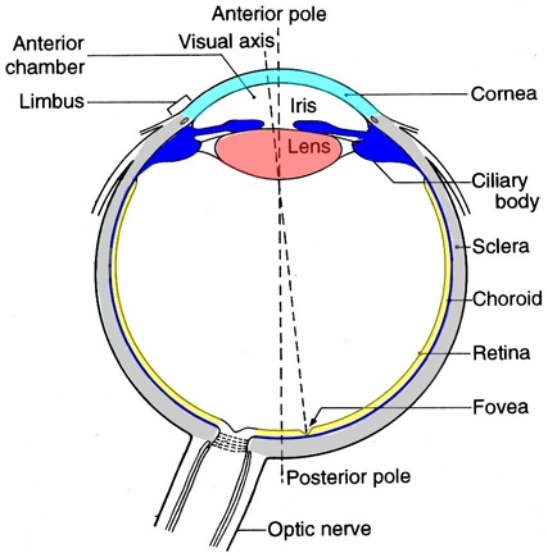

Figure 1.1 The eye. Adapted from Bron (1997)

The principle component of the cornea is the stroma, a specialised connective tissue composed of fibrils of collagen embedded in an amorphous ground substance. The stromal components are maintained by living cells (keratocytes). The cornea is exceptional among living tissues in its ability to transmit light, a property that results from a unique microscopic and ultramicroscopic structure of collagen fibrils. The ability of the cornea to refract light is a consequence of its transparency, a constant

refractive index, and a precise curvature. The formation and maintenance of the constant curvature is poorly understood, but is likely to result from biomechanical properties determined by the arrangement of structural elements, principally collagen fibrils, throughout the tissue (Maurice 1984). The cornea is continuous with the sclera at a junction called the limbus. The cornea and sclera together form the tough outer layer of the eye which protects and keeps in place the delicate intraocular structures. The rigidity of the corneal-scleral envelope is maintained by a dynamic balance between its biomechanical properties and the pressure of fluid inside the eye (the intraocular pressure, IOP).

The common features in all corneal functions are the collagen fibrils and their organization. Much is known of the microscopic short-range organisation of stromal collagen. Less is known about long-range morphology (i.e. how collagen is distributed throughout the extent of the whole cornea) and how it relates to fundamentally important biomechanical and optical properties.

1.1 Background

The present study originates from an initial investigation into mechanical stress induced by surgical manipulation of the human cornea (Misson and Stevens 1990). It was then common practice in cataract surgery to suture corneal wounds with fine nylon thread. Irregular tension of the sutures caused corneal distortion and consequent optical astigmatism which compromised the quality of vision after surgery. A method was needed that easily identified tight sutures so that suture removal or replacement could be performed before the healing process made distortion permanent. The early study

hypothesised that mechanical stress induces birefringence in the cornea and that this could be determined by polariscopy. A method of polariscopy using commercially available 'circular' polarizing filters was briefly outlined although its use in determining suture-related stress had limited success. The methods were not pursued because changes in surgical technique made suturing redundant in the majority of cataract procedures.

An incidental finding of 'circular' polariscopy was clear visualisation of corneal retardation which was noted to be similar to that of certain inanimate crystalline materials (Misson 1990; Bour 1991). It was well established by the time of the original study that the central cornea acts as a birefringent retarder with axis orientated 'down and in' (superotemporal to inferonasal) and causing a phase retardation of approximately $^{1}/_{10}$ of a wavelength. Retardation is determined by birefringence (double refraction) which, in turn, is related to structure of the cornea (Bour 1991; Maurice 1988). The presence of central corneal retardation was interpreted as a preferred orientation of collagen within that region (Shute 1974).

Retardation behaviour in non-central corneal regions was less well understood and the literature at that time reported several conflicting patterns. A biaxial pattern was favoured (Blokland and Verhelst 1987; Bour 1991) in which two loci of zero retardation ('axes') are symmetrically placed about the geometric corneal centre. In this pattern a zone of finite retardation exists between the axes coinciding with the corneal centre and corresponding to the central retardation previously described.

Understanding corneal structure in general and the distribution of collagen in particular is important to the understanding of the biomechanical response of the cornea to surgery, injury and disease. This understanding is therefore of scientific, humanitarian and commercial interest. The currently accepted model of corneal stromal structure (Meek 2009) is derived from x-ray scatter techniques applied to dead *ex vivo* corneal tissue. The x-ray derived model is compatible with known anatomy, but it is not compatible with the birefringence data of living corneas. In particular it does not explain the retardation due to the hypothesised 'preferred' central orientation of corneal collagen, nor does it explain the biaxial retardation pattern.

The inconsistency between the birefringence data of the living cornea and the currently accepted corneal structural models is the basis for this thesis.

1.2 Thesis Outline

Chapter 2 is an introduction to the cornea with particular emphasis on basic sciences relevant to the present study

Chapter 3 reviews the theory of birefringence from an optical crystallographic perspective. Uniaxial and biaxial optical anisotropy are introduced. Analytic expressions for refractive index and birefringence of a domed birefringent surface are derived.

In Chapter 4 the principles introduced in Chapter 3 are used to model the birefringent characteristics of a dome of optically negative biaxial material with similar properties to those published for the cornea. Partial refractive indices, birefringence and principle

vibration directions at each point on a model corneal surface are calculated. Contours of equal refractive index (equirefringence), equal birefringence (equibirefringence) and equal retardation (equiretardation = isochromes) are derived. A confocal spherical elliptic pattern of birefringent elements is predicted and the implications with respect to corneal structure are discussed.

The theory of polariscopy is explored in Chapter 5 using the Mueller calculus which simplifies calculation of polarized light transmission through birefringent media and multiple optical components. The theory is verified experimentally on physical models in §5.4. A practical technique *elliptical polarization biomicroscopy* (EPB) is proposed.

In Chapter 6 EPB is tested on a physical model and its results are interpreted.

In Chapter 7 EPB is used on human subjects *in vivo* and verifies previous published findings relating to corneal retardation, isotropes, isochromes, and preferential orientation of structural elements/collagen within the stroma. Furthermore, the use of calibrated retarders allows the optic sign of the cornea to be determined. Birefringence is estimated from the distribution of corneal retardation. Data is presented that supports previous findings of negative biaxial behaviour for the central cornea. A significant deviation from this behaviour is found in the peripheral cornea. Furthermore, a fibrillar microstructure is observed within the stroma of the central corneal.

The fibrillar microstructure is explored in greater depth in Chapter 8. It is established that this is a previously undescribed fine structure conforming to the confocal spherical

elliptic distribution of birefringent structural elements. The pattern is similar to that described in Chapter 4.

The isochrome patterns are examined in detail is Chapters 9, 10 and 11. It is established that the central cornea behaves according to the negative biaxial model, but the peripheral cornea does not. Experimental measurement and a theoretical analysis confirm that deviation from biaxial behaviour of the peripheral retardation is due to a non-biaxial pattern of birefringence rather than variations in corneal thickness.

Some preliminary clinical findings using EPB are presented in Chapter 12. In particular the use of the method for visualising corneal pathology is demonstrated.

Chapter 13 is a synthesis of the study's findings resulting in a novel unified model of corneal stromal organisation.

The basic scientific, biomechanical and clinical consequences of the model are discussed and further avenues of investigation are proposed in Chapter14.

2 The Cornea

The eyeball approximates to two fused spheres: the larger (radius 11.5 mm) comprising the scleral envelope and the smaller (radius 7.8 mm) corresponding to the cornea (Figure 2.1a,c). The cornea resembles a convex meniscus watch-glass and occupies the anterior one sixth (approx 1.3 cm^2) of the surface area of the eye ball. When viewed from the front (sagittal view, Figure 2.1b) the cornea is elliptical and widest in the horizontal meridian (11.7mm) compared to the vertical (10.6 mm) (Bron, Tripathi et al. 1997).

The corneal profile is aspheric in that it is approximately bell-shaped with flatter sides that have been slightly compressed vertically: a geometry that has been described as 'aspherotoridal' (Wang 2006). The central 6-7 mm (apical cap) is prolate ellipsoidal with near-constant curvature at its apex (radius 7.5 – 8mm), but flattening off towards the periphery (Figure 2.1d).

Most corneas are not spherically radially symmetric, but are approximately ellipsoidal which accounts for the variations in refraction seen clinically as regular astigmatism. The topographic patterns of left and right corneas of an individual often show non-superimposable mirror-image symmetry (enantiomorphism) (Dingeldein and Klyce 1989).

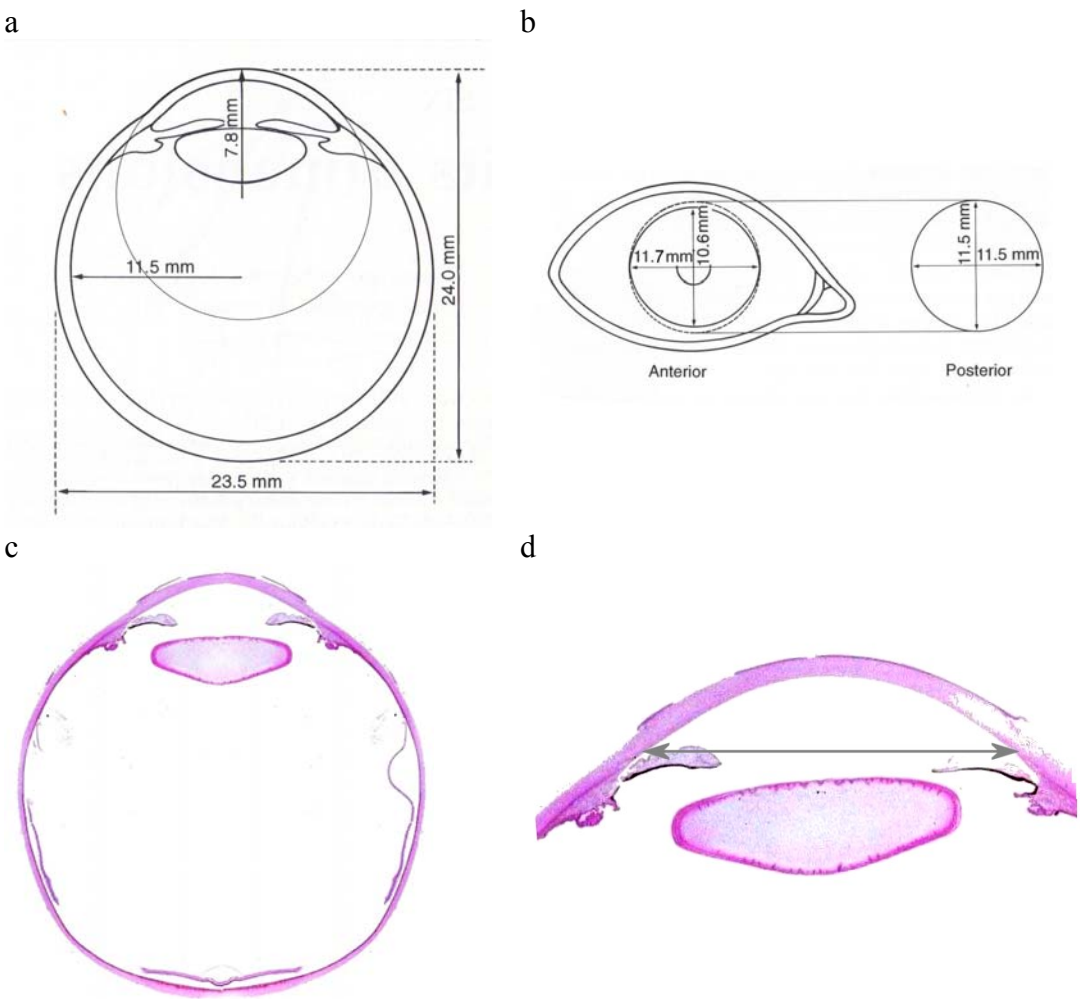

Figure 2.1 The eye and cornea

(a) Approximate geometry and dimensions of the human eye. (b) General proportions of external (anterior) and internal (posterior) surfaces (adapted from Bron (97Bron, Tripathi et al. 1997)).
(c) Transverse histological section through human eye x1.5.
(d) Histological section through the anterior chamber of a human eye showing general features of the cornea in cross-section. Arrow bar indicates 11.5mm.

2.1.1 Corneal zones and orientations

Although the cornea is a continuous structure, it is clinically useful to divide it into 3 zones: central, peripheral and limbal.

The optical (central) zone is critical for normal image formation and, for the normal non-astigmatic cornea, is defined as the central near-spherical 3-4mm diameter area that overlies the entrance pupil. Astigmatism is a disorder of refraction due to meridional differences in curvature of the central zone: corneorefractive surgery is aimed at

modifying the curvature of this zone. The peripheral zone is an annulus approximately 4 – 10/11 mm in diameter and flattens gradually towards the limbus. The limbal zone is that part of the cornea beyond the peripheral zone (approx >10mm diameter) and is the junction between cornea and sclera. There is a reversal of the corneal curvature at the limbus which marks the anatomical continuation of the transparent cornea with the opaque sclera.

Throughout the present work standard anatomical terminology and convention will be observed (Figure 2.2). This takes into consideration mid-line mirror symmetry of eyes and standardises right/left eye comparisons. Angular measurements of corneal meridians are taken with zero at temporal horizontal and rotating superior/nasal/inferior i.e. clockwise for right eyes and anticlockwise for left eyes (Figure 2.2; Left eye).

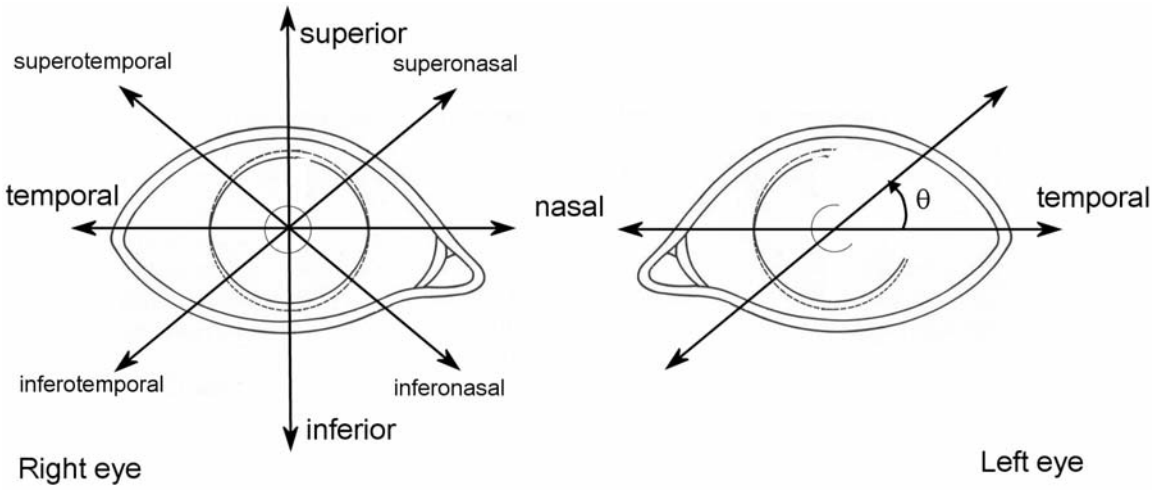

Figure 2.2 Anatomical definitions and orientations

Right and left eyes are depicted in standard form (i.e. as if the observer is looking at the subject). Superior/inferior = above/below; temporal = towards the temple; nasal = towards the nose; oblique orientations as depicted. Angular measurements (θ, left eye) are measured from horizontal temporal to superior i.e. clockwise from temporal horizontal in right eyes and anticlockwise from temporal horizontal in left eyes

2.1.2 Corneal thickness

There is currently a lack of data with respect to the variation of thickness throughout the cornea (topographic pachymetry) although the central cornea has been well documented. Corneal thickness increases from approximately 550µm centrally to up to 1.2mm at the limbus (Maurice 1969). The geometric corneal centre (intersection of vertical and horizontal corneal meridians) does not necessarily coincide with the thinnest part of the cornea, the visual axis (line or sight) or the corneal apex.

The increase in corneal thickness towards the periphery corresponds to a difference in the average radii of curvature of the anterior and posterior corneal surfaces of 7.8mm and approx 5.8mm respectively. The posterior corneal surface flattens to the periphery at a greater rate than the anterior curvature (Patel, Marshall et al. 1993).
The anatomical explanation of increased thickness in terms of stromal lamellae is not clear (Ruberti, Sinha Roy et al. 2011) although one hypothesis is that it results from encroachment into the peripheral cornea by fibril bundles originating in the sclera.

2.2 Microscopic Structure of the Cornea

The human cornea consists of five morphologically distinct layers throughout its extent (Figure 2.3). The superficial epithelium consists of five to six layers of cells, is 50 - 90µm thick, and merges with the conjunctival epithelium at the limbus. It has a protective role, but is primarily concerned with interaction with the percorneal tear film in maintaining an optically smooth surface. In primates including humans, but not in other mammals, the epithelium overlies Bowman's layer, a thin (8 – 14 µm) acellular homogenous zone that separates it from the third stromal layer. The stroma (Figure

2.3b) forms the greatest bulk (c. 90%) of the cornea and accounts for the transparency, curvature and refraction of the cornea as a whole. It is approximately 550μm thick centrally increases to over 800μm at the periphery (Bron, Tripathi et al. 1997; Radner, Zehetmayer et al. 1998) and exceeds 1mm at the limbus. The innermost (fifth) layer of the cornea is the endothelium which secretes a basement membrane, Descemet's membrane, between it and the stroma. The corneal endothelium is a monolayer of flat hexagonal cells that pump water from the stroma thereby maintaining it in the state of relative dehydration necessary for transparency. In adults endothelial cells have limited, if any, capacity to replicate so their loss (e.g. due to trauma or surgical damage) results in permanent stromal water-logging (oedema), loss of corneal transparency and consequent loss of vision. Descemet's membrane, the fourth corneal layer, is an acellular and well defined resistant sheet 10 – 12 μm thick.

The five morphological layers can be condensed into three functionally distinct units: the stroma sandwiched between anterior and posterior membranes formed respectively by the epithelium/Bowman's layer, and Descemet's membrane/endothelium. The stroma is the main subject of this study so will be considered in further detail.

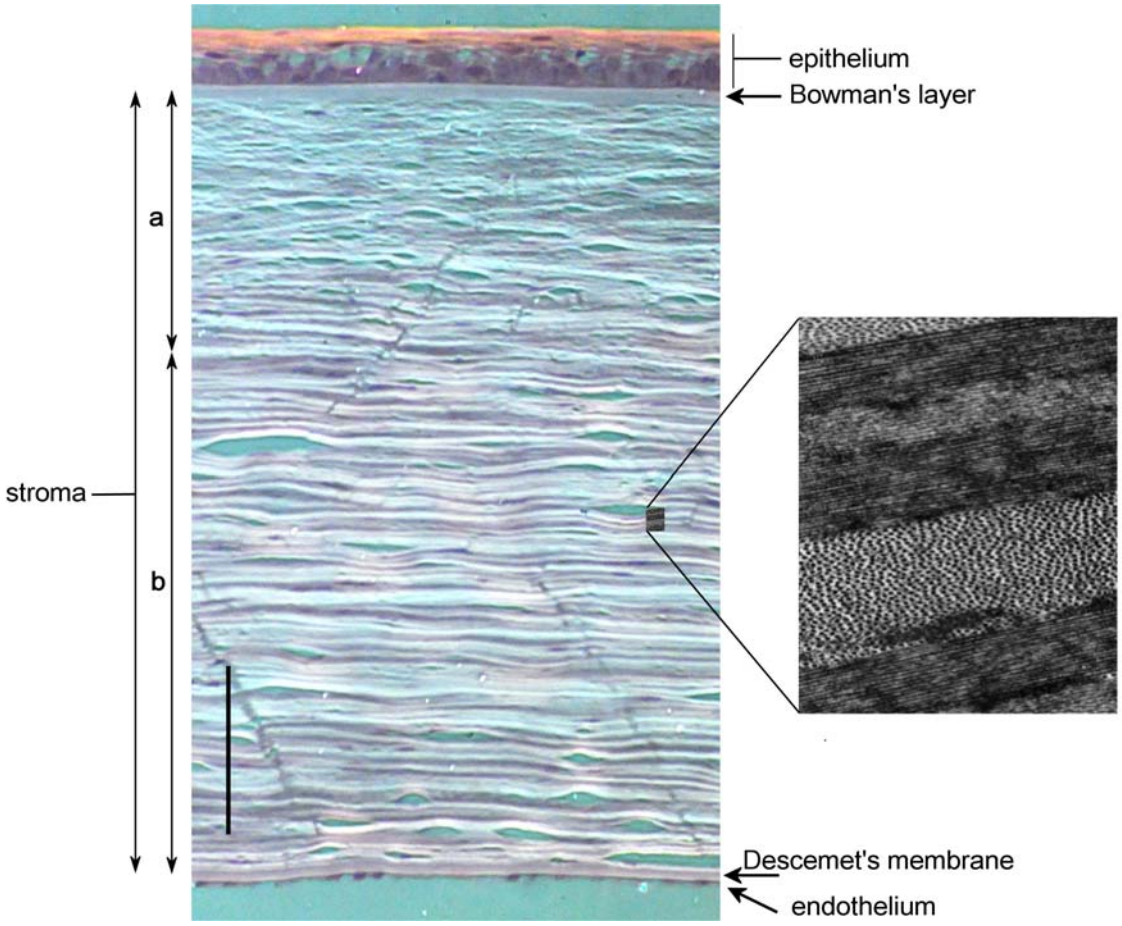

Figure 2.3 Transverse section through a typical human cornea

Light microscopic view (left) of whole cornea showing five layers. Note the extent of the stroma which is composed of multiple layers (lamellae) that are interwoven in the anterior one third (a) and more distinct in the posterior two thirds (b). Anterior above, posterior below, vertical bar on left is 100µm.
Electron micrograph (right) of the small area of corneal stroma as indicated. Note collagen fibrils cut parallel and perpendicular to the plane of view. The central lamella is approximately 1 µm thick. From Bron (1997)

2.2.1 The corneal stroma

The composition of both corneal stroma and sclera is almost identical in that both are made of compact interlacing bundles of predominantly type I collagen (although other collagen types are present) surrounded by an amorphous proteoglycan-rich ground substance (Bailey 1987). The collagens (Kadler, Baldock et al. 2007) are a large family of triple helical proteins with many functions. The fibril-forming collagens are major tensile elements of vertebrate connective tissues and predominate in the cornea. The

molecules of type I and similar collagens are long and organised into fibrils which aggregate into bundles of different types depending on the function of the tissue in which they are deposited. In the sclera the fibrils and bundles are irregular in diameter and distribution. By contrast, stromal collagen fibrils are uniform in diameter (20 – 40nm) and organized into a highly ordered, lattice-like configuration possibly by interaction with small leucine-rich proteoglycans (SLRPs). The SLRPs (e.g. lumican, decorin) are long-chain molecules that bind collagens and other matrix molecules and are thought to regulate a number of functions, including collagen fibrillogenesis, which is essential to development and tissue repair.

The difference in organization of collagen in the sclera and corneal stroma determines the opacity of the former and transparency of the latter (Maurice 1957; McCally and Farrell 1990). Furthermore, the tensile properties of stromal collagen fibrils, the orientation and distribution of fibrils, and the constant force of the intraocular pressure account for the precise constant curvature of the cornea essential for vision.

The collagen architecture of the stroma is of critical importance to both the biomechanical behaviour and transparency of the cornea. Thus to understand the response of the cornea to disease, injury and surgical manipulation, one requires knowledge of the stromal collagen distribution and structure: an understanding that, at present, is incomplete.

2.2.2 Lamellar organization: transverse section

Collagen fibrils within the corneal stroma, but excluding the thin anterior Bowman's layer, are organised into ribbon-like bundles that appear as layers (lamellae) in transverse histological sections (Figure 2.3). Fibril bundles form the basic

structural/mechanical unit of the stroma. Fibrils run parallel within bundles except where the bundles split or branch. Bundles in the anterior $^{1}/_{3}$ of the stroma tend to be smaller (0.5 – 30 μm wide, 0.2 – 1.2 μm thick) and interwoven compared to the posterior $^{2}/_{3}$ where bundles are larger (100 – 260μm wide, 1.0 – 2.5 μm thick) and the lamellar structure is well-defined (Komai and Ushiki 1991; Freund, McCally et al. 1995). The number of lamellae throughout the thickness of the stroma varies as a function of radius from 300 in central areas of the cornea increasing to 500 lamellae in the periphery correlating with the observed increase in thickness. No terminations of lamellae/bundles have been observed in non-superficial stroma so it is assumed that they run from limbus-to-limbus (Maurice 1984). Superficial bundles occasionally terminate in Bowman's layer (Bron, Tripathi et al. 1997). Within small volumes of stroma, particularly in the posterior two thirds, adjacent bundles run roughly parallel to themselves and to the corneal surface. Branching and interweaving of bundles in the plane of lamellae occur throughout the stroma (Radner and Mallinger 2002). Successive bundles throughout the thickness of the stroma cross each other at varying angles but many are near-orthogonal. Although the microstructure of isolated volumes of stroma may appear uniform, there are variations in antero-posterior microstructure throughout the extent of the cornea as a whole (Bron, Tripathi et al. 1997; Bron 2001). The difference in the amount of interweaving between the anterior $^{1}/_{3}$ and posterior $^{2}/_{3}$ of the stroma is thought to impart different mechanical properties to these two regions (Randleman, Dawson et al. 2008) that may be of both surgical and biomechanical importance (Bron 2001).

2.2.3 Lamellar organization: Stromal architecture

Anatomical studies have concentrated on the short-range organization of collagen with few investigations of the overall distribution of collagen fibrils for the whole stroma, partly because of technical difficulties in tracing fibrils that approximately follow the corneal curvature. An early study (Kokott 1938) postulates that superficial lamellae of the stroma have a vertical preference, middle layers follow the insertions of the rectus muscles and deep layers show an elliptic distribution that becomes more circular towards the periphery. This study, based on microdissection of human corneas, has been criticised and alternative methods including birefringence measurement were proposed for the indirect determination of fibril alignment (Maurice 1988).
X-ray scatter studies (Daxer and Fratzl 1997; Meek and Boote 2004) have produced data on corneal fibril orientation and maps of preferred fibril orientation have been published (see e.g. Meek and Boote 2009). Small-angle light scatter (McCally and Farrell 1990), confocal microscopy, optical coherence tomography and second-harmonic imaging microscopy (Morishige, Wahlert et al. 2007) have also produced structural data for fibril organization within small volumes of stroma. It has not been possible, at present, to map large continuous areas with such high resolution techniques.

The current view, derived mainly from x-ray scatter data, is that there is a preferential orientation of central stromal lamellae up to 1 – 2 mm from the limbus. The orientated components are posterior stromal (Abahussin, Hayes et al. 2009) whereas the anterior stroma has no preferred orientation (Morishige, Takagi et al. 2011). The x-ray data is interpreted as representing two orthogonal preferred orientations in the vertical and horizontal meridians (Meek, Dennis et al. 2003; Meek and Boote 2009).

The limbus is structurally different from the central corneal zones. Circumferentially orientated limbal collagen fibrils are identified by Maurice as being of biomechanical importance (Maurice 1988). X-ray scatter data in the limbal regions is interpreted as indicating a change in direction of stromal collagen to form the circumferential band (ligamentum circulare corneae) (Radmer. Zehetmayer et al. 1998; Meek and Boote 2004). Several models of the circumcorneal band have been proposed which acknowledge that this structure may be a composite of fibrils running in such a way that each fibril does not necessarily run the full extent of the band (Figure 2.4). Further x-ray data identifies dominant 'reinforcing' fibres entering the peripheral cornea along the horizontal and vertical meridians, but not reaching the optical zones (Figure 2.4c). The origins might be associated with the horizontal rectus muscles (a concept proposed by Kokott) and that the composite of superimposed fibrils form a rhombic pattern with mid-line body symmetry.

The latest model to be proposed is a combination of the central vertical-horizontal preference model with the reinforcing arcuate/rhomboidal model (Meek 2009) . This composite model will be considered in greater detail in Chapter 13.4 in the light of the findings of the present study.

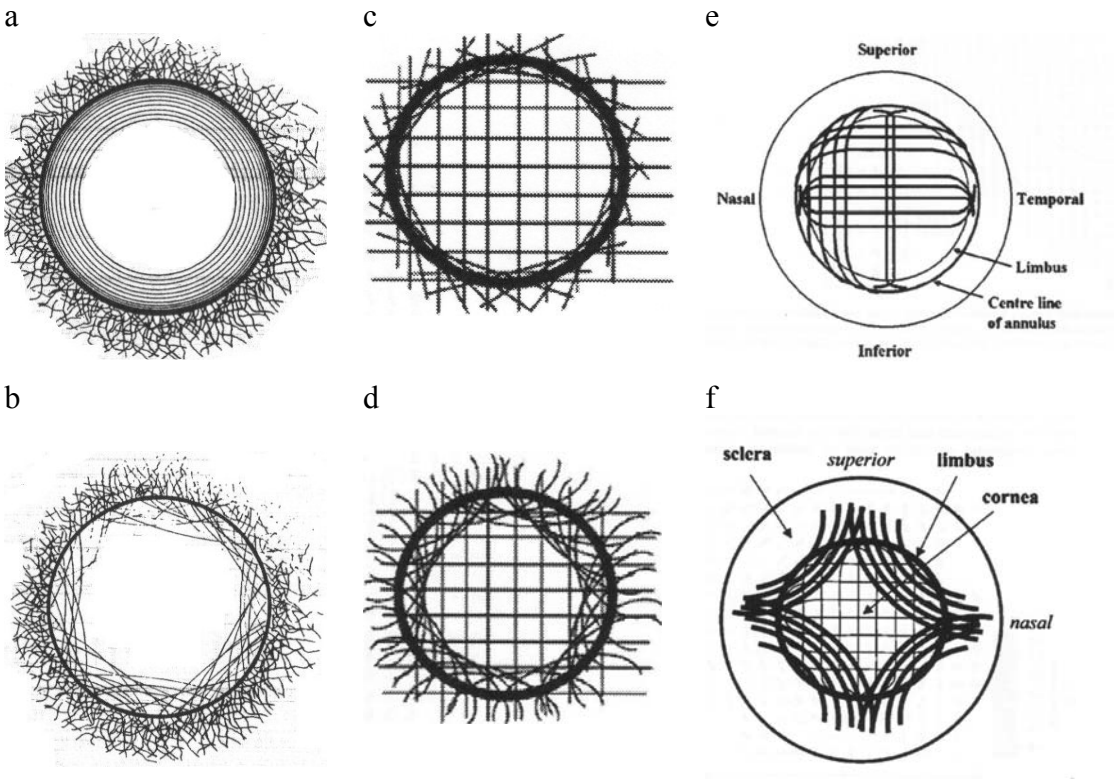

Figure 2.4 Models of corneal fibril orientation

(a) circumferential band; (b) fibrils tethered in the sclera passing into the peripheral cornea (Maurice 1988); (c) and (d) alternative models of horizontal and vertical preferred orientations modified to account for the circumcorneal annulus (note similarity of (b) and (d)) (Meek and Boote 2004); (e) vertical and horizontal preferred orientation and a change in fibril direction at the limbus to form the circumcorneal annulus (from (Boote, Dennis et al. 2005); (f) model (e) modified by the addition of peripheral arcuate fibrils (Meek 2009).

2.3 Biomechanical properties

The practical importance of understanding stromal structure, particularly the fibrillar/bundle/lamellar distribution, relates to its association with corneal biomechanics.

At its most fundamental, corneal biomechanics determines the static state of the cornea, the maintenance of corneal curvature and containment of the intraocular pressure. The response of the cornea to deforming forces is of physiological, clinical, and pathological importance. Physiological deforming forces include those due to the actions of the eyelids, the extraocular muscles in normal eye movements and internally derived forces from the action of the ciliary muscle in accommodation. Deforming forces from external sources include those applied deliberately as in the clinical measurement of tonometry (intraocular pressure measurement) or associated with contact lenses (e.g. orthokeratology). Certain corneal diseases such as keratoconus and keratoglobus result from a breakdown in biomechanical properties of corneal collagen. Furthermore, the biomechanical response of the cornea to accidental or deliberate trauma (e.g. surgery) is of clinical importance.

Using *ex vivo* techniques, the cornea stress-versus-strain and other biomechanical responses including intralamellar strength (Smolek 1993) and elasticity (Hjortdal 1996) are found to be non-linear and dependent on corneal region, depth within the stroma and meridian. *In vivo* methods based on measuring the dynamic response of the cornea to a deforming force (e.g. the Ocular Response Analyzer (ORA), Reichert Inc., Depew, New York, Optical coherence elastography, high-resolution ultrasound strain imaging) are the subjects of ongoing investigations, but again show non-linear, viscoelastic and

anisotropic biomechanical behaviour. Correlation of biomechanical and structural data has been attempted (Meek and Newton 1999) but, as yet, there is no coherent detailed account of the interrelation of corneal biomechanics and structure (Ruberti, Sinha Roy et al. 2011).

Corneal biomechanics are determined by stromal structure, specifically the intrinsic mechanical properties and geometry of stromal collagen and interlinking structures. The greater interweave of the anterior $^1/_3$ of the stroma and fibril insertions into Bowman's membrane are thought to contribute to the maintenance and stability of the corneal curvature. The circumferential arrangement of peripheral / limbal fibrils act as a purse-string in the maintenance of the differences in curvature between the cornea and sclera (Maurice 1984; Hjortdal 1996). A correlation between the orthogonal horizontal/vertical preferred orientations determined by x-ray studies and mechanical anisotropy has been reported (Elsheikh, Brown et al. 2008).

Computational models have been developed to further understanding of the biomechanical performance of the cornea particularly with respect to predicting the outcomes of surgery and understanding the origins of some corneal conditions (e.g. keratoconus), disease processes, and the response of the cornea to pathological insult. Many are based on civil and geotechnical engineering principles and necessarily make assumptions about the biomechanical properties of the cornea. Earlier computational models of corneal biomechanics were based on finite element modelling, analytic and other models. Current models have included the structural interpretations of Meek et al. (Pandolfi and Manganiello 2006; Li and Tighe 2006).

In a recent review Ruberti et al. conclude that there is no comprehensive biomechanical model that combines the known properties of the cornea (Ruberti, Sinha Roy et al. 2011). Furthermore they acknowledge a lack of understanding in the regional variations of corneal material properties *in vivo* as being an important factor in the known unpredictability of these models.

In addition to their conclusions about biomechanical properties, Ruberti et al. highlight several aspects of the cornea that remained incompletely understood. Of these, the following have particular relevance to the present study:

1) the reversal of curvature at the limbus with associated structural changes in collagen organization
2) the influence of the four rectus muscles with lines of force acting in the plane of corneal stroma potentially affecting stromal architecture
3) increase in thickness of stroma from centre to periphery

2.4 Corneal optics

The cornea is the principal image-forming component of the eye so has the same properties as an optical lens i.e. a smooth surface, geometric curvature, transparency and a refractive index different from the surrounding media (air/tears anteriorly; aqueous posteriorly). The refractive indices of air (1.000), tears (1.336), cornea (1.376), and aqueous (1.336) are well known as is the central keratometric cornea radius (7.0 – 8.8mm). Thus for optometric purposes, the total power of the air, tear, cornea, aqueous system can be expressed as a single dioptric power of +38 to +48 dioptres ($^2/_3$ of the refracting power of the eye).

Corneal visible light transmission (Figure 2.5) is essentially that of water (aqueous) and ranges from approximately 98% at 700nm to 80% at 400nm (Farrell, McCally et al. 1973). Ultraviolet <310nm is strongly absorbed by the stroma, but there are additional peaks of transmission in the infra red that are not present for water/aqueous humour.

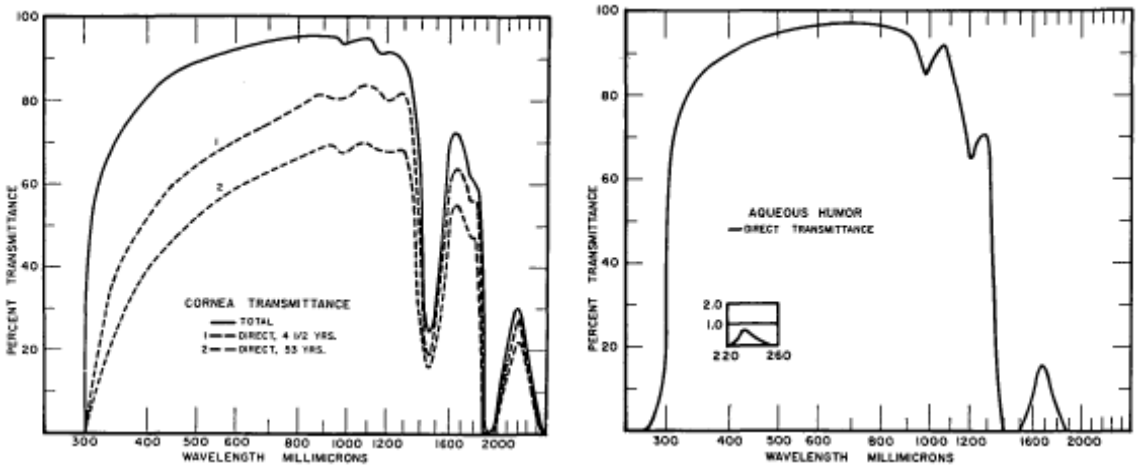

a b

Figure 2.5 Light transmittance of (a) cornea, (b) aqueous humour

from (Boettner and Wolter 1962)

Light transmission through the corneal stroma requires minimal absorption and minimal scatter. Light absorbent structures such as pigment or blood are normally absent from the cornea. Light scatter results from local fluctuations in refractive index which is the difference in refractive index of the stromal collagen fibrils (n = 1.41) and cells (keratocytes), and the optically homogenous (Hart and Farrell 1969) ground substance (n = 1.36) (Leonard and Meek 1997). Keratocytes are scarce, flattened in the corneal plane and have cytoplasm that contains specific proteins (crystallins) which matched it to the refractive index to the surrounding matrix (Jester 2008). The cornea would be opaque if each collagen fibril acted as an independent scatterer. Maurice (Maurice 1957) hypothesised that fibrils did not act in this way but that each fibril formed part of

an hexagonal crystalline lattice with spacings of less that λ/2 for visible light. In this environment only the zero-order Bragg condition is satisfied so scattered waves interfere destructively in all directions except that of the incident light resulting in transparency. The crystalline lattice theory has been questioned as short-range order extends only to about 120nm (Sayers, Koch et al. 1982). Subsequent theoretical models do not require perfect order for transparency (Cox, Farrell et al. 1970; Benedek 1971). An additional model (Twerskyt 1975) in which fibrils were composites of an inner core with an outer coat that matched the interfibrillar matrix is supported experimentally (Fratzl and Daxer 1993). More recently the theory of photonic band structure and photonic crystals (Vukusic and Sambles 2003) have been applied to models of corneal and scleral light transmission (Ameen, Bishop et al. 1998). Whilst these models require a high degree of organization, they are thought to be relevant to the explanation of corneal transparency (Meek 2009). All theoretical explanations of corneal transparency have assumed monochromatic light and as yet cannot explain the corneal light transmission curve.

Although the mechanisms of corneal transparency remains incompletely understood, the necessary conditions for minimal stromal scatter are uniformly small diameter of its refractile (n = 1.41) collagen fibrils (c. 30nm) which are closely spaced (c. 55nm) in an optically homogenous matrix (n = 1.36). This contrasts with the sclera which comprises less orderly arranged collagen fibrils with diameters ranging from 25nm to 480nm.

2.4.1 Birefringence

Birefringence (§ 3.4.3, §15.3.2) is the ability of some transparent materials to decompose light into two orthogonally polarized rays with different velocities. Each

light ray transmitted through a birefringent material is therefore subject to two orthogonal refractive indices depending on the atomic/molecular/ structural symmetry of the material in the particular direction of transmission.

The types of birefringence are:

1) Crystalline (intrinsic): birefringence resulting from asymmetries of molecular binding forces within a crystalline material.
2) Form: birefringence resulting from the assembly of parallel and uniformly thin cylindrical fibrils embedded in an homogenous ground substance of different refractive index (Bour 1991; Born and Wolf 2005). Form birefringence therefore arises from symmetries/asymmetries at a supramolecular level and is independent of intrinsic crystalline birefringence.
3) Induced: molecular/structural alignment with resulting birefringence may be induced in both isotropic and anisotropic materials by externally applied forces. Birefringence may be generated or altered in elastic anisotropic materials (elastic birefringence), or in isotropic materials (stress-induced or stress birefringence) by mechanical force. Birefringence may also be induced by electric (Pockels effect) and magnetic (Faraday effect) forces. A particular variant of electric-field induced birefringence is the alignment of liquid crystal molecules now ubiquitously used, together with sheet polarizers, in electronic displays. Stress-induced birefringence ('photoelasticity') is used in engineering analysis.

The cornea is birefringent and this has clinical and structural implications. The physiological significance of corneal birefringence, if any, is unclear. The conditions necessary for corneal birefringence are those for corneal transparency with additional

structural/molecular constraints particularly of the stroma. Other ocular structures are also birefringent although the cornea is the principle birefringent, and hence retarding, element (Bour 1991;Blokland and Verhelst 1987; Bueno and Jaronski 2001). Within the retina, the nerve fibre layer (Blokland 1985) and Henle's layer of the macula (Brink and van Blokland 1988) are significantly birefringent and act as intraocular retarders. The crystalline lens (Weale 1979; Brink 1991; Bueno and Cambell 2001), tears, aqueous and vitreous do not contribute significantly to the total ocular retardation.

Total corneal birefringence is the sum of form and intrinsic components (Maurice 1957; Maurice 1984) throughout the thickness (500 – 600um) of the multilaminar corneal stroma. Form birefringence contributes $^{2}/_{3}$ and intrinsic (collagen fibril) birefringence contributes $^{1}/_{3}$ of total corneal birefringence. The structural basis for corneal birefringence is closely linked with that of corneal transparency so any theory of one must be compatible with the other.

Birefringence manifests itself as optical retardation (§3.2, Eq. 3.1). The central cornea behaves as a simple retarder with retardance (see §15.3.2) ranging from between 0 and 0.25 λ (Naylor and Stanworth 1954; Bone 1980; Shute 1974). A study of 73 subjects reported 80% of retardations between 40 and 140nm (0.03λ – 0.12λ) with slow axis orientated 10° – 20° nasally downward (Knighton and Huang 2002). Other studies (Weinreb, Bowd et al. 2002; Zhou and Weinreb 2002) at near infra-red wavelengths (e.g. 780 nm) show similar orientations of the slow axis, and retardances ranging from 0.01 to 0.16 λ (median 0.05 λ). There is no significant difference between adults and

children (central corneal retardation 10 – 77nm: slow axis -11° to 71° nasally downwards) (Irsch and Shah 2012).

Central cornea retardation is interpreted as representing a preferred orientation of collagen within central corneal regions (Shute 1974). Birefringence away from the central cornea has a pattern thought to be analogous to some crystalline materials and will be described in detail in Chapter. 4 *et seq.*

Some authors have assumed that corneal birefringence is due to intrinsic mechanical forces (e.g. Mountford 1982; Ichihashi, Khin et al. 1995; Volkov, Malyshev et al. 1990). Whilst birefringence may be induced in the cornea by externally applied mechanical forces (Nyquist 1968; Misson and Stevens 1990), stress birefringence (strictly speaking, this is elastic birefringence) is of negligible importance in the normal cornea as are the other forms of induced birefringence (Maurice 1957).

As with many authors before him, Maurice hypothesised that birefringence might be a useful tool in determining the structural and biomechanical properties of the cornea (Maurice 1988): a hypothesis that will be explored in this study.

2.5 Chapter Summary

1) The cornea is a convex meniscus-like structure forming the front window of the eye.
2) The three corneal functions are transparency, refraction and protection
3) The cornea accounts for up to $^{2}/_{3}$ of the refracting power of the eye (+38 to +48 dioptres).
4) The cornea is divided into central (optic), peripheral and limbal zones.
5) The corneal is aspheric and differences in meridional curvature account for astigmatism.
6) The cornea varies from 550μm thick at the centre to over 1mm thick at the limbus.
7) The front corneal curvature is less than the back corneal curvature.
8) The cornea consists of 5 anatomical layers in cross section: epithelium (external), Bowman's layer, stroma, Descemet's membrane, endothelium (inner).
9) The stroma is the thickest layer and composed predominantly of type 1 collagen arranged in bundles seen in cross-section as layers (lamellae).
10) Typical dimensions of collagen bundles are 2 μm thick and 0.2mm wide. Lengths of bundles are not known but they are thought to run across the stroma from limbus-to-limbus.
11) Stromal collagen bundles cross at a range of angles with many near orthogonal
12) Bundles interweave predominantly in the anterior $^{1}/_{3}$ of the stroma where they are thought to contribute to the stability of corneal curvature.

13) Lamellae in the posterior $^{2}/_{3}$ of the stroma are more defined with little interweave.

14) A model of stromal structure in the central cornea, derived from x-ray scatter studies, comprises vertically and horizontally-orientated fibrils superimposed on a background of randomly orientated fibrils that curve acutely at the limbus.

15) Collagen fibrils form a circumferential structure in the limbal cornea (circumcorneal annulus) which is thought to maintain the difference in curvature between cornea and sclera.

16) 'Reinforcing' scleral-anchored fibrils with higher concentrations in the vertical and horizontal meridians are possibly associated with the insertions of the rectus muscles. These fibres are superimposed on the circumcorneal annulus.

17) Mechanical properties maintain the curvature and resilience of the cornea and eye to internal and external deforming forces.

18) Biomechanical models have been formulated in an attempt to predict the behaviour of corneas e.g. in response to surgery.

19) There is no adequate biomechanical model of the cornea.

20) The mechanisms of corneal transparency are incompletely understood.

21) Corneal transparency relies on the regular arrangement of collagen fibrils of uniform diameter and spacing.

22) The cornea is birefringent.

23) Birefringence is dependent on the cornea being transparent.

24) Birefringence is a consequence of the structure of the stroma and is attributed to intrinsic birefringence of collagen fibrils ($^{1}/_{3}$) and form birefringence ($^{2}/_{3}$) due to the regular arrangement of similar fibrils in an homogenous matrix.

25) The mechanisms of transparency and birefringence are interrelated.

26) The central corneal birefringence is due to a preferred orientation of central corneal collagen.

27) The current models of corneal structure cannot account for the central corneal birefringence.

28) Birefringence may be used as a tool in determining corneal structure.

3 A Theoretical review of refractive index, birefringence and retardation

The principle aim of this chapter is to introduce the concepts and theory of optical crystallography in preparation for the derivation of a computational model of corneal refractive index, birefringence and retardation in Chapter 4.

Birefringence is studied routinely in mineralogy and crystallography where polarization microscopy is used to determine the optical characteristics of minerals and other crystalline materials. This study will apply the principles of optical crystallography to investigate corneal birefringence. The terminology, concepts and conventions used here are those of optical crystallography and, where relevant, are briefly stated. The reader is referred to standard textbooks (Wahlstrom 1979; Born and Wolf 2005) for detailed explanations. A general introduction to light and polarization are given in Appendix §15.3).

According to electromagnetic theory, the transmission of light through a transparent medium depends on the symmetry of the local electron environment of that material. Two broad categories of media exist: isotropic and anisotropic.

3.1 Isotropic materials

Homogenous optically isotropic materials transmit light with equal velocity in all directions and therefore have a constant direction-independent refractive index. The molecular structure of these materials is such that any light ray is presented with the same electronic environment whatever the direction of transmission. Isotropic materials include gases, liquids, glasses, and crystals belonging to the isometric (cubic) system.

A convenient geometric representation of refractive index is the optical indicatrix or index ellipsoid (Fletcher 1892): a geometric figure in which refractive indices for monochromatic light are plotted in their direction of vibration in 3-dimensional Cartesian space. The length of each radius vector from the origin to the surface of the figure measures the refractive index of the material for light waves vibrating parallel to that direction. To find the refractive index for a light wave travelling in any direction, the wave normal is constructed through the origin of the indicatrix. The required refractive index is the radius of a slice through the origin perpendicular to the wave normal.

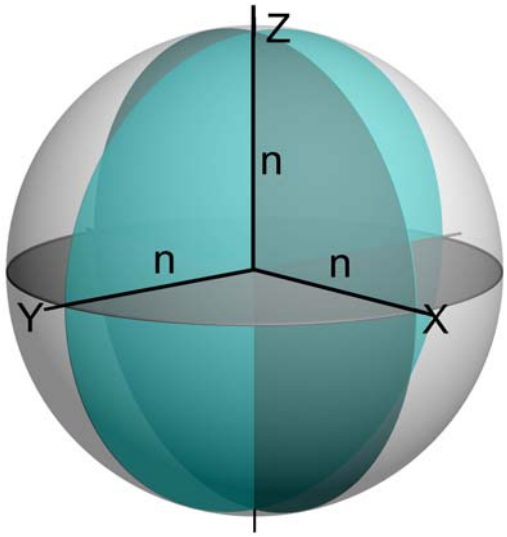

Figure 3.1 The isotropic indicatrix
showing circular sections in the x, y and z-planes; refractive index n

The isotropic indicatrix is a sphere (Figure 3.1). Thus any wave normal will have a corresponding perpendicular circular section indicating an equal refractive index in all vibration directions in the line of propagation. A characteristic of isotropic media is to transmit light in any polarized state without alteration.

3.2 Anisotropic materials

The speed of light in optically anisotropic materials is direction-dependent in a way that relates to anisotropy of the molecular binding forces or structural features such as molecular alignment from mechanical and other externally-applied forces. Thus refractive index in optically amnisotropic materials is direction dependent. Two categories of optically anisotropic material, uniaxial and biaxial, can be defined according to the presence respectively of two or three principle refractive indices i.e. the refractive indices along the x, y and z-semiaxes of the index ellipsoid.

Birefringence (b) is the difference between the maximum (N) and minimum (n) orthogonal refractive index along a particular light path

$$b = N - n$$

Light travelling a particular path can be considered to be composed of two orthogonally polarized rays with each orthogonal ray travelling at a different velocity determined by the relevant refractive indices.

Retardation (Λ) is the distance by which one ray (the slow ray) is delayed with respect to the other (the fast ray). It is defined as the product of the light path distance (d) through an anisotropic material with birefringence (b):

$$\Lambda = db$$

Eq. 3.1

The interference phenomena that result from retardation are readily detected and allow birefringence measurement (§15.3.2).

3.3 Uniaxial optical anisotropy

If two of the semiaxes of the index ellipsoid are of equal length but differ from the third axis, the crystal has two principal refractive indices (ε and ω), the index ellipsoid is an ellipsoid of revolution (i.e. has circular symmetry) about the z-axis and there is a single circular section (Figure 3.2).

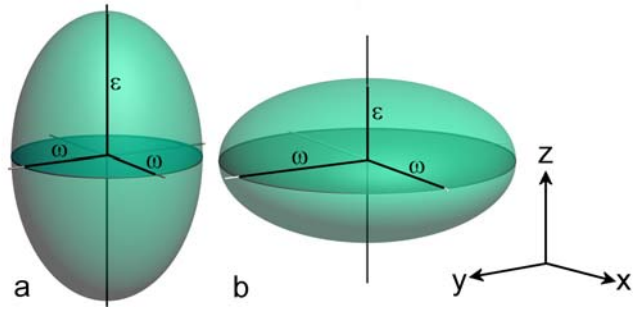

Figure 3.2 The uniaxial indicatrix

Note two principal refractive indices, ε and ω.
a) positive (ε – ω >0) ; (b) negative (ε – ω<0)

A single axis perpendicular to the circular section and, by convention, coinciding with the z-axis (the crystallographic optic axis, which is hereafter referred to as the optic axis and must not be confused with the physiological optic axis of the eye) represents the direction of transmission of a ray that is subject to refractive index ω only and therefore undergoes no double refraction. Such crystals are termed uniaxial and are characteristic of the hexagonal and tetragonal crystal systems. Directions of wave-normals through the origin of the ellipsoid other than along the optic axis are associated with elliptical sections of the ellipsoid with semiaxes ω and ε' where ε' can be calculated from ε, ω and the angle the light vibration makes with the optic axis. Two uniaxial states may exist in which the index ellipsoids are either prolate (ε>ω) (Figure 3.2a) or oblate (ε<ω) (Figure 3.2b) and are termed positive (ε–ω>0) or negative (ε–ω<0) respectively. Thus light travelling in directions other than along the optic axis are subject to two orthogonal

refractive indices ε and ω if perpendicular to the optic axis and ε<ω elsewhere. The quantity |ε−ω| is the birefringence of the material and |ε'−ω| is the partial birefringence for a given direction.

3.4 Biaxial optical anisotropy

The general case of unequal semiaxes results in a scalene ellipsoid with the equation:

$$\frac{x^2}{\alpha^2}+\frac{y^2}{\beta^2}+\frac{z^2}{\gamma^2}=1$$

Eq. 3.2

where, by convention (Johannsen 1914; Wahlstrom 1979), α<β<γ correspond to the principal indices of refraction of the crystal respectively along the x, y and z-axes (Figure 3.3). Such an index ellipsoid now lacks circular symmetry. Two circular sections are present with radii equal to the refractive index β (m, m', Figure 3.3b, d) and, as in the uniaxial index ellipsoid, each circular section has a perpendicular optic axis (A, A', Figure 3.3). Thus two optic axes are present and the crystal is termed biaxial. Biaxial birefringence is defined by the three principal refractive indices that form the semiaxes of the index ellipsoid and is characteristic of orthorhombic, monoclinic and triclinic crystal systems. By convention, the optic axes always lie in the x-z plane which is termed the optic plane; the acute angle between the optic axes is denoted as 2*V* (optic angle) or more specifically $2V_z$ and $2V_x$ (Figure 3.3b, d) when the z-axis and the x-axis are respectively the acute bisectrices of the optic angle. The optic normal is the y-principal vibration direction perpendicular to the optic plane. An optical sign can also be defined: a positive biaxial crystalline material has its principle vibration direction z (greatest refractive index γ) as acute bisectrix of the angle of the optic axes

((γ−β) > (β−α), optic angle $2V_z$, Figure 3.3a, b); x (greatest refractive index α) is the acute bisectrix in negative crystals ((γ−β) < (β−α), optic angle $2V_x$ Figure 3.3c, d). $2V_z$ and $2V_x$ are related to α, β and γ by:

$$\cos 2V_z = \cos(180° - 2V_x) = \frac{\alpha}{\beta}\sqrt{\frac{(\gamma+\beta)(\gamma-\beta)}{(\gamma+\alpha)(\gamma-\alpha)}} \approx 1 - 2\left[\frac{(\beta-\alpha)}{(\gamma-\alpha)}\right]$$

Eq. 3.3

As in the uniaxial case, birefringence is the maximum and minimum orthogonal refractive index along a particular light path but is defined in terms of α, β and γ and intermediate refractive indices α' and β' depending on the direction of the transmitted light ray.

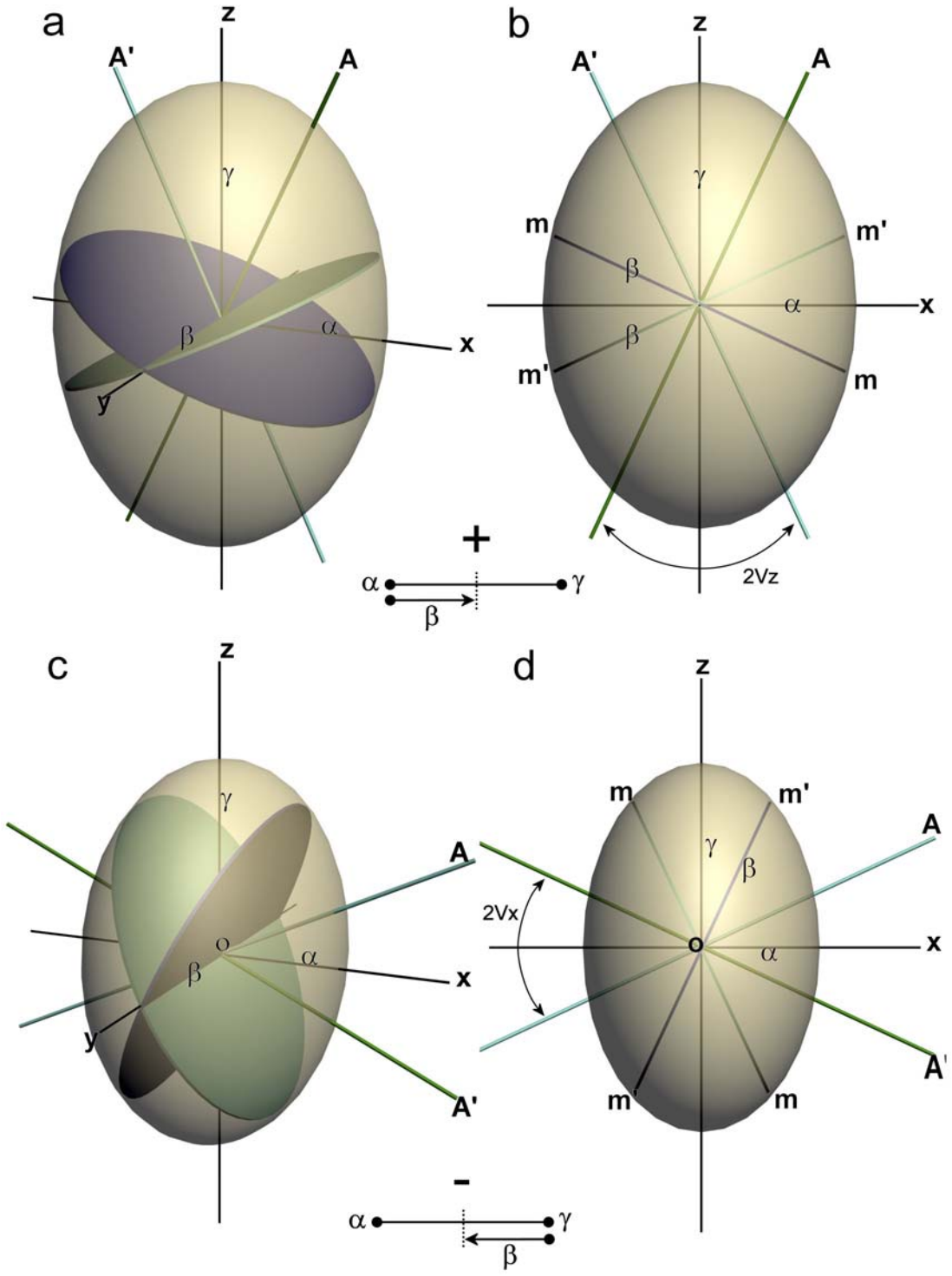

Figure 3.3 The biaxial index ellipsoid.

(a) (b) positive (γ−β) > (β−α); (c) (d) negative (γ−β) < (β−α); (a) (c) oblique view, (b) (d) optic normal (y-axis) view. See text for annotations.

3.4.1 Refractive index

Referring back to Eq. 3.2 and applying it to a negative biaxial index ellipsoid (Figure 3.3c, d, Figure 3.4, $(\gamma-\beta) < (\beta-\alpha)$), let ρ be an intermediate refractive index such that $\alpha < \rho < \gamma$. The position of ρ in the index ellipsoid may be determined from the intersection of a central sphere of radius ρ and the index ellipsoid (Figure 3.4b).

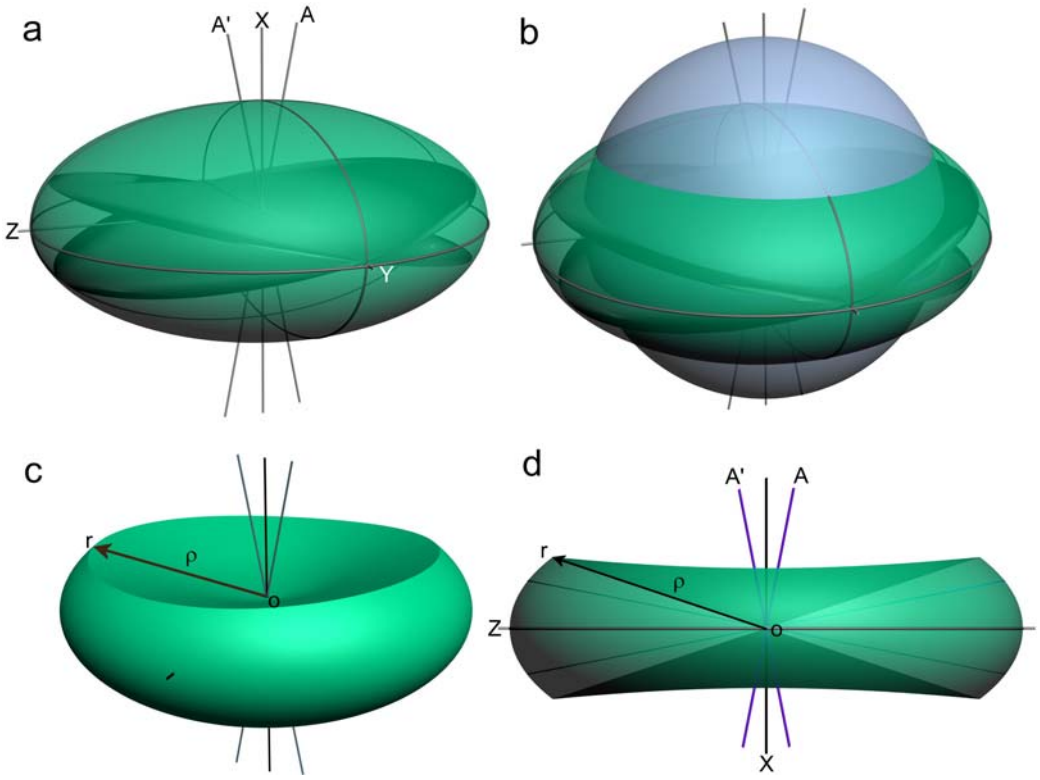

Figure 3.4 The negative biaxial index ellipsoid

(a) index ellipsoid, general view; (b) intersection of index ellipsoid (green) and sphere (blue-grey) radius o r = ρ. (c) oblique view of resultant surfaces; (d) horizontal view along y-axis. Origin o; geometric axes x, y, z with refractive indices respectively $\alpha < \rho < \gamma$; optic axes A A'

The equation of the sphere $x^2 + y^2 + z^2 = \rho^2$ may be rearranged to

$$\frac{x^2}{\rho^2} + \frac{y^2}{\rho^2} + \frac{z^2}{\rho^2} = 1$$

Eq. 3.4

which on subtraction from Eq. 3.2 gives

$$x^2\left(\frac{1}{\alpha^2}-\frac{1}{\rho^2}\right)+y^2\left(\frac{1}{\beta^2}-\frac{1}{\rho^2}\right)+z^2\left(\frac{1}{\gamma^2}-\frac{1}{\rho^2}\right)=0$$

Eq. 3.5

This is a central cone that passes through the curve of intersection of the index ellipsoid and sphere, and describes the position in space of all radius vectors (vibration directions) of the ellipsoid for refractive index ρ (Figure 3.4c, d).

The optic normals for rays that are travelling at a velocity determined by ρ are perpendicular to the vibration direction and thus form a second cone

$$\frac{x^2}{\left(\frac{1}{\alpha^2}-\frac{1}{\rho^2}\right)}+\frac{y^2}{\left(\frac{1}{\beta^2}-\frac{1}{\rho^2}\right)}+\frac{z^2}{\left(\frac{1}{\gamma^2}-\frac{1}{\rho^2}\right)}=0$$

Eq. 3.6

This cone, the reciprocal of Eq. 3.5 (Figure 3.5a, b), represents the locus of directions in which a light ray may travel at a constant velocity i.e. subject to a particular refractive index ρ. It may therefore be regarded as a cone of equal refractive index or equirefringence cone.

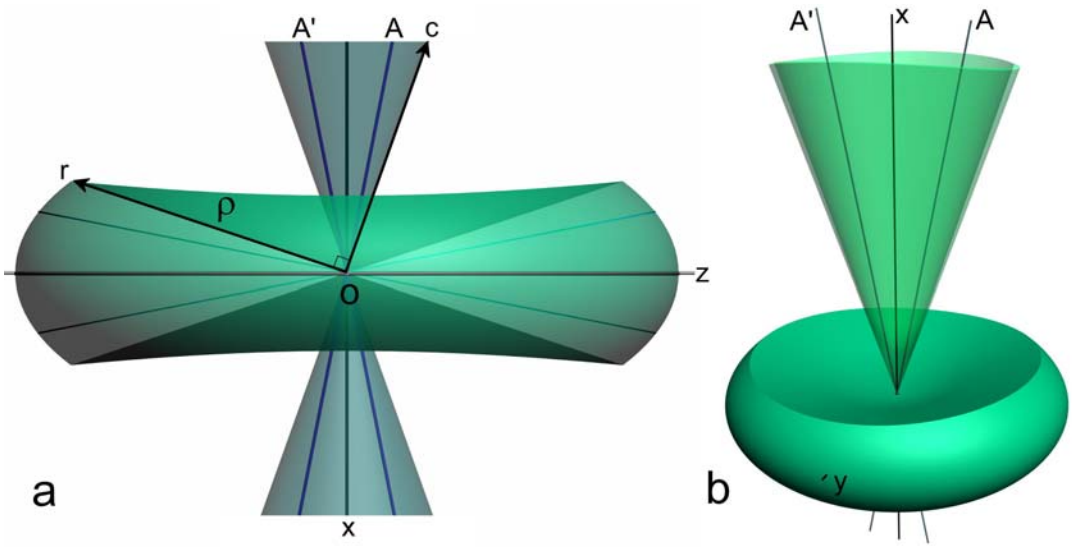

Figure 3.5 Cone of normals to cone radius ρ

as described by Eq. 3.6. (a) view along y-axis; (b) oblique view. Annotations as in Figure 3.4

3.4.2 Projection onto a spherical surface

The above theory may now be used to determine the refractive indices and birefringence imposed on parallel rays incident on a spherically curved refracting surface. The intersections of the cones of equal refractive index of the index ellipsoid with a unit sphere are now considered (Figure 3.6a). The intersection of sphere with equirefringence cone of refractive index ρ generates a three-dimensional curve termed a spheroconic or spherical ellipse (s in Figure 3.6b, c) which is the locus of points of equal refractive index (equirefringence curves) on the spherical surface.

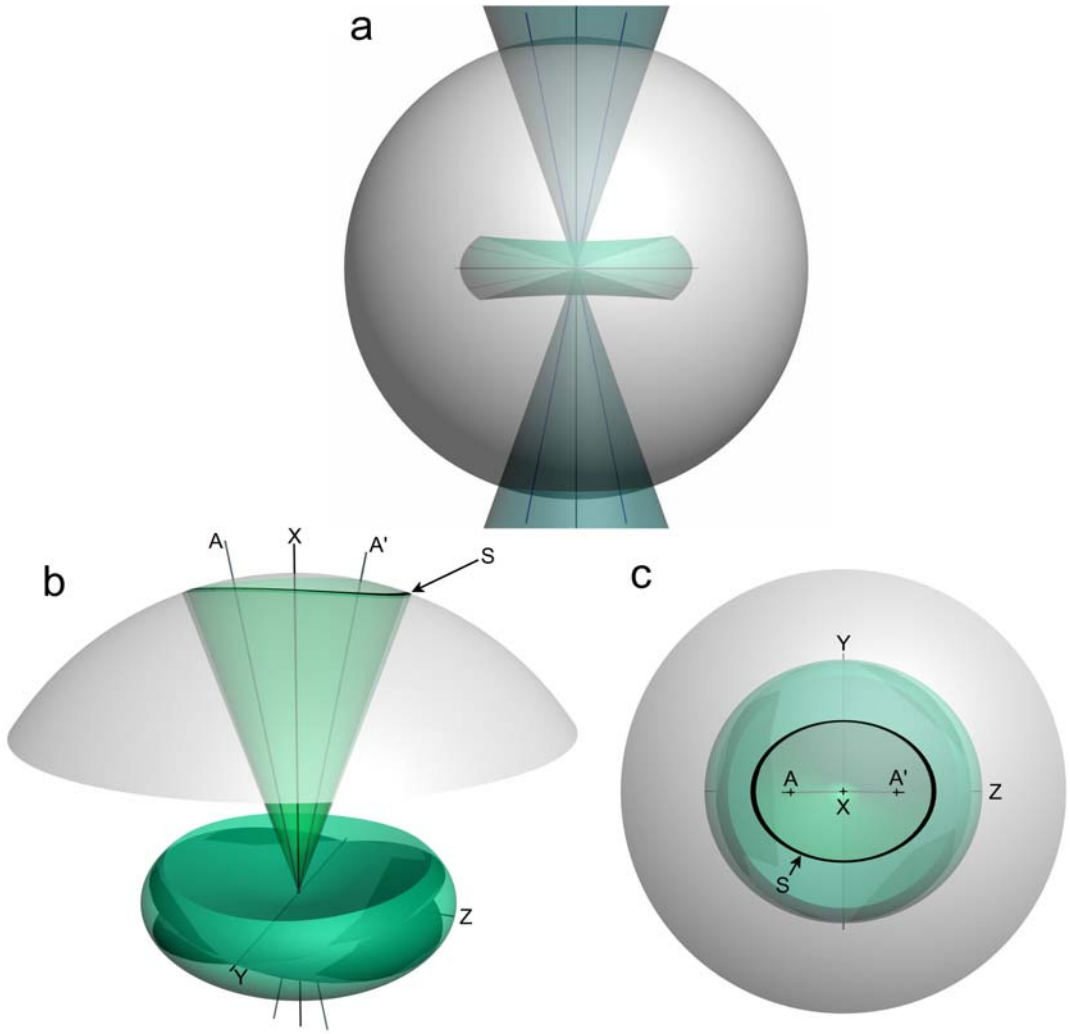

Figure 3.6 Generation of spherical ellipses (spheroconics)

Intersection (s) of the cone of equal refractive index (green) of the index ellipsoid (blue-green) with a unit sphere (transparent grey). Annotations as in Figure 3.4 (a) view along y-axis, unit sphere complete; (b) oblique view, unit sphere partly removed; (c) view along x-axis.

Expressions for the orthographic projection of the spheroconic equirefringence curves so generated are derived from Eq. 3.6 by subtraction from $x^2 + y^2 + z^2 = 1$, the equation of a unit sphere. Thus, for the x – y plane:

$$x^2 \frac{\frac{1}{\alpha^2} - \frac{1}{\gamma^2}}{\frac{1}{\alpha^2} - \frac{1}{\rho^2}} + y^2 \frac{\frac{1}{\beta^2} - \frac{1}{\gamma^2}}{\frac{1}{\beta^2} - \frac{1}{\rho^2}} = 1$$

Eq. 3.7

for the y – z plane:

$$y^2 \frac{\frac{1}{\alpha^2}-\frac{1}{\beta^2}}{\frac{1}{\alpha^2}-\frac{1}{\rho^2}} + z^2 \frac{\frac{1}{\alpha^2}-\frac{1}{\gamma^2}}{\frac{1}{\alpha^2}-\frac{1}{\rho^2}} = 1$$

Eq. 3.8

and for the x – z plane:

$$x^2 \frac{\frac{1}{\alpha^2}-\frac{1}{\beta^2}}{\frac{1}{\alpha^2}-\frac{1}{\rho^2}} + z^2 \frac{\frac{1}{\gamma^2}-\frac{1}{\beta^2}}{\frac{1}{\gamma^2}-\frac{1}{\rho^2}} = 1$$

Eq. 3.9

Where $\alpha<\beta<\gamma$ as previously defined, ρ is an arbitrary refractive index such that $\alpha<\rho<\gamma$, and x, y and z are points on a unit sphere with the same origin as the index ellipsoid.

3.4.3 Birefringence

An equation determining contours of equal birefringence (equibirefringence curves) for a crystal plate under conoscopic illumination was derived by Wright (Wright 1923). This configuration is geometrically equivalent to a dome of biaxial birefringent material illuminated with parallel rays as in §3.4.2. An adaptation of Wright's equation describes distribution of birefringence on the surface of the unit sphere:

$$b^2 = \frac{\alpha^2\beta^2(l^2+m^2)+\beta^2\gamma^2(m^2+n^2)+\gamma^2\alpha^2(n^2+l^2)-2\alpha\beta\gamma\sqrt{\alpha^2l^2+\beta^2m^2+\gamma^2n^2}}{\alpha^2l^2+\beta^2m^2+\gamma^2n^2}$$

Eq. 3.10

where the birefringence $b = \gamma' - \alpha'$ of any section with direction cosines l, m, n which, in a unit sphere, may be equated to the coordinates x, y, z.

The model assumes monochromatic light and a dome of constant thickness that has negligible optical effects other than birefringence. If one assumes a biaxial negative model, the orthographic distribution of birefringence in the y – z plane may be

calculated by substituting the Pythagorean equivalent of $l^2 = 1 - m^2 - n^2$ into Eq. 3.10 and taking the positive square root giving the birefringence function:

$$b(m,n) = \sqrt{\frac{\alpha^2\beta^2(1-n^2) + \beta^2\gamma^2(m^2+n^2) + \gamma^2\alpha^2(1-m^2) - 2\alpha\beta\gamma\sqrt{\alpha^2(1-m^2-n^2) + \beta^2m^2 + \gamma^2n^2}}{\alpha^2(1-m^2-n^2) + \beta^2m^2 + \gamma^2n^2}}$$

Eq. 3.11

Furthermore, Eq. 3.11 may be simplified for the section function (one-dimensional distribution) of birefringence along the optic plane (z-axis: y = m = 0):

$$b(0,n) = \sqrt{\frac{\alpha^2\beta^2(1-n^2) + \beta^2\gamma^2n^2 + \alpha^2\gamma^2 - 2\alpha\beta\gamma\sqrt{\alpha^2(1-n^2) + \gamma^2n^2}}{\alpha^2(1-n^2) + \gamma^2n^2}}$$

Eq. 3.12

and along the optic normal (y-axis: z = n = 0):

$$b(m,0) = \sqrt{\frac{\alpha^2\beta^2 + \beta^2\gamma^2m^2 + \alpha^2\gamma^2(1-m^2) - 2\alpha\beta\gamma\sqrt{\alpha^2(1-m^2) + \beta^2m^2}}{\alpha^2(1-m^2) + \beta^2m^2}}$$

Eq. 3.13

3.4.4 Retardation

If the domed surface is allowed to have a finite thickness then the retardation Λ(m, n) at any point (n, m) on the planar projection of that surface may be calculated as the product of birefringence (b) and path difference (τ) (Eq. 3.1, see also §15.3.2):

$$\Lambda(m, n) = b(m, n).\ \tau(m, n)$$

Eq. 3.14

where τ is the thickness function as defined in §15.2

3.5 Chapter Summary

1) Birefringence occurs in optically anisotropic materials and is the splitting of incident light into two orthogonally polarized light rays with different velocities and hence different refractive indices for the particular light ray direction.
2) Birefringent materials are uniaxial or biaxial.
3) Uniaxial materials are characterised by a single direction of zero birefringence (optic axis) and defined by two principle refractive indices ε and ω.
4) Biaxial materials are characterised by two optic axes and defined by three principle refractive indices $\alpha<\beta<\gamma$.
5) Birefringent materials may be represented geometrically as an index ellipsoid with principle axes corresponding to principle refractive indices. The uniaxial ellipsoid has two axes equal and in an ellipsoid of revolution, the biaxial ellipsoid is a scalene ellipsoid with axes of three different lengths.
6) Optical sign further defines uniaxial and biaxial birefringence: uniaxial is positive if $\varepsilon-\omega>0$ (prolate index ellipsoid) or negative if $\varepsilon-\omega<0$ (oblate index ellipsoid); biaxial is positive if $(\gamma-\beta) > (\beta-\alpha)$, negative if $(\gamma-\beta) < (\beta-\alpha)$.
7) Biaxial materials can be further quantified by the angle (2V) formed between the two optic axes at the origin of the index ellipsoid such that 2V is the acute bisectrix of the z-axis and x-axis respectively in positive and negative materials.
8) An analytic expression is derived from the biaxial model for refractive indices and birefringence projected onto a spherical surface.
9) A method is derived for the calculation of retardation over the planar extent of a the spherical projection of the biaxial index ellipsoid.

4 Retardation and Birefringence of the Human Eye

In this chapter a review of the literature establishes that corneal birefringence approximates to negative biaxial behaviour at least in the optic zones. A theoretical model, based on the results of Chapter 3, is created that describes the refractive index distribution, orientations of vibration direction and birefringence for transmitted monochromatic light throughout an area corresponding to the central and paracentral corneal zones. A model of retardation is derived from corneal thickness models. Finally properties analogous to those of the cornea are identified in a physical model comprising a 30μm section of the mineral aragonite (orthorhombic $CaCO_3$) cut perpendicular to the optic normal.

4.1 Literature review

The ability of fragments of cornea to change the properties of transmitted polarized light was demonstrated as early as 1815 (Brewster 1815). The first detailed account of phenomena related to corneal retardation is that of Valentin (1861) who described a dark cross-like figure and peripheral coloured rings (isochromatic rings, isochromes) when observing excised whole human corneas between crossed polarizers (Figure 4.1). The cross (isogyre: Figure 4.1a) either remained independent of orientation or broke into two hyperbolae (Figure 4.1b) when the cornea was rotated relative to the planes of polarization. The retardation was then tested by observing the effect on the equivalent of a unit retarder and quarter-wave retarder and found to be optically negative. By analogy with similar phenomena observed with mineral crystals (Figure 4.1c, d), Valentin postulated that some human corneas had properties similar to a curved optically negative biaxial crystal plate whereas others had uniaxial-like properties. Valentin commented on the differences from true biaxial isochromatics of the coloured

fringes (Figure 4.1 compare a, b with c, d) in that they did not conform to the expected pattern (one was observed to be rhombic with sharp corners) and that under moderate magnification, the rings consisted of unevenly spread colour-fields. Whilst Valentin is much cited in the early literature, he has also been misquoted in favour of an exclusively uniaxial model of corneal birefringence (Stanworth and Naylor 1950) and appears to have been largely neglected in the post 1950s literature.

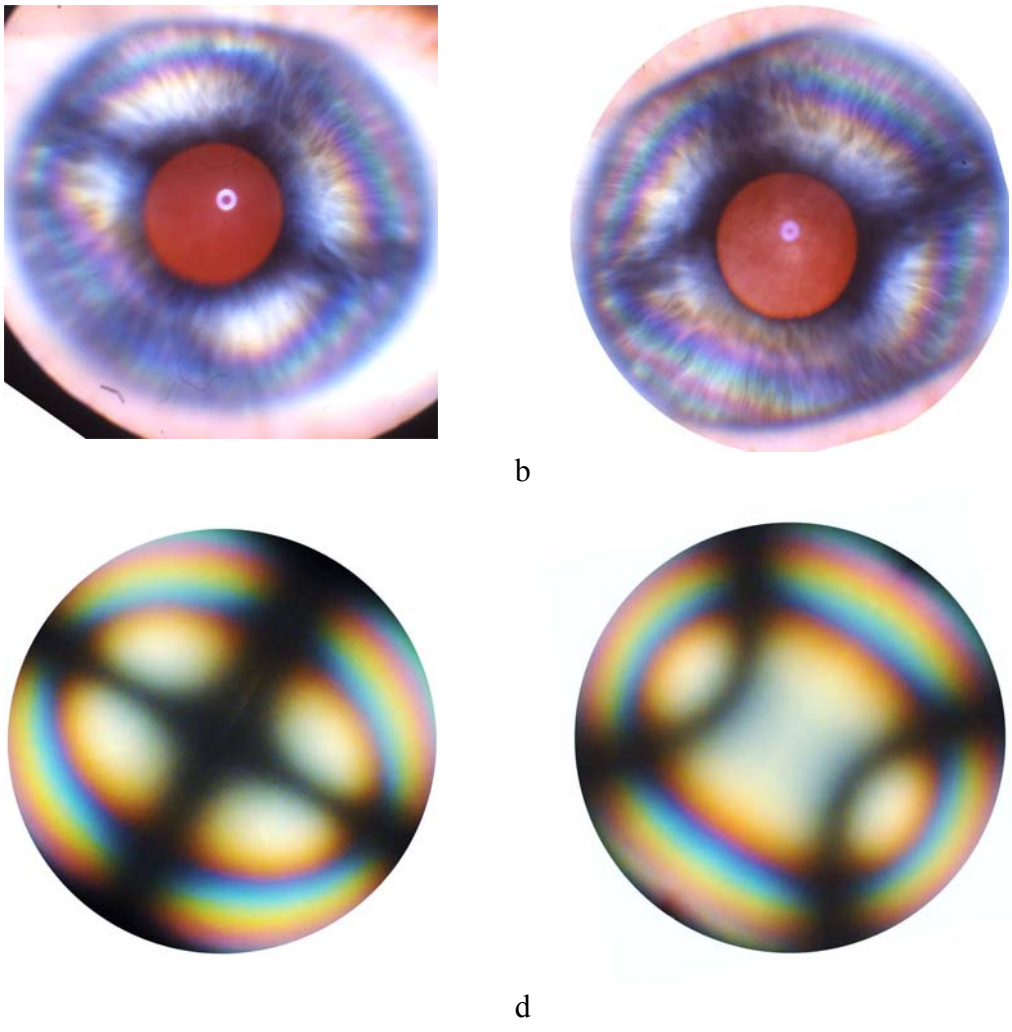

a b c d

Figure 4.1 The cornea and a biaxial crystal observed between crossed polarizers

Images of cornea (upper row: a, b) between crossed polarizers showing isogyres and isochromes with parallel incident illumination. A thin section of a typical negative biaxial material (aragonite) under conoscopic illumination (lower row: c, d). Note cross-shaped isogyre parallel to polarization axes (a, c) and conjugate hyperbolic isogyres with polarization axes at 45° to the position in (b, d). Note elliptic isochromes in true biaxial crystal (c, d) but rhombic pattern in cornea (a, b). (see §4.6 for details of c and d).

Numerous other early authors studied corneal birefringence and their historical importance is reviewed elsewhere in the literature (Stanworth and Naylor 1950; Bour 1991). Of note is the finding of Cogan (1941) who first described the 'polarization cross' in the human eye *in vivo* and isolated it to the cornea although he made no mention of the isochromes which would have been easily visible by his technique. The 'polarization cross' is a manifestation of the isogyres described by Valentin.

Whilst the central cornea behaves as a simple birefringent plate (§2.4.1), the pattern of peripheral birefringence becomes more complex and, as observed by Valentin, is manifest as isochromes. The usual description of corneal isochrome distribution is 'diamond-shaped' although there is a lack of published data concerning their origins, characteristics, and interpretation. Despite this apparent neglect, an understanding of the corneal isochromes gives at least qualitative clues to potentially useful corneal characteristics such as structure and biomechanics as will be detailed in the present study.

Following Valentin, attempts were made to classify the pattern of corneal birefringence in terms of known patterns observed in crystalline materials: uniaxial (Stanworth and Naylor 1950), biaxial (Blokland and Verhelst 1987) and non-uniaxial/biaxial (Jaronski and Kasprzak 2003) behaviour was proposed. The accepted view, and the one that will be developed further in this study, is that the cornea as a whole is biaxial (Bour 1991; Knighton, Huang et al. 2008). The biaxial model explains the observed retardation of light incident along the visual axis, the observed isogyre configuration and the distribution of birefringence in central corneal zones. Other characteristics of corneal birefringence of note are that it is linear and the cornea has negligible depolarising effect (Charman 1980), it is not significantly pleochroic and has no polarizing power

(Bueno and Jaronski 2001). In humans the fastest and slowest principle axes are respectively normal and tangential to the corneal surface. This agrees with the experimental *in vivo* findings that, when the cornea is examined *en face*, the slowest principle axis is at or near the corneal vertex and orientated in a superotemporal-inferonasal direction (Blokland and Verhelst 1987; Knighton, Huang et al. 2008). Whilst not stated, other than by Valentin, such an orientation of principle refractive indices implies that the biaxial birefringence is of negative optical sign (see §3.2). This deduction is supported by observations of optically negative biaxial birefringence in small areas of corneas using conoscopic polarization microscopy in rabbits (Kikkawa 1955; Kikkawa 1957) and man (Bone and Draper 2007).

Table 4.1 Parameters for corneal model

Parameter	Symbol	Value	Source/derivation
Corneal radius of curvature	k	7.7 mm	Gullstrand's No. 1 schematic eye (Rabbetts 1998)
Corneal radius:orthographic projection	r	6 mm	(Tripathi and Tripathi 1984)
Corneal cap radius relative to unit sphere	R	0.75	R = r/k
Mean corneal refractive index	n	1.37700	(Maurice 1984)
Optic angle	2V	35°	(Blokland and Verhelst 1987)
Maximum corneal birefringence	$(\gamma-\alpha)$	1.59×10^{-3}	(Blokland and Verhelst 1987)
Partial principle birefringence	$(\gamma-\beta)$	0.14×10^{-3}	Calculated: Eq. 3.3, 2V, $(\gamma-\alpha)$
Minimum principle refractive index	α	1.376205	Calculated: $\alpha = n-\frac{1}{2}(\gamma-\alpha)$
Intermediate principle refractive index	β	1.377655	Calculated: $\beta = \gamma-(\gamma-\beta)$
Maximum principle refractive index	γ	1.377795	Calculated: $\gamma = n+\frac{1}{2}(\gamma-\alpha)$

4.2 Methods

Equations Eq. 3.2 - Eq. 3.9 may be applied to realistic values relevant to the human cornea which, for the purpose of this study, is assumed to approximate to a cap of a

spherical shell of uniform and negligible thickness (Table 4.1). If a corneal refractive index of 1.377 (Maurice 1984) is taken as a mean value, values for α, β and γ may be derived from published values of maximum corneal birefringence (Bour 1991). The first comprehensive quantitative biaxial data is that of van Blokland and Verhelst (1987) and will be used in this study. These authors used a coordinate system in which the axis perpendicular to the corneal surface was defined as the 'z-axis' (here referred to as Z to avoid confusion) and the orthogonal 'x-' and 'y-' axes (referred to here as X and Z) were in the plane of the cornea. Using this system, the Z-axis was found to be the fastest (minimum refractive index, η_z) and X-axis slowest (maximum refractive index, η_x). The difference in refractive indices between the slowest (X) and fastest (Z) axes $|\eta_x - \eta_z| = 1.59 \times 10^{-3}$ and that between the Y and X axes $|\eta_x - \eta_y| = 0.14 \times 10^{-3}$. Thus van Blockland & Verhelst's coordinate system, which is essentially that also used by Knighton, Huang et al. (2008), is the reverse of the optical crystallographic convention in which the orthogonal x- y- and z-axes are respectively assigned refractive indices $\alpha<\beta<\gamma$ (Table 4.2). The confirmation that human corneal birefringence has negative optical sign (Bone and Draper 2007) allows the following working definitions: $\alpha = \eta_z$, $\beta = \eta_y$ and $\gamma = \eta_x$. Thus $\gamma - \alpha = |\eta_x - \eta_z| = 1.59 \times 10^{-3}$ and $\gamma - \beta = |\eta_x - \eta_y| = 0.14 \times 10^{-3}$. Furthermore, the acute angle $2V = 2V_x$ so the plane of interest in the present model, using the conventional axes, is the y – z plane. The x-axis is aligned with the direction of observation and perpendicular to the corneal surface, the z-axis is aligned with the optic plane, and the y-axis is aligned with the optic normal.

Parameter	Convention			
	Crystallographic	van Blokland and Verhelst (1987)	Knighton *et al.* (2008)	Relationship to corneal surface
Axes	*x*	*z*	*Z*	Perpendicular
	y	*y*	*Y*	Tangential
	z	*x*	*X*	Tangential
Principal refractive indices	α	η_z	n_z	Perpendicular
	β	η_y	n_y	Tangential
	γ	η_x	n_x	Tangential
Relationship	$\alpha < \beta < \gamma$	$\eta_z < \eta_y < \eta_x$	$n_z < n_y < n_x$	

Table 4.2 Coordinate system conventions

from Misson (2010)

4.3 Results 1: Refractive index

Values of principle refractive indices α, β and γ representing a typical cornea (Table 4.1) substituted into Eq. 3.7 - Eq. 3.9 generate sets of spheroconics representing distributions of a given refractive index, ρ, on the surface of an idealised spherical shell of biaxial crystalline material (equirefringence curves, Figure 4.2).

Note that in Figure 4.2 the equirefringence curves are plotted in increments of 10% for $\alpha<\rho\leq\beta$ and 1% increments for $\beta<\rho\leq\gamma$ in order to give a general impression of their distribution. The equirefringence curves comprise two populations of spherical ellipses confocal about the poles of the optic axes. One population (x-ellipses) is centred about the pole of the acute bisectrix of the optic axes (x-axis) and the other population (z-ellipses) is centred about the obtuse bisectrix (z-axis). The x- and z-ellipses intersect at right angles. Tangents to each curve at the point of intersection give the mutually perpendicular vibration directions of the two sets of waves in the wave front emergent at that point (Figure 4.3 b) (recall that vibration direction (Eq. 3.5) bears a reciprocal relationship to the wave-normal velocity surface (Eq. 3.6)).

The unshaded part of the unit sphere in Figure 4.2 is a cap with a base-radius of 0.78 (see Table 4.1) representing the area of a typical human cornea. The x-axis (acute bisectrix) passes through the model corneal apex. The orthographic projection of this area only is depicted in Figure 4.3 for equal increments of ρ as determined using Eq. 3.7. The general form of the equirefringence curves in orthographic projection is given in Figure 4.3 a where the x-ellipses and z-ellipses represent 2.5% (i.e. $^{1}/_{40}$) incremental steps from α to β and from β to γ respectively. It should be noted that an ellipse for value α is the equatorial equirefringence curve that passes through the poles of the y- and z-axes and so is outside of the area representing the cornea. The ellipses for value γ and β are respectively the great circles passing through the poles of the x- and y-axes and the x- and z-axes. The most peripheral x-ellipse represented is that of 37.5% α to γ (i.e. $\alpha+^{15}/_{40}(\gamma-\alpha) = 1.3768013$) with the ellipses $\alpha' = 1.3768410 = \alpha+^{16}/_{40}(\gamma-\alpha)$ and $\alpha'' = 1.3773180 = \alpha+^{28}/_{40}(\gamma-\alpha)$. The general form in orthographic projection along the x-axis (acute bisectrix) of the x-ellipses is elliptical and of the y-ellipses is hyperbolic with both centred on the point of the x-axis (corneal apex). Both are confocal about the points of the optic axes where the refractive index is β. The z-ellipse labelled γ' has refractive index $\gamma' = 1.3777155 = \alpha+^{38}/_{40}(\gamma-\alpha)$. Equirefringence curves representing 2.5% incremental steps form β to γ are fewer in number than from α to β as expected from the ratio $(\gamma-\beta)/(\gamma-\alpha) \approx 0.9$

Throughout the projection, apart from the optic axes, each point has two orthogonal intermediate refractive indices α or α' and γ' or γ such that $\alpha<\alpha'<\beta<\gamma'<\gamma$. For the negative biaxial model depicted here, the distributions of vibration directions (Figure 4.3b) of slow rays (refractive index γ' or γ) are aligned with the ellipses (x-ellipses) and the orthogonal fast rays (refractive index α or α') are aligned with hyperbolae (z-

ellipses). The projections of the index ellipsoid are outlined in the lower half of the figure. Note that the slow axis with principle refractive index γ is aligned with the optic plane at the apex/centre of the sphere/cornea and that the fast/slow axes are both equal to β at the position of the optic axes i.e. there is no birefringence for light transmitted at these points. At the corneal apex, where the index ellipsoid is observed along its x-axis, the refractive indices are $\alpha = 1.3762050$; $\beta = 1.3776550$; $\gamma = 1.3777950$ as in Table 4.1.

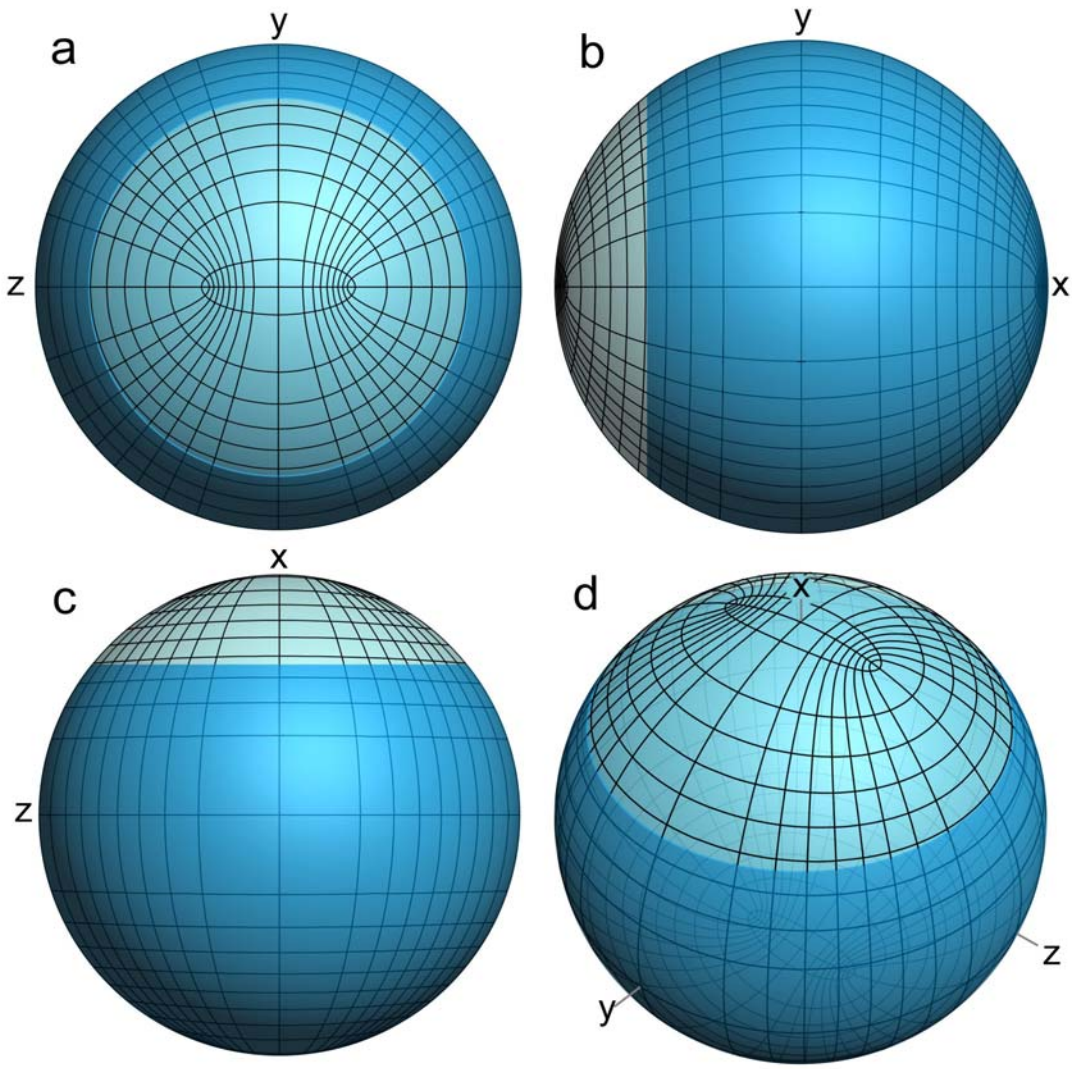

Figure 4.2 Three-dimensional representation of spheroconics ρ with parameters α, β, γ as defined in Table 4.1**.**

Note for $\alpha < \rho \leq \beta$ increments of ρ are 10% ($\gamma - \alpha$) and $\beta < \rho \leq \gamma$ increments of ρ are 1% ($\gamma - \alpha$).
Unshaded area is the spherical cap with base radius 0.78 representing the cornea.
Orthographic view along:

a) x-axis (acute bisectrix) including optic axes, optic plane and optic normal: x-ellipses are elliptic, z- ellipses are hyperbolic.
b) z-axis (obtuse bisectrix): z- ellipses are elliptic, x-ellipses are vertically hyperbolic
c) y- axis (optic normal): x-ellipses are horizontal, z-ellipses are vertical.
d) Perspective view showing general distribution of spheroconics

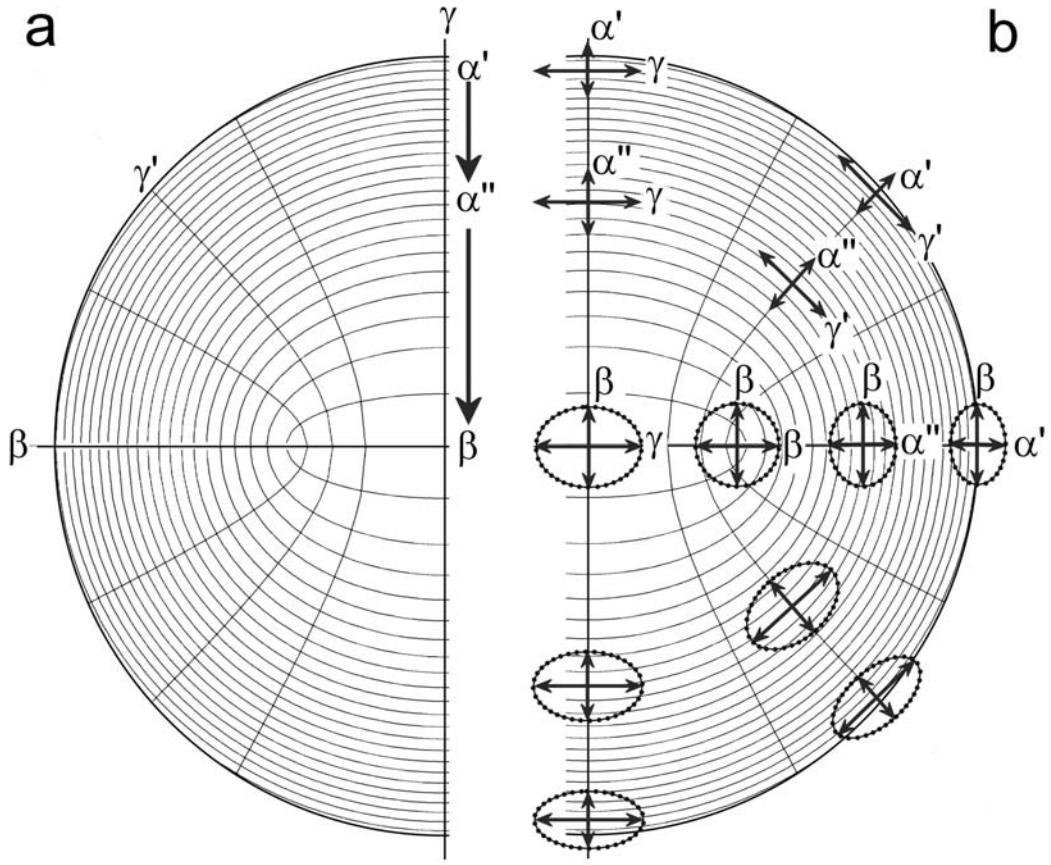

Figure 4.3 Orthographic projection of lines of equal refractive index of model cornea with principle/partial refractive indices α<α'<β<γ'<γ

Arrows indicate vibration direction at selected points on the surface of the model cornea with the length of arrows proportional to refractive index. Dotted ellipses represent projection of index ellipsoid on corneal surface

Substitution of other published biaxial results both for total birefringence (γ-α) (Bour 1991) and partial birefringence (γ-β) (Knighton, Huang et al. 2008) do not significantly alter the qualitative appearance of the equirefringence curves generated by the data of van Blokland and Verhelst (Blokland and Verhelst 1987). As β approaches γ the figure tends to a uniaxial negative form (α < β = γ) and the optic axes converge to the x-axis. In the negative model depicted here, the optic axes move together and the x-ellipses become more circular. As β approaches α, the figure tends to a uniaxial positive form (α = β < γ), the optic axes converge to the z-axis (i.e. diverge from the x-axis) and the x-

ellipses increase in ellipticity. Whilst the typical pattern of birefringence is biaxial, data exists for a negative near-uniaxial pattern (Pattern 3, Knighton, Huang et al. 2008)) in which there is minimal central corneal retardation. In the negative uniaxial case the z-ellipses become great circles passing through the x-axis and the x-ellipses are circumferential about the x-axis analogous respectively to lines of longitude and latitude.

4.4 Results 2: Birefringence

The distribution of lines of equal birefringence for a thin spherical shell of birefringent material (Figure 4.4a) may be obtained from Figure 4.3a by joining points of equal birefringence ($\gamma' - \alpha'$). More precisely, we use b(m, n), the analytical solution of Eq. 3.11 after substitution of α, β and γ as used previously and for coordinates (m, n) in the y-z plane. Once again the equibirefringence contours (Figure 4.4) are confocal about the optic axes where there is zero birefringence, and exhibit a saddle-back distribution for intermediate values (the geometric form of the contours is that of nested Cassinian curves). The contours become increasingly elliptical towards the periphery. The boundary of a theoretical cornea with base radius 0.78 is included in Figure 4.4 and, as previously, the y- and z- axes are respectively horizontal and vertical.

In one dimension (Figure 4.4b) along the optic plane (z-axis), birefringence vanishes at the points of the optic axes located at $y = \pm 0.29649$ which correspond to the foci of the equirefringence curves. The two distributions of birefringence along optic plane and optic normal are equal ($d = (\gamma-\beta) = 0.00014$) at the model corneal apex which corresponds to the x-axis of this model and of the negative biaxial indicatrix. Similar

results were published for a biaxial corneal model although it is not clear how they were derived (Blokland and Verhelst 1987; Knighton, Huang et al. 2008).

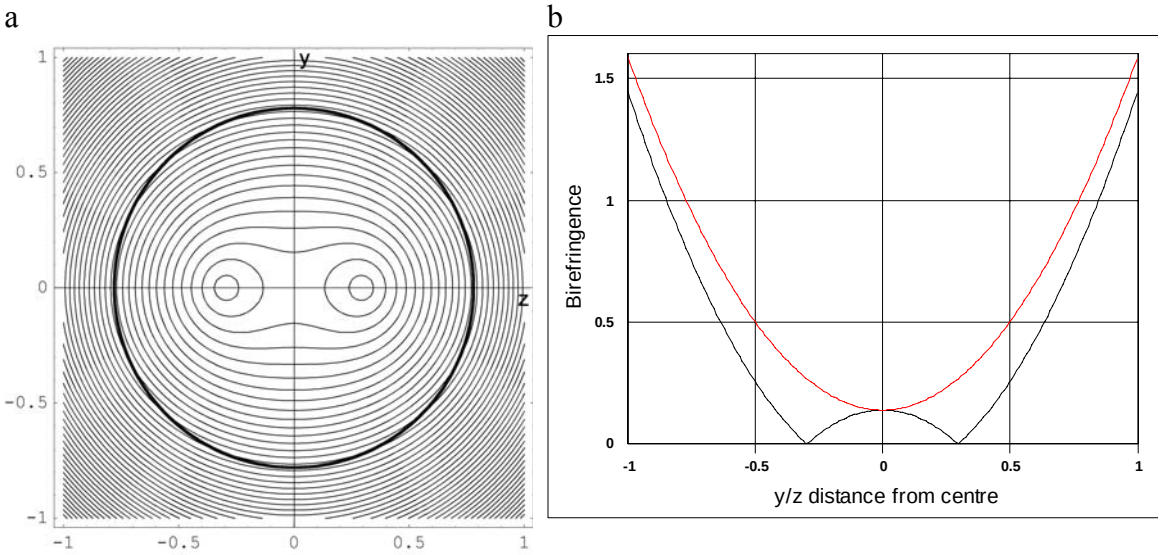

Figure 4.4 Distribution of birefringence according to Eq. 3.11 for unit sphere.

$\alpha = 1.3762050$, $\beta = 1.3776550$, $\gamma = 1.3777950$.
(a) Contours at 2% γ-β. Circle represents approximate diameter of average cornea; z-axis horizontal; y-axis vertical, scales in arbitrary length units.
(b) Section function (Eq. 3.12) through optic plane (z-axis, black, lower graph) and optic normal (y-axis, red, upper graph).

4.5 Results 3: Thickness, Retardation and Isochromes

The distribution of retardation, and hence isochromes, on the model corneal surface are given by $\Lambda(m, n) = b(m, n).\tau(m, n)$ (Eq. 3.14). The birefringence function, $b(m, n)$, is that of §4.4 so we require a corresponding light path length function $\tau(m, n)$. Models of corneal thickness are detailed in Appendix §15.2. Two models are tested here. Initially the spherical model (§15.2.3) with realistic corneal parameters is used to predict the distribution of isochromes. Secondly the astigmatic ellipsoidal τ model (§15.2.4.2) is used to determine the effect on isochromes of meridional variation in corneal thickness.

4.5.1 Thickness models

An accurate computational model of the shape of the entire cornea has yet to be developed although there are useful geometric models of curvature for the optically important central zones. The aims of previous published models are predominantly to predict curvature and refractive properties, but these are less suited to derivation of thickness data. As the current study requires realistic estimation of variation of peripheral thickness, it is necessary to develop a computational thickness model. Spherical and ellipsoidal models are used: derivations and characteristics are detailed in Appendix §15.2.

To the author's knowledge there is no readily available data relating peripheral corneal thickness variation to refractive errors including astigmatism. It will therefore be assumed that regional changes in peripheral thickness occur and the general term 'astigmatic' will be used to describe meridionally symmetric anterior curvature variations (i.e. mirror symmetry of curvature/thickness variation about a meridional axis). The corneal thickness models will be used for illustrative purposes and as approximations for the derivation of general conclusions rather than precise calculation of quantitative physiological parameters.

Both the spherical and ellipsoidal models allow for the interrelationship of the functions $t_s(m,n)$, $t(m,n)$ and $\tau(m,n)$ representing the sagittal thickness, radial thickness and light path length respectively. For a given point (m,n) the refracted path length, τ , can be taken to be a value between t_s and t (Figure 15.5). For the purposes of this study it is sufficient to know that $t<\tau<t_s$. This is relevant when modelling the patterns of

birefringence and takes into consideration limitations of the geometric models (see Appendix §15.2). The derivation of the function $t_s(m,n)$ (Eq. 15.5) is given in §15.2.4.

4.5.1.1 Spherical model

The spherical model (see Figure 15.3; Appendix §15.2.3) assumes that the cornea has spherical anterior and posterior surfaces of radii r_f and r_b respectively. The centres of curvature are on the central axis of rotation of the surfaces, but with r_b posteriorly displaced by an amount equal to the central corneal thickness (t_0). This model in radially symmetric, i.e. does not model astigmatism. The benefit of this model is its simplicity and that it can be readily related to keratometric data (see §15.5.1).

4.5.1.2 Conic model

The conic model (Appendix §15.2.4) assumes that the anterior and posterior corneal surfaces are ellipsoidal and each surface is characterised by parameters that equate to the intersections of the surface with a 3-dimensional Cartesian coordinate system. The flexibility of this model allows variation in meridional curvatures of both conic surfaces i.e. astigmatism.

Three variants of the model were used. E0 represents an anastigmatic (radially symmetric) cornea. Ea represents a high degree of 'physiological' astigmatism of approximately 5 dioptres that may be taken as an upper bound of what, exceptionally, can occur *in vivo*. Ex is an 'extreme astigmatic' surface that has no real anatomical counterpart, but will be used later when investigating peripheral birefringence in Chapter 11. The spherical model may be derived from the elliptical model by an appropriate choice of parameters.

The general form of the anastigmatic model (E0) is shown in Figure 4.5 The parameters a = 1 = b, c = 0.93 are chosen to approximate (after appropriate scaling) to corneal values with a central (spherical) curvature of 7.7mm (Figure 4.5a) and a central corneal thickness of 550 μm. The posterior curvature is assumed to be spherical with a radius 6.5mm (a = b = c = 0.84 (Figure 4.5c). The sagittal distance (t_s) is the difference between anterior and posterior curvatures at a given point (m,n) on the projection of the corneal surface onto the x-y (or y-z) plane (Figure 4.5d). A general impression of the surfaces may be seen in the 3-dimensional graph of the bisected surfaces (Figure 4.5 b). The contours of the astigmatic surfaces Ea and Ex are shown in Figure 4.6 in which the anterior surface contour is given in the left column and sagittal thickness (t_s) is on the right. The section functions of the heights of the maximum and minimum meridians and relevant sagittal thicknesses are given in Figure 4.7.

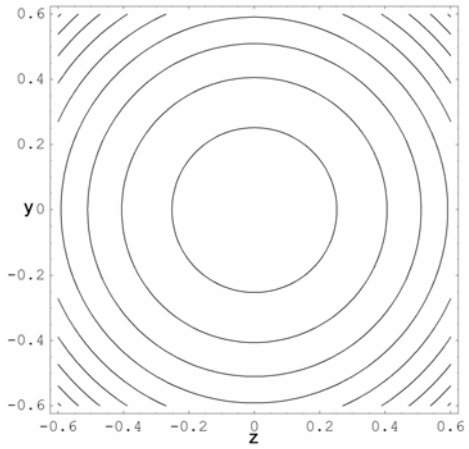

a Front surface, anastigmatic
(y- and z-axes in fractions of unit sphere)

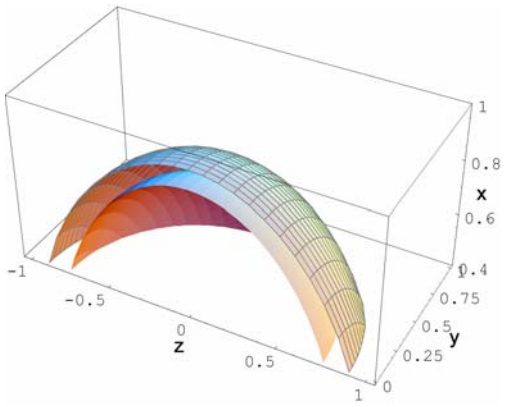

b Three-dimensional reconstruction

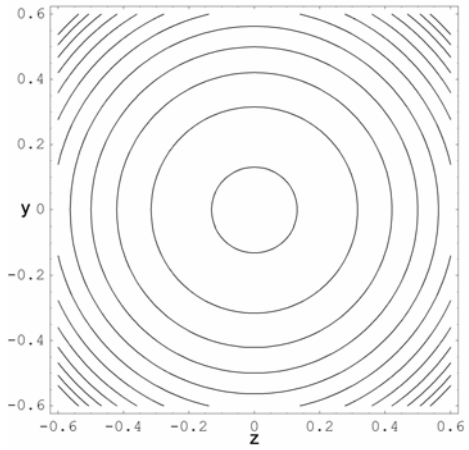

c Back surface (spherical)

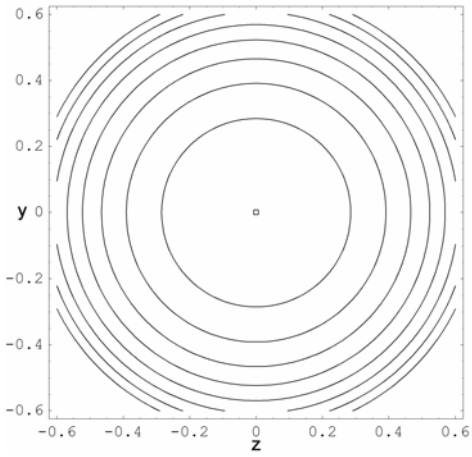

d difference (sagittal thickness)

Figure 4.5 Anastigmatic corneal thickness model: radially symmetric surfaces (E0).

(a) Contour plot of anterior surface; parameters a = b = 1.0, c = 0.93 (central height 0.93, central contour 0.90)
(b) Contour plot of posterior surface; parameters a = b = c = 0.86 (central height 0.86; central contour 0.85)
(Contours at 0.05 unit intervals, decreasing outwards).
(c) A bisected 3-dimensional representation of the surfaces.
(d) Contour plot of sagittal thickness (t_s) i.e. anterior – posterior surfaces (central point 0.7, contours at 0.01 intervals, increasing outwards).
Scales in fractions of unit sphere such that (x, y, z) = (1, 0, 0), (0, 1, 0), (0, 0, 1) are radii of unit sphere.

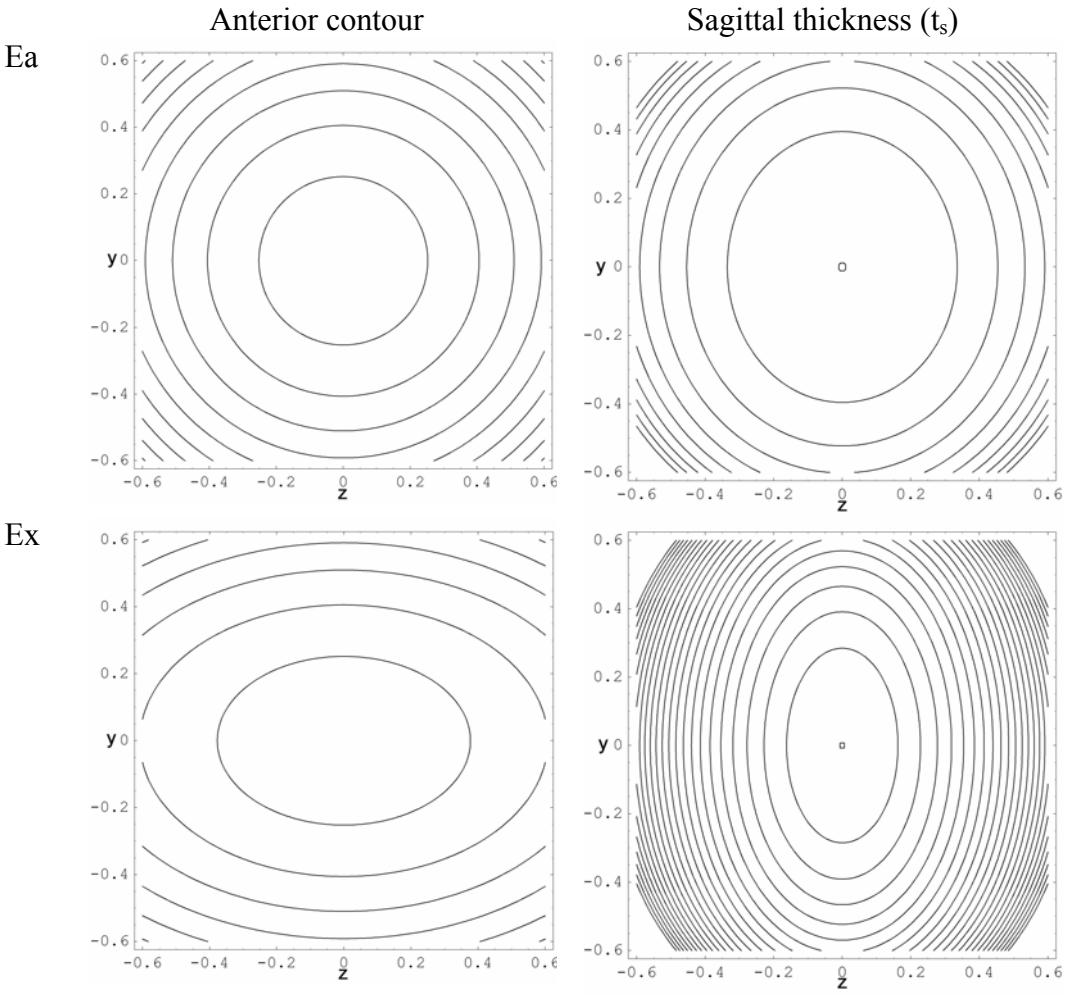

Figure 4.6 Astigmatic corneal models.

Anterior corneal contour plot on left, sagittal thickness (t_s) on right. Ea (upper row) representing approximate anterior corneal astigmatism of approximately 5 dioptres (parameters a = 0.94, b = 0.964, c = 0.93, d= f = h =0.86; see 15.2.4.2). Ex (lower row) representing extreme astigmatic state used in evaluation of isochrome model (parameters a = 1, b = 1.498, c = 0.93, d= f = h =0.86). Central corneal parameters, scales, and contour intervals as in Figure 4.5.

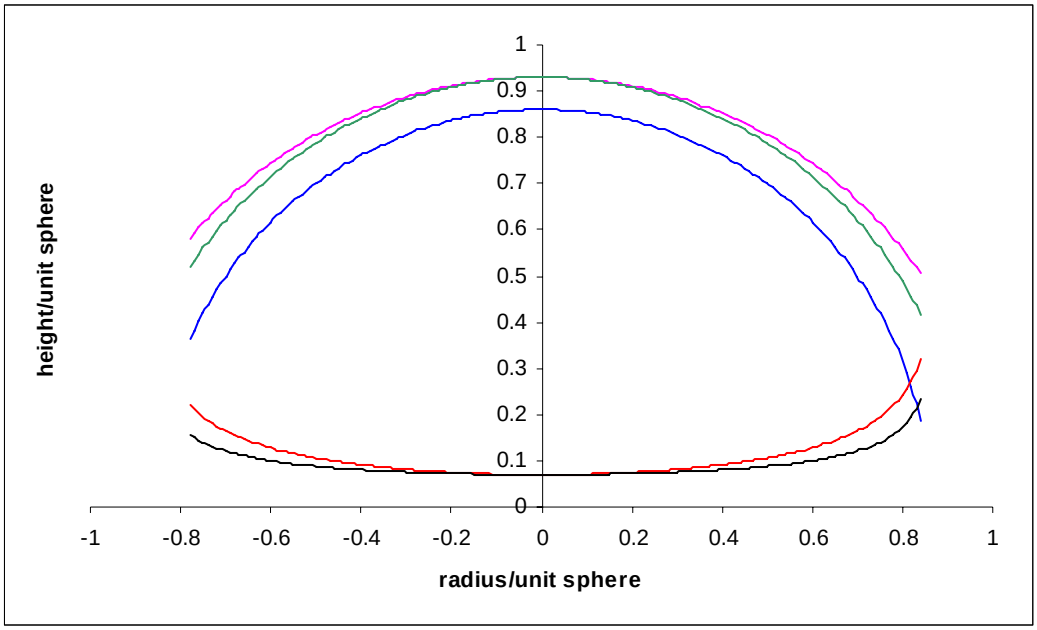

a

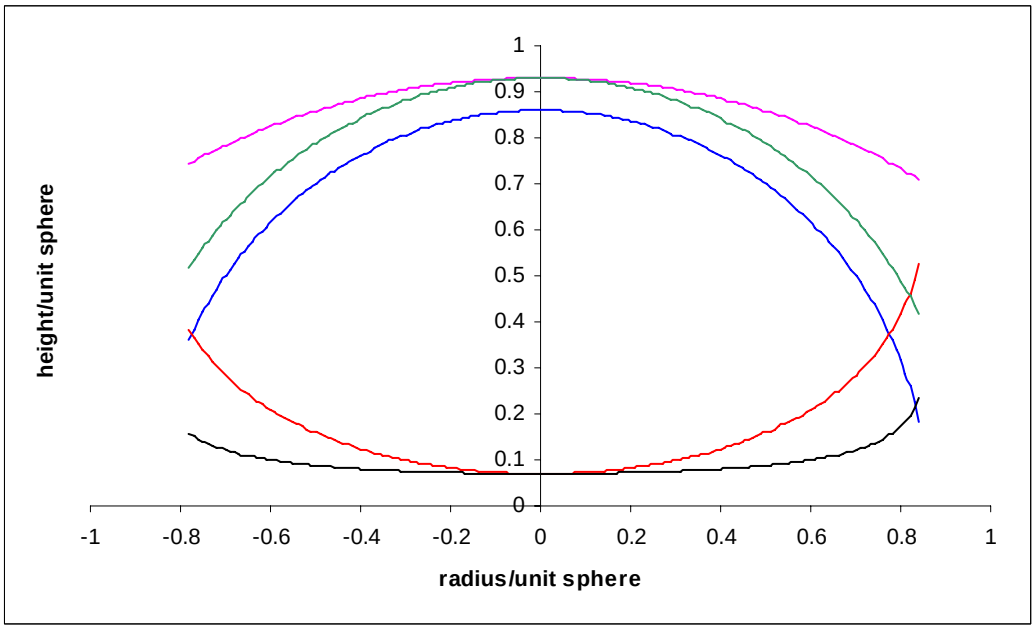

b

Figure 4.7 Elliptic corneal model: section functions

(a) Ea parameters a = 0.94, b = 0.964, c = 0.93, d= f = h =0.86;
(b) Ex parameters a = 1, b = 1.498, c = 0.93, d= f = h =0.86
Upper curves represent corneal surface height profiles (from lower to upper) of posterior surface (blue) and anterior surface steep meridian (green) and anterior surface flat (pink) meridian. Lower curves (red:maximum; black: minimum) are sagittal thickness profiles (anterior – posterior) as a function of distance from the corneal apex/centre.
horizontal axis = radius; vertical axis = height/thickness; scales in fractions of unit sphere such that (x, y) = (1, 0), (0, 1) are radii of unit circle / sphere.

4.5.2 Retardation: Spherical model

The retardation function Λ(m, n) was calculated using τ(m,n) determined for a hypothetical spherical cornea with mean refractive index n = 1.376, front radius (r_f) 7.7mm, back radius (r_b) 6.8mm and central corneal thickness (t_0) 0.5mm. The overall pattern of equiretardation contours (Figure 4.5) is similar to the Cassinian curve configuration of equibirefringence (Figure 4.4a). Two foci of zero retardation are surrounded by a saddle-back configuration that opens out to elliptical and then near circular contours in the periphery. The boundary of a model cornea is included in Figure 4.5 (black circle) as is the ½ λ equiretardation contour (red contour) which forms an ellipse within the corneal boundary. If the thickness of the dome increases to the periphery uniformly in all meridians, then the spacing between successive equirefringence lines and hence isochromatics, will be correspondingly narrowed.

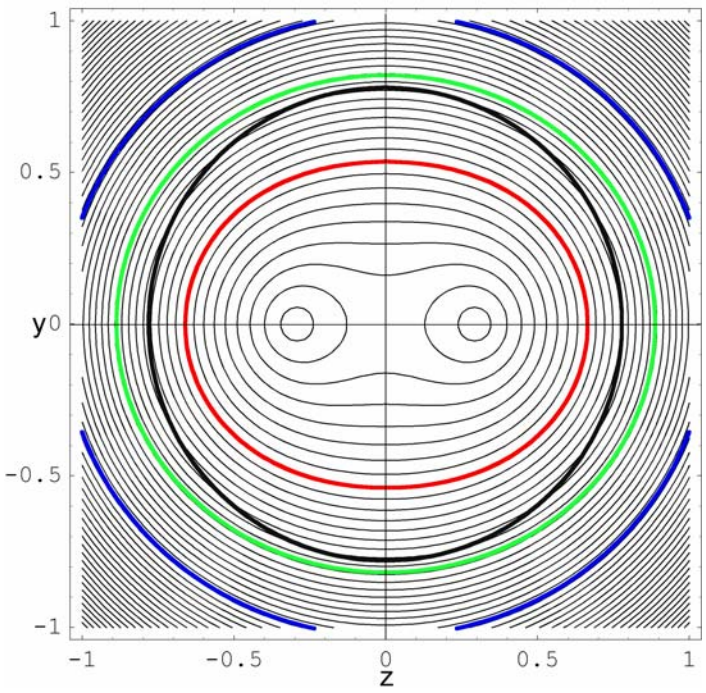

Figure 4.8 Equiretardation contours for spherical model.

Contours at 2% intervals and 0.5λ (red), 1λ (green) and 1.5λ (blue). Black circle indicates approximate corneal boundary (base radius 0.78 of unit sphere). Unts are fractions of unit sphere as in Figure 4.5

4.5.3 Retardation: Astigmatic model

In reality, most corneas are astigmatic and show meridional variations in curvature and thickness. It is necessary to determine the effect of these variations on equirefringence contours if the pattern of biaxial isochromes is to be modelled. Eliciting, detecting and analyzing isochromes will form a large part of the experimental investigations later in this study and will be discussed in detail in Chapter 7 *et seq*.

An astigmatic conic model (Ea, §15.2.4.2) is used to derive a thickness function corresponding to approximately 5D astigmatism. The meridional curvature of the anterior corneal surface only is varied in this model which is assumed to represent a maximum bound of reality as explained in §4.5.1. The parameter values a = 0.94, b = 0.964, c = 0.93, f = g = h = 0.86 are taken to represent typical corneal values and correspond to a model cornea with central thickness 539μm.

The model is further modified to allow rotation such that the meridians of maximum and minimum curvatures/thickness can be orientated at any angle Θ from horizontal. This allows the effect of meridional changes in thickness on equiretardation contours to be determined. Representative results are presented in Figure 4.9 where the meridians of maximum sagittal thickness are respectively orientated at $\Theta = 0$, $\pi/4$ and $\pi/2$ relative to horizontal. The thickness contours are presented in the left hand column and the resultant effects on predicted retardation/isochromes are central and right hand columns. The equiretardation contours in the conic model are similar at all orientations of the astigmatic model indicating that physiologically realistic variations in corneal thickness have little effect on the equiretardation contour pattern.

Θ	Thickness profile	Isoretardation	0.5λ (inner), 1λ, 1.5λ (outer) isoretardation contours
π/2	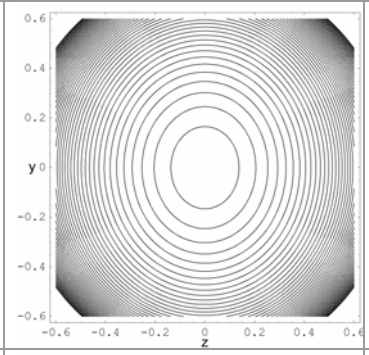	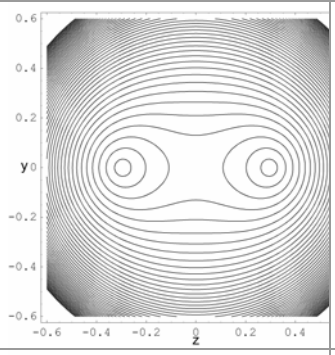	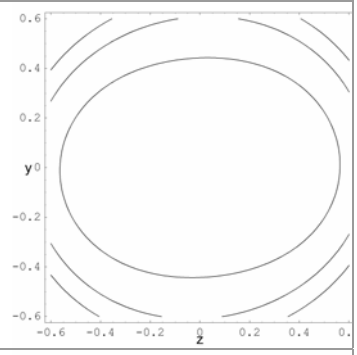
π/4	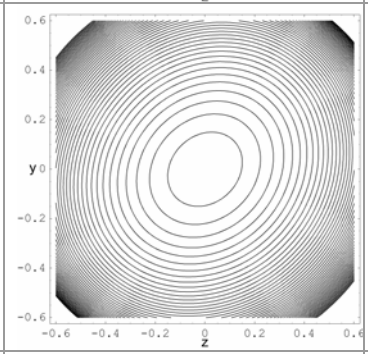	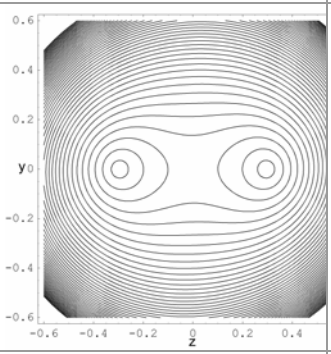	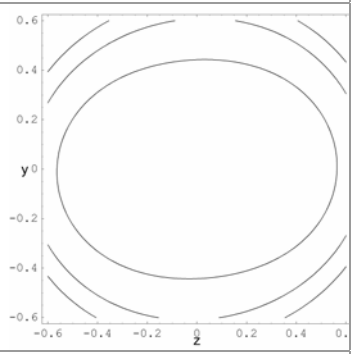
0	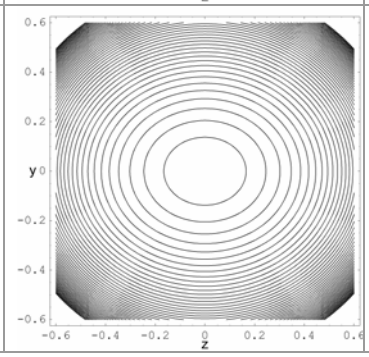	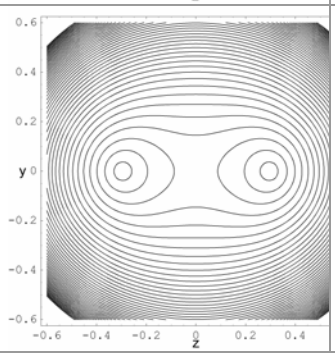	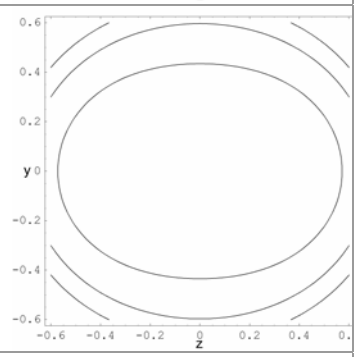

Figure 4.9 Equiretardation contours of astigmatic corneal thickness model Ea

1st column: corneal thickness contours rotated by Θ = 0, π/4 and π/2
2nd column: Isoretardation contours as in Figure 4.5
3rd column 0.5λ (inner), 1λ and 1.5λ isoretardation contours
Parameters α = 1.376205, β = 1.376345, γ = 1.377795; a = 0.94, b = 0.964, c = 0.93 f = g = h = 0.86.
Scales and axes as in Figure 4.5

4.6 A physical analogue of corneal birefringence

Returning to Valentin's original comparison of the pattern of corneal birefringence to naturally occurring crystals, it is logical to ask if there is any such material that exists that might be a useful physical analogue of the living cornea, or at least can be used for comparative purposes. The benefits of such a model are that it is a pure biaxial material, is physically robust, and can be studied under conditions unfavourable for biological materials. Such a model was reported by Blokland and Verhelst although no details are published (Blokland and Verhelst 1987), or given in van Blokland's PhD thesis (Blokland 1986).

A dome of negative biaxial crystalline material with construction similar to that of the cornea is required. It is impractical and prohibitively expensive to fabricate such a structure, but an optical equivalent is to observe a flat plate of appropriate crystalline material with convergent polarized light under a petrological microscope. This method is termed conoscopy and is one of the basic techniques of optical crystallography as applied to mineralogy (see e.g. Johannsen 1914; Wahlstrom 1979); although it has also been applied to small areas of *ex vivo* cornea (Mishima 1960; Bone and Draper 2007). Minerals have higher refractive indices and birefringences than biological material, but this can be compensated for by scaling (e.g. using thin sections). The required parameters therefore are negative biaxiality, retardation of 60 - 120nm normal to the surface, and 2V of approximately 30°. Muscovite and aragonite are two minerals with the required characteristics. Muscovite mica (2V = 35°) is a well-known rock forming mineral and can be easily cleaved into thin sheets perpendicular to the optic normal although the higher 2V makes isochromes difficult to study with the available light

microscopic methods. Aragonite ($\alpha = 1.530$, $\beta = 1.682$, $\gamma = 1.686$; $2V = 18°$), an orthorhombic polymorph of $CaCO_3$ (the other hexagonal polymorph is calcite/Iceland spa), is less well know and has a lower 2V than that described for the cornea. It is relatively soft and may be cut in such a way as to generate isotropes and isochromes that are within the range of those observed in the cornea.

For the images created for this study a Vickers M72 petrological microscope was used and adapted for digital photomicrography (Nikon D90 camera back). Conoscopic polarization microscopy with a Bertrand lens was performed according to standard methods with ×40 NA 0.65 objective and white light (Wahlstrom 1979). A 30μm section of aragonite cut (near) perpendicular to the optic normal ($\gamma - \beta = 0.004$, hence Λ = 120nm) was used throughout and examined under conoscopic illumination with crossed polarizing filters (Figure 4.10b, d, Figure 4.1). A similar 30μm thick cleavage plate of muscovite was used for comparison (Figure 4.10a, c).

In all cases dark cross/hyperbolic isogyres are observed with peripheral elliptic isochromes. For the particular microscopic configuration used in the study, isochromes were better defined for aragonite. The isogyres have a cross-like configuration (0° position; Figure 4.10a, b) when orientated with the optic axial plane parallel to one of the polarization axes. The limbs of the cross break into conjugate hyperbolae when the crystal is rotated away from this position. The hyperbolae appear to pivot around the points of the optic axes until the optics axial plane is at 45° from the polarization axes when the hyperbolae are symmetric (Figure 4.10c, d). The isochromes remain unchanged by orientation.

The hyperbolic isogyres of muscovite are more widely spaced than aragonite reflecting the difference in locations of the optic axes of each mineral (2V = 35°muscovite, 18° aragonite). Furthermore, the sample of aragonite used in this study generated isochromes that were clearly within the field of view and resemble more closely those of the human cornea. Aragonite, rather than muscovite, will therefore be used as a reference of a true negative biaxial material with which the birefringent properties of the cornea can be compared. This will be explored more in §11.1.

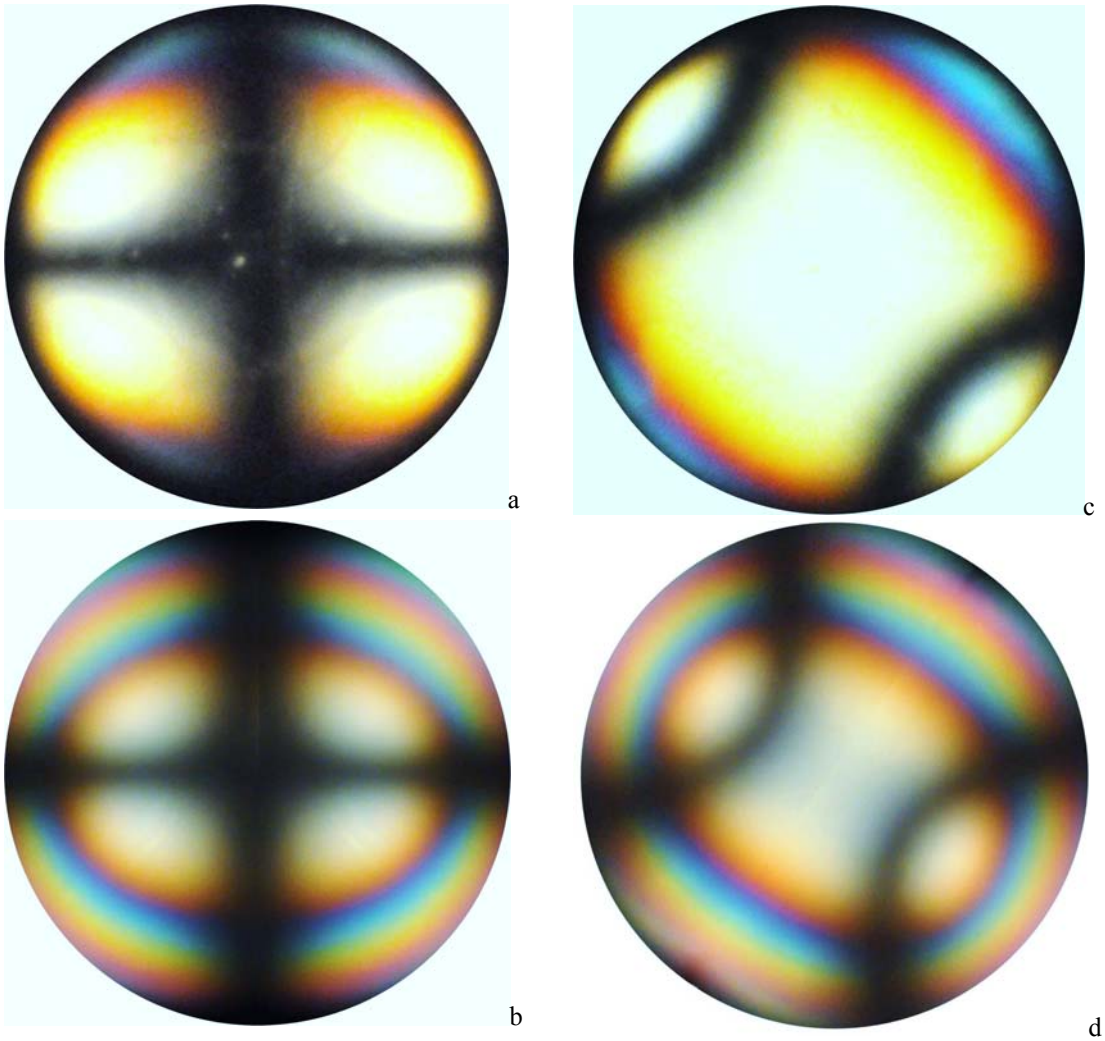

Figure 4.10 Muscovite (a, c) and aragonite (b, d) 30µm sections.

Conoscopic images observed with Vickers M72 polarizing microscope in 0° (a, b) and 45° (c, d) positions: Bertrand lens,400x NA 0.65 objective, white light. Note cross-like and hyperbolic isogyres and peripheral coloured elliptic isochromes.

4.7 Discussion

In this theoretical study the principles of optical crystallography are applied to measured and derived parameters relevant to the central 7 – 8 mm (central and paracentral zones) of the human cornea. Aspects of the theoretical model have been published elsewhere (Misson 2010). Standardised optical crystallographic definitions are adhered to and it is proposed that this convention be used in subsequent studies in order to avoid confusion. The present study shows that the negative biaxial model of corneal birefringence predicts a characteristic distribution of refractive indices and vibration directions across the model corneal surface. In particular, lines of equal refractive index/vibration direction form orthogonal spherical ellipses. In orthographic projection, such as when observing the cornea *en face* (i.e. along the normal to the corneal centre, and x-axis as defined in this study), the vibration directions of slow rays (with refractive indices γ to γ' to β) follow an elliptic (x-ellipse) distribution and the orthogonal directions of fast rays (with refractive indices α to α' to β) follow a hyperbolic (z-ellipse) distribution. The biaxial corneal model is based on the optics of a crystalline material with uniform structure and physical properties. This is not the case for the cornea which, in reality, is heterogeneous, of finite thickness, and composed predominantly of locally and globally aligned meshworks of collagen fibrils in a matrix.

4.7.1 A biaxial model of corneal structure

The question arises as to the structural implications of the biaxial model of corneal birefringence and the implications of the results of this study. This will be discussed in

greater detail in later chapters and specifically in §13.4 , but several observations will be made here.

Corneal form birefringence is that of a Weiner type 1 mixed body (ground substance is of lower refractive index than the fibrils) and is therefore uniaxial with slow axis (direction of highest refractive index and therefore greatest retardation of light velocity) along the length of the fibril (length-slow) (Bour 1991; Born and Wolf 2005). Furthermore the fibrillar elements are predominantly type 1 collagen which is also intrinsically positive (length slow) uniaxial birefringent (His 1856; Wolman and Kasten 1986). Thus the structural elements of the corneal stroma are positive uniaxial (length slow), yet the cornea as a whole has a pattern of birefringence/retardation similar to a negative biaxial crystalline structure. This apparent paradox has structural implications and implies a particular configuration of bundles/lamellae.

Consider a homogenous flexible uniaxial positive length-slow birefringent fibre where the greatest refractive index (ε) is along its length and the lowest principal refractive index (ω) across its width. A distribution of vibration directions (but not birefringence) qualitatively similar to a biaxial pattern results if such fibres were orientated on part of the surface of a sphere according to the depicted confocal elliptic (x-ellipse) pattern as indicated in Figure 4.2 and Figure 4.3. In such a configuration, ε corresponds to γ, γ' and β respectively at the centre (perpendicular to the optic normal), at intermediate positions and perpendicular to the optic plane. Similarly ω corresponds to β at the centre, α'' and α' at intermediate locations tending to α in the periphery. An overlying hyperbolic (z-ellipse) array of fibres, if of sufficient density, crossing the elliptic (x-ellipse) fibres at right angles causes negation of birefringence at the points of the optic axes. Elsewhere, this fibre configuration results in a pattern of vibration direction,

refractive index and birefringence emulating biaxial behaviour. Conversely, positive biaxial behaviour results if the fibres are uniaxial negative and in a predominantly elliptic distribution, or uniaxial positive in a predominantly hyperbolic distribution.

Thus the observed positive biaxial behaviour of the whole cornea can be explained by an overlapping meshwork of orthogonal negative birefringent fibre-like elements with spherical elliptic geometry as depicted in Figure 4.2 and Figure 4.3. The spheroconic elements overlap, run parallel or orthogonal to adjacent spheroconic elements, and are of varying ellipticity, but confocal about the positions of the observed null-points of birefringence (optic axes of the biaxial model). The populations of z-ellipses are less dense than the x-ellipses which increase in major and minor diameters but decreasing in ellipticity (i.e. become more circular) towards the corneal periphery.

Whilst the collagen bundles/lamellae seem a likely candidate for the uniaxial birefringent structural elements, these and alternative structures will be discussed in greater detail in §13.4 where a novel model of corneal structure will be proposed.

Of general note is the symmetry required for biaxial optics. Inspection of Figure 4.2 and Figure 4.3 indicates that biaxiality has a 2-fold rotational symmetry about a central point and two axes of reflection whereas there is infinite rotational and reflection symmetry in the uniaxial case. It is postulated, therefore, that 2-fold rotational symmetry and two axes of reflection characterise some aspect of corneal lamellar structure and that these conditions of symmetry are a requirement for models of corneal stromal lamellar structure.

The association between lamellar distribution and birefringent optics allows for a more general assertion that any structural model must be compatible with the observed pattern of birefringence.

The accepted view that isochromes are quadrangular disagrees with the elliptic patterns predicted by the biaxial model. Previous descriptions of isochromes are anecdotal and there is no convincing study, to the author's knowledge, of isochrome distribution. Furthermore, several authors have attempted to analyse the birefringent properties of the isochromes and relate this to corneal structure (see §13.1). Their results and interpretation, possibly biased by assumptions of uniaxial behaviour, require further clarification in the light of more recent studies both of corneal birefringence optics and corneal structure (see §2.2.3).

To test the biaxial model it is therefore necessary to accurately determine the magnitude and distribution of corneal birefringence as a whole and the distribution of isochromes in particular. The next aim of the present study is to devise and apply a simple method for observing, recording, and analyzing the birefringent behaviour of human corneas *in vivo*.

4.8 Chapter summary

1) The central cornea behaves as a linear retarder of magnitude ≈50nm with slow axis nasally downward by ≈20° from horizontal.
2) There is great intersubject variability in central retardation (magnitude and azimuth).
3) The optic zones of the cornea behave like a negative biaxial material.
4) A negative biaxial theoretical model is developed using the crystallographic coordinate convention with the x-axis normal to the surface.
5) The negative biaxial model of corneal birefringence predicts a characteristic spherical elliptic (spheroconic) configuration of orthogonal refractive index (equirefringence) contours when projected onto a spherical surface.
6) At each point of the corneal surface, there is an intersection of paired orthogonal equirefringence contours.
7) For each equirefringence contour centred on the x-axis, there exists a complementary orthogonal spherical elliptic counterpart with its centre on the z-axis.
8) When projected onto the y-z-plane, orthogonal spheroconic equirefringence contours of the negative biaxial model have an elliptic/hyperbolic configuration.
9) Contours of equal birefringence (equibirefringence contours) projected onto a spherical surface are centred on the x-axis and confocal with the positions of the intersection of the biaxial optic axes with the surface.

10) Birefringence is zero at the optic axes and finite at the intersection of the x-axis with the spherical surface where the maximum principle refractive index is on the optic plane joining the loci of the optic axes.
11) The configuration of equibirefringence contours follows a ‘saddle-back’ central configuration, a ‘figure-of-eight’ intermediate configuration and elliptic peripheral configuration (Cassinian curves).
12) Contours of equal retardation (equiretardation contours) are derived from the equibirefringence function and models of corneal thickness
13) Equiretardation contours of the corneal model follow the pattern of equibirefringence contours with zero retardation at the positions of optic axes (isotropes).
14) The retardation at the centre of the model negative biaxial cornea is finite with its slow axis along the optic plane (i.e. along a line connecting the isotropes).
15) Physiological variations in meridional corneal thickness representing high astigmatism have little effect on equiretardation contours.
16) A useful comparative physical demonstration of negative biaxial optics is monocrystalline aragonite in thin section observed with conoscopic polarized illumination with the petrological microscope.
17) Biaxial birefringent behaviour implies structural symmetry comprising 2-fold rotational symmetry and two axes of reflection coincident with the corneal centre.

5 Polariscopy

In previous chapters, a negative biaxial model predicted the distribution of refractive index, birefringence and retardation of the human cornea. Furthermore it was postulated that the cause of the observed retardation of the living cornea was due to a spherical elliptic distribution of birefringent elements. Disparity between the biaxial model and limited *in vivo* descriptions of isochromes raised doubts of the validity of this model in the corneal periphery.

The aim of this section is to develop a method to determine the retardation of the human cornea *in vivo* and hence test the validity of the biaxial model. The requirements are that the method is quick, efficient, safe, inexpensive and can be used in an everyday clinic setting on a larger number of naïve subjects *in vivo*.

5.1 Polariscopy

Polariscopy is any method that uses polarized light to determine the distribution of retardation in a transparent material. Polarimetry is a method that derives quantitative information using polariscopic techniques. Polariscopy/polarimetry is commonly used to detect stress-induced birefringence in photoelastic stress analysis, for the identification of gemstones, and in petrology. In the latter case, specially adapted microscopes (petrological or polarizing microscopes) are used to determine and analyze the birefringent properties of crystalline minerals in thin sections of rock. Polariscopy may be performed with light transmitted or back-reflected through a sample. Furthermore retarders of known properties can be inserted into the light path to test the

birefringent properties of the sample (e.g. to determine magnitude and direction of retardation).

The discipline of polariscopy has developed its own terminology. Thus the term 'fringe' is synonymous with isochrome and refers to the coloured lines in a birefringent sample as seen with the polariscope using white light. They represent lines of equal retardation and, in photoelastic terms, are lines which join points with equal maximum shear stress magnitude. Isoclinics may be equated to isogyres as previously defined and represent the locus of points of extinction i.e. optically isotropic areas of the sample when linear polarized light is transmitted without alteration and is negated (extinguished) by a second orthogonal polarizing filter (analyzer). A focal area of isotropic trasmission is termed an isotrope. In photoelasticity, isoclinics identify the locus of points in the sample along which the principal stresses are in the same direction as the vibration directions of the polarizer/analyzer.

Polariscopy with reflected light is used in photoelastic stress analysis where a reflective prototype is coated in a photoelastic material. Careful interpretation of results is required as a simple relationship between induced birefringence and stress only occurs with normal incidence illumination and reflection alters the state of polarization.

The use of photoelastic terminology in the study of corneal birefringence is potentially confusing as it has been taken to imply that corneal birefringence is photoelastic. This assumption has misled a number of previous investigators (e.g. Mountford 1982; Ichihashi, Khin et al. 1995; Volkov, Malyshev et al. 1990). As stated in §2.4.1, photoelasticity is insignificant in corneal optics where retardation, and hence the fringes/isochromes and isoclinics/isogyres, results from form and crystalline

birefringence. The use of photoelastic terminology which might suggest otherwise will be avoided.

5.1.1 Ophthalmic polariscopy

The simplest polariscopic studies of whole cornea have been on isolated dissected specimens between crossed polarizers. This was the method of earlier investigators such as Schiötz, Valentine and later Naylor and Stanworth (cited in Bour 1991)) and from which the conflict regarding uniaxial or biaxial behaviour arose (§13.1). Polarization microscopy of histologically prepared corneal sections (e.g. Figure 2.3) significantly advanced understanding of corneal cross-sectional architecture (e.g. Tripathi and Tripathi 1984; Bron, Tripathi et al. 1997). What studies there are do not take full advantage of the rotational stage of the polarizing microscope and describe the polarization phenomena without reference to orientation of the sample relative to the planes of polarization of the polarizer/analyzer. Human *ex vivo* studies have also been limited by small sample numbers and possible confounding factors such as post mortem changes and fixation artefact.

In vivo biomicroscopy of the human eye in white unpolarized light is a standard technique used routinely in clinical practice, but gives little structural information about the stroma and its lamellar organisation. Biomicroscopy of the human cornea *in vivo* using reflected linear polarized light was first described in some detail by Koeppe (1921), who identified an interweaving network of lines in the stroma. These findings were later confirmed by Mishima (Mishima 1958; Mishima 1960) who proposed that the observed effects were due to peripheral radial and central interlacing populations of collagen fibrils. It was suggested that linear polarization biomicroscopy might be a

useful technique for the evaluation of corneal stromal structure in health and disease. The 1950-70s saw pioneering investigations into corneal birefringence and polarization physiological optics, but thereafter interest declined apart from the key finding that established the biaxial model (Blokland and Verhelst 1987). Up to this time the principle driving force behind the research was to determine and understand normal physiology and anatomy. Clinical investigations were limited to unsuccessful attempts to use stress-induced birefringence to measure intraocular pressure (Nyquist and Cloud 1970) and to measure glucose concentration in the aqueous humour of the anterior chamber by determining optical rotation (Rabinovitch, March et al. 1982). Attempts to directly visualise stress birefringence induced in the living human cornea by surgical manipulation (Misson and Stevens 1990) did not progress.

Developments in ophthalmic polarimetry gained momentum with the advent of scanning laser polarimetry (SLP) (Dreher, Reiter et al. 1992), a technique developed to analyse the retinal nerve fibre layer in order to diagnose and monitor glaucoma. The relatively weak retinal birefringence was dominated by that of the cornea and early SLP devices had a fixed retarder (60nm orientated slow 15° nasally downward) to compensate for the corneal retardation (Dreher and Reiter 1992). Initial results from numerous studies (see Garway-Heath, Greaney et al. 2002 for summary) showed the technique to be inferior to others in its ability to discriminate normal from glaucomatous eyes and this was found to result from the naïve assumption about the constancy of the magnitude and azimuth of the corneal retardation. This assumption also probably accounted, at least in part, for the failure of the aqueous humour glucose measurements (Rabinovitch, March et al. 1982; Malik 2009). Further studies (Knighton and Huang 2002; Weinreb, Bowd et al. 2002) more accurately defined the extent and variability of

human central corneal retardation which led to the introduction of SLP with a variable retarder and a consequent increase in the accuracy of the technique (Tannenbaum, Hoffman et al. 2004) . Despite this, SLP has now largely been superseded by optical coherence tomography (OCT), an interferometric technique that measures the echo-time delay and magnitude of back-scattered or reflected light to construct a 2- and 3-dimensional image of ocular cellular (e.g. retinal) components (Huang, Swanson et al. 1991).

Compensation of ocular birefringence remains important in OCT in that similar polarization states are required in the reference and sample beams to maximise interference. A natural development of OCT is polarization-sensitive OCT which, at the time of writing, is not yet commercially available but promises to further extend the diagnostic facility of interferometric techniques by measuring retardation data as well as scatter/reflection (Pircher, Hitzenberger et al. 2011). Other extensions of OCT currently under development include dual-beam-scan Doppler optical coherence angiography (OCA) (Makita, Jaillon et al.) and polarization-sensitive swept-source OCT (Yamanari, Makita et al. 2011). All techniques that image birefringent structures within the eye and beyond the cornea require the initial compensation of corneal retardation, thus a clear understanding of magnitude, orientation and spatial distribution of retardation across the corneal surface is essential for the accuracy of these techniques.

Apart from the sophisticated techniques outlined above and biomicroscopy using simple semi-fixed linear polarizers, more complex experimental investigations into corneal retardation have been performed with methods such as phase stepping polarimetry (Jaronski and Kasprzak 1998) and liquid crystal polarimetric techniques (Bueno 2000). Mueller matrix polarimetry greatly advanced the understanding of the birefringent

properties of the human eye *in vivo* (Blokland and Verhelst 1987). To date, the phase stepping techniques are of low resolution (c. 250μm), but confirm previous findings using simpler techniques. Scanning laser polarimetry has been effectively used to study corneal birefringence in a small number of subjects (Knighton, Huang et al. 2008). The recent methods have disadvantages of expense, complexity and inaccessibility.

Although linear polarization biomicroscopy is relatively easy to perform, a fundamental disadvantage is that only birefringent elements (collagen fibrils in the case of corneas) orientated with principle axes at or near 45º to the axes of polarization are visible. An additional practical disadvantage is the need for a specially modified slit-lamp biomicroscope with two rotateable, but mutually orthogonal, polarizing filters placed in the illumination and observation light paths respectively.

A simple, inexpensive and accessible polariscopic technique using reflected 'circular' polarization was first used to demonstrate corneal isochromatic rings (Blokland and Verhelst 1987) and later used empirically in conjunction with a slit-lamp biomicroscope to detect possible stress birefringence in corneas that had undergone surgical manipulation (Misson and Stevens 1990). This technique has potential for the qualitative and semi-quantitative examination of human corneas *in vivo* although the basic principles of the technique and interpretation of results are yet to be detailed. The purpose of the present chapter it to determine the theoretical bases for the various types of polariscopy that can be used *in vivo* and which might have clinical use.

The basic principles of polarized light, retardation and interference are outlined in §15.3 together with an introduction to the computational methods using Stokes vectors and Mueller matrices.

5.2 Polariscopy with monochromatic light

The theory of biomicroscopy using reflected linear polarized light was established using geometric analysis (Mishima 1960) based on previous well established theory (see e.g. Johannsen 1914). Such calculations become increasingly complicated if more than three optical elements are involved, but can be simplified by the use of Stokes vectors and Mueller matrices as detailed in §15.3(Shurcliff 1962; Clarke and Grainger 1971; Collett 1993). Polariscopic configurations (Figure 5.1) are reviewed in terms of Stokes vectors and Mueller matrices and the theory of reflection polariscopy is developed.

Figure 5.1 Polariscope configurations

See text for details.

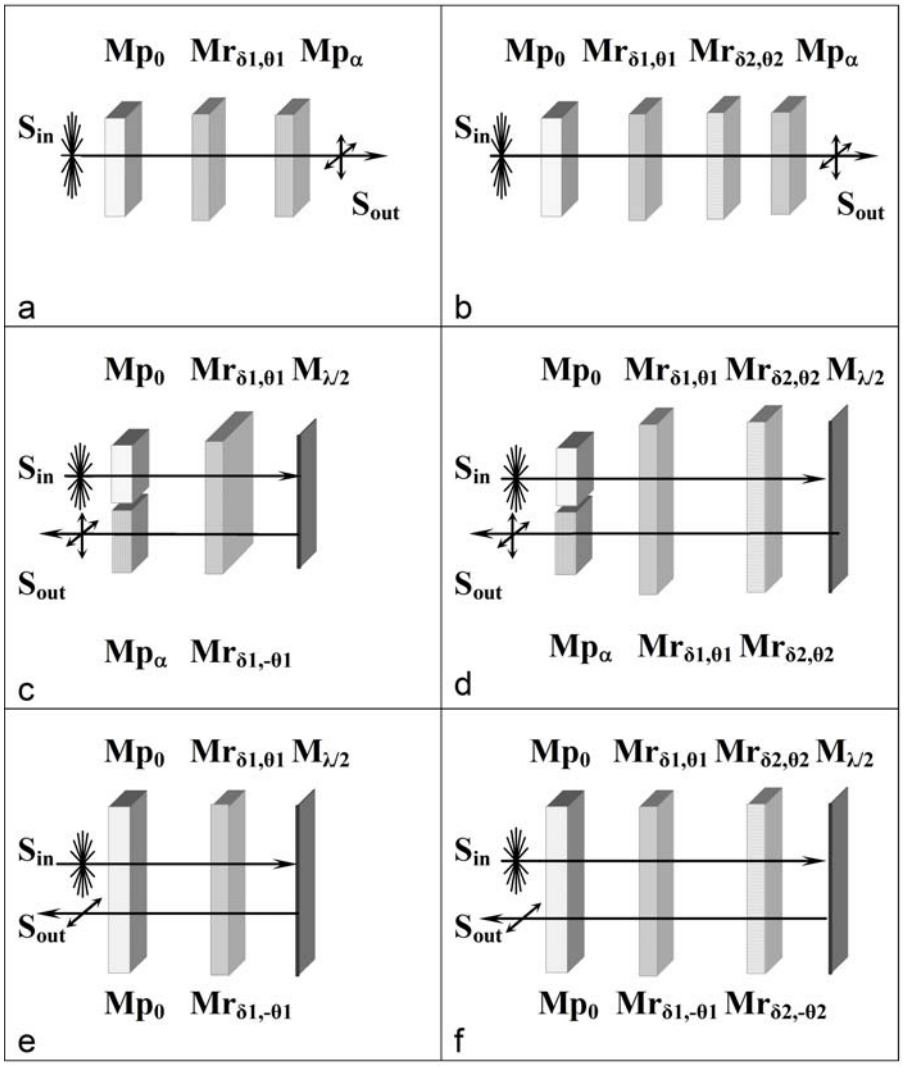

5.2.1 Transmitted polarized light

The simplest arrangement (Figure 5.1a) is a retarder placed between orthogonal polarizing filters as in transmitted light polariscopy and polarization microscopy (e.g. the petrological microscope). Let $\mathbf{S_{in}}$ be the Stokes vector of incident un-polarized light transmitted through a linear polarizer with horizontal axis ($\alpha = 0$) defined by the Mueller matrix $\mathbf{Mp_0}$. Emergent linear polarized light then passes through an arbitrary retarder, retardance δ_1, axis θ_1 ($\mathbf{Mr_{\delta,\theta}}$), and becomes elliptically polarized. The light finally passes through a second polarizer ($\mathbf{Mp_\alpha}$) with axis orthogonal ($\alpha = \pi/2$) or parallel ($\alpha = 0$) to the first. The Stokes vector $\mathbf{S_{out}}$ describes the emergent beam:

$$\mathbf{S_{out}} = \mathbf{Mp_\alpha} \,.\, \mathbf{Mr_{\delta 1,\theta 1}} \,.\, \mathbf{Mp_0} \,.\, \mathbf{S_{in}} \qquad \textbf{Eq. 5.1}$$

Using $\mathbf{S_{in}} = [1,0,0,0]^T$, the Stokes vector for non-polarized light of unit intensity, standard Mueller matrices, orthogonal ($\alpha = \pi/2$) polarizers (polarizer and analyzer), and normalizing light intensity output, Eq. 5.1 (see Table 5.1) solves to:

$$\mathbf{S_{out}} = [\sin^2(2\theta_1).\sin^2(\delta_1/2), -\sin^2(2\theta_1).\sin^2(\delta_1/2), 0, 0]^T$$

and $$S_{0\perp} = \sin^2(2\theta_1).\sin^2(\delta_1/2) \qquad \textbf{Eq. 5.2}$$

where $S_{0\perp}$ is the first Stokes parameter of the output for orthogonal polarizers. The intensity of emergent light, here taken to be equal to $S_{0\perp}$, is dependent on both the retardance (δ_1) and the angle of linear polarization relative to the fast axis of the retarder (θ_1). There are four maxima and four minima of intensity if $\mathbf{Mr_{\delta 1,\theta 1}}$ is rotated through one cycle. Transmission is a minimum (extinction) when the axis of retardation is

parallel to an axis of polarization (i.e. $\theta=½n\pi$, where n belongs to the set of integers, $\mathbb{Z}$) and is maximum at $\pm\pi/4$ to a polarization axis (i.e. $\theta=¼(2n+1)\pi$) where:

$$S_{0\perp} = \sin^2(\delta_1/2). \qquad \textbf{Eq. 5.3}$$

Similar calculations determine $S_{0\parallel}$ the first Stokes parameter/output intensity for parallel polarizers and selected values of θ_1 and δ_1. Results are listed in Table 5.1. These are solutions to Eq. 15.9 (Johannsen 1918, p.343 ff), the general expression for light intensity transmitted by a birefringent crystal plate between a polarizer and analyzer. Note the general rule that light transmission through parallel polarizers ($S_{0\parallel}$) is the complement to that transmitted through orthogonal polarizers ($S_{0\perp}$)

i.e. $S_{0\parallel} = 1 - S_0$.

Table 5.1 Solutions to Eq 5.1 as, function of δ_1, θ_1, α

		$\mathbf{Mp_\alpha \cdot Mr_{\delta 1,\theta 1} \cdot Mp_0 \cdot S_{in}}$			
		$S_0 = ¼(2+\cos(2\alpha)+\cos(2(\alpha-2\theta_1)-2\cos(\delta_1)\sin(2(\alpha-\theta_1))\sin(2\theta_1)$ $=\cos^2(\alpha)+\sin(2\theta_1)\sin(2(\alpha-\theta_1))\sin^2(\delta_1/2)$			
		$\alpha = \pi/2$		$\alpha = 0$	
		$S_{0\perp}$ orthogonal polarizers Fig 4.1d		$S_{0\parallel}$ parallel polarizers Fig 4.1f	
δ_1	θ_1	$\sin^2(2\theta_1).\sin^2(\delta_1/2)$	Eq. 5.2	$1-\sin^2(2\theta_1).\sin^2(\delta_1/2)$	Eq. 5.2b
δ_1	$0\pm\pi/2$	0	1.2a	½	1.2b
δ_1	$\pm\pi/4$	$\sin^2(\delta_1/2)$	Eq. 5.3	$1-\sin^2(\delta_1/2)$ $=$ $\cos^2(\delta_1/2)$	1.3b
$\pi/2$	θ_1	$2\cos^2(\theta_1).\sin^2(\theta_1)$ $=$ $¼(1-\cos(4\theta_1))$	1.4a	$¼(3+\cos(4\theta_1))$	1.4b
$\pi/2$	$\pm\pi/4$	½	1.5a	½	1.5b

5.2.2 Retarder train, transmitted linear polarized light

Now consider a similar configuration to §5.2.1, but with linear polarized light passing successively through two arbitrary retarders ($\mathbf{Mr_{1\ \delta1,\ \theta1}}$, $\mathbf{Mr_{2\ \delta2,\ \theta2}}$) with respective retardances δ_1 , δ_2 and azimuths of fast axes θ_1, θ_2 (hereafter referred to as 'axis') (Figure 5.1b). As before, the emergent light passes through a second polarizer ($\mathbf{Mp_\alpha}$) orientated with angle α relative to $\mathbf{Mp_0}$:

$$\mathbf{S_{out}} = \mathbf{Mp_\alpha}.\ \mathbf{Mr_{2\ \delta2,\ \theta2}}.\ \mathbf{Mr_{1\ \delta1,\ \theta1}}.\ \mathbf{Mp_0}\ .\ \mathbf{S_{in}} \qquad \textbf{Eq. 5.4}$$

The results for particular values of δ_1, δ_2, θ_1, θ_2 are given in Table 5.2

Table 5.2 Solutions to Eq 5.4 as function of δ_1, δ_2, θ_1, θ_2, α

				$\mathbf{Mp_\alpha}.\ \mathbf{Mr_{2\ \delta2,\ \theta2}}.\ \mathbf{Mr_{1\ \delta1,\ \theta1}}.\ \mathbf{Mp_0}\ .\ \mathbf{S_{in}}$			
				½(1+ sin(δ_1)sin(δ_2) sin(2θ_1)sin(2(α–θ_2)) +cos(2(α–θ_2)[cos^2(δ_1/2)cos(2θ_2) + sin^2(δ_1/2)cos(4θ_1–2θ_2)] + cos(δ_2)sin(2(α–θ_2))[sin^2(δ_1/2)sin(4θ_1–2θ_2) – cos^2(δ_1/2)sin(2θ_2)]			
				orthogonal polarizers $\alpha = \pi/2$ $S_{0\perp}$ Figure 5.1d		parallel polarizers $\alpha = 0$ $S_{0\parallel}$ Figure 5.1f	
δ_1	θ_1	δ_2	θ_2	½(1+ sin(δ_1)sin(δ_2)sin(2θ_1)sin(2θ_2) – cos^2(δ_1/2)[cos^2(2θ_2) + cos(δ_2)sin^2(2θ_2)] + sin^2(δ_1/2)[–cos(4θ_1–2θ_2)cos(2θ_2) + cos(δ_2) sin(4θ_1–2θ_2)sin(2θ_2)])		½(1 – sin(δ_1)sin(δ_2)sin(2θ_1)sin(2θ_2) + cos^2(δ_1/2)[cos^2(2θ_2) + cos(δ_2)sin^2(2θ_2)] + sin^2(δ_1/2)[cos(4θ_1–2θ_2) cos(2θ_2) – cos(δ_2) sin(4θ_1–2θ_2)sin(2θ_2)])	
δ_1	$\pi/4$	δ_2	θ_2	½(1 + sin(δ_1)sin(δ_2)sin(2θ_2) – cos(δ_1)[cos^2(2θ_2) + cos(δ_2)sin^2(2θ_2)])	2.1a	½(1 – sin(δ_1)sin(δ_2)sin(2θ_2) + cos(δ_1)[cos^2(2θ_2) + cos(δ_2)sin^2(2θ_2)])	2.1b
δ_1	$\pi/4$	δ_2	$\pi/4$	sin^2(δ_1/2 + δ_2/2)	Eq. 5.5	cos^2(δ_1/2 + δ_2/2)	Eq. 5.6
δ_1	$\pi/4$	δ_2	0	sin^2(δ_1/2)	Eq. 5.12	cos^2(δ_1/2)	Eq. 5.13
δ_1	$\pi/4$	δ_2	$-\pi/4$	sin^2(δ_1/2 – δ_2/2)	Eq. 5.7	cos^2(δ_1/2 – δ_2/2)	Eq. 5.8
$\pi/2$	$\pi/4$	δ_2	$\pm\pi/4$	½(1 – sin(δ_2)) = ½(cos(δ_1/2) – sin(δ_2/2))^2	2.5a	½(1 + sin(δ_2)) = ½(cos(δ_1/2)+sin(δ_2/2))^2	2.5b
$\pi/2$	$\pi/4$	δ_2	0	½	2.6a	½	2.6b
$\pi/2$	$\pi/4$	$\pi/2$	$\pi/4$	1	2.8a	0	2.8b
$\pi/2$	$\pi/4$	$\pi/2$	$-\pi/4$	0	2.9a	1	2.9b

NB $\delta_1 = \pi/2 = \lambda/4$

Firstly note the greater complexity of the derived expressions particularly of the general case. Fixing the retarder axis at ±45° (i.e. $\theta = \pm\pi/4$) to $\mathbf{Mp_0}$, when the retarders have parallel principle axes, $\theta_1=\theta_2= ¼(2n+1)\pi$ for integer values n, Eq. 5.4 solves to:

$$S_{0\perp} = \sin^2(\delta_1/2 + \delta_2/2).$$

Eq. 5.5

and $$S_{0\parallel} = \cos^2(\delta_1/2 + \delta_2/2)$$

Eq. 5.6

Furthermore, when retarders have orthogonal principle axes, $\theta = -\theta_2 = ¼(2n+1)\pi$, then

$$S_{0\perp} = \sin^2(\delta_1/2 - \delta_2/2).$$

Eq. 5.7

and $$S_{0\parallel} = \cos^2(\delta_1/2 - \delta_2/2)$$

Eq. 5.8

The above simplifies for crossed polarizers to:

$$S_{0\perp} = \sin^2(\Delta/2).$$

Eq. 5.9

and for parallel polarizers to:

$$S_{0\parallel} = \cos^2(\Delta/2).$$

Eq. 5.10

where Δ is the sum of output retardances of any number of retarders in a train.

5.2.3 'Circular' polariscope

A further case (not illustrated) represents the 'circular' polariscope. Here the system has five elements: two polarizers and two retarders as in §5.2.2, and a centrally-placed arbitrary retarder $\mathbf{Mr}_{\delta,\theta}$. Furthermore, the fixed retarders are $\delta_1 = \delta_2 = \pi/2$ (i.e. quarter wave) and $\theta_1 = -\theta_2 = \pi/4$ such that:

$$\mathbf{S}_{out} = \mathbf{Mp}_{\alpha} \cdot \mathbf{Mr}_{\pi/2,-\pi/4} \cdot \mathbf{Mr}_{\delta,\theta} \cdot \mathbf{Mr}_{\pi/2,\pi/4} \cdot \mathbf{Mp}_{0} \cdot \mathbf{S}_{in} \qquad \textbf{Eq. 5.11}$$

solves to

$$S_0 = \tfrac{1}{2}\,(1 + \cos(2\alpha)\cos(\delta) + \cos(2\theta)\sin(2\alpha)\sin(\delta))$$

for arbitrary α, θ and δ;

$$S_{0\perp} = \sin^2(\delta/2) \qquad \textbf{Eq. 5.12}$$

and

$$S_{0\parallel} = \cos^2(\delta/2) \qquad \textbf{Eq. 5.13}$$

Thus for orthogonal and parallel polarizers, the output intensity depends on δ only and is independent of θ i.e. there is no extinction and hence no isoclines/isogyres.

5.2.4 Reflected linear polarized light

Consider again plane monochromatic light ($\mathbf{S}_{in}$) polarized with a linear polarizer ($\mathbf{Mp}_0$) and transmitted through an arbitrary retarder ($\mathbf{Mr}_{\delta 1,\theta 1}$) as before. Now let the light emergent from the retarder undergo normal or near-normal incidence reflection,

represented by $\mathbf{M}_{\lambda/2}$, which causes a half-wavelength phase shift ($\lambda/2$, $\delta_1 = \pi$) and is represented by the standard Mueller matrix for an ideal normal incidence reflector

$$\mathbf{M}_{\lambda/2} = \begin{bmatrix} 1 & 0 & 0 & 0 \\ 0 & 1 & 0 & 0 \\ 0 & 0 & -1 & 0 \\ 0 & 0 & 0 & -1 \end{bmatrix}$$

This reverses the handedness and azimuth of the incident elliptically polarized light. The reflected light then emerges through the train in reverse order from the opposite direction to pass through a second polarizer ($\mathbf{Mp}_{\pi/2}$) with axis orthogonal ($\alpha = \pi/2$) to the first. Note that after refection, the axis of any $\mathbf{Mr}_{\delta 1}$ changes to $-\theta_1$. The arrangement is summarised in Eq. 5.14, Figure 5.1c:

$$\mathbf{S}_{out} = \mathbf{Mp}_{\alpha} \cdot \mathbf{Mr}_{\delta 1,-\theta 1} \cdot \mathbf{M}_{\lambda/2} \cdot \mathbf{Mr}_{\delta 1,\theta 1} \cdot \mathbf{Mp}_{0} \cdot \mathbf{S}_{in}$$

Eq. 5.14

Thus $S_{0\perp} = \sin^2(2\theta_1).\sin^2(\delta_1)$

Eq. 5.15

which becomes

$$S_{0\perp} = \sin^2(\delta_1)$$

Eq. 5.16

when $\theta_1 = ¼(2n+1)\pi$.

A modification of this model may be obtained by holding both the first and second polarizer at the same angle, say $\alpha = 0$, whence Eq. 5.14 solves to

$$S_{0\parallel} = \cos^2(\delta_1)$$

Eq. 5.17

when $\theta_1 = ¼(2n+1)\pi$.

In the arrangements modelled in Eq. 5.14, the emergent light intensity, as in the previous case of transmitted linear polarized light, is dependent on both δ_1 and θ_1. Once again it is maximum at $\theta_1 = ¼(2n+1)\pi$, but the effect of the retarder is doubled. When a = 0, the arrangements modelled in Eq. 5.14, Figure 5.1e has the advantage that a single polarizer can be used for both the incident and emergent beam.

Inspection of the solutions presented in Table 5.3 reveals two other significant findings. Firstly, the retarder has no effect if aligned with one of the principle directions of the polarizer ($\theta_1 = 0, \pi/2 \ldots n\pi/2, \forall n \in \mathbb{Z}$). Secondly, if the retarder is aligned with principle axes between those of the polarizer and retards one quarter of a wavelength, there is no transmission if the analyzer is parallel to the polarizer and full transmission if the polarizer and analyzer are in the crossed position. This is the principle underlying the use of 'circular polarizing' filters for glare reduction (Shurcliff 1962). Here the azimuth of reflected linear polarized light emergent from the system is orthogonal to $\mathbf{Mp_0}$ and is therefore extinguished. A less intuitive result arises when $\delta_1 = \lambda/4$ ($\pi/2$ radians) and is an azimuth other than $\theta_1 = 0$ or $\pm\pi/4$, in this case $S_{0\perp} = \sin^2(2\theta_1)$ or $S_{0\parallel} = \cos^2(2\theta_1)$ respectively for crossed or parallel polarizers i.e. the output intensity is a function of twice the angle of azimuth.

Table 5.3 Solutions to Eq 5.14 as function of δ_1, θ_1, α

		$\mathbf{Mp_\alpha.Mr_{1\delta 1,-\theta 1}.M_{\lambda/2}.Mr_{1\delta 1,\theta 1}.Mp_0.S_{in}}$			
		½ (1+cos(2 θ_1)cos(2(α+θ_1))+cos(2δ_1) sin(2θ_1)sin(2(α+θ_1)))			
		orthogonal polarizers $\alpha = \pi/2$ $S_{0\perp}$ Fig 4.1d		parallel polarizers $\alpha = 0$ $S_{0\parallel}$ Fig 4.1f	
δ_1	θ_1	$\sin^2(2\theta_1).\sin^2(\delta_1)$	Eq. 5.15	$1 - \sin^2(2\theta_1).\sin^2(\delta_1)$	Eq. 5.15b
δ_1	$0, \pm\pi/2$	0	3.2a	1	3.2b
δ_1	$\pm\pi/4$	$\sin^2(\delta_1)$	Eq. 5.16	$1 - \sin^2(\delta_1) = \cos^2(\delta_1)$	Eq. 5.17
$\pi/2$	θ_1	$\sin^2(2\theta_1)$	3.4a	$1 - \sin^2(2\theta_1) = \cos^2(2\theta_1)$	3.4b
$\pi/2$	$\pm\pi/4$	1	3.5a	0	3.5b

5.2.5 Retarder train, reflected linear polarized light

The reflected case can be extended to include multiple retarders. A double-pass of light transmitted and then reflected through a polarizer and two retarders as depicted in Figure 5.1d can be represented by Eq. 5.18:

$$\mathbf{S_{out}} = \mathbf{Mp_{\alpha} \cdot Mr_{1\,\delta 1,-\theta 1} \cdot Mr_{\delta 2,-\theta 2} \cdot M_{\lambda/2} \cdot Mr_{\delta 2,\theta 2} \cdot Mr_{1\,\delta 1,\theta 1} \cdot Mp_{0} \cdot S_{in}}$$

Eq. 5.18

now,

$$\mathbf{Mr_{\delta 2,-\theta 2} \cdot M_{\lambda/2} \cdot Mr_{\delta 2,\theta 2} = Mr_{2\delta 2,\theta 2}}$$

Eq. 5.19

and

$$\mathbf{Mr_{1\,\delta 1,-\theta 1} \cdot M_{\lambda/2} = Mr_{1\,\delta 1,\theta 1}}$$

Eq. 5.20

So Eq. 5.18 is equivalent to:

$$\mathbf{S_{out}} = \mathbf{Mp_{\alpha} \cdot Mr_{1\,\delta 1,-\theta 1} \cdot Mr_{2\delta 2,\theta 2} \cdot Mr_{1\,\delta 1,\theta 1} \cdot Mp_{0} \cdot S_{in}}$$

Eq. 5.21

taking note of the reversal of sign due to emergence from the reflected system and the half-wave phase difference due to normal incidence reflection. Note also that matrix multiplication is not commutative so this system is not equivalent to the transmitted scenario (Eq. 5.4 Figure 5.1b) with two retarders of double δ_1, δ_2.

The specific cases of $S_{0\perp}$ and $S_{0\parallel}$ solutions for arbitrary θ_1, $\theta_1 = \pi/4$ (first retarder fixed at 45° from horizontal and the plane of first-pass incident polarized light) and various values of δ_1, δ_2, θ_2 are presented in Table 5.4. The solution for the general case for arbitrary angle α is lengthy and serves no purpose in this study so will be omitted.

Table 5.4 Solutions to Eq 5.18 as function of δ_1, δ_2, θ_1, θ_2, α

				$\mathbf{Mp_\alpha \cdot Mr_{1\,\delta1,-\theta1} \cdot Mr_{\delta2,-\theta2} \cdot M_{\lambda/2} \cdot Mr_{\delta2,\theta2} \cdot Mr_{1\,\delta1,\theta1} \cdot Mp_0 \cdot S_{in}}$			
				orthogonal polarizers $\alpha = \pi/2$ $S_{0\perp}$ Fig 4.1d		parallel polarizers $\alpha = 0$ $S_{0\parallel}$ Fig 4.1f	
				$(\cos(\delta_2)\sin(\delta_1)\sin(2\theta_1)+ \sin(\delta_2)[\cos^2(\delta_1/2)\sin(2\theta_2) - \sin^2(\delta_1/2)\sin(4\theta_1-2\theta_2)])^2$	Eq 5.22	$1-(\cos(\delta_2)\sin(\delta_1)\sin(2\theta_1)+ \sin(\delta_2)[\cos^2(\delta_1/2)\sin(2\theta_2) - \sin^2(\delta_1/2)\sin(4\theta_1-2\theta_2)])^2$	5.23
δ_1	$\pi/4$	δ_2	θ_2	$(\cos(\delta_2)\sin(\delta_1) + \cos(\delta_1)\sin(\delta_2)\sin(2\theta_2))^2$	5.24	$1-(\cos(\delta_2)\sin(\delta_1) + \cos(\delta_1)\sin(\delta_2)\sin(2\theta_2))^2$	5.25
δ_1	$\pi/4$	δ_2	$\pi/4$	$\sin^2(\delta_1+\delta_2)$	Eq. 5.29	$\cos^2(\delta_1+\delta_2)$	Eq. 5.30
δ_1	$\pi/4$	δ_2	0	$\cos^2(\delta_2)\sin^2(\delta_1)$	5.26	$1-\sin^2(\delta_2).\sin^2(\delta_1)$	5.27
δ_1	$\pi/4$	δ_2	$-\pi/4$	$\sin^2(\delta_1-\delta_2)$	Eq. 5.31	$\cos^2(\delta_1-\delta_2)$	Eq. 5.32
$\pi/2$	$\pi/4$	δ_2	any θ_2	$\cos^2(\delta_2)$		$\sin^2(\delta_2)$	5.28
$\pi/2$	$\pi/4$	$\pi/2$	any θ_2	0		1	
π	$\pi/4$	δ_2	$\pi/4$	$\sin^2(\delta_2)$	Eq. 5.33	$\cos^2(\delta_2)$	
π	$\pi/4$	$\pi/2$	0	0		1	
π	$\pi/4$	$\pi/2$	$\pm\pi/4$	1		0	
π	$\pi/4$	π	any θ_2	0		1	

NB $\delta_1 = \pi/2 = \lambda/4$

When $\theta_1 = \theta_2 = \pi/4$, and more generally for ¼$(2n+1)\pi$ i.e. when θ_1 and θ_2 are parallel,

Eq. 5.18/Eq. 5.21 solves to

$$S_{0\perp} = \sin^2(\delta_1+\delta_2) \qquad \textbf{Eq. 5.29}$$

$$S_{0\parallel} = \cos^2(\delta_1+\delta_2) \qquad \textbf{Eq. 5.30}$$

Furthermore, when $\theta_1 = -\theta_2 = \frac{1}{4}(2n+1)\pi$ i.e. when θ_2 is orthogonal to θ_1.

$$S_{0\perp} = \sin^2(\delta_1 - \delta_2)$$

Eq. 5.31

$$S_{0\parallel} = \cos^2(\delta_1 - \delta_2)$$

Eq. 5.32

Thus in these specific orientations the effect of reflection is a simple double pass through the retarders with summation and doubling of component retardations. Note that this simple relationship does not hold for $\theta_1 \neq \theta_2 \neq \pi/4$ when the output intensity follows the equations of Table 5.4. Another result of note (Eq. 5.33, Table 5.4) is for light transmitted and reflected through a single polarizer with horizontal azimuth, a quarter wave retarder ($\delta_1 = \lambda/4 = \pi/2$) placed at 45° to the plane of incident polarization ($\theta_1 = \pi/4$) and an arbitrary retarder (δ_2, θ_2). The incident linear polarized light is converted into right circular before entering and being reflected back through the arbitrary retarder which causes a further phase shift of one half wavelength. The reflected beam is then allowed to exit the same quarter-wave retarder and polarizer through which it entered the system. The solution,

$$S_{0\parallel} = \sin^2 \delta_2$$

Eq. 5.33

indicates that the intensity of emergent light depends only on δ_2, and is independent of the orientation of the retardance axis θ_2. Thus there is no extinction (i.e. no isoclinics/isogyres) as noted previously and the output intensity is a function solely of retardation. The effect is similar to that of a 'circular' transmission polariscope as previously outlined and will be the basis for a simple examination instrument.

5.2.6 Synopsis

There are several general points to be highlighted from the results presented above and in Table 5.1 – Table 5.4. Firstly, the general solutions for arbitrary $\delta_1, \theta_1, \delta_2, \theta_2$ are not straightforward functions except in the most simple of cases such as those of Table 5.1 and Table 5.3 (Eq. 5.2a., Eq. 5.2b, Eq. 5.15, Eq. 5.15b). The intensity of emergent light for both transmission (single pass) and reflection (double pass) models are a $\cos^2$ function with parallel polarizers (Eq. 5.6, Eq. 5.8, 5.25, 5.27) and a $\sin^2$ function with orthogonal ('crossed') polarizers (Eq. 5.5, Eq. 5.7, 5.24, 5.26). Also, for both single and double pass models, the superimposition of two retarders is additive if there respective fast/slow axes are parallel (Eq. 5.5, Eq. 5.6, 5.24, 5.25) and subtractive if their axes are orthogonal (Eq. 5.7, Eq. 5.8, 5.26, 5.27). The summation properties will be used in this study to determine δ and θ of an unknown retarder (e.g. the cornea) given a reference retarder of known parameters.

The effect of a reflected double pass is to double the retardation of a single retarder (cf Eq. 5.2 and Eq. 5.15; Eq. 5.2b and Eq. 5.15b, Table 5.1, Table 5.3). The effect of a reflected double pass through two retarders at arbitrary orientations however cannot be simplified to a doubling of the effect of single pass retardations. This is formalised in Eq 5.22, 5.23 etc, Table 5.4.

5.3 Transmission and reflection polariscopy with white light

The discussion thus far has assumed monochromatic light; the chromatic effects with a white light source will now be considered.

For the purpose of this study, a wave band $\lambda = 360 – 780$nm and a 'reference' wavelength $\lambda_0 = 560$nm are used. That particular reference is chosen as it is a standard used by some authorities in optical crystallography (Wahlstrom 1979), it simplifies numeric calculation ($560 = 35 \times 2^4$) and is a multiple of the retardation of the commercially available wave plates used in this study. Furthermore, it is approximately mid-way in the visible electromagnetic spectrum and near the peak sensitivity (555nm) of human photopic vision. Retarders of, or approximating to, 140nm ('quarter wave') are typically used in the construction of commercially available 'circular' polarizing filters employed elsewhere and in this study.

For polychromatic light a clear distinction is made between retardation (Λ, an absolute linear measurement typically expressed in nm) and retardance (δ, a relative phase measurement typically expressed as an angle or fraction of a wavelength; see §15.3.2) where

$$\delta = 2\pi \Lambda / \lambda$$

Eq. 5.34

Zero dispersion will be assumed in calculations i.e. that Λ remains independent of wavelength. This expression for δ can be substituted into the relevant solution for any of the previous configurations.

5.3.1 Transmission through one or more retarders

By combining Eq. 5.34 with Eq. 5.2 and Eq. 5.2b (Table 5.1) a function (spectral transmission function, STF) is defined that representing the light transmission through a retarder Λ orientated at an angle θ between crossed ($T_\perp$) and uncrossed ($T_\parallel$) polarizers:

$$T_\perp (\Lambda, \theta, \lambda) = \sin^2(2\theta).\sin^2(\pi \Lambda /\lambda)$$

Eq. 5.35

$$T_\parallel (\Lambda, \theta, \lambda) = 1 - \sin^2(2\theta).\sin^2(\pi \Lambda /\lambda)$$

Eq. 5.36

Substituting the wavelength variables stated above results in a set of spectral transmission curves for any particular retarder.

Setting λ = 360 – 780nm and selecting retarder path differences Λ =280 – 1680 nm in 280nm increments, the spectral transmission (light intensity for a given wavelength) curves given by Eq. 5.35, Eq. 5.36 are shown in Figure 5.2. Here the polarizers are crossed ($\alpha = 90°$) in the left column and uncrossed ($\alpha = 0°$) on the right.

The fast/slow axes of retardation $\theta_1 = \pm\pi/4$ rads. i.e. they are 45° relative to the axes of polarization.

Transmission is zero (Table 5.1 and related text) for crossed polarizers with zero retardation and when the retarder axes are parallel / orthogonal to the principle directions of the polarizer (position of extinction). The converse is true for parallel polarizers i.e. there is maximum transmission of all wavelengths with zero retardation or with the retarder parallel/orthogonal to the polarization axis. The predicted spectral transmission curves for crossed polarizers are the complement of those for parallel polarizers. Looking more closely at a 560nm retarder at ±45° to crossed polarizers,

transmission is minimum at $\lambda = 560$nm and maximum $\lambda = 373.35$nm. For parallel polarizers these parameters are reversed. Thus a 560nm retarder appears reddish violet between crossed polarizers, but green (the complementary colour) between parallel polarizers. With increasing values of Λ, for both crossed and uncrossed polarizers, the spectral transmission curves become increasingly sinusoidal which, for large values of Λ, are interpreted by the eye as off-white.

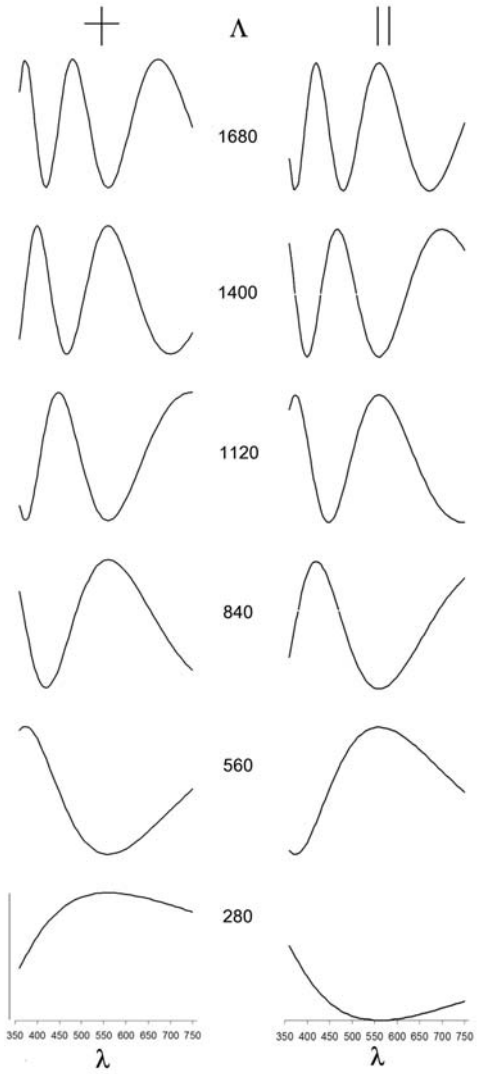

Figure 5.2 Spectral transmission curves from 360 – 780nm for retarder (Λ)

Crossed polarizers (left) and parallel polarizers (right) as generated by Eq. 5.35 & Eq. 5.36. Retarder at 45° to axes of polarization

The superposition of two retarders between crossed and uncrossed polarizers (Figure 5.1b; Table 5.2) may be considered in a similar way by substituting relevant variations of Eq. 5.34 for δ_1 and δ_2. Referring to Table 5.2, the two retarders add if parallel and subtract if orthogonal with an interference colour determined by Eq. 5.34. When $\theta_2 = 0$, the second retarder has no effect and the overall retardance, and hence interference colour is that due to δ_1.

5.3.2 Reflected double-pass through a single retarder

Double-pass through a single retarder is similar to transmission (see §5.3.1) except the retardation is doubled by reflection. The spectral transmission curves follow Eqs Eq **5.22** and 5.23 of Table 5.4 and are identical to those of Figure 5.2 except the vertical Λ scale is halved. Thus double-pass, single retarder STFs can be defined:

$$R1_{\perp}(\Lambda, \theta, \lambda) = T_{\perp}(2\Lambda, \theta, \lambda)$$

Eq. 5.37

$$R1_{\parallel}(\Lambda, \theta, \lambda) = T_{\parallel}(2\Lambda, \theta, \lambda)$$

Eq. 5.38

5.3.3 Reflected double-pass through two retarders

The chromatic effect of reflection through two superimposed retarders as described above follow Eq 5.22 and 5.23 of Table 5.4. Here the effects and associated calculations are considerably more complicated than for a single retarder. Parallel polarizers will be considered; the case for crossed polarizers is omitted as it is not relevant to the remainder of this study. The relevant STF, based on Eq 5.25, Table 5.4

representing the light transmitted and reflected through this configuration for given λ, Λ_1, Λ_2, θ_2 and fixed $\theta_1 = \pi/4$ is defined:

$$R2(\Lambda_1, \Lambda_2, \theta_2, \lambda) = 1 - (\cos(2\pi\Lambda_2/\lambda)\sin(2\pi\Lambda_1/\lambda) + \cos(2\pi\Lambda_1/\lambda)\sin(2\pi\Lambda_2/\lambda)\sin(2\theta_2))^2$$

Eq. 5.39

This function is used to calculate the spectral transmission curves for $\lambda = 360 - 780$nm; $\Lambda_1 = 140 - 560$nm; $\Lambda_2 = 0 - 560$nm, both in 140nm increments; $\theta_1 = \pi/4$, $\theta_2 = -\pi/4$, 0, $+\pi/4$.

Firstly, and most simply, with retarders in the $\theta_2 = \pm 45°$ position, there is summation and subtraction as before with the overall retardation being doubled by reflection. The spectral transmission curves are given in Figure 5.3 in the right ($-\pi/4$) and left ($+\pi/4$) column of each of the four panels representing Λ_1 = 140, 280, 420 and 560 respectively. Note that there is upward displacement of the left column of each panel with increasing Λ_2 equivalent to incremental decrease in total retardation (subtraction: $\Lambda_1 - \Lambda_2$) and a corresponding downward displacement in the right column indicating addition ($\Lambda_1 + \Lambda_2$). The central column of each panel depicts the spectral transmission curves for the given Λ_1, but with the second retarder (Λ_2) in the zero ($\theta_2 = 0$) position. This is a more complicated function of Λ_1 and Λ_2, but reduces to the $\cos^2$ function of Λ_1 when $\Lambda_2 = 0$ (lowest graph, middle column of each panel).

Of particular note when comparing the predicted spectral transmission curves for $\theta_2 = -\pi/4$, 0, $+\pi/4$, the difference is least for low values of Λ_1 and Λ_2. Furthermore for monochromatic light, $\lambda = 560$nm, there is extinction (zero transmission) for all θ_2, $\Lambda_2 =$

0, 280 and 560 nm, Λ_1 = 140, 420 nm, and maximum transmission for all θ_2, Λ_2 = 0, 280 and 560 nm, Λ_1 = 280, 560 nm. This finding will be used later when devising a technique for determining the distribution of corneal retardation.

For each particular value of Λ_2, the difference between the curves for $\theta_2 = 0, \pm\pi/4$ is least for Λ_1 = 140nm. For the reference λ_0 = 560nm, 140nm is a quarter wavelength and, referring to Table 5.4 Eq 5.28 the transmitted intensity is proportional to $\sin^2\delta_2$ and independent of orientation. This becomes increasingly approximate for wavelengths further removed from λ_0, but the deviation is less for 140nm than for higher values of Λ_1. In other words, the interference colours produced by an arbitrary retarder with reflected light through a Λ_1 = 140nm fixed retarder/polarizer will vary less with orientation than for Λ_1 > 140nm. Furthermore for Λ_1 = 140nm, Λ_2 = 280nm and all θ_2 the spectral transmission curves are similar in that there is extinction around λ = 560nm and transmission increasing towards λ = 360nm and λ = 780nm thus giving a dark purple/red interference colour. The spectral waveforms become increasingly sinusoidal for greater Λ_2 which translate to more desaturated interference colours. These observations will be used further in subsequent chapters.

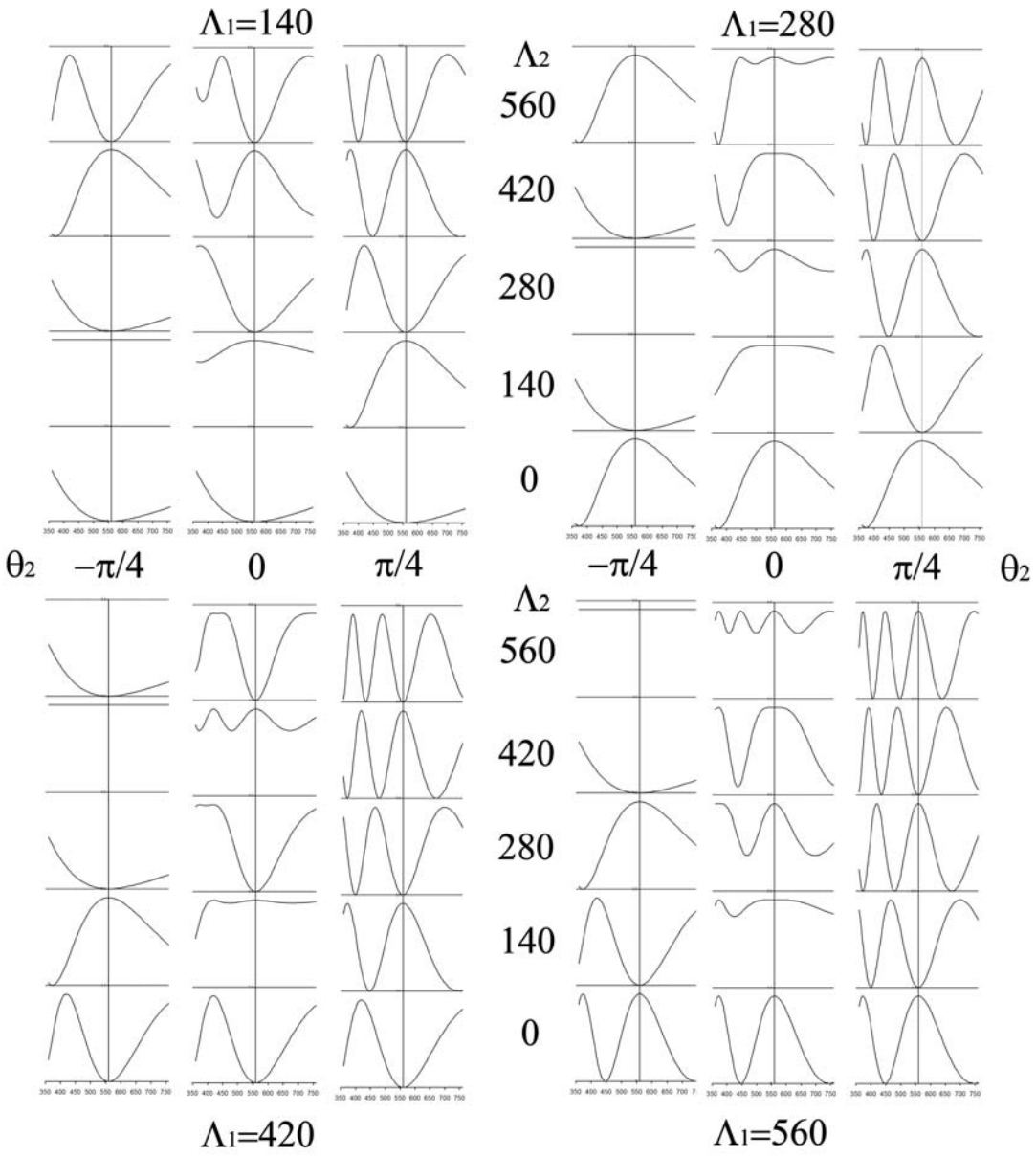

Figure 5.3 Spectral transmission curves for white light λ = 360 – 780nm reflected through linear polarizer and two superimposed retarders as determined by the STF.

Retarder Λ_2 = 0, 140, 280, 420 and 560nm (horizontal rows) orientated at $\theta_2 = -\pi/4, 0, +\pi/4$ (left central and right columns of each panel). Retarder Λ_1 = 140, 280, 420 and 560nm (quadrants) with fixed orientation at $\theta_1 = +\pi/4$. Central vertical line in each graph is at λ = 560nm. See text for details and definitions.

5.4 Experimental validation of theory

The theoretically derived spectral characteristics of light transmitted/reflected through known single retarders/retarder pairs are now verified experimentally.

5.4.1 Methods

A petrological/metallurgical photomicroscope (Reichert Zetopan Pol) that allows both transmitted and coaxial (normal-incidence) reflected light examination was used (Figure 5.4, Figure 5.5). The vernier graduated rotating microscope stage allows precise orientation of specimen/retarders/polarizers. Micro spectrophotometry was performed by attaching a digital spectrometer (Ocean Optics 2000+, SpectraSuite Software) to the photographic window of the microscope (S in Figure 5.4).

Several retarders were obtained and verified using a Berek compensator (see §15.4). Five (two 140nm mica; 315nm polymer; 540nm polymer, 555nm quartz) were chosen for further study because of their magnitude and stability of retardation, lack of pleochroism and constant dispersion. Orientated single or stacked pairs of retarders were mounted on the microscope stage for measurement in transmission (light green pathway Figure 5.4). For measurement by reflection, the carefully orientated retarders were mounted on a face-surfaced metallic mirror and observed with the incident-light illumination facility of the microscope (pink pathway Figure 5.4, Figure 5.5). The angles from horizontal of the retarders' slow axes, θ_1 and θ_2, are as previously defined (§5.2.5), and are summarised in Figure 5.6. Monochromatic light, when required, was generated using a 560nm (FWHM 10nm) interference filter.

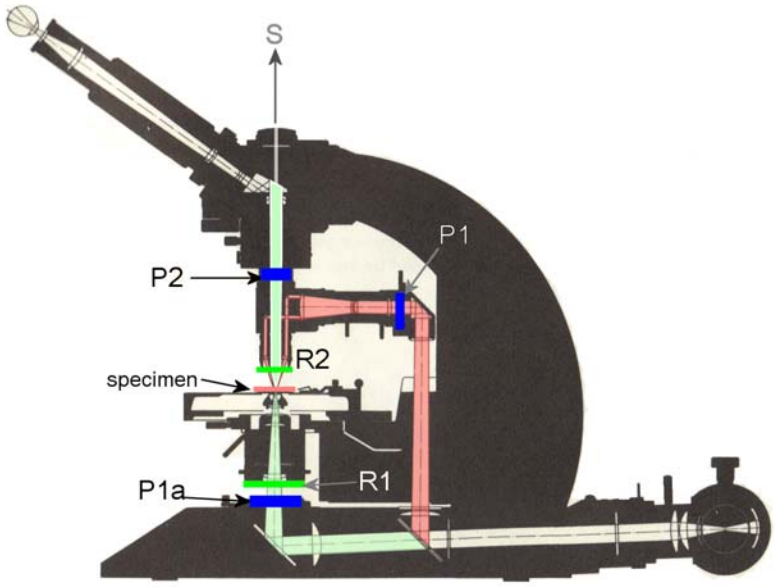

Figure 5.4 Polarizing microscope (Zetopan Pol, Reichert Berlin) adapted for transmission and reflection.

Transmission illumination (light green) through polarizer P1a, retarder R1, specimen, analyzer P2 to eyepiece or spectrometer (S).
Normal incidence reflection illumination (pink) via polarizer P1, retarder R2, specimen, retarder R2, analyzer (P2), eyepiece/spectrometer (S).

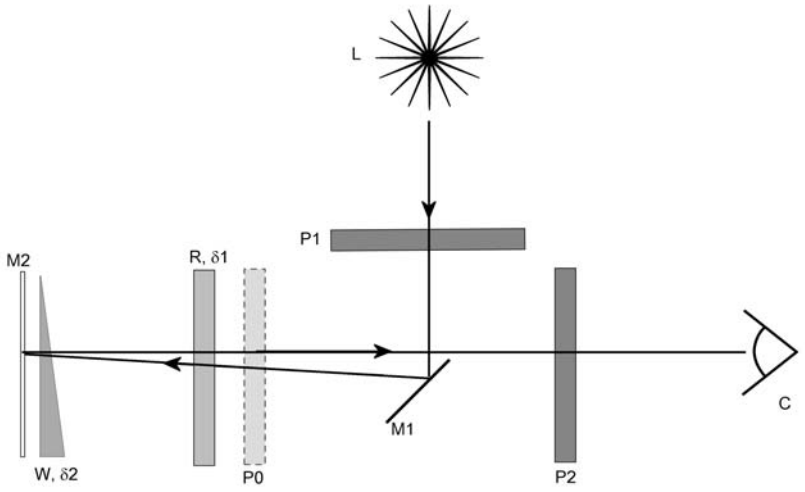

Figure 5.5 Schematic of experimental setup for reflected polarimetry

Linear polarized light generated from light source L by linear polarizer P1 and projected via mirror M1 through first retarder R, second retarder W and reflected back via mirror M2 through, W, R and polarizer P2 to detector/camera/eye C. Polarizers P1, P2 could be replaced by single polarizer P0.

Two polarizing options were available for reflected light: double pass through a single polarizer (path L M1 P0 R W M2 W R C, Figure 5.5) or single pass through two polarizers (path L P1 M1 R W M2 W R P2 C, Figure 5.5). This study will concentrate on the first, double pass option.

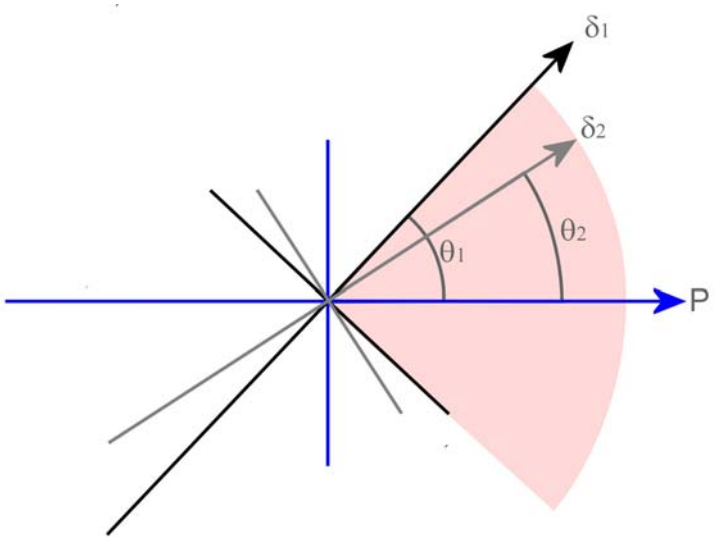

Figure 5.6 Definition of variables

P (blue lines) axis of polarizer (analyzer is orthogonal); δ_1, δ_2, retarders with slow axes in direction of arrows at angle θ_1, θ_2 from P.

Spectrometric data was processed using SpectraSuite (Ocean Optics) software. The normalized spectral data was compared graphically with the spectral transmission curve predicted by the appropriate STF as summarised in §5.3.3 and Figure 5.3.

5.4.2 Results: Transmitted light

White light transmission through three fixed retarders (140nm mica; 315nm polymer; 555nm quartz) between polarizers was characterised spectroscopically. Experimental findings were compared to the theoretical spectra predicted respectively for the STFs $T_{\perp}$ and $T_{\parallel}$ (Eq. 5.35 Eq. 5.36, §5.3.1). In all cases the retarder was examined at 45° to extinction/maximum transmission (θ_2) between crossed and uncrossed polarizers as previously outlined. The experimental configuration was that of Figure 5.1(a). Results are given in Figure 5.7. There is good correspondence between experimental (black curve: crossed polarizers; blue curve: parallel polarizers) and theoretical values (red curve).

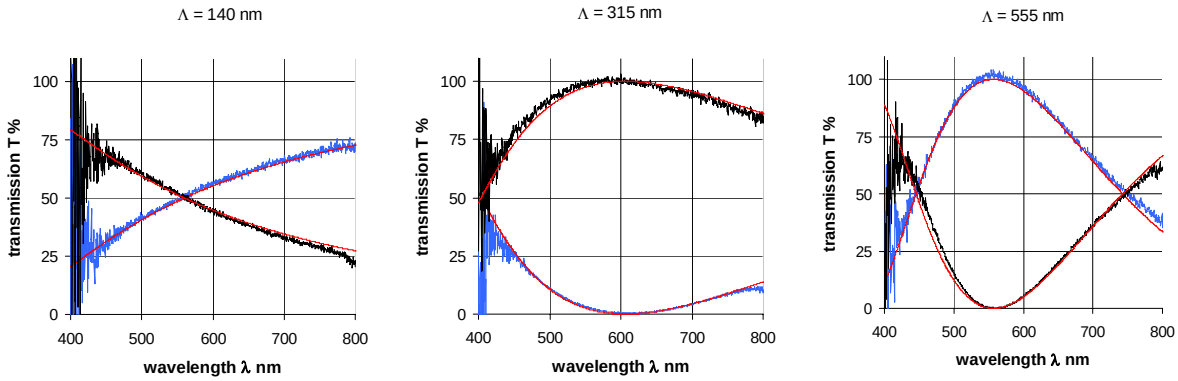

Figure 5.7 Experimental and theoretical (red) transmission spectra

140, 315 and 555nm retarders between crossed (black) and parallel (blue) polarizers; x-axis wavelength (nm); y-axis normalised intensity.

5.4.3 Results: Reflected light

Spectroscopic analysis was performed using the polarizing microscope configured for coaxial (normal-incidence) reflected illumination through single or superimposed pairs of retarders as described above. The experimental combination and notation is given in

Figure 5.8 where Λ_1 is the retardance of a 140nm or 540nm retarder fixed at 45° (θ_1) to the polarization directions of polarizer/analyzer and Λ_2 is the retardance of the second retarder (140, 315, 555nm) that can be freely orientated (θ_2).

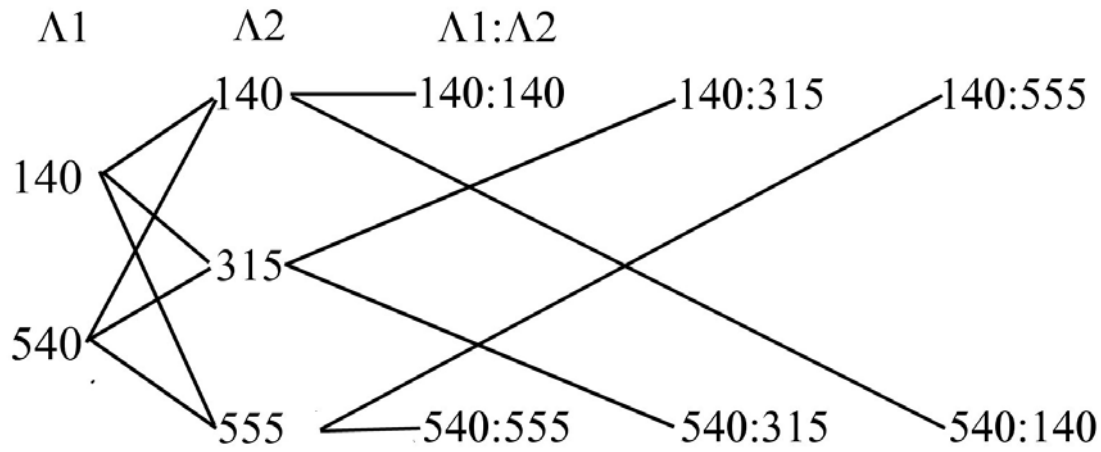

Figure 5.8 Experimental combinations of retarders

Coaxial (normal-incidence) reflected illumination. Spectral transmissions of individual retarders Λ_1 = 140, 540nm and Λ_2 = 140, 315 and 555nm are given in Figure 5.9. Spectral transmissions of retarder combinations Λ_1: Λ_2 are given in Figure 6.7

The spectra for reflection through single retarders alone are presented in Figure 5.9 and compared to theoretical spectra derived from STF R2(Λ_1, Λ_2,θ_2,λ) (Eq. 5.39, §5.3.3). The experimental configuration was that of Figure 5.1(e). The transmission spectra for reflection (double-pass) through single retarders are similar to the spectra for single-pass light transmission through retarders with approximately double the retardation (cf Figure 5.7) thus supporting the theoretical conclusion that reflection through a retarder under these conditions doubles its retardance.

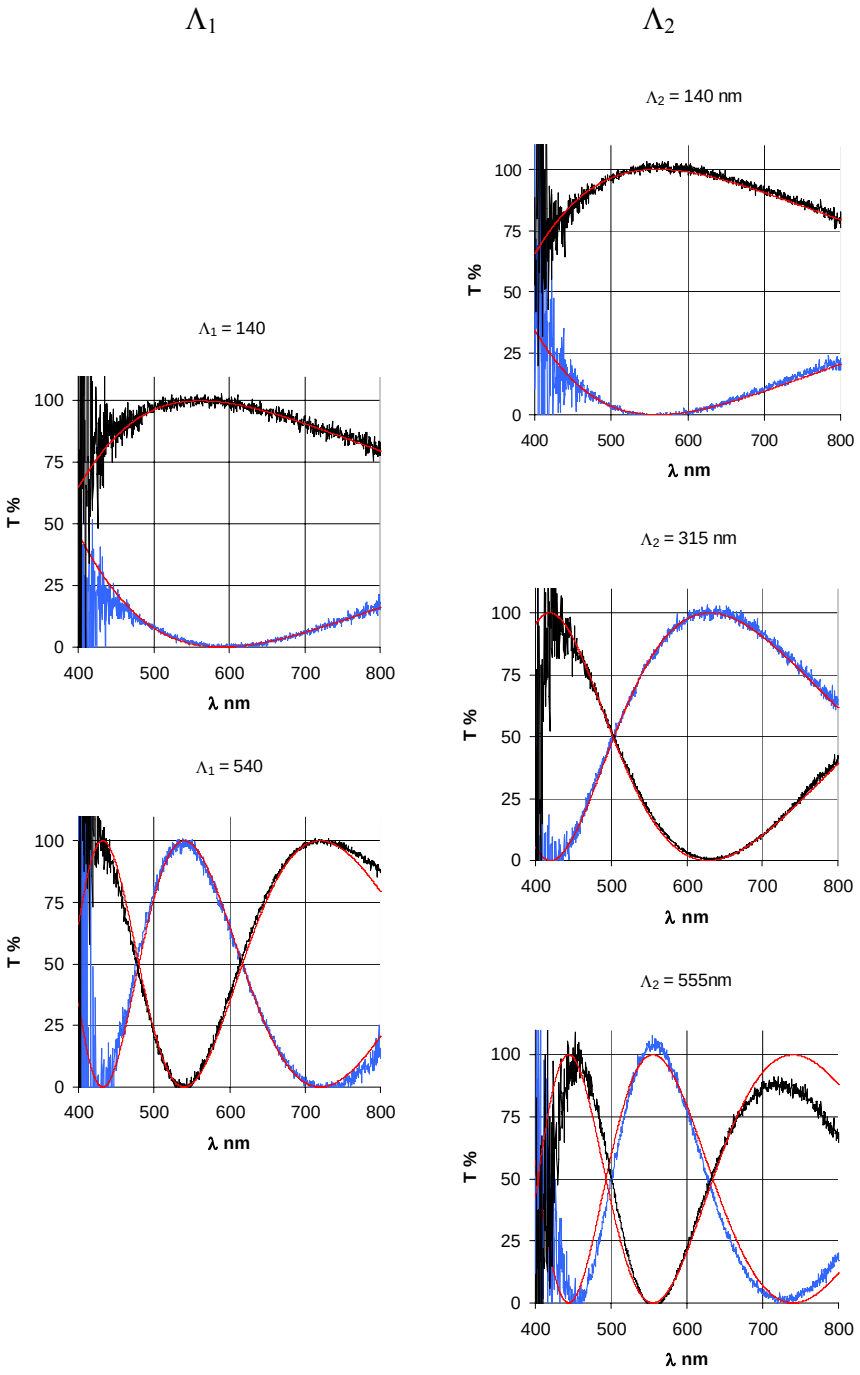

Figure 5.9 Experimental and theoretical (red) transmission spectra for the two sets of retarders: coaxial (normal-incidence) reflected illumination

Λ_1 = 140, 540nm and Λ_2 =140, 315, 555nm retarders between crossed (black) and parallel (blue) polarizers. Horizontal axis: wavelength λ nm; vertical axis transmission T %

The three Λ_2 retarders were then superimposed at $\theta_2 = -45°$, 0° and +45° on each of the two Λ_1 retarders which had fixed orientations of $\theta_1 = 45°$. In this part of the experiment the polarizer/analyzer of the microscope (P1, P2, Figure 5.5) were removed and a single polarizer (P0 Figure 5.5) placed in the illumination/observation path before the first retarder (R in Figure 5.5). This configuration is equivalent to parallel polarizer/analyzer (Figure 5.1(f)). Spectra for the Λ_1: Λ_2 configurations defined in Figure 5.8 are given in Figure 5.10.

Inspection of all figures shows close agreement of the experimental data with the predicted spectra as derived from the appropriate STFs for the configurations tested.

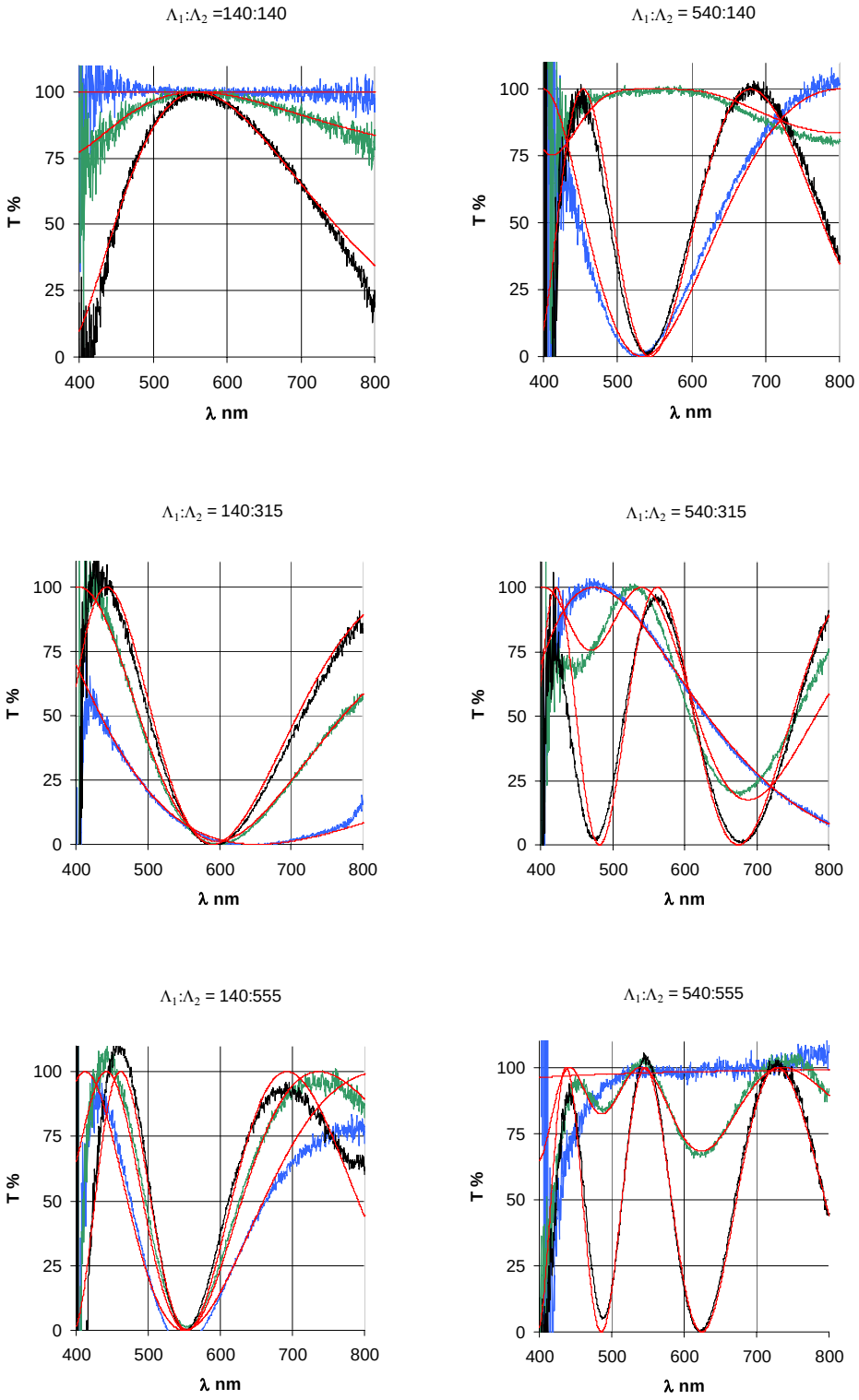

Figure 5.10 Experimental and theoretical (red) transmission spectra for light reflected through retarder pairs

Λ_1: Λ_2 = 140:140, 140:315, 140:555, 540:140, 540:315, 540:555;
$\theta_1 = 45°$ $\theta_2 = -45°$ (blue), 0° (green), +45° (black). (Retardations, Λ, in nm)

5.5 Discussion

To the author's knowledge, this is the first detailed application of Mueller matrices to polariscopy in general and ophthalmic polariscopy in particular although the method has been used in retinal birefringence scanning (Hunter, Sandruck et al. 1999). For simple configurations, the Mueller matrix methods confirm well established principles derived by standard geometric methods. The great facility of Mueller matrices becomes apparent when dealing with retarder trains where geometric methods become unwieldy. This is especially true for reflected light configurations where subtleties such as reversals in angles and changes in phase are easily overlooked as exemplified in Eq. 5.18 – Eq. 5.21.

The aim of this chapter was to identify a simple method using reflected light for the semi-quantitative analysis of an arbitrary retarder of unknown and possibly variable retardance and orientation such as the *in vivo* cornea. The magnitude of unknown retardance is less than several wavelengths of visible light (0 – 3000nm). Review of Figure 5.1 shows that configuration (d) and (f) are possible candidates. Configuration (d) requires two polarizers, but configuration (f) requires coaxial illumination through one polarizer only and one known retarder in order to analyse an unknown retarder against a reflecting background.

The theory of configuration (f) are detailed in §5.2.5. A Spectral Transmission Function (STF) is derived that allows for quantitative exploration of the system defined in terms of δ_1, θ_1 for the fixed known retarder, δ_2, θ_2 for the unknown retarder and a reference wavelength λ_0. If δ_1 is an odd number of quarter wavelengths (of λ_0) and fixed at $\theta_1 = 45°$ ($+\pi/4$ rads) to the polarisation axis, an arbitrary retarder δ_2 will show

maximum light absorption at λ_0, independent of orientation (θ_2). Conversely if the fixed retarder δ_1 has retardance of an integer number of half wavelengths (even number of quarter wavelengths of λ_0) then there is peak transmission at λ_0 for arbitrary retarders δ_2 of integer numbers of half wavelengths, but absorption at λ_0 for δ_2 of odd number of quarter wavelengths (Figure 5.3, Λ_1 = 280nm, 560nm). Furthermore, the absorption/transmission at λ_0 will be orientation (θ_2) dependent (Figure 5.3, Λ_1 = 280nm, 560nm; compare $\theta_2 = -\pi/4$, 0 and $+\pi/4$).

So, a fixed retarder of odd number of quarter wavelengths δ_1 using configuration (f) is required to detect all orientations of retardations δ_2 simultaneously in a birefringent specimen. Furthermore, comparing transmission spectra for Λ_1 = 140 and 420nm (Figure 5.3) for low arbitrary retardations (Λ_2) shows fewer peaks/troughs (less colour desaturation) for Λ_1 = 140nm at higher Λ_2 at $\theta_2 = \pm\pi/4$ and a greater peak-peak amplitude (higher colour contrast) at $\theta_2 = 0$ than for Λ_1 = 420nm. Thus visibly clearer results will be obtained using a retarder of quarter wavelength rather than higher odd multiples of a quarter wavelength.

The spectral characteristics of addition and subtraction of parallel and orthogonal retarders facilitate the analysis of fast/slow axis orientation of an unknown retarder. This is particularly evident from the orientation-dependence of the absorption spectra of integer half wavelength Λ_1, (Figure 5.3, Λ_1 = 280nm, 560nm). The difference in spectra between $\theta_2 = \pm\pi/4$ together with the progressive desaturation towards $\theta_2 = 0$ exaggerates the orientation/summation effect which is accentuated with higher Λ_1 (e.g. Figure 5.3; Λ_1 = 560nm).

The theory is validated by the close agreement between theoretically derived and experimentally determined spectral transmission curves. Some deviation of

experimental data from predicted values were observed and results from imperfections in the retarders (dispersion, pleochroism) and the experimental method (imprecise orientation). Furthermore polarization effects (e.g. partial polarization due to reflection) within the experimental apparatus required careful spectrometer calibration and account for the deviations from predicted values.

The configuration of Figure 5.1f (§5.2.5, §5.3.3) has the potential to be a useful tool in determining the retardation properties of living human corneas. For the device to be of use in a clinical setting the quantitative experimental/theoretical data must be translated to easily and immediately observable visual phenomena such as colour changes. The spectral data predicts visibly detectable retardation-dependent hue changes with coaxial polariscopy. The next chapter defines precisely the qualitative and observable retardation-related phenomena.

5.6 Chapter Summary

1. Linear algebraic methods (Mueller matrices) are used to determine the properties of polarimetric systems
2. Multiple retarder trains are modelled in transmission and reflection
3. The methods are adapted for polychromatic light
4. Spectral characteristics are determined for white light transmission and reflection though single and two-retarder systems.
5. The theory is verified experimentally for up to two retarders with both transmitted and reflected polarized light
6. A method of reflection polariscopy is identified that has potential use in determining retardation of the human cornea *in vivo.*

6 Experimental basis for a clinical method

The preceding chapter identifies a polariscopic configuration suitable for examining retardation phenomena of the human cornea *in vivo*. The purpose of this chapter is to correlate the theoretically and experimentally determined spectral characteristics with a visual phenomenon that can be interpreted by an observer or easily recorded digitally. A simple technique, elliptical polarisation biomicroscopy (EPB) is described.

6.1 Chromatic effects of retardation

The first part of this section examines experimentally the effect on white light of the configurations previously presented. In particular it relates the theoretically derived spectral transmission curves to the observed interference colours.

6.1.1 The quartz wedge

An elongated wedge of clear quartz acts as graded retarder. The wedge is cut with its longer dimension parallel to the normal of the optic axis of the crystal in the direction of the lower (slow) principle refractive index (γ). Retardation of the wedge increases in proportion to its thickness from approximately 100nm to a maximum of about 2200nm. Quartz approaches an 'ideal' retarder by exhibiting no pleochroism and dispersion curves that are nearly parallel (i.e. birefringence is almost constant) for all visible wavelengths. The quartz wedge was calibrated for retardation between crossed linear polarizing filters at $\theta = 45^{\circ}$ and 550 nm (see Appendix §15.4).

6.1.2 Method

The quartz wedge was photographed (Nikon D90, 60mm Micro Nikkor lens) at various rotations in transmitted light (Figure 5.1a) and reflected polarized light with and without interposed retarders (Figure 5.1c, d, e, f; Figure 6.1). Polarizers and retarders could be rotated independently. Definitions of θ, θ_1 and θ_2 are the angles from horizontal of the slow axes of retardation, as previously defined (Figure 5.6). Monochromatic light, when required, was generated using a 550±5nm interference filter, otherwise incandescent (quartz-halogen) white light was used. Digitised images were manipulated when necessary using Paint Shop Pro 7 (Ver. 7.04; Corel, Ottawa, ON, Canada) graphic software and image analysis was performed with ImageJ software (Rasband 1997-2012).

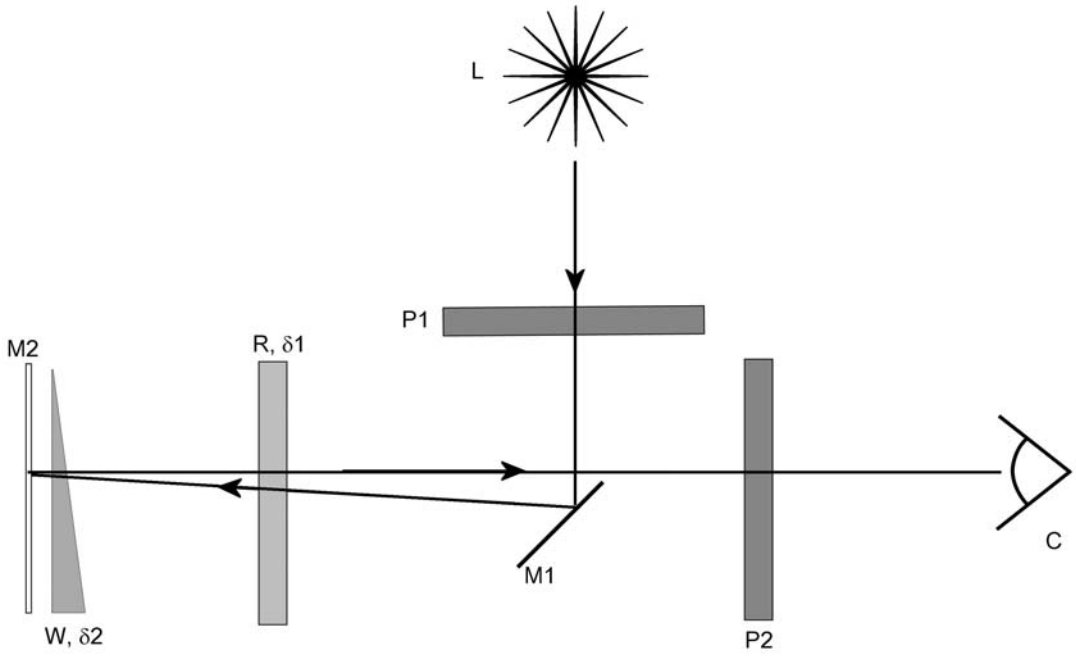

Figure 6.1 Schematic experimental setup:

Wedge (W, δ_2) orientated at θ_2, optional retarder R, δ_1 orientated at θ_1; polarizer (P1) orientated at α = 0; polarizer (analyzer, P2) orientated at α = 0 or 90°. Mirrors M1/M2; Light sources L, observer/camera C.

6.1.2.1 Transmitted monochromatic light

The wedge was orientated with slow axis at 45˚ to the principal axis of the first linear polarizing filter (polarizer) (extinction occurs when the wedge is orientated at either 0° or 90° to the crossed polarization directions). The second polarizing filter (analyzer) was either in the uncrossed ($\alpha = 0°$) or crossed ($\alpha = 90°$) position.

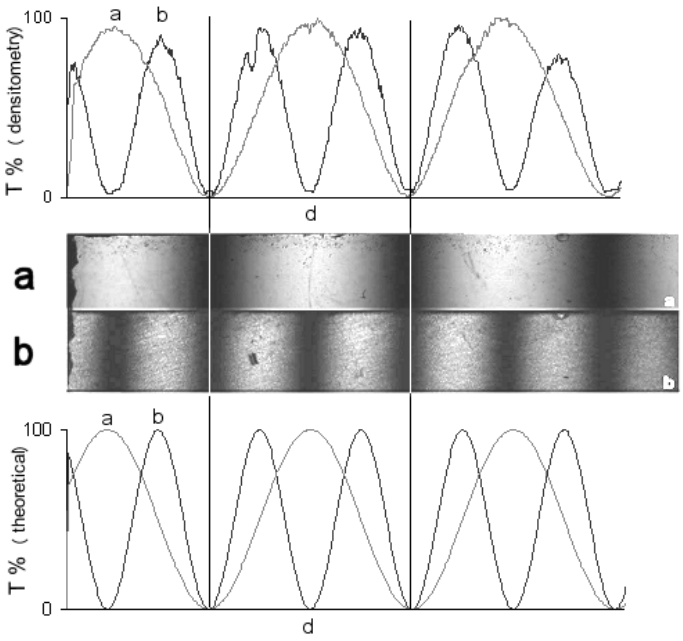

Figure 6.2 Wedge in monochromatic light

(a) crossed polarizers: transmission.
(b) crossed polarizers: reflection.
Upper graph: densitometry of (a) grey line; (b) black line.
Lower graph: predicted light transmission (a) grey line Eq. 5.3, (b) black line Eq. 5.16.
Vertical axes: normalised light transmission, T %; horizontal axes distance along wedge from thin end, d (arbitrary length units).
Long vertical lines are one wavelength retardation (550nm) apart.

An alternating series of light and dark bands are visible (Figure 6.2 centre portion a) between crossed polarizing filters. The intensity of light transmission is determined by Eq. 5.3 (Figure 6.2, lower graph black curve). Lines of minimum transmission correspond to retardations of an integer number of wavelengths. The densitometric analysis of transmission with increasing wedge thickness is shown in Figure 6.2, (upper graph black curve) and agrees with that predicted. When polarizers are parallel complete transmission occurs in the 0/90° positions and the pattern is the same at θ = 45° but shifted by half a wavelength: thus dark bands equate to odd integer numbers of half wavelengths, as predicted by Eq. 5.2. At intermediate orientations of the wedge

(i.e. not 0, 45 or 90°) the bands are present but fainter increasing in density from 0 to a maximum at 45° and then decreasing again to vanish at 90°.

6.1.2.2 Transmitted white light

With white light, interference colours replace the dark bands seen with monochromatic light (Figure 6.3). The colours are as predicted by the STF $T_{\perp}$ and $T_{\parallel}$ (Eq. 5.35, Eq. 5.36, §5.3.1) and represented graphically as spectra in Figure 6.3 adjacent to the relevant interference colour. Interference colours for parallel and crossed polarizers are complimentary.

Between crossed polarizers, the reddish violet hue corresponding to a retardation of Λ = 550/60nm rapidly turns to blue with a slightly increased retardance. This 'sensitive tint' (Wahlstrom 1979) allows estimation of retardance at or near 550/560nm. Similar, but desaturated, hue changes are seen near Λ = 1120nm and Λ = 1680nm. With parallel polarizers a hue change similar to, but spectrally different from Λ = 550nm with crossed polarizers identifies Λ = 280nm (½λ), 840nm ($^3/_2$ λ) etc.

The progression of interference colours and their interrelationship with birefringence and thickness of colourless birefringent materials with parallel dispersion curves forms the basis for the Michel-Lévy chart used in optical crystallography (Wahlstrom 1979). Interference colours (Figure 6.3) due to increasing retardation are grouped into 'orders' whereby the conspicuous red/pink bands with crossed polarizers (yellow-green bands with parallel polarizers) indicate the upper limit of each order corresponding approximately to integer multiples of 560nm. With parallel polarizers, the conspicuous pink bands correspond to $\{n + ½: n \in \mathbb{Z}\}$ orders where n is the interference order with crossed polarizers.

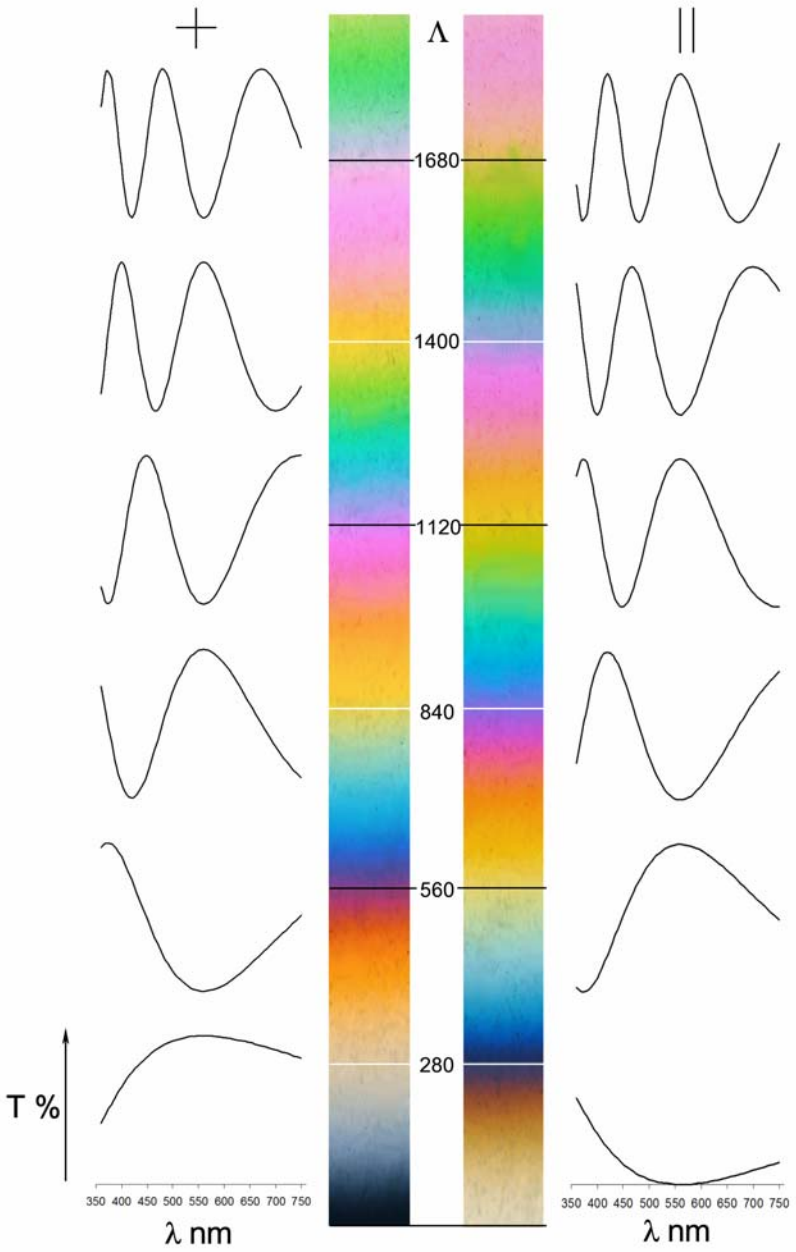

Figure 6.3 Quartz wedge (central two images, thin end below) observed in white light between crossed polarizers (left) and parallel polarizers (right)

Transmission spectra (derived from Eq. 5.35, Eq. 5.36, §5.3.1) are given for the adjacent wedge at path differences (Λ nm) indicated by horizontal bars. Crossed polarizers (+ left columns); parallel polarizers (|| right columns). Horizontal axes: wavelengths λ nm; vertical axes: normalised transmission T.

6.1.3 Reflected light

The experimental configuration is shown in Figure 6.1, with polarizers either parallel or crossed, and with wedge alone or wedge and superimposed retarder. When required, single or stacked parallel 140nm polymer retarders were used to give fixed retardations of approximately Λ_1 = 140, 280, 420 and 560nm. This method was not used in the previous quantitative study because minor inaccuracies of orientation and multiple reflections from surfaces degrade the quantitative results. Such inaccuracies are less significant in this qualitative study.

6.1.3.1 Monochromatic light, wedge only

In the simplest case the quartz wedge was observed alone with monochromatic (550nm) light. As with the transmission experiments for crossed polarizers extinction occurred at the 0/90° position and dark bands are observed with maximum contrast in the 45° position. The dark bands have twice the spatial frequency (integer multiples of half wavelengths of 550nm) of those observed with transmitted polarized light (Figure 6.2 b). With parallel polarizers the dark bands occur at odd integer multiples of quarter wavelengths of 550nm.

6.1.3.2 White light: wedge

The experiment was repeated with white light illumination. In this case the wedge was photographed at 10° intervals from $\theta_2 = -45°$ to $\theta_2 = +45°$ together with additional images at 22.5°, 45° and 67.5° (Figure 6.4). In the ±45° positions, for both crossed and parallel polarizers, the coloured fringes were identical to the transmitted case but with twice the spatial frequency. These are the expected results from a double pass through the retarder as predicted by Eq. 5.39.

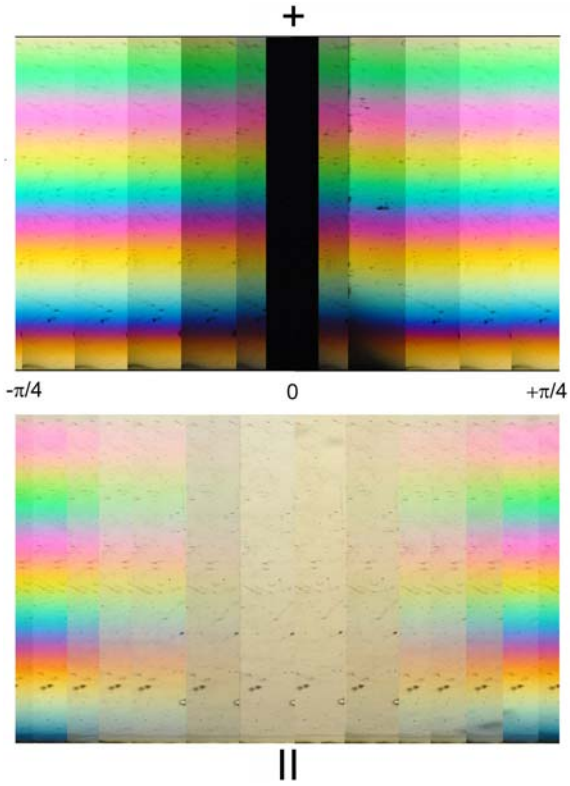

Figure 6.4 Quartz wedge orientated $-45° \leq \theta_2 \leq 45°$
Observed in reflected polarized light with polarizers crossed (+ upper) and uncrossed (|| lower)

6.1.3.3 White light: wedge, retarders and parallel polarizers

The experiment was repeated with a retarder (Λ_1 = 140, 280, 420, 560nm) fixed at θ_1 = +45° placed in the light path as depicted schematically in Figure 6.1 and with parallel polarizers. The wedge was photographed as described above at 10° intervals from θ_2 = –45° to θ_2 = +45° together with additional images at 22.5°, 45° and 67.5°. Composites of the results are presented in Figure 6.5.

For Λ_1 = 140nm with the wedge at θ_2 = 0°, the interference fringes appear similar to those observed with the wedge alone observed with reflected light, crossed polarizers at θ_2 = 45°. This result may be predicted from Eq. 5.39 and indicated graphically in Figure 5.3 which if compared to Figure 6.3 (left columns, and doubling the value of Λ to account for a double pass): the two sets of spectra are similar, but not identical. At θ_2

= ±45° the slow axes of both retarders are respectively perpendicular and parallel so subtraction/addition occurs. Under these condition, the fringes are identical to those of the single wedge at $\theta_2 = \pm 45°$ with parallel polarizers, but displaced up or down by the equivalent of 140nm. This is evident if columns $\theta_2 = \pm 45°$ of the left upper panel of Figure 5.3 are compared. Similar results, but with correspondingly greater displacement, may be seen with $\Lambda_1 = 420$nm (Figure 5.3 left lower panel)

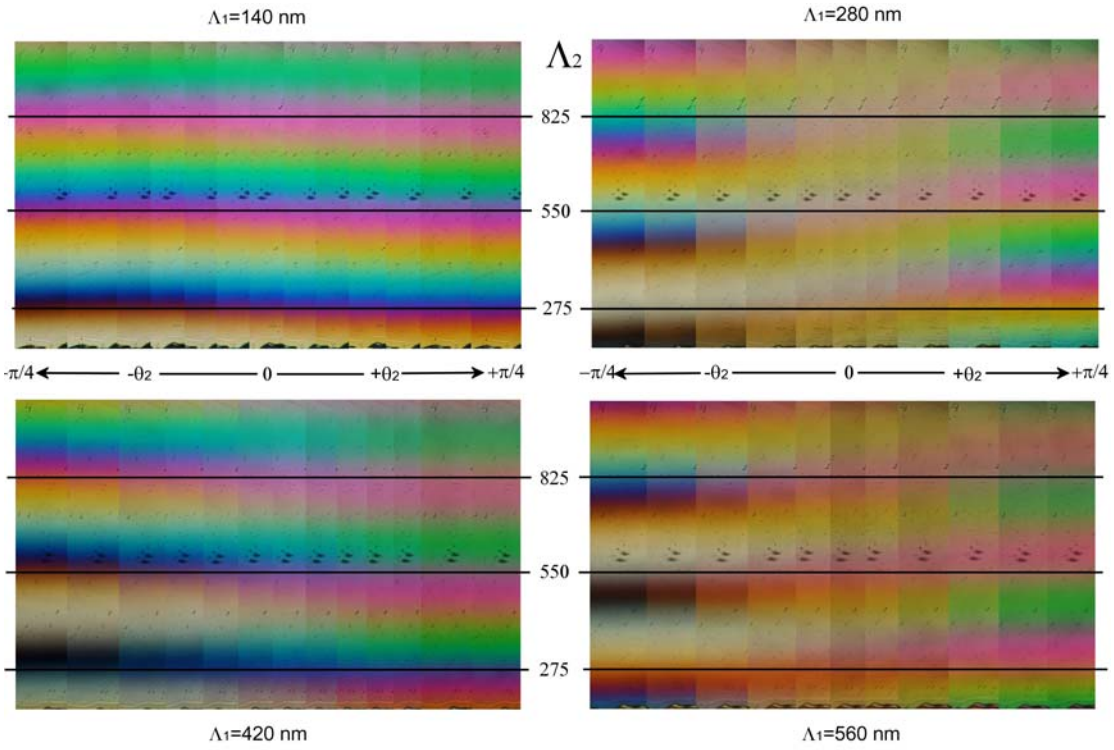

Figure 6.5 Quartz wedge and fixed retarder

Wedge orientated $-\pi/2 \leq \theta_1 \leq \pi/2$ observed in reflected light through linear polarizer and additional retarder ($\Lambda_1 = 140, 280, 420, 560$nm) fixed at $\theta_1 = +45°$.
Note the direct correspondence with the predicted spectral transmission curves Figure 5.3 §5.3.3.

With $\Lambda_1 = 280$ and 560nm subtraction and addition occur at $\theta_2 = \pm 45°$ with a corresponding displacement of the fringes according to the added/subtracted value of Λ_1 to/from Λ_2 of the wedge. At $-45° < \theta_2 < +45°$ the spectral transmissions have a desaturated waveform as predicted by the STF R2 (Eq. 5.39 §5.3.3).

There is direct correspondence between Figure 6.5 and Figure 5.3 where the theoretical transmission spectra respectively represent the lower halves of the right, central and left segments ($\theta_2 = -\pi/4, 0, +\pi/4$) of each of the panels in Figure 6.5. In particular, the spectral curves found in §5.3.3 relate directly to the interference colours in Figure 6.5. So, for example, in Figure 6.5 (bottom right) the graph of transmission spectra with superimposed $\Lambda_1 = 550$nm and $\Lambda_2 = 560$nm retarders can be seen to be a light grey at the $\theta_2 = -45°$, desaturated orange /pink at $\theta_2 = 0°$ and saturated orange/pink at $\theta_2 = +45°$. Of particular note are the colour changes when $\Lambda_1 = 140$nm as outlined above.

Whilst there is a rotation (θ_2)-related colour change for the fringes at any particular wedge retardation, the perceived colour changes are small throughout the range $-\pi/2 \leq \theta_2 \leq \pi/2$. This is an approximation of the finding for monochromatic light and a quarter wave retarder where it was found that intensity of transmitted light was a $\sin^2$ function and independent of orientation (Eq. 5.33 §5.2.5) noting that a $\Lambda_1 = 140$nm retarder is a quarter wave retarder for the standard wavelength $\lambda_0 = 560$nm.

A general point arises here that for odd fractions of a quarter wavelength retardation Λ_1, the interference colours at half-wavelength intervals of Λ_2 remain saturated, whereas the same Λ_2 with even fractions of quarter wavelength retardation Λ_1 are desaturated. This is evident in Figure 6.5 where there is no apparent change in saturation of the two left panels ($\Lambda_1 = ¼$ and $¾ \times 560$nm) whereas there is progressive desaturation towards $\theta_2 = 0$ for the right hand panels ($\Lambda_1 = ½$ and 1×560nm). Furthermore the change in hue in

the range $-\pi/2 \leq \theta_2 \leq \pi/2$ are more evident for the right hand panels. Similar conclusions may be drawn from inspecting the predicted spectra in Figure 5.3, §5.3.3.

Reflection polariscopy with a $\Lambda_1 = 140$nm fixed retarder and linear polarizer generates isochromes that are continuous in intensity at any orientation for a given retardation although there are orientation-specific changes in spectral characteristics. The spectral changes translate to an observed subtle change in hue. This configuration is suitable for determining the pattern of isochromes, and hence retardation, throughout a variably birefringent material.

Reflection polariscopy with a fixed retarder (Λ_1) of integer multiples of half-wavelengths gives a clearly defined orientation-specific interference colour change determined by subtraction or addition of orthogonal or parallel slow/fast axes of fixed/unknown retarder (Λ_2). Reflection polariscopy with such a fixed retarder allows determination of the orientation of fast/slow axes of an unknown retarder.

The red-purple to indigo blue (lower to higher Λ) interference colour transition is evident in Figure 6.5. In conventional transmission polarization microscopy a similar colour change is noted for retardations of 550 – 580nm and indicates the transition from first to second-order interference colours (see §6.1.2.2). This colour change (termed a 'sensitive tint' (Wahlstrom 1979)) has a practical use in determining the fast/slow directions of an unknown retarder: if a 560nm retarder with known axes is superimposed on an unknown retarder then characteristic and different interference

colours result from subtraction/addition when principle axes are orientated respectively orthogonal/parallel even for relatively small retardations.

Results analogous to polarization microscopy are seen here except that the 'sensitive tint' transition occurs at $\Lambda_2 = 280$nm and similar colour transitions of 'higher order' at integer multiples thereof (see top left panel Figure 6.5). Qualitative colour changes representing addition (increase in 'order' of interference colours when there is superposition of like axes of retardation of two retarders) and subtraction (decrease in order of interference colours on superposition of opposite axes of retardation of two retarders) are also evident (see bottom right panel Figure 6.5: subtraction on left, addition on right).

6.2 'Circular' polarizers

Inexpensive commercially available laminates of appropriately orientated retarders and linear polarizers are readily available as 'circular polarizing filters' for use in digital photography. Two such filters of different construction were obtained for this study. The first (circular polarizing filter, Jessops, UK), referred to as 140P, comprises a 140nm polymer retarder/dichroic linear polarizer laminate. The second (550P) is of similar construction, but with a 550nm retarder (circular polarizing filter, Green.L, Shenzhen, China). The retardations of each were verified using the Berek compensator as previously detailed (§5.4.1, §15.4.1). Both retarders are orientated relative to the polarizer such that right-handed elliptical/circular polarization is generated. The polarizer/retarder laminates are essentially equivalent to the linear polarizer/retarder

combinations explored in previous chapters, but offer the convenience of the combination in one robust unit that is easily positioned and orientated.

The use of the term 'circular polarizer' should be avoided as, in the case of 140P, circular polarization is only achieved with incident monochromatic light 4 x 140nm = 560nm. The 550P is erroneously designated as a 'circular' polarizer as it is essentially a laminate of a linear polarizer and 'full-wave' retarder. Such a combination generates linear polarized light, but only at $\lambda = 550$nm. Thus both 140P and 550P are better described as elliptical polarizers.

The correspondence of 140P and 550P with previous findings was tested in a similar way to that presented in §6.1.3.

6.2.1 Methods

The configuration shown in Figure 6.6 is obtained by placing the 140P or 550P retarder/polarizer in the illuminating/observation path whilst observing the wedge against a reflecting surface. The technical details are as previously described (§6.1.3). In this case, however, the target is a wedge of similar design to that used previously but with a superimposed graduated scale. Calibration of the graduated wedge was performed at 560nm as detailed in §15.4. The wedge calibration function is $\Delta_w = 0.052.d + 0.24$ where Δ_w is wedge retardance i.e. retardance of the wedge in wavelength multiples of the calibrating wavelength (560nm in this case; the corresponding retardation is Λ_w in nm), d is the wedge scale reading.

The wedge (W, Figure 6.6) is illuminated and observed/photographed (c) through a single linear polarizing filter, 140P and 550P (R-P0) as previously described (§6.1.3). The wedge is orientated in positions of addition and subtraction relative to 140/550P.

It is assumed that 140P and 550P have retardances approximating to ¼λ_0 and 1λ_0 respectively where λ_0 = 560nm.

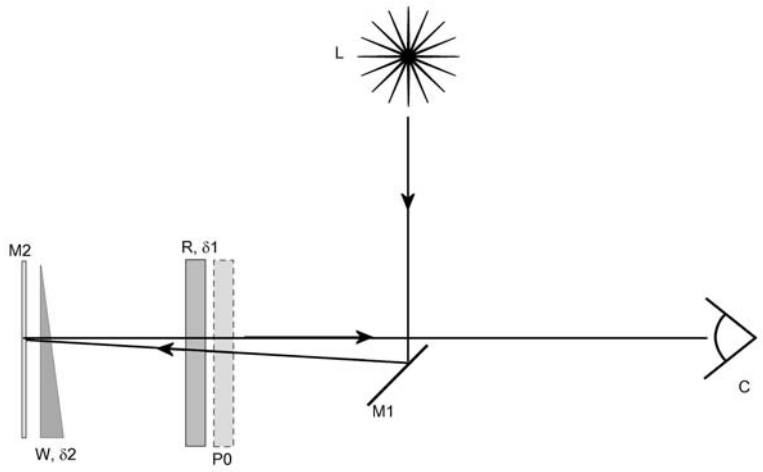

Figure 6.6 Experimental setup

Laminated elliptical polarizers represented by combination of retarder R and polarizer P0 (140P, 550P). Annotations as noted in Figure 6.1

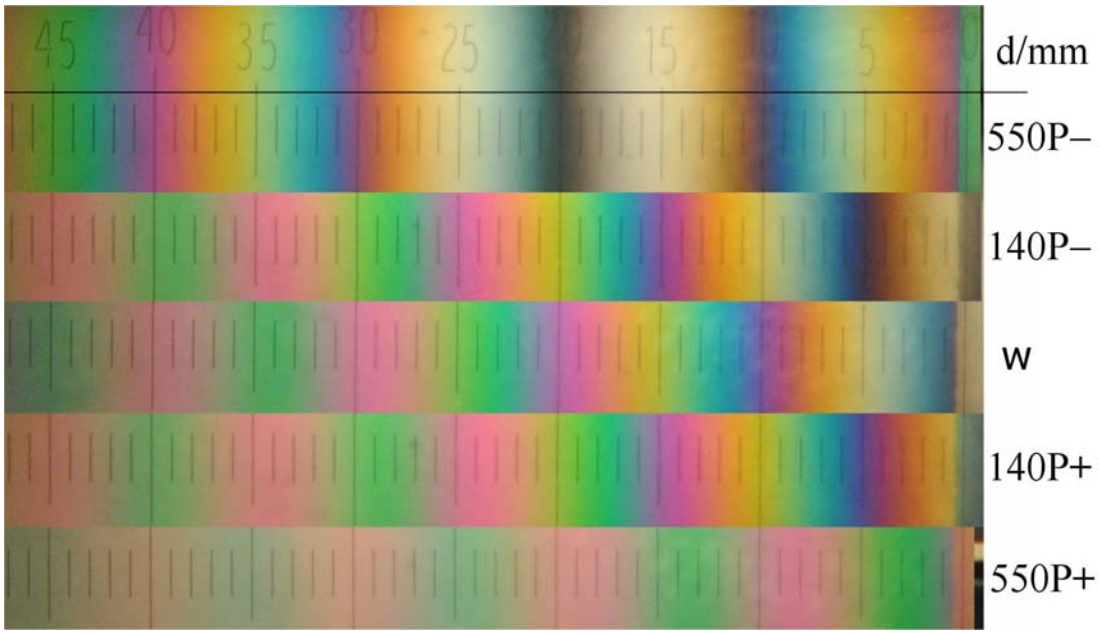

Figure 6.7 Graduated quartz wedge: coaxial reflected white light illumination/observation with/without 140P and 550P

w: linear polarizer without retarder (45° to wedge). 140P and 550P in subtraction (–) and addition (+) positions; d is wedge scale in mm from thin end i.e. increasing thickness to left.

6.2.2 Results: graduated wedge

Results are shown in Figure 6.7 which is a composite of the graduated wedge illuminated/observed under the above condition through a plane linear polarizer (0), 140P and 550P in subtraction (–) and addition (+) positions. First note the distribution of isochromes with the plane polarizer alone (0): this is identical to a wedge observed in transmitted light through parallel polarizers, but with double the wedge retardation as detailed in §6.1.3.2. Note particularly the extinction isochrome (black) at approximately d = 0 corresponding to a wedge retardation Λ_w = 140nm ($\Delta_w = ¼\lambda_0$, total retardation Λ_T = 280nm, $\Delta_T = ½\lambda_0$; see calibration curve Figure 15.9). With 140P and 550P in the subtraction position this isochrome moves to the left to d = 5 and d = 20 respectively i.e. positions of $\Lambda_w \approx$ 280nm (½ λ_0) and 700nm (1¼ λ_0) ($\Lambda_T \approx$ 560nm (λ_0) and 1400nm (2 ½λ_0)) respectively.

With 140P and 550P in the subtraction positions, the isochromes move to the right by a corresponding amount. Thus the green/yellow isochrome for plane polarized light (0) at d = 25 ($\Lambda_w \approx$ 840nm (1½ λ_0)) moves to d = 20 ($\Lambda_w \approx$ 700nm (1¼ λ_0)) and thence to d = 5 ($\Lambda_w \approx$ 280nm (½λ_0)).

In summary, 140P and 550P respectively cause a shift in isochromes by 140nm (≈¼λ_0) and 550nm (≈ 1λ_0) in a direction dependent on addition or subtraction.

Not shown here, but identified in §6.1.3.3, is the orientation sensitivity of the isochromes. Thus 550P and plane polarized generated isochromes are orientation specific, being maximum and zero at 45° and 0° to the polarization axis respectively. The 140P generated isochromes remain independent of orientation apart from their hue

which changes between subtraction and addition (e.g. compare isochrome at d = 5, ± 140nm (¼λ_0), Figure 6.7).

The 'sensitive-tint' (first order black and subsequent red-blue transition, cf §6.1.2.2) interference colours generated by 140P (¼λ_0) in both addition and subtraction positions occur at d = 5, 15, 25 corresponding to wedge retardations of approximately Λ_w = 280, 560 and 840nm.

6.3 Conclusion/ synthesis

When observing an arbitrary retarder with coaxial reflected illumination through 140P, a characteristic retardation-dependent interference pattern is generated. The continuity of contours of equal retardation (isochromes) is independent or orientation of retarder relative to 140P thereby allowing instantaneous examination of all regions of the test object without the need to adjust the instrument parameters. The chromatic difference between low-order isochromes in addition and subtraction positions for 140P is subtle, but it is exaggerated and easily seen with 550P (e.g. compare isochromes at d = 20 for ±550P, Figure 6.7). Furthermore, the low-order ('extinction' isochromes) of both 140P and 550P are easily identified as black / dark blue bands and indicate the position in the test object of retardance/retardation ½λ = 280nm (d = 5 for ±140P, Figure 6.7) and 1¼λ = 700nm (d = 20 for –550P, Figure 6.7) interference contours respectively. For 140P 'sensitive tint' colour changes occur at small integer multiples (e.g. n = 1, 2, 3, 4) of 280nm allowing these isochromes to be easily identified by eye or photographically. Higher integer multiples of these retardations have corresponding similar, but progressively more desaturated interference colours.

The filters 140P and 550P have complementary functions in a coaxial polariscopic configuration: 140P defines isochrome/ equiretardation contours (particularly Λ = 280nm) whilst 550P may be used to determine fast/slow axes of retardation by observing subtraction/addition phenomena.

The living human cornea is superimposed on a reflecting background (the posterior corneal surface and the iris) and has a range of retardations within that tested here. The technique of coaxial reflection polariscopy with 140P and 550P filters is therefore a possible method for retardation determination of the *in vivo* human cornea. For convenience, coaxial reflection polariscopy with 140P and 550P filters, will be referred to as *elliptic polarization biomicroscopy* (EPB): 'elliptic' referring to the general state of polarization of light in the system. This is the subject of the next chapter.

6.4 Chapter Summary

1) The quartz wedge is established as a useful birefringent target for testing polariscopic systems.
2) For monochromatic light in transmission between crossed polarizers destructive interference, seen as dark fringes, occurs at integer multiples of the wavelength of the incident light.
3) For monochromatic light in transmission between parallel polarizers dark fringes (as in (2)) occur at odd integer multiples of half wavelengths of the incident light.
4) Interference colours are maximal with retarder rotated at 45° to the polarizer axes. When the retarder is parallel/orthogonal to polarizers extinction occurs with crossed polarizers and transmission without interference occurs with parallel polarizers.
5) For monochromatic light in reflection between crossed polarizers destructive interference seen as dark fringes occurs at integers multiples of half wavelength of the incident light.
6) For monochromatic light in reflection between parallel polarizers dark fringes (as in (5)) occur at odd integer multiples of quarter wavelengths of the incident light.
7) For white light in transmission with crossed/uncrossed polarizers, characteristic retardation-related coloured fringes due to wavelength-dependent selective interference are seen.

8) The coloured fringes seen with parallel polarizers are complementary to those seen with crossed polarizers.

9) For a retarder (Λ) observed with transmitted white light between polarizers, a characteristic abrupt colour change (purple-red to blue; 'sensitive tint') occurs at integer multiples of about Λ=560nm for crossed polarizers and at Λ= integer multiples of 560nm + 280nm for parallel polarizers (transmitted light).

10) The 'sensitive tint' spectral characteristics are different for crossed and parallel polarizers.

11) Reflection halves the spacing of the fringes in both (7) and (8) as observed in (6) and (7). Otherwise the spectral characteristics are identical.

12) The 'sensitive-tint' colour changes of (9) are seen in reflection, but occur at integer multiples of Λ = 280nm for crossed polarizers and Λ= integer multiples of 280nm + 140nm for parallel polarizers.

13) When two retarders are stacked and observed with parallel polarizers and white light, the interference colours (Figure 6.5) are as predicted in Figure 5.3.

14) If one of the retarders in (13) is Λ_1 = 140nm a 'sensitive tint' colour change is seen at small integer multiples of Λ_2 = 280nm retardation of the second retarder.

15) The 140nm/unknown double retarder configuration is relatively insensitive to orientation of the unknown retarder.

16) If one of the retarders in (13) is 560nm an exaggerated orientation-dependent colour change is observed indicating addition and subtraction phenomena allowing for determination of the fast/slow axis of the unknown.

17) Laminates of linear polarizer and 140nm (140P) or 550nm (550P) retarders are commercially available as 'circular polarizing' filters.

18) The 140P/550P laminates produce qualitative identical results to the theoretically and experimentally established combinations presented in previous chapters.
19) The laminates can be used to determine the distribution of retardation (140P) and slow/fast axes of retardation (550P) in the human cornea *in vivo*.
20) Coaxial reflection polariscopy with 140P and 550P filters is referred to as *elliptic polarization biomicroscopy* (EPB).

7 Corneal elliptic polarization biomicroscopy: preliminary and macroscopic findings. Normal Human corneas *in vivo*

The principles of elliptic polarization biomicroscopy (EPB) have been determined theoretically and verified on experimental models. The previous section proposed that coaxial reflection polarimetry can be used to investigate the human cornea *in vivo*. The 140P filter defines isochrome/equiretardation contours and 550P determine fast/slow axes of retardation by observing subtraction/addition phenomena.

The purpose of this chapter is to explore the practicality of EPB and to use the results to determine some fundamental data for the human cornea *in vivo*.

7.1 Method

Much of this and subsequent chapters will be developing, using and interpreting the results of EPB with slit-lamp biomicroscopy and conventional digital photography (See Appendix 15.5.2).

The basic configuration of Figure 5.1f, Eq. 5.18, Table 5.4 may be obtained by placing the 140P or 550P retarder/polarizer in the illuminating/observation path of the slit-lamp biomicroscope whilst observing the anterior segment of an eye or other reflective test object (Figure 7.1). In practice this is similar to the common ophthalmic clinical practice of holding an indirect (e.g. 90 dioptre) fundoscopy lens for slit-lamp biomicroscopic examination of the posterior segment of the eye. There is no mechanical or optical modification of the slit-lamp.

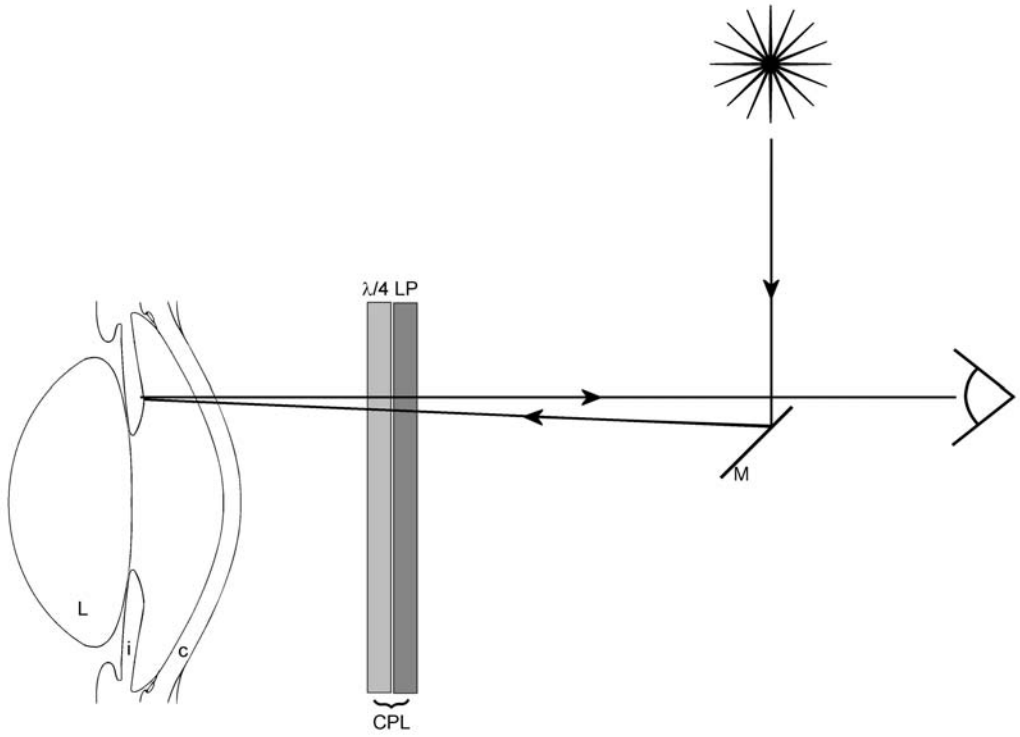

Figure 7.1 Schematic configuration of corneal examination with 140P/550P

Slit-lamp optics are simplified to a simple light source transmitted through the retarder/polarized laminate (CPL) and cornea (c) then reflected from intraocular structures such as the iris (i) and lens (L) back through CPL to the eye/camera. Symbolism as in Figure 6.1.

Observations/photography was performed in a darkened room with a Topcon SL-D7 photo slit-lamp with a Nikon D70 (6.1 megapixels) camera back. Near coaxial (≤ 15º from the observation axis) white incandescent light illumination was used and, for this part of the study, images were taken at a magnification of 6× or 10×. The slit beam width/height was varied according to the requirements of the image and most images were recorded by proximal indirect illumination or retroillumination (see §15.5.2). Initial images of a 0.1mm micrometer grid scale were recorded at each magnification for later measurement calibrations. Images were stored as Tiff files (2240 × 1488 pixels). Analysis of digital images (densitometry, linear and angular measurement) was performed with ImageJ v1.345 image analysis software (Rasband 1997-2012) following

appropriate calibration. Measurement and analysis was performed using unenhanced digital images, however, for the purpose of publication, the contrast, brightness and sharpness of figures presented in this text were enhanced using commercially available image processing software (Paint Shop Pro, Ver. 7.04; Jasc Software). The same software was used in annotating and preparing diagrams throughout this work. Subject positioning was as for any routine slit-lamp examination with chin and forehead firmly placed on appropriate rests. For most purposes, the subject was asked to look ahead in the primary position or to look at a fixation target to ensure stable fixation. All subjects gave informed verbal consent to both examination and the recording of anonymised data including year of birth, gender, the presence/absence of previous eye conditions/surgery.

7.2 A pilot study

A preliminary pilot study was performed on 5 healthy trained volunteers (IL01, 02, 03, 04, 06) according to the method outlined above (§7.1). The following results are qualitative, but serve as a basis for more detailed study in subsequent chapters.

7.2.1 140P

Examination of all subjects with white light through 140P reveals qualitatively similar findings (Figure 7.2). Under low magnification (6 - 10×) two dark patches are observed straddling the pupil typically aligned inferonasal - superotemporal, the latter is larger and less well defined. By comparison with the results of previous chapters, the dark patches are assumed to be areas of low or zero birefringence under the particular prevailing conditions of illumination and position of the cornea. The cornea is therefore

isotropic in these areas which will be termed isotropes by comparison with similar phenomena described in optical crystallography. The centre of the cornea/optical zone therefore has a non-zero retardation in the cases studied. Coloured, approximately diamond-shaped, rings with horizontal and vertical apices are present at the corneal periphery. The centrifugal progression of colours is that expected for interference colours due to increasing birefringence such as those observed previously for the quartz wedge under similar conditions (Figure 6.7, 140P±). In keeping with previous studies, the rings will be termed isochromes and assumed to represent contours of equal retardation.

a b

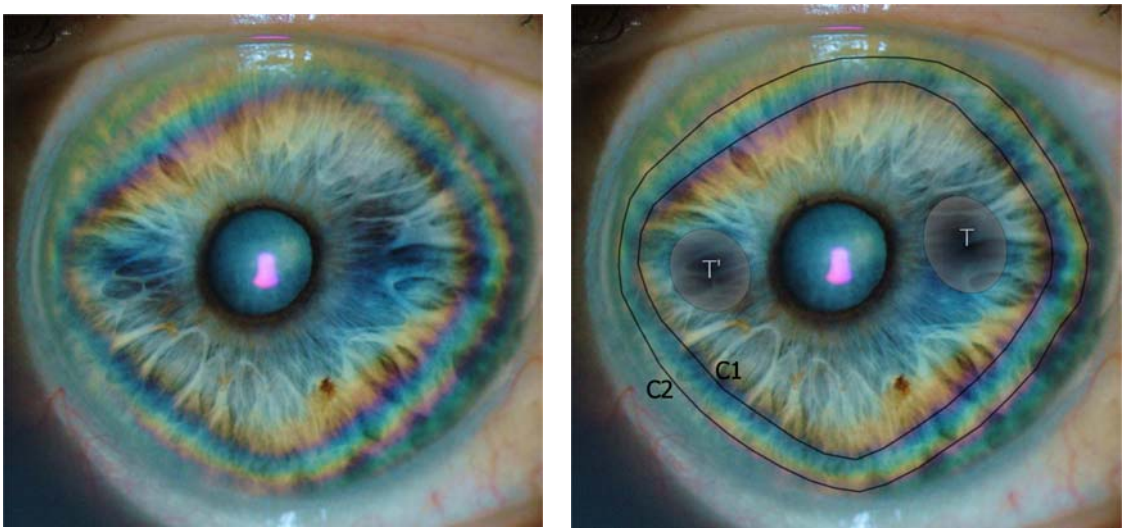

Figure 7.2 A typical image with 140P

a) Left eye, subject IL01. b) annotated image indicating isotropes (T, T') and two isochromes corresponding to first (c1) and second (c2) order fringes.

The intensity of isochromes remains constant although their hue varies subtly depending on the orientation of slow direction of P140 relative to the corneal azimuth (Figure 7.3). Isochromes in quadrants aligned with the slow direction of the retarder demonstrate subtraction phenomena and those in quadrants orthogonal to the slow direction (i.e.

aligned with fast direction) show addition. This is best seen by observing the prominent 'first order' isochrome which is black and blue in quadrants respectively parallel and orthogonal to the retarder slow axis.

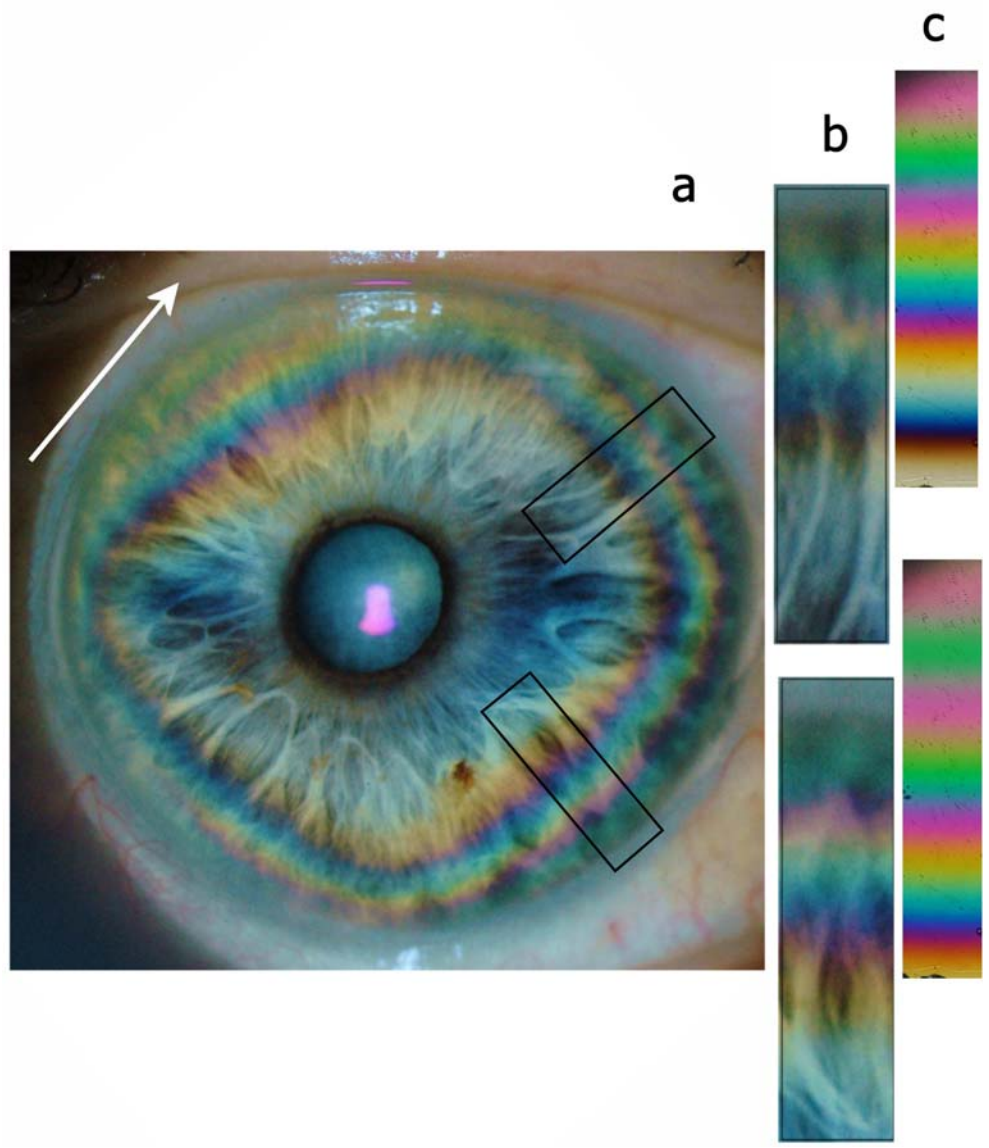

Figure 7.3 Addition and subtraction phenomena and correspondence of observed isochromes with quartz wedge interference colours.

a) Isochromes as in Figure 7.2; b) magnified sections of isochromes as indicated in (a); c) quartz wedge photographed as in Figure 6.6 and Figure 6.7 (140P±) i.e. with reflected polarized light, parallel polarizers, parallel fast/slow axes (addition, bottom) and perpendicular fast slow axes (subtraction, top). White arrow (top left) indicates slow direction of 140P.

The observed colour progression is in accordance with Figure 6.5 with Λ_1 = 140nm and Figure 6.7, 140P±. The implication of this is that the slow-direction of the cornea follows the isochrome contour.

The prominent black/blue corneal isochrome (c1 in Figure 7.2b) is comparable to the 280nm (½λ) isochrome of the quartz wedge identified in §6.1 and §6.2. It is a constant feature of the five cases examined with 140P in this preliminary study and will be used as a landmark in subsequent investigations. More peripheral blue/purple ('sensitive tint' §6.1.3.3) isochromes represent increasing integer multiples of 280nm. The isochrome pattern in all cases is a distorted diamond-shape as shown in Figure 7.2 and Figure 7.3 with four apices approximately in the vertical and horizontal meridians. Radial colour progression is similar in all cases and approximately equivalent to a maximum peripheral retardation of up to 840nm (three blue/purple fringes; c1 and c2 in Figure 7.2 correspond to 280nm and 560nm). There is intersubject variation in shape of the isochrome distribution, but approximate bilateral (right/left) intrasubject symmetry (Figure 7.4).

At higher magnification all cases have a fibrillar microstructure visible within the central corneal areas between and associated with the isotropes. This microstructure becomes less defined towards the corneal periphery. Clarity of the central fibrils is increased by pupil dilatation where light can be reflected from the anterior lens capsule. The fibrillar structure is the subject of Chapter 8 and will not be discussed further here.

7.2.2 550P

The 550P filter was used in the same way as 140P in the same 5 pairs of eyes as detailed above. Findings were different from those of 140P (Figure 7.4). Isochrome intensity showed meridional variation and was maximal in the directions of principle (fast/slow)

axes of the retarder and barely visible at 45° to these positions. As with 140P, isochromes in quadrants aligned with the slow direction of the retarder demonstrated subtraction and those in quadrants orthogonal to the slow direction showed addition (Figure 7.4, lower images). Here, the chromatic changes were greater than with 140P in that subtraction resulted in low-order colours (black, blue etc) and addition resulted in high-order colours (desaturated greens, pinks).

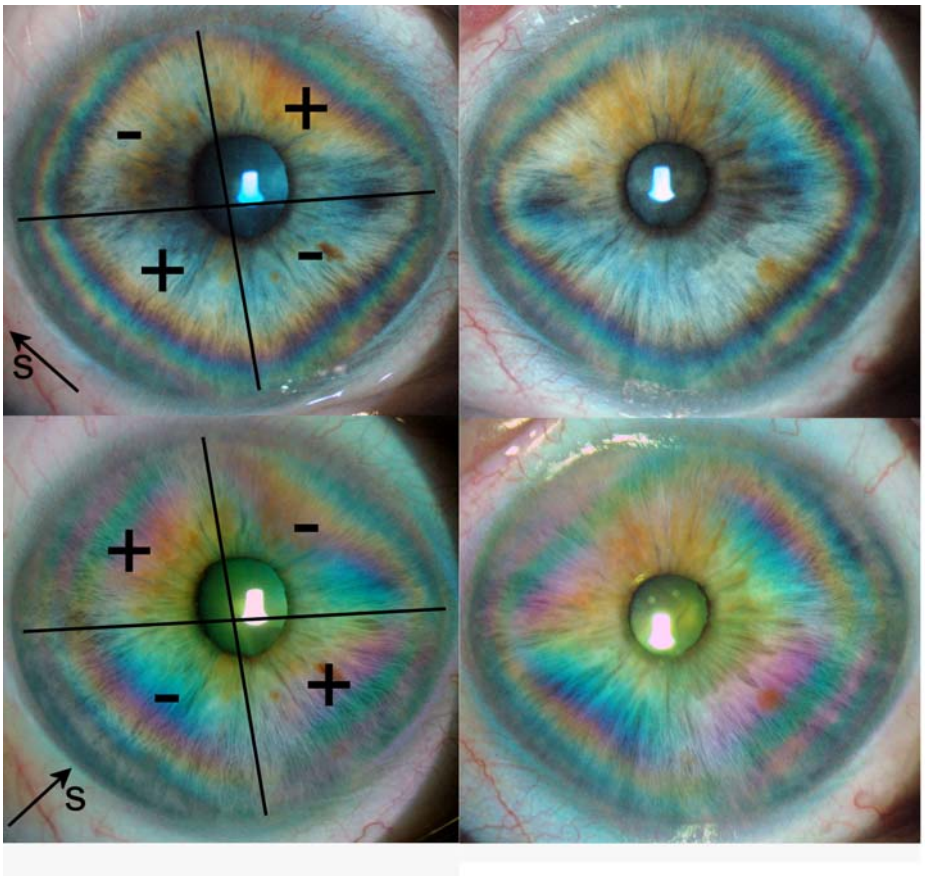

Figure 7.4 Right/Left eye pair of subject IL01. 140P upper, 550P lower.

Arrow pointing in direction of slow axis of retarder. Note addition and subtraction effects (Left column annotations), such that there is subtraction (reduction in order of interference colours) in quadrants aligned with the slow retarder axis. See text for details

The observed chromatic effects of addition and subtraction are compatible with those identified with 140P. Furthermore they conform to the predicted theoretical results and

those measured from the physical model of superimposed retarders as detailed in Chapters 5, 5.4 and 6, and as illustrated in Figure 5.3, Figure 6.5 and Figure 6.7.

The observed addition/subtraction phenomena with 550P confirm the findings with 140P that the slow direction of retardation is parallel to the isochrome contours (fast direction is perpendicular to the contours) in those parts of the cornea where isochromes are observed.

Chapters 9 and 10 will explore the isotropes and isochromes in greater detail.

7.3 Chapter Summary

1. EPB is a technique for the identification and photography of corneal polarization phenomena in human eyes *in vivo*.
2. EPB uses readily available routine ophthalmic examination instruments (slit-lamp biomicroscope) and inexpensive, commercially available 'circular' polarizing filters (retarder/polarizer laminates). No mechanical/optical modification of the slit-lamp is necessary.
3. EPB results may be digitised by routine ophthalmic/digital photography and subsequently processed using conventional image processing software.
4. EPB with two commercially available 'circular polarizer' laminates: 140P and 550P generated complimentary data of magnitude and retardation axes of cornea retardation as described in §6.2.
5. Results confirm relevant findings summarised in §6.4.
6. Corneal retardation phenomena comprise patches of low retardation (isotropes) and peripheral continuous coloured rings (isochromes).
7. Corneal isotropes are symmetrically placed about the corneal centre and are aligned in an approximate supero-temporal to inferonasal direction with the temporal isotrope typically larger in area.
8. The central cornea/corneal optical zone has non-zero retardation in the cases studied.
9. Corneal isochromes conform to the interference colours expected from both the previous theoretical and physical models.

10. The prominent and reproducible blue-black/purple (‘sensitive tint’) corneal isochromes indicate retardation of multiples of 280nm with a maximum peripheral retardation approaching 840nm.
11. Addition and subtraction phenomena are observed as predicted by theoretical and physical models.
12. The observed pattern of summation indicates that the slow direction of retardation of the peripheral cornea follows the contour of the observed isochromes.
13. The slow direction of the central cornea is aligned with the centre of the isotropes
14. The isochrome pattern is a distorted diamond-shape with four apices approximately in the vertical and horizontal corneal meridians.
15. The isotropes do not appear to be aligned with the isochrome apices.
16. The observed peripheral isochromes do not conform to the pattern expected from a biaxial model which predicts an elliptical isochrome pattern with isotropes aligned on the long axis symmetrically about the centre.
17. A central fibril-like fine-structure is identified.

8 Microscopic Findings: Corneal fine structure

The purpose of this chapter is to investigate further the findings noted in Chapter 7 of a fine-structure within the central corneal zones as observed with P140 slit-lamp biomicroscopy. Much of the data from this chapter has been published elsewhere (Misson 2007; Misson, Timmerman et al. 2007).

Unlike peripheral isochromes, which require reflection from the iris, examination of central corneal zones depends on reflection from the front surface of the crystalline lens and is greatly facilitated by dilatation of the pupil (mydriasis). Mydriasis is part of a routine ophthalmological clinical examination and is safely, easily and temporarily achieved using anticholinergic (e.g. tropicamide) and sympathomimetic (e.g. phenylephrine) agents administered as eye drops. Back-reflection through the cornea can be enhanced by utilising the reflectivity of artificial prosthetic intraocular lenses (IOLs) that are implanted as part of cataract surgery.

An eye that has undergone cataract surgery with an IOL implant is termed pseudophakic to distinguish it from a phakic eye which has the natural lens *in situ*. There are many types of IOL, but the one utilised in this study (Alcon Acrysof MA60BM) is a typical 3-piece design comprising a central biconvex optic of flexible acrylic and two PMMA supporting springs (haptics) that keeps the optic stably positioned behind the iris and centred on the visual axis (Figure 8.1). The reflectivity of the front surface is unintentional, but relates to the relatively low front curvature, surface smoothness and high refractive index (n = 1.55) of the acrylic relative to that of aqueous (n = 1.336).

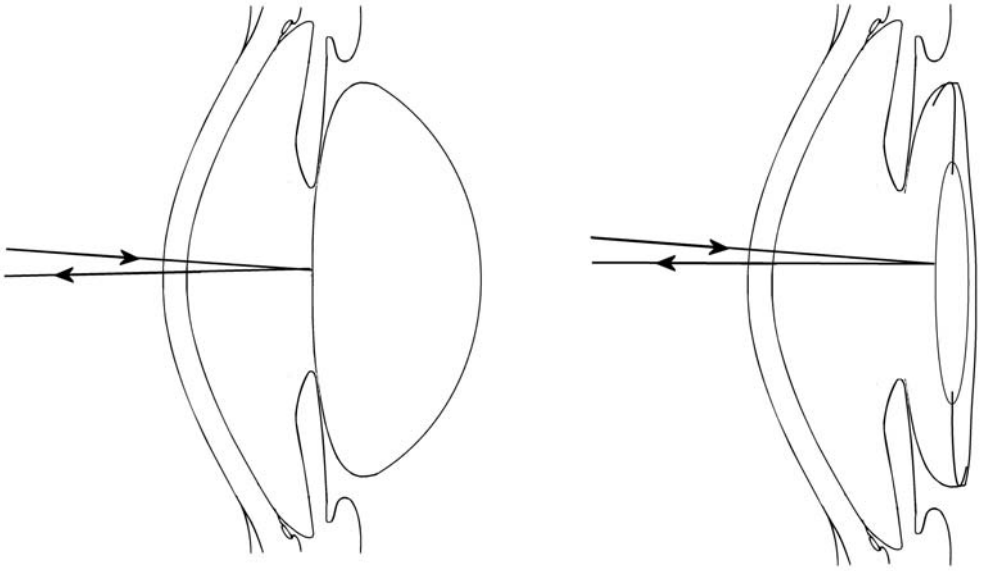

a) Phakic eye.
The natural crystalline lens is *in situ*.

b) Pseudophakic eye: the natural lens has been replaced by an artificial IOL. Note position behind the iris within the original lens capsule.

Figure 8.1 Schematic diagram of phakic (a) and pseudophakic (b) eyes with near-normal illumination/reflection

8.1 Methods

The study population comprised phakic and pseudophakic sub-populations. The phakic sub-population comprised 38 volunteers (16 male, 22 female; age range: 22 – 89yrs, mean: 68.5 yrs, sd: 16.4 yrs). The right and left eye of each phakic subject was examined and photographed as previously described. The pseudophakic population comprised 10 subjects (4 male, 6 female; age range: 60 – 86yrs, mean: 74 yrs) from whom 9 eye pairs and 1 right eye were studied. All pseudophakic eyes had undergone uneventful sutureless small-incision phacoemulsification cataract surgery with implantation of Alcon Acrysof MA60BM acrylic intraocular implants at least 6 months previously.

EPB was performed on both pseudophakic and phakic eyes according to the methods described previously (§7.1) but at the higher magnification of 16× and with particular regard to structures within the central corneal zones. The 140P filter alone was used. Particular care was taken at all times to ensure uniform position of illumination and the filter. Eyes were observed and photographed in the primary position (i.e. eyes looking straight ahead) in a way that maximised reflection from the anterior lens/IOL surface. Informed verbal consent was obtained from each subject. None of the subjects had any evidence of on-going ocular disease apart from early cataracts in 9 phakic subjects. Pupils were dilated with tropicamide 1% and phenylephrine 2.5% according to standard clinical diagnostic procedure. Corneal curvature was measured with the autokeratometer facility of a Carl Zeiss IOLMaster biometer at the time of photography.

Digital images were processes and assessed as previously described (§7.1). Angular and linear measurements (interfocal distance and interfocal angle, see Results for definition) of digital images were estimated manually using ImageJ software (Rasband 1997-2012) following calibration against targets of known dimensions. All linear measurements are in millimetres and angular measurements are in degrees above horizontal from the temporal aspect of the cornea (i.e. 0º = horizontal, 45º = superotemporal-inferonasal, – 45º = inferotemporal-superonasal). Measurements where taken using unenhanced digital images although, for the purpose of publication, the contrast, brightness and sharpness of text figures were enhanced using commercially available image processing software (Paint Shop Pro, Ver. 7.04; Jasc Software). The overlays of Figure 8.2 were traced manually.

Basic statistical analyses were performed on numeric data and included Pearson product moment correlation of right/left eye comparative data.

8.2 Results

Examination of all subjects reveals qualitatively similar findings at the level of the corneal stroma. At magnification of 16x, with the eye in the primary position, two overlaying patterns of fibrillar structures are visible within the central corneal areas. A clearly defined elliptical pattern typically with its major axis in a superotemporal-inferonasal direction with foci placed approximately mid-way between the corneal centre and periphery (Figure 8.2c, d). The foci are within the isotropes described previously with lower power magnification in Chapter 7. The form of the observed fibril distributions is independent of orientation of the circular polarising filter.

A second population of apparently hyperbolic fibrils are seen that appear orthogonal to, and confocal with, the elliptical fibrils. The hyperbolic fibrils are roughly symmetric about the major and minor axes of the ellipses. The temporal elliptic/hyperbolic focus is more diffuse in some eyes and then gives rise to a pear-shaped distortion of the elliptical fibrillar distribution (Figure 8.2a, b). Fibrils running along the major axes of the ellipses (i.e. between the foci) pass through the corneal centre where they are approximately linear.

The elliptical fibril pattern is increasingly circular towards the corneal periphery where fibrils become less clearly defined. Hyperbolic fibrils are less distinct than elliptic fibrils and are most readily observed looping around the foci, but become less curved and less dense towards the corneal centre where they are almost linear.

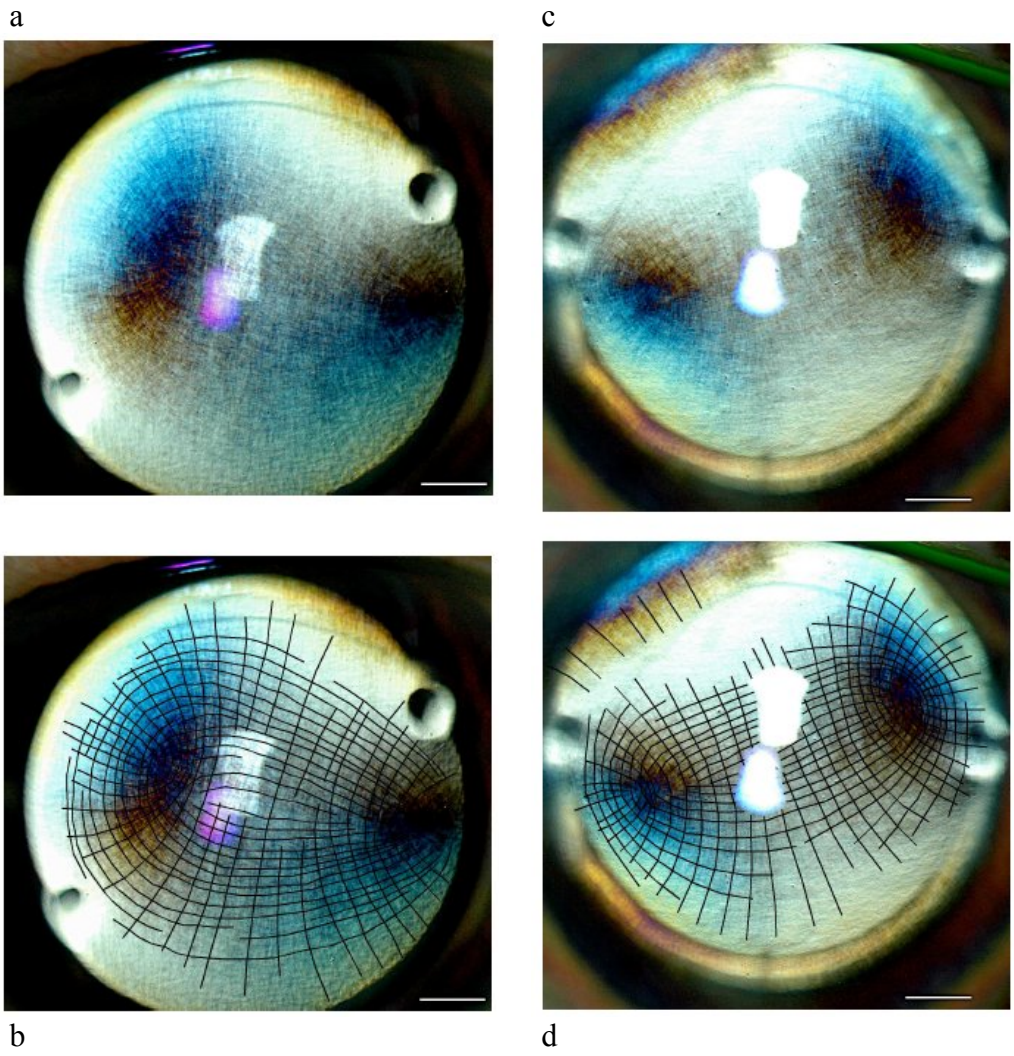

Figure 8.2 Pseudophakic eyes showing typical appearance

(a)(b) Right eye subject P41; (c)(d) Left eye subject P42. Lower row (b)(d), drawn overlay to accentuate fibrillar pattern. Note pear-shaped distribution in (a)(b) and elliptic distribution in (c)(d). Horizontal bar is 1mm.

Pairs of eyes exhibit approximate mirror symmetry (Figure 8.3) although considerable variation occurs between subjects. A hybrid pattern of several superimposed ellipses was observed in each eye of one subject and a curved distortion of the major elliptic axis was noted in three subjects (two pairs, one right eye, see Table 8.1).

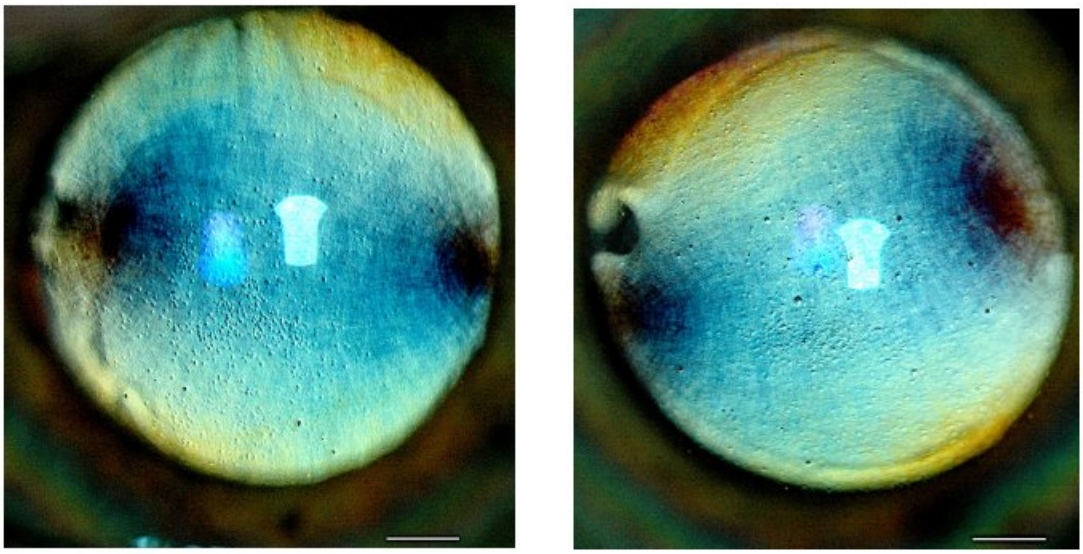

Figure 8.3 Right (a) left (b) eye pair showing approximate mirror symmetry
Subject P43. Horizontal bar = 1mm.

The angle of a line joining temporal and nasal foci from horizontal was measured in all cases (interfocal azimuth where 0º = horizontal, 45º = superotemporal-inferonasal, –45º = inferotemporal-superonasal). The distance between the two foci (interfocal distance) was measured in millimetres and in degrees subtended at the centre of curvature of the cornea for the ten pseudophakic eyes where corneal curvature was known. The angular measurement is a normalisation of data for eyes of different proportions. Results are shown in Table 8.1 and Table 8.2, and right-left eye pairs are compared graphically in Figure 8.4.

The pattern of fibrils at the isotropes is shown in detail in Figure 8.5 where elliptic fibrils enter from the right and overlap hyperbolic fibrils from the left.

Table 8.1 Summary statistics for the 38 phakic subjects

from (Misson 2007)

Table 1. Summary statistics

	Right	Left
Distribution type		
Ellipse	15	17
Curved ellipse	3	2
Pear	19	18
Hybrid	1	1
Interfocal distance (mm)		
Mean	5.53	5.59
Range	3.05–6.95	3.32–6.92
S.D.	0.98	0.94
Angle (deg)		
Mean	14.8	15.6
Range	–7 to 87	3–71
S.D.	16.1	12.6

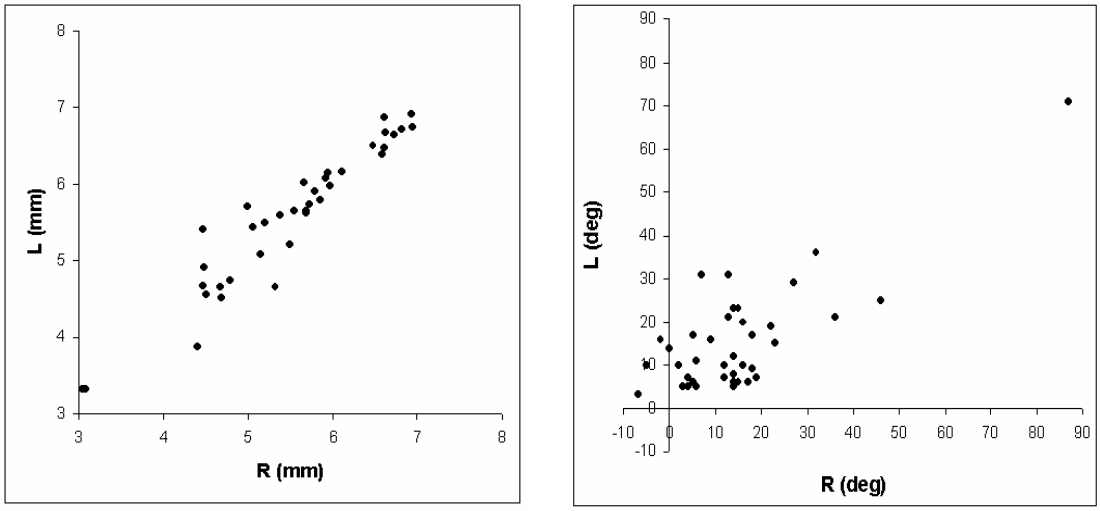

a b

Figure 8.4 Comparison of Right v Left eyes of the 38 phakic subjects

(a) Interfocal distances R2 = 0.9113, p< 0.0001; (b) interfocal angle R2 = 0.5906, p< 0.0001. From (Misson 2007)

Table 8.2 Right/Left interfocal distance, interfocal azimuth and corneal radius of the ten pseudophakic subjects

	Right				Left			
	Interfocal distance (mm)	(deg)	Interfocal azimuth (deg)	Corneal radius (mm)	Interfocal distance (mm)	(deg)	Interfocal azimuth (deg)	Corneal radius (mm)
n	10	10	10	10	9	9	9	9
Mean	40.5	34	19.6	7.67	4.64	35.9	14.8	7.63
Max	5.85	44.5	45	8.00	5.78	44.5	36	7.85
Min	3.05	22.8	–7	7.43	3.32	24.8	3	7.43
SD	0.97	7.50	15.4	0.16	0.94	7.46	10.0	0.14

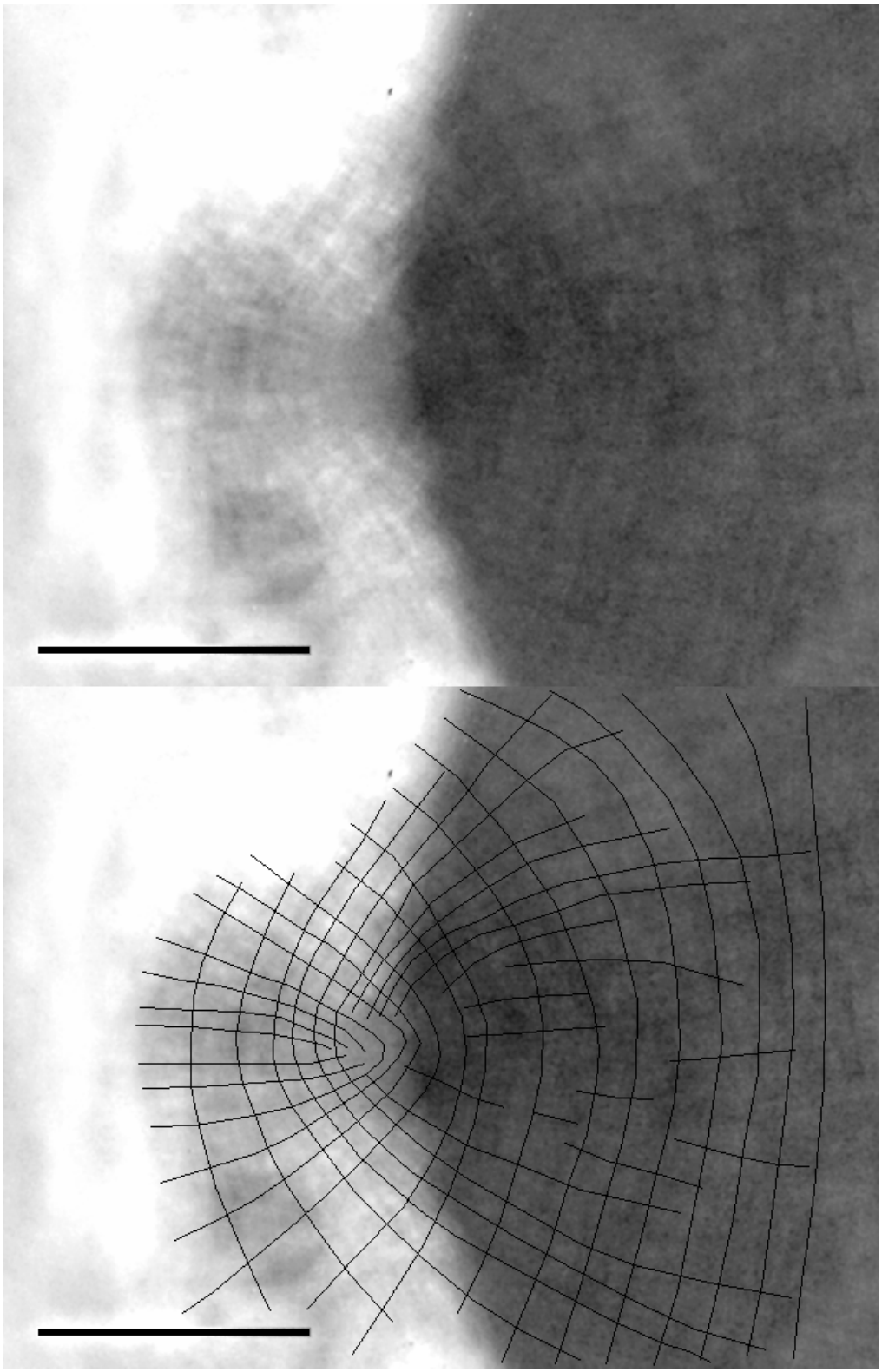

Figure 8.5 Detail at isotrope

Central elliptic fibrils from right, peripheral hyperbolic fibrils from left. Scale bar = 1mm

8.3 Discussion

The fibrillar structures are consistently observed in all subjects. The pattern of fibrillar structures resemble the theoretically derived orthogonal spherical elliptic equirefringence curves of the biaxial model derived in Chapters 3 and 4. The significance of this will be discussed in Chapter 13. The alignment of central fibrillar structures is in keeping with that of the central corneal retardation.

This aspect of the study confines itself to examining eyes in the primary position and is dependent on light reflected from the anterior lens/IOL surface. The area of cornea studies is therefore limited by the amount of pupil dilatation and the diameter of the IOL to less than a 3mm radius of the corneal centre i.e. the corneal optical zone. There is little dependence of the measured orientations of fibrillar structures with rotation of 140P although the image quality was noted to degrade if the filter was not held near perpendicular to the direction of illumination/observation. This is explained by the known changes in retardation when a given retarder is tilted relative to the direction of incident light (the principle of the Berek retarder §15.4). The type of cataract surgery performed on the patients in this study involved a small (*c.* 4mm) peripheral corneal incision that causes minimal disruption of architecture or optical properties of the cornea. Whilst some corneal stromal remodelling might take place post-operatively, it is unlikely that it would involve the whole of the corneal stroma. Thus, although some caution should be used in interpreting quantitative results in pseudophakic eyes, there is no apparent deviation from phakic eyes.

8.4 Chapter Summary

1) Biomicroscopy with P140 at 16× magnification reveals populations of fibrillar structures that follow a basic pattern of confocal ellipses and hyperbolae.
2) Superior quality images with increased contrast are obtained in pseudophakic eyes where the reflectivity of the anterior surface of the intraocular lens is exploited.
3) There is varying degrees of distortion of ellipses/hyperbolae between subjects allowing for pear-shaped, curved elliptic and hybrid (superimposed) patterns to be identified.
4) There is approximately mirror interocular symmetry.
5) The two foci of the ellipses/hyperbolae are within the macroscopically observed isotropes.
6) The foci are aligned superotemporal-inferonasal, with the inferonasal focus typically being more distinct.
7) There is considerable inter subject variation in interfocal distance and azimuth.
8) The observed elliptic/hyperbolic pattern of fibril-like structures resemble the spheroconic distributions of refractive indices predicted from the model of a spherical biaxial birefringent structure.

9 Corneal Isotropes and Isochromes

This chapter presents a detailed study of corneal isotropes and isochromes as determined with EPB and the 140P filter. The previous pilot study (Chapter 7) on pairs of eyes in five subjects is now expanded to eye pairs in 25 normal subjects. The aims are:

1) to develop a set of measurements that quantify the principle characteristics of peripheral isochromes and central isotropes as determined with 140P
2) to quantify the peripheral isochrome pattern
3) quantify the location of isotropes
4) to relate the pattern of corneal isochromes and isotropes to known measurable corneal parameters
5) further clarify the validity of the biaxial model of corneal birefringence particularly in the corneal periphery.

9.1 Subjects and Methods

Each eye of 25 volunteers (12 male, 13 female; age range: 19 – 86yrs, mean: 68.4 yrs, sd: 15.2 yrs) was observed and photographed according to the method of EPB described in §7.1. As before, informed verbal consent was obtained from each subject, data was record anonymously and none of the subjects had evidence of on-going ocular disease. Pupils were not dilated for this part of the study. Basic keratometric data (min/max

central corneal curvatures (k1, k2) and axis of greatest curvature (a2)) were obtained for all cases using an IOLabmaster autokeratometer / biometer (Zeiss).

9.2 Quantification and parameters

In previous chapters, the 280nm isochrome was identified as the boundary between magenta and blue/black isochromes and analogous to the 560nm 'sensitive tint' retardation for crossed polarizers (§§6.3and 7.2). The ease of identification and measurement of the 280nm isochrome landmark allows quantification of images and subsequent analysis.

The author is unaware of any previous attempts to quantify isochromes so the following measuring system is proposed. The shape of the 280nm isochrome is determined in polar form by plotting its distance from the geometric corneal centre against azimuth angle from the nasal horizontal meridian anticlockwise for right eyes and clockwise for left eyes (Figure 9.1a). Distance values can be expressed in arbitrary units, millimetre values or distances relative to the horizontal white-to-white (limbus-to-limbus) corneal diameter. The latter is preferred for comparative purposes (Figure 9.1a).

The following measurements (Table 9.1) were collected by visual estimation using ImageJ image analysis software (Rasband 1997-2012): relative distance (r_a) from corneal centre to 280nm isochrome at 15° intervals; relative magnitude and azimuth of the nasal, vertical, temporal and inferior 280nm isochrome maxima ($R_{n/s/t/i}$, $AR_{n/s/t/i}$) (Figure 9.1a); maximum diametric distance between horizontal or vertical 280nm isochrome maxima ($D_{h/v}$) with their respective azimuths ($AD_{h/v}$) measured from nasal horizontal at the intersection of the diameter with a horizontal line drawn through the

corneal centre (Figure 9.1b); inter-isotrope distance (Id) and inter-isotrope azimuth (Ia) (Figure 9.1c) with Ia measured as for $AD_{h/v}$.

The interisotrope distance is normalized by conversion into the angle subtended by the centre of the isotropes at the centre of curvature of the mean anterior corneal keratometric radius (½ (k1+k2)) as previously outlined (§8.2). As with the relative distance measurements, this allows comparison between cases.

Figure 9.1 Definition of isochrome and isotrope parameters: right eye. subject IO29

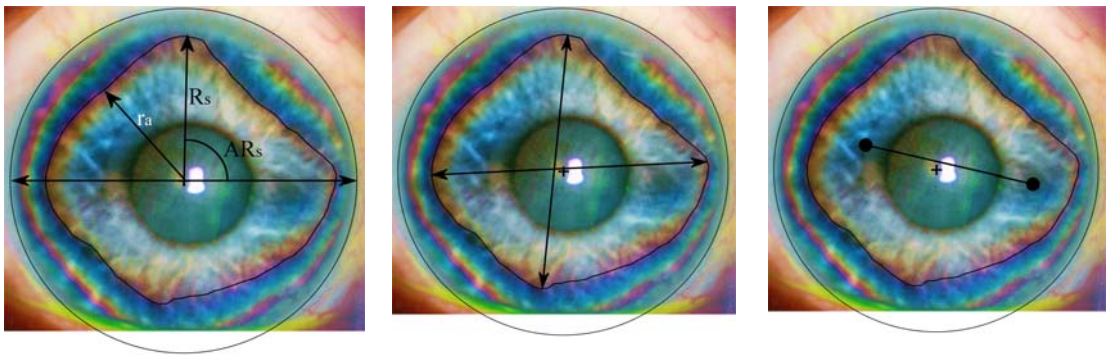

a) Horizontal white-to-white diameter (ww) and distance of 280nm isochrome (outlined with black continuous line) from corneal centre (r_a). Isochrome maxima measured from corneal centre (Rs shown) with azimuth anticlockwise (right eye) from nasal horizontal (ARs shown).

b) Maximum diametric distance between horizontal or vertical 280nm isochrome maxima ($D_{h/v}$). The respective azimuths ($AD_{h/v}$) are measured from nasal horizontal at the intersection of the diameter with a horizontal line drawn through the corneal centre.

c) inter-isotrope distance (Id). The inter-isotrope azimuth (Ia) is measured as $AD_{h/v}$

NB azimuths are measured from nasal horizontal: right eyes, anticlockwise; left eyes, clockwise; see Table 9.1 for parameter definitions.

Table 9.1 Definitions of isochrome / isotrope parameters

Abbreviation	Parameter
ww	Horizontal white-to-white corneal diameter
r_a	Radial distance relative to ww from corneal centre to 280nm isochrome at azimuth a
R_n, R_s, R_t, R_i	Maximum r in nasal, superior, temporal or inferior meridians
r_n, r_s, r_t, r_i	Minimum r in nasal-superior, superior-temporal, temporal-inferior or inferior-nasal meridians
$AR_{n/s/t/i}$, $Ar_{n/s/t/i}$	Azimuths of $R_{n/s/t/i}$ / $r_{n/s/t/i}$
D_h, D_v	Maximum diametric distance relative to ww between horizontal or vertical 280nm isochrome maxima
$AD_{h/v}$	Azimuths of D_h and D_v
Id	Inter-isotrope distance
Ia	Inter-isotrope azimuth
k1, k2	Maximum and minimum keratometric radii
a1, a2	Axes of k1 and k2. NB only a2 is documented as a1 is orthogonal

9.3 Results

A summary of the isotrope / isochrome parameter data for the right eyes of the 25 subjects is given in Table 9.2. Images of the right cornea of nine representative subjects are given in Figure 9.2.

9.3.1 Isotropes

Right eye inter-isotrope distance (Id) has a mean value of 0.47 relative to the horizontal corneal diameter (range: 0.39 – 0.56 sd 0.06). Inter-isotrope azimuth (Ia) has a mean value of 141° (range 4° – 177° sd 52°) anticlockwise from the nasal horizontal hemimeridian. Thus, on average, the orientation of a line connecting the isotropes runs superotemporal to inferonasal at an angle from horizontal of 39° although there is considerable intersubject variation. The centre of Ia always lies close to the geometric corneal centre (corneal apex).

9.3.2 Isochromes

Data for r_a are plotted in Figure 9.3 for all 25 cases and summarised in Figure 9.4. Inspection of the numeric/graphic data indicates four maxima of r_a at approximately 1°, 102°, –176° and –86° with minima of r_a approximately mid-way between these points. The order of magnitudes of the maxima proceed: nasal > superior ≈ inferior ≈ temporal. These findings are seen in the representative images of nine right eyes in Figure 9.2. Whilst there is intersubject variability, the overall 280nm isochrome pattern is approximately rhomboidal, thus confirming the findings of the preliminary investigation (§ 7.2.1).

Table 9.2 Summary data for the right eyes of 25 normal subjects

M:F 12:13 mean age 68.4 years (range 19 – 86 years, SD 15.2 years)

Parameter	Mean	min	max	sd	units
R_n	0.42	0.37	0.46	0.02	rel. distance
R_s	0.38	0.34	0.42	0.02	
R_t	0.38	0.34	0.42	0.02	
R_i	0.39	0.34	0.43	0.02	
AR_n	1	–6	11	4	degrees
AR_s	102	95	112	4	
AR_t	–176	–184	–163	5	
AR_i	–86	–92	–78	3	
D_h	0.80	0.73	0.87	0.03	rel. distance
D_v	0.77	0.72	0.83	0.03	
AD_h	1	–7	9	5	degrees
AD_v	97	94	103	3	
Id	0.47	0.39	0.56	0.06	rel. distance
2V	43	35	52	6	degrees
Ia	141	4	177	52	
k1	7.56	7.16	8.01	0.24	mm
k2	7.73	7.37	8.24	0.23	
a2	81	4	155	46	degrees

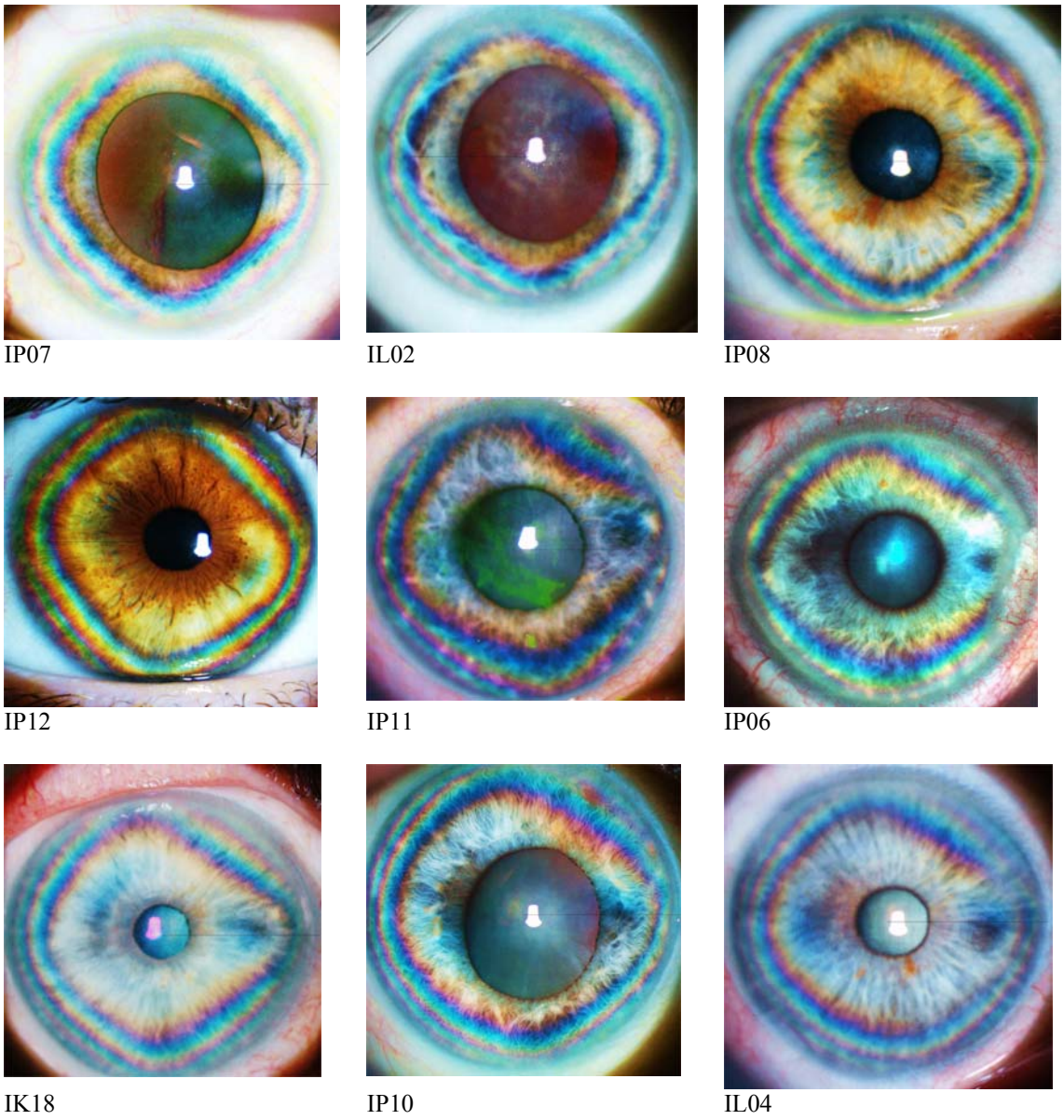

Figure 9.2 Isochromes and isotropes of nine right eyes

Nine right eyes showing diamond-shaped configuration (IP 07, 02, 08); Rhomboidal configuration (IP12,11, 06) and mixed/progressively more circular configuration (IK18, IP10, IL04). The distribution of the 280nm isochrome for each is shown graphically in Figure 9.3 and Figure 9.4. Note the paired isotropes on either side of the pupil aligned approximately superotemporally–inferonasally.

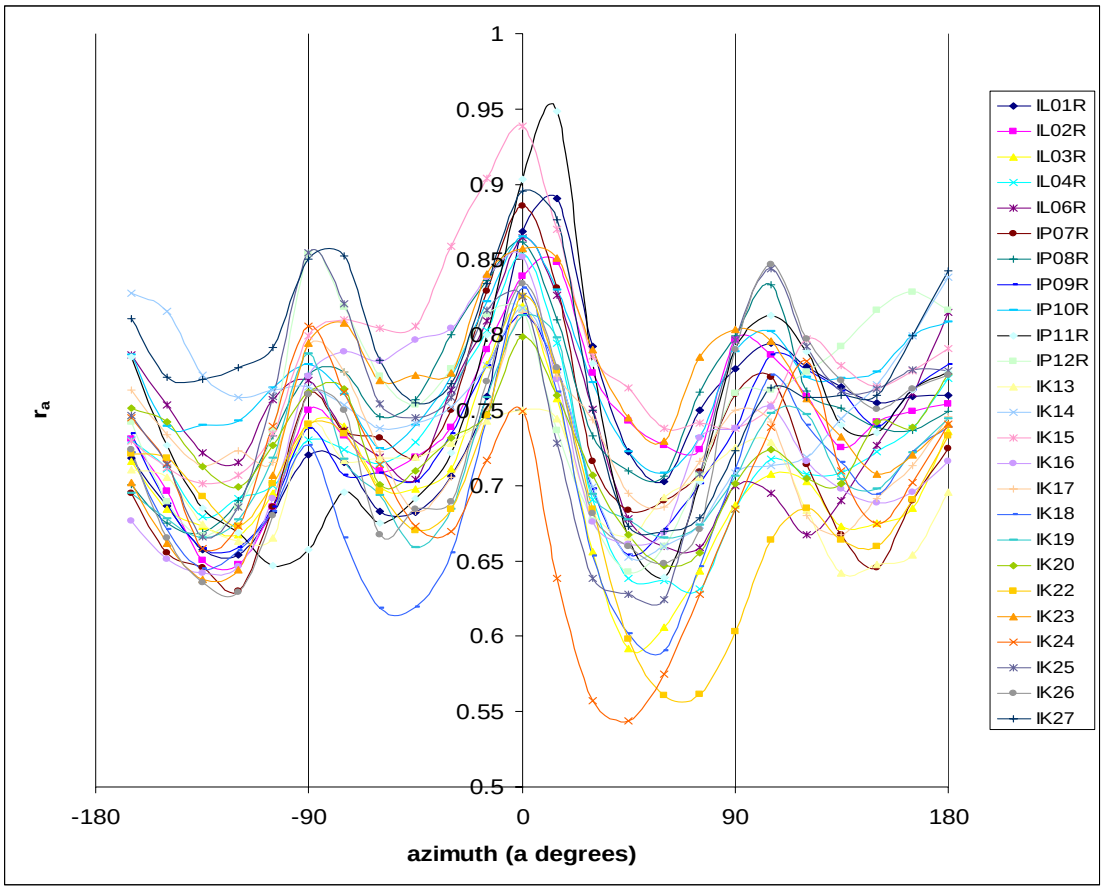

Figure 9.3 Raw 280nm isochrome r_a data

Relative distance of 280nm isochrome form corneal centre (r_a) vs. azimuth as defined in text and Figure 9.2. Right eyes of 25 subjects.

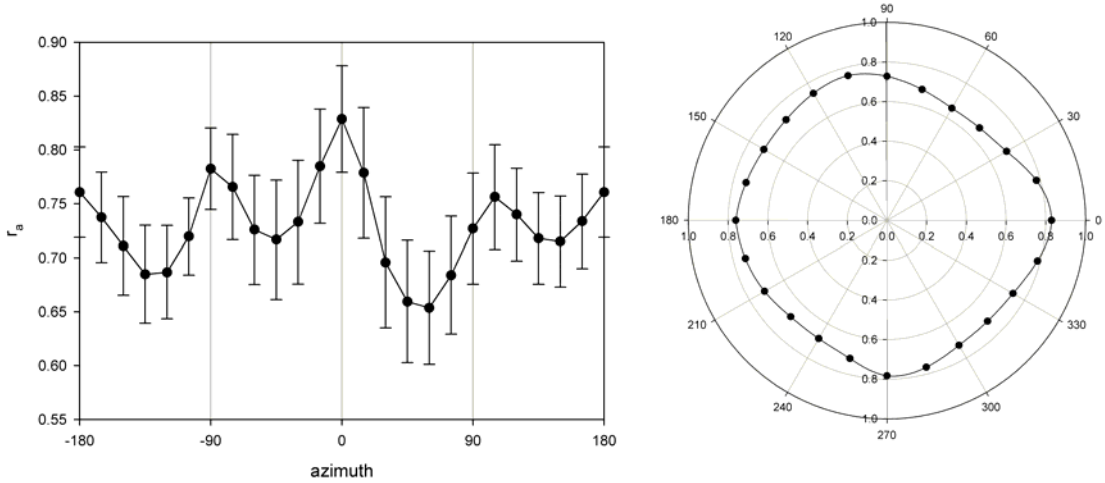

Figure 9.4 Mean ±sd of 280nm isochrome distribution as in Figure 9.3 n = 25

9.3.3 Right/Left eye comparison

Complete data sets were available for eleven right/left eye pairs. Inter-eye comparison for interisotrope distance and azimuth are presented in Figure 9.5 and averaged r_a data in Figure 9.6

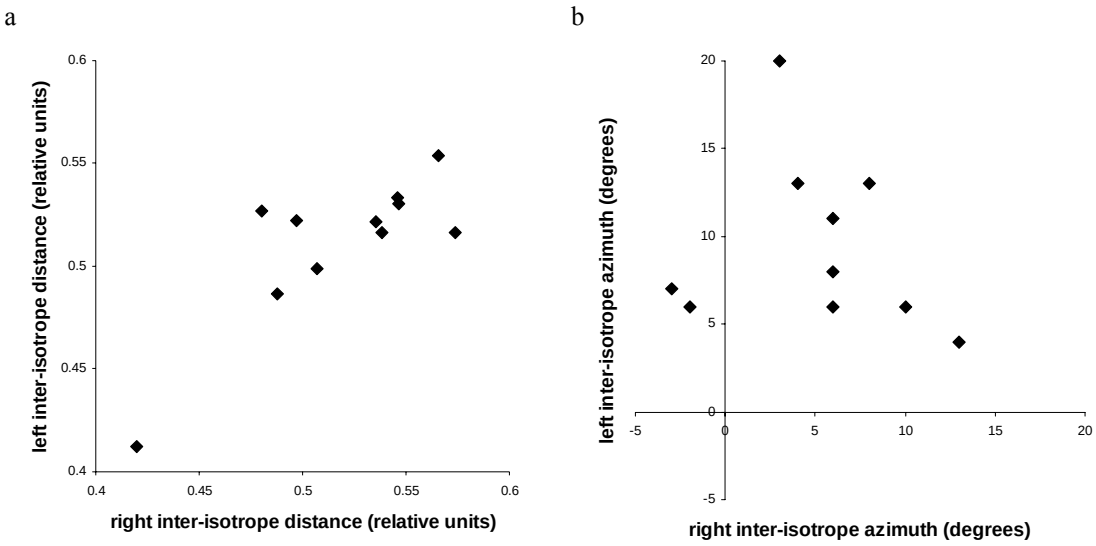

Figure 9.5 Right/left eye isotrope comparison
a) Inter-isotrope distance; b) inter-isotrope azimuth.

For isotropes, the right/left side appear correlated for interisotrope distance, but there appears to be no such correlation for azimuth. However, the Wilcoxon Matched Pairs Test on both data sets indicate no significant difference (R vs. L interisotrope difference: T = 90, Z = 1.2448, p = 0.21; R vs. L azimuth: T = 9, Z = 1.8857, p = 0.06). Small numbers and imprecision in defining isotropes manually may confound the findings which need confirmation with larger subject numbers.

Comparison of r_a for eye pairs (Figure 9.6) shows midline symmetry i.e. right/left eye isochromes are bilaterally symmetric.

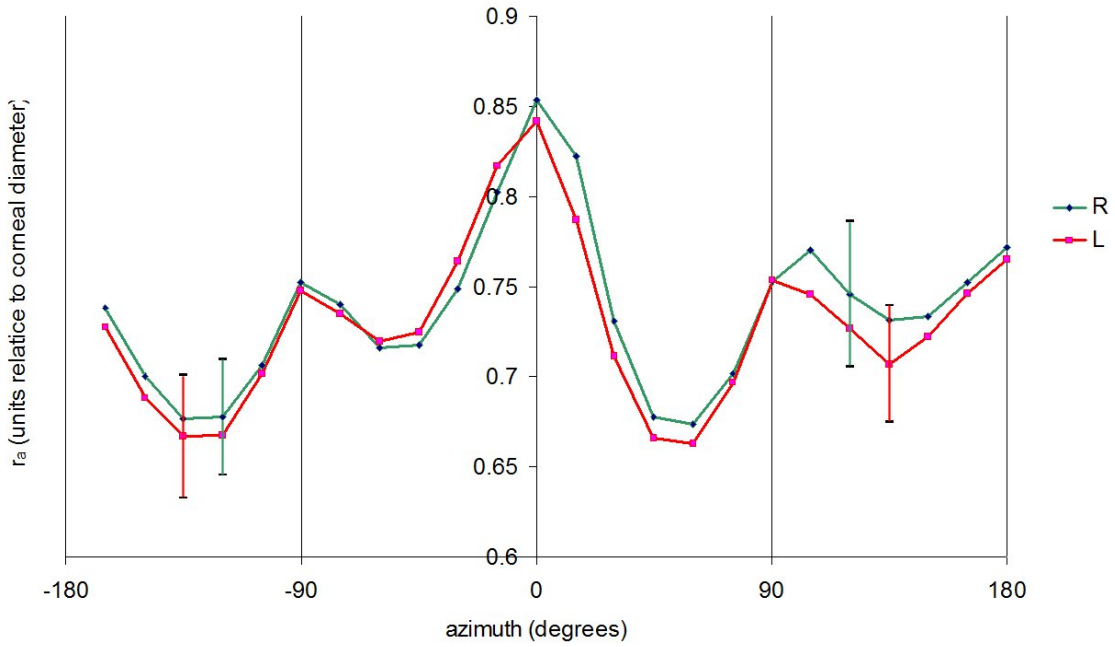

Figure 9.6 Mean r_a of 11 Right/Left eye pairs

Error bars indicate representative ±sd for right (green) and left (red) eyes (other data points omitted to avoid confusion)

9.3.4 Correlation between parameters

Correlation matrices did not reveal any significant meaningful correlations between parameters (Table 15.2). In particular, there was no correlation between keratometric data and any other parameter. Of note is that there was no correlation with magnitude (difference between k2 and k1) or axis of keratometric astigmatism (a2) with relevant linear or angular isochrome parameters. Furthermore, there was no correlation between the inter-isotrope distance or azimuth with the relevant linear/angular isochrome parameters. In all cases the Wilcoxon matched pairs test indicated a significant difference ($p < 0.001$) respectively between Id or Ia and all relevant parameters.

9.4 Discussion

To the author's knowledge, the present study is the first attempt to quantify peripheral corneal isochromes in the human eye *in vivo* in a sizeable number of subjects.

The presence of two isotopes is compatible with the biaxial model. The interisotrope distance (Id) expressed as an angle subtended at the centre of the radius of mean curvature for the corneal apex is equivalent to the crystallographic optic angle 2V of a biaxial crystal (see §3.4). Here 2V = 2asin(Id/(k1+k2)) where k1 and k2 are the keratometric radii. A published value of 2V = 35° for two eyes (see § 3.4.1, and Blokland and Verhelst (1987)) is within the range of this study (35° – 52°) although a higher mean value of 43° ±6°(sd) was found.

Whilst not specifically stated in the original work (Blokland and Verhelst 1987) or subsequently (Knighton, Huang et al. 2008), there is sufficient published data to conclude that the biaxial model has negative sign (see §4.1 and Misson (2007)) as suggested by Valentin (1861). If the biaxial model is assumed then a negative sign is confirmed by the finding that the slow direction of retardation is tangential to isochromes (see § 7.3; a positive sign predicts the slow direction orthogonal to isochrome tangents).

On average, the orientation of a line connecting the isotropes (cf optic plane of a biaxial interference pattern, see §3.4) runs superotemporal to inferonasal at an angle from horizontal of 39° although there is considerable intersubject variation. The centre of Ia lies close to the geometric corneal centre (corneal apex). These findings may be interpreted in terms of a negative biaxial model where the principle refractive index, γ, runs in the direction of optic plane (see §3.4, Figure 3.3). Thus the slow axis of maximum retardation for normal incidence illumination occurs near or at the corneal

apex and in orientated in a superotemporal to inferonasal direction: a conclusion in agreement with previous studies (§4.1).

The superotemporal to inferonasal alignment of isotropes is independent of the azimuth and distance parameters of isochrome maxima/minima. There is no obvious association with the measured parameters of isochrome distribution, azimuths of maxima, inter-isotrope distances/orientation with standard corneal parameters of keratometric radii and axes, or peripheral corneal thickness. Furthermore there is no association of the peripheral maxima with inter-isotrope magnitude or orientation suggesting that the peripheral and central corneal regions have different birefringent properties and are therefore structurally distinct.

If one assumes illumination of the cornea with parallel rays then, as the cornea curves to the periphery, the path length for light transmitted by the cornea progressively increases towards the limbus. Thus a high value of r_a, i.e. a more peripheral location of the 280nm isochrome, relates to a lower value of birefringence compared to the same radius from the corneal centre along the azimuth of a lower r_a value. The corneal birefringence is inversely proportional to r_a so is consequently at a minimum along the nasal < superior ≈ inferior ≈ temporal horizontal/vertical meridians at azimuths of 1°, 102°, −176°, −86° respectively. By a similar argument, peripheral corneal birefringence is a maximum approximately equidistant (radially) between minima (i.e. corresponding to minima of r_a). This confirms the conclusion previously made that the peripheral cornea does not conform to biaxial behaviour (§7.3.16). The computation of peripheral corneal birefringence will be detailed in Chapter 10.

The intersubject variability of extent and pattern of corneal retardation noted here is also a feature of other studies (Knighton and Huang 2002; Knighton, Huang et al. 2008) and

may have contributed to past incorrect conclusions in studies with small numbers of subjects. The midline mirror (right eye / left eye) symmetry of isochrome pattern / retardation is also in keeping with findings of central corneal retardation (Knighton and Huang 2002) although there are no previous reports, to the author's knowledge, identifying this symmetry in the corneal periphery.

This study is limited to a relatively small number of subjects thus subtle correlations may not be apparent. Furthermore isochrome measurements presented here relate only to those due to a retardation of 280nm. This isochrome is chosen because it is easily defined and traced, and is conveniently located in the mid-corneal periphery. Adjacent peripheral isochromes run in similar paths so it is not unreasonable to study the 280nm isochrome in isolation within the constraints of this study. The calculation of 2V assumes that the corneal surface behaves as a perfect sphere with a single centre of curvature. For this initial study, such an approximation of corneal geometry is acceptable if its limitations are acknowledged (§4.5.1) More precise determinants of corneal topography, and their relationship to corneal retardation phenomena, will be considered in Chapter 10.

The central cornea conforms to the biaxial model in that two isotropes approximately symmetric about a cornea centre are present. Furthermore, there is a measurable retardation at the corneal centre with one axis (the slow axis in this case) connecting the isotropes. If corneal geometry (including thickness) is assumed to be radially symmetric then the observed rhomboidal pattern of peripheral isochromes does not conform to the biaxial model which predicts elliptic peripheral isochromes.

9.5 Chapter Summary

1) Parameters are devised for the quantification of isochromes and isotropes.
2) The qualitative results of the pilot study detailed in Chapter 7 are confirmed.
3) Isotropes straddle the corneal centre and are orientated superotemporal-inferonasal direction at about 39° from horizontal.
4) The superotemporal-inferonasal isotrope axis corresponds to the slow direction of central corneal retardation.
5) The angle subtended by the isotropes to the approximate centre of anterior cornea curvature, 2V, ranges form 35° to 52° (mean 43°).
6) Isochromes (as quantified by the 280nm isochrome) are quadrangular with maximum distance from the corneal centre nasal (1°) > superior (102°) ≈ inferior (–86°) ≈ temporal (–176°) hemi-meridians.
7) Birefringence is inversely proportional to the distance of isochromes from the corneal centre so is minimum at the isochrome maxima i.e. nasal < superior ≈ inferior ≈ temporal hemi-meridians.
8) Birefringence is maximum mid-way between birefringence minima.
9) There is approximate mirror symmetry between eye pairs for both isochromes and inter-isotrope distance.
10) There is intersubject variability for isochrome distribution, interisotrope distance and interisotrope azimuth corresponding to equivalent variations in central and peripheral corneal retardation.

11) The intersubject variation may have led to erroneous conclusions in previous studies with small subject numbers.
12) There is no correlation with any isochrome/isotrope parameter with basic central corneal keratometric data.
13) There is no correlation between isotrope orientation and orientation of isochrome maxima/minima.
14) The central cornea conforms to the biaxial model, but the peripheral cornea does not.

10 Isochromes, Corneal Topography and Pachymetry

The pattern of isochromes corresponds to the pattern of retardation. Retardation is the product of birefringence and optical path length (§3.4, §3.4.4 Eq. 3.1). It has been shown that peripheral corneal isochromes are not circular so the peripheral cornea is not radially symmetric with respect to retardation (§9.5). Furthermore the isochromes do not conform to a pattern predicted by the biaxial model and a geometrically radially symmetric cornea (§9.4).

Corneas are not geometrically radially symmetric in that there is meridional variation in peripheral corneal thickness and curvature in any given eye (chapter2). Regional light path length variations are a possible explanation for the observed retardation variation and might be compatible with a pattern of birefringence as predicted by a biaxial model. The principle aim of this chapter is to establish the validity or otherwise of the biaxial model by examining the extent to which variations in corneal optical path length and/or birefringence account for the observed corneal isochrome patterns.

10.1 Methods

Peripheral corneal thickness was measured using a Pentacam corneal topography system (Oculus, Inc., Wetzlar, Germany, §15.5.1.3). The Pentacam uses a rotating Scheimpflug camera and a blue (475 nm) light-emitting diode slit light source which rotate together around the visual axis of the eye (Figure 10.1). The device software presents a real-time image of the subject's eye which allows manual alignment and focussing in the anteroposterior, horizontal and vertical axes. Once the corneal apex is

correctly positioned the Pentacam activates automatically and fifty slit images of the anterior segment are obtained in approximately two seconds. The Pentacam collects information from up to 25,000 data points (O'Donnell and Maldonado-Codina 2005) and determines a profile of cornea thickness, and anterior and posterior corneal surface curvatures.

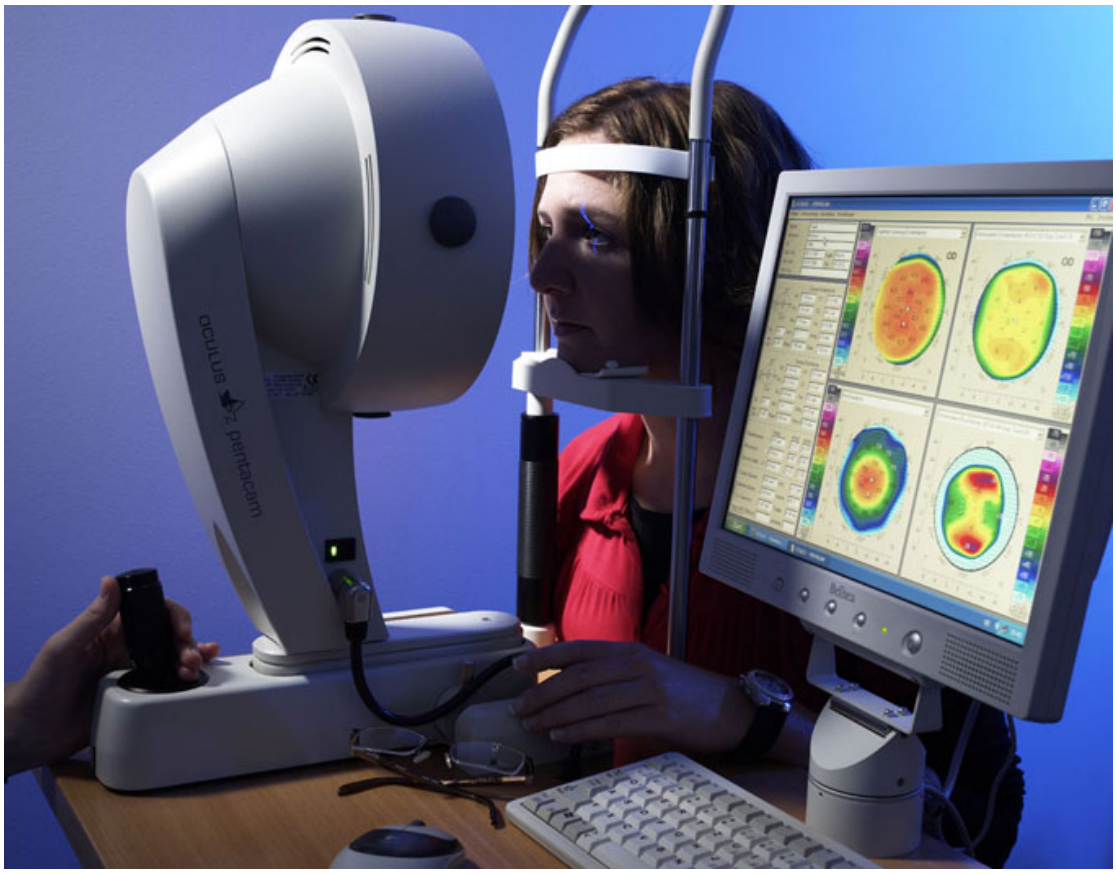

Figure 10.1 The Pentacam corneal topography system (Oculus, Inc., Wetzlar, Germany)

Pentacam corneal topography and topographic pachymetry were performed on each eye of five subjects according to the manufacturer's instructions. Subjects were seated with chin on chinrest and forehead against a positioning strap (Figure 10.1). Eye stability was maintained by asking the subject to observe the machine fixation target. Data was

reviewed at the time of measurement and checked for artefact (e.g. due to blinking or fixation losses). Inadequate scans were rejected and repeated when necessary.

Standard Pentacam parameters were recorded for each eye and comprise corneal thickness, front and back sagittal (axial) and tangential (instantaneous) curvatures (§15.2.1), front and back corneal elevations relative to a spherical model over the measurable area of each cornea. Additional parameters relevant to this study were derived manually from the Pentacam data presentation software. An initial pilot study determined a value of 740µm as a representative average thickness for the cornea along the 280nm isochrome. The polar distribution of the 740µm thickness contour (740µm isopach) at 15° increments ($p740_a$) was determined in a similar way to r_a with which it is compared.

A further means of determining possible relationships between the isochrome distribution and Pentacam parameters is to compare the 280nm isochrome distribution (r_a) with the Pentacam-derived parameters at a fixed radius from the corneal centre. The pilot determined that a radius of 4mm from the corneal geometric centre was a reasonable estimate of the mean isochrome distance (r_a). Thus corneal thickness, tangential (instantaneous) and sagittal (axial) curvatures of the anterior (front) and posterior (back) corneal surfaces were determined at 15° increments at a radius of 4mm from the corneal geometric centre (Table 10.1). This data will also be used in §11.2.

Elliptic polarization biomicroscopy with P140 was performed on each eye and data recorded as previously described (§9.2). As before, data from right eyes were used in the detailed analyses. Position coordinates for r_a were determined visually using ImageJ

on digital P140 EPB images and subsequently translated to the Pentacam analysis software. Using these coordinates, the position of the 280nm isochrome was located on the Pentacam pachymetric/topographic analysis for each subject allowing pachymetry (pr_a) at 15° incremental points of the 280nm isochrome (i.e. corresponding to r_a). Corneal thickness and sagittal (axial) curvatures were also recorded at each of the four sets of 280nm isochrome maxima and minima.

10.1.1 Estimation of birefringence

Retardation (Λ) is the product of birefringence (b) and path difference (τ), $\Lambda = \tau b$ (Eq. 3.1) so birefringence may be calculated if Λ and τ are known. Determining the contour of Λ = 280nm (r_a) and Pentacam analysis allows measurement of the corneal thickness (t) and front radius of sagittal curvature (r_f) at any point on that contour (r_a). The path distance (τ) may be estimated by calculation and some assumptions about corneal geometry.

First assume that the anterior corneal surface is spherical at the point of incidence f of ray I at some distance r_a from the axis of the geometric corneal centre (C of, Figure 10.2). The front corneal curvature at f is r_f and the corneal thickness at this point is t. The angle of incidence of I at f from the normal of N is θ and the angle of refraction of I on entering the cornea is α. By similar triangles, $\sin\theta = r_a/r_f$, and by Snell's law $\sin\alpha = \sin\theta/n$ where n is corneal refractive index at that point. As distances and curvatures are very small, we assume that the back corneal surface approximates to the plane b b'. Let τ be the light path distance travelled by I through the cornea from f to bb'.

Now, cosα = t/τ, hence

$$\tau = \frac{t}{\sqrt{1 - \frac{r_a^{\,2}}{n^2 r_f^{\,2}}}} \qquad \text{hence} \quad b = \frac{\Lambda}{t}\sqrt{1 - \frac{r_a^{\,2}}{n^2 r_f^{\,2}}}$$

where Λ = 280nm, n = 1.376 and r_a , r_f , t are Pentacam measured variables.

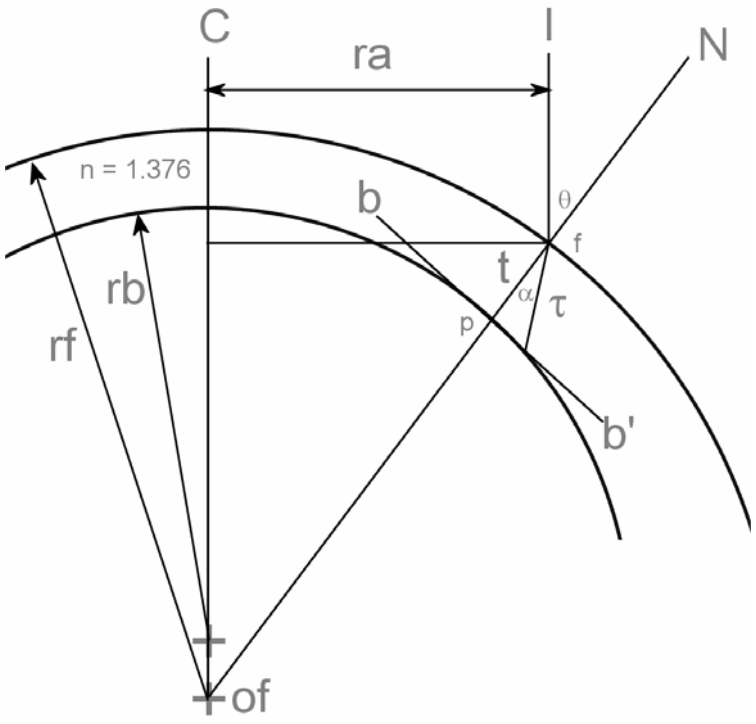

Figure 10.2 Calculation of path distance (τ)
Definition of corneal curvature/ thickness parameters.

The assumptions here are that the value of n is valid for the peripheral cornea, the origin of r_f coincides with the normal of the geometric corneal centre, and that the posterior corneal curvature is sufficiently small in the area of interest to be reasonably approximated to a planar surface. A further assumption is that the corneal birefringence is sufficiently small not to influence the magnitude and direction of τ.

10.2 Results 1: isochrome distribution and topographic pachymetry

Corneal thickness and isochrome distribution are examined in this section and relevant parameters are listed in Table 10.1. A typical data-set is presented in Figure 10.3. Horizontal, superonasal-inferotemporal, vertical and superotemporal-inferonasal meridian profiles for the left eye of subject P11 are presented in Figure 10.4 where the 280nm isochrome is indicated by the grey vertical bar. An example of corneal thickness profiles plotted in the right eye of subject IP11 along the meridians of the isochrome maxima/minima is given in Figure 10.5. The positions of isochrome maxima (Figure 10.5, lower two images) coincide approximately with the corresponding second order interference colours of the minima (Figure 10.5, upper two images). This indicates a retardation variation of approximately 280nm at radially equivalent peripheral corneal positions. The corneal thickness shows little change throughout its extent whereas the position of the 280nm isochrome is variable and appears not to be related to thickness.

Table 10.1 Topographic parameters: summary results

Symbol	Definition	mean	min	max	sd	units
r_a	Radial distance from corneal geometric centre to the 280nm isochrome at azimuth a°	4.32	3.39	5.50	0.41	mm
p740a	Distance from geometric corneal centre of the 740µm isopach at azimuth a°	4.12	2.90	5.71	0.58	mm
p r_a	Corneal thickness at r_a	759	647	897	57	µm
SCf ra	Sagittal curvature of front corneal surface at r_a	7.97	7.54	9.55	0.37	mm
P4a	Pachymetry at 4mm radius from geometric centre at azimuth a°	730	650	835	47	µm
TCf4a	Tangential curvature of front corneal surface at 4mm radius at azimuth a°	8.83	7.34	11.85	0.88	mm
TCb4a	Tangential curvature of back corneal surface at 4mm radius at azimuth a°	8.61	5.74	16.01	1.89	mm
SCf4a	Sagittal curvature of front corneal surface at 4mm radius at azimuth a°	7.89	7.00	9.14	0.31	mm
SCb4a	Sagittal curvature of back corneal surface at 4mm radius at azimuth a°	6.51	6.05	7.75	0.33	mm

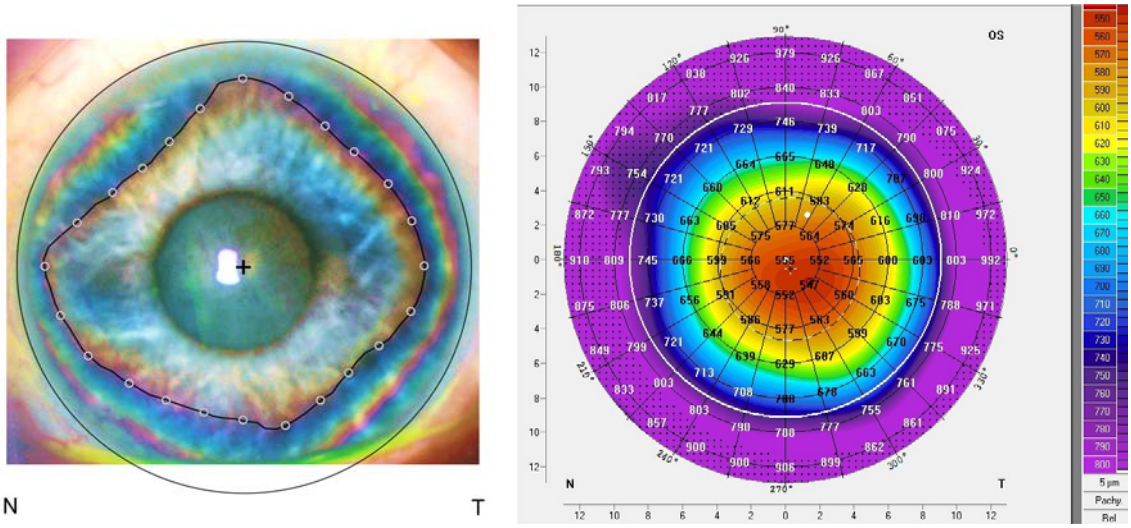

a b

Figure 10.3 A typical data set Left eye of subject P11

(a) P140 EPB image showing isochromes; 280nm isochrome outlined in black with white circles at 15° increments (Pr_a) from corneal centre (+); N – nasal, T – temporal. (b) typical Pentacam data set here showing topographic pachymetry. Isopachs are coloured according to right-hand scale here increasing 550µm (red) – 800µm (purple) in 10µm increments

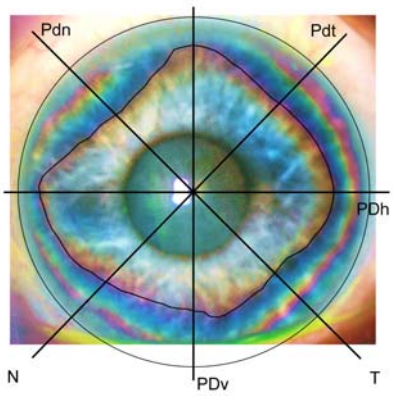

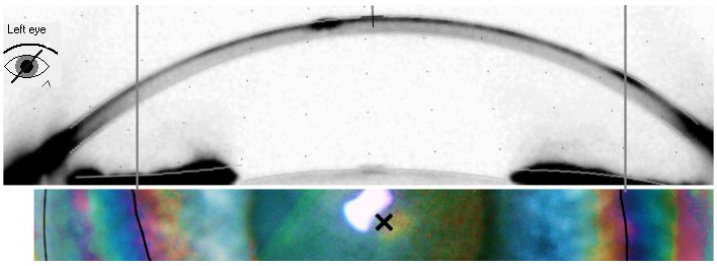

Pd_t Superotemporal – inferonasal profile

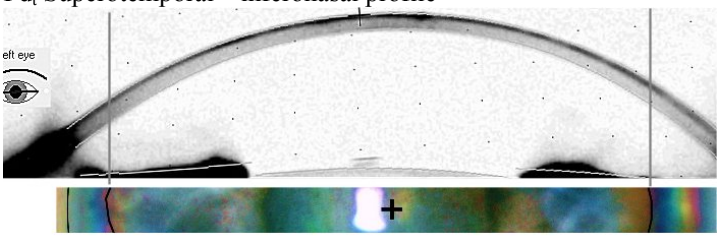

PD_h Horizontal profile

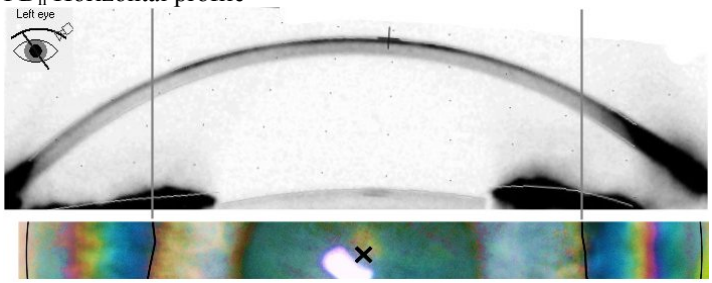

Pd_n Superonasal – inferotemporal profile

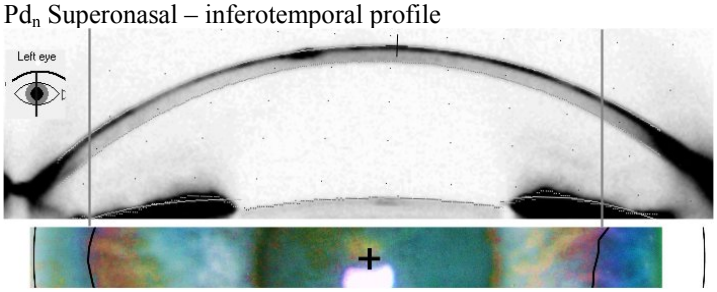

Pd_v Vertical profile

Figure 10.4 Corneal thickness profile and isochromes

Corneal thickness profile for horizontal/vertical 280nm maximum (PDh/v) and for superotemporal-inferonasal (t)/superonasal-inferotemporal (n) 280nm minimum (Pdt/n). Left P140 EPB image. Right Pentacam Scheimpflug images (above) and corresponding section of P140 image. The 280nm isochrome is identified in black and its corresponding location translated to the Pentacam images (vertical grey line). Note uniformity of corneal thickness but variability of 240nm isochrome position. Left eye, subject P11.

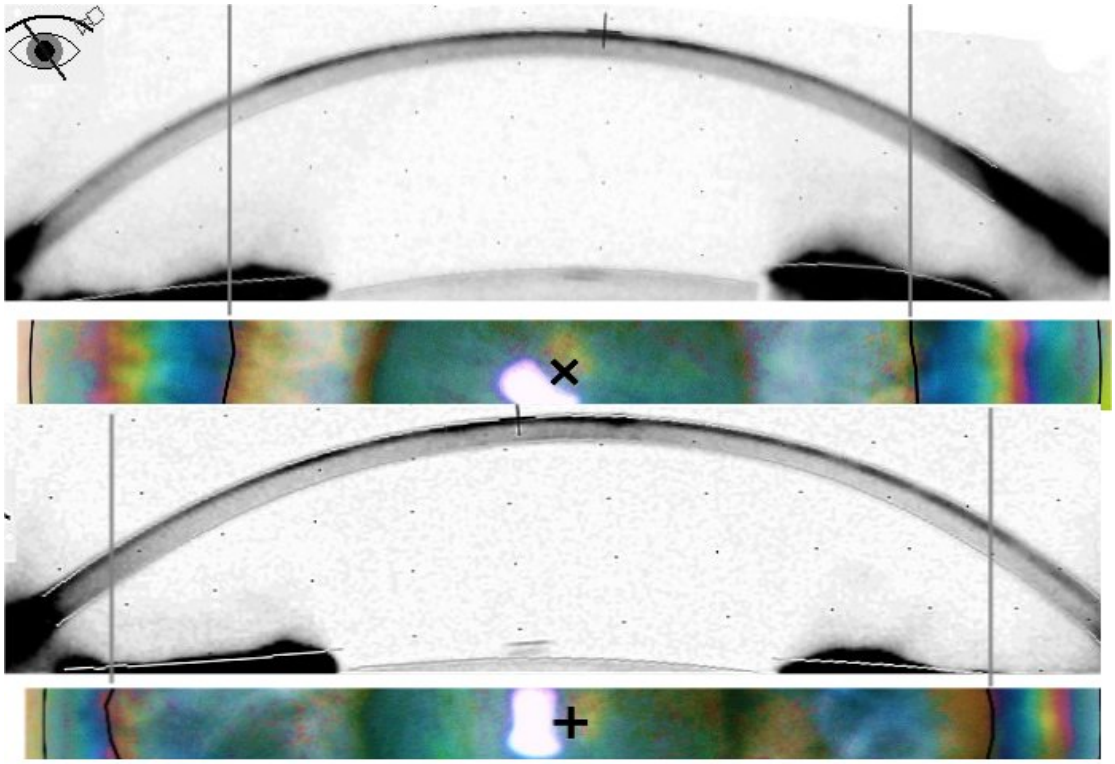

Figure 10.5 Topographic comparison of isochrome maxima and minima

Figure as Figure 10.4. Pd_n Superonasal – inferotemporal profile (upper) and PD_h Horizontal profile (lower). Note relative positions of 280nm isochrome (vertical bars) equating to a birefringence difference of approximately one order (280nm) between similar corneal locations of Pd_n (upper) relative to PD_h (lower).

10.2.1 Relationship of r_a to topographic pachymetry

The EPB isochrome images of the five eyes studied, r_a and $p740_a$.are presented in Figure 10.7. Of note that the isochromes are quadrangular, but the isopachs are circular / elliptical.

The independence of isochromes (mean ±sd r_a) and corneal thickness (mean ±sd $p740_a$) is shown in Figure 10.6a. Comparison of r_a and $p740_a$ in Figure 10.6b shows no correlation between these two data sets.

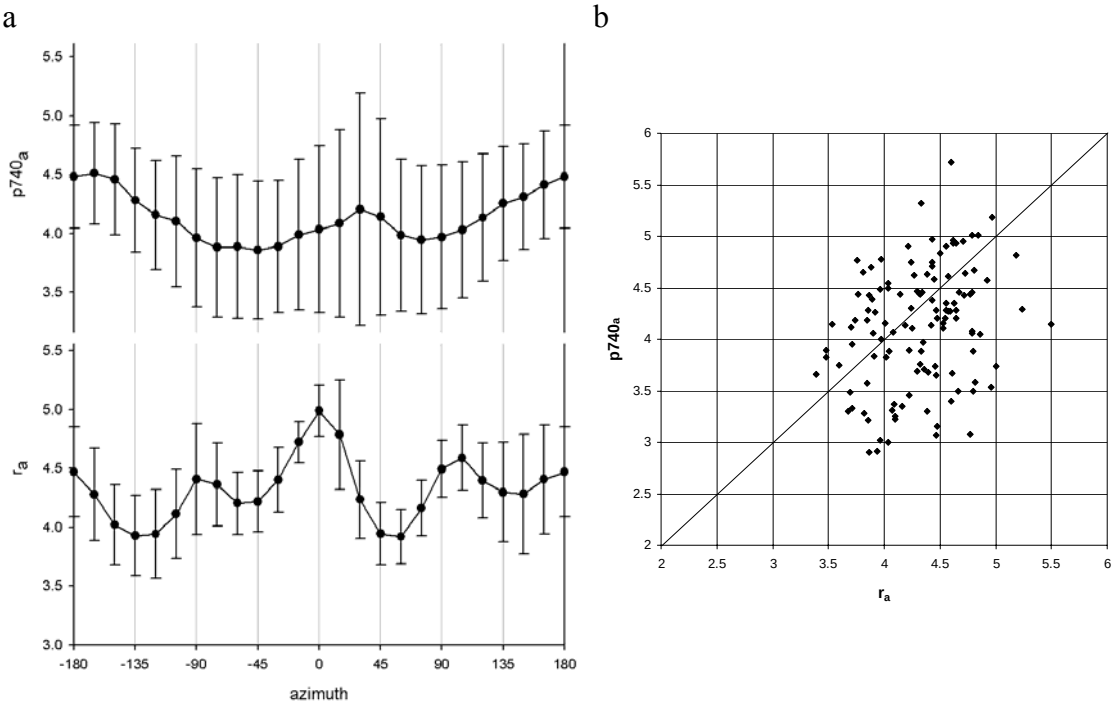

Figure 10.6 Comparison of r_a and $p740_a$

a) Mean (±sd) r_a and $p740_a$.
Vertical axis: r_a radius relative to corneal horizontal radius; $p740_a$ thickness ×100μm.
b) r_a (horizontal) v $p740_a$ (vertical).
Note no apparent correlation between isochrome distribution and peripheral corneal thickness distribution ($R^2 = 0.076$).

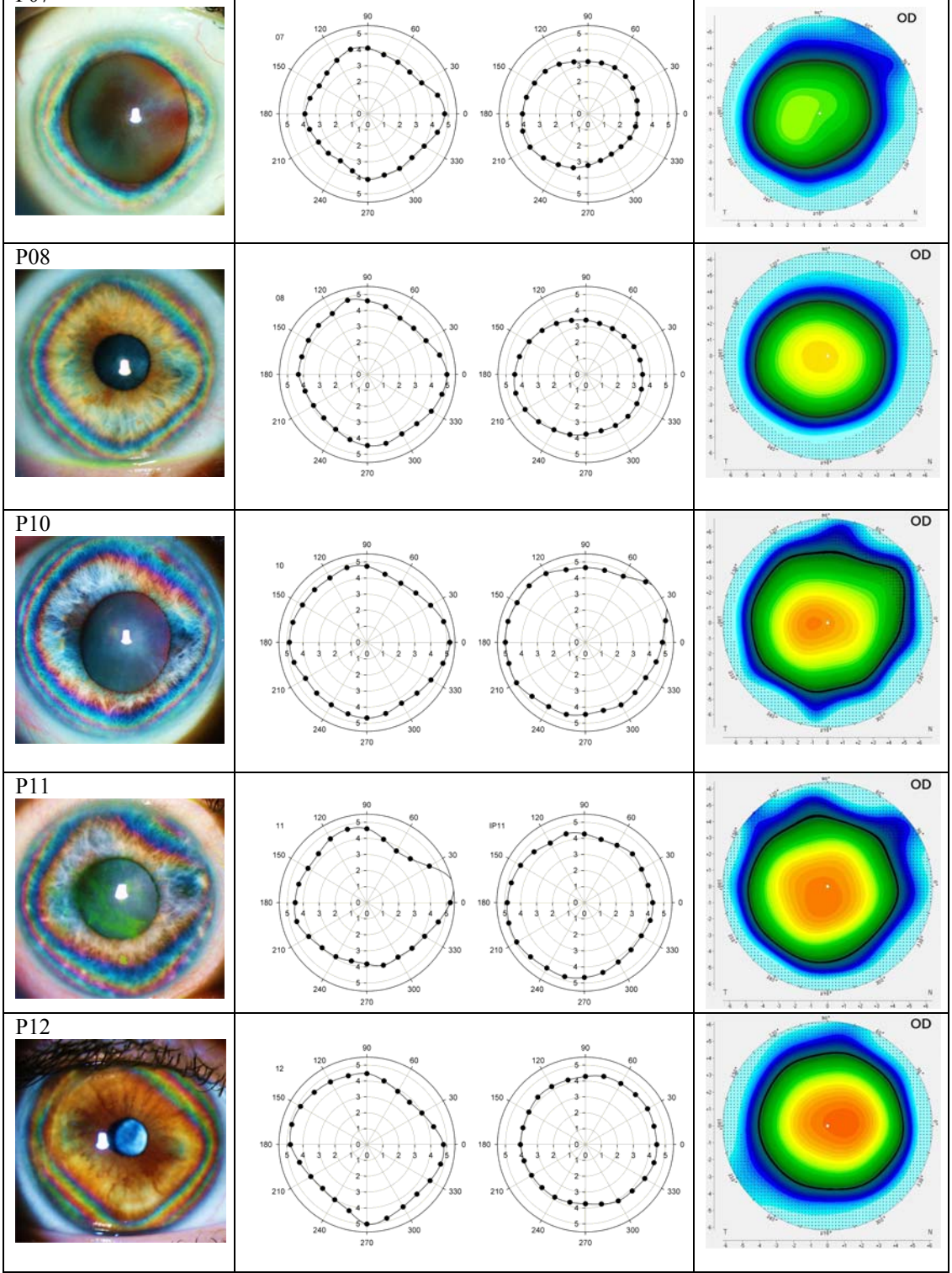

Figure 10.7 Isochromes and isopachs.

Isochrome images (left outer column) with corresponding isopachs as displayed by Pentacam software (right outer column, 740 µm isopach highlighted in black). Polar graphs of the 280nm isochrome (r_a), left inner) and the 740µm isopach ($p740_a$, right inner).

10.2.2 4mm radius data

Mean values of Pentacam-derived parameters measured at 4mm radius from the corneal centre are summarised in Table 10.1, Figure 10.8 and once again there appears to be no relationship to r_a.

The conclusion of this section is that peripheral corneal retardation as manifest by the pattern of isochromes is independent of corneal thickness.

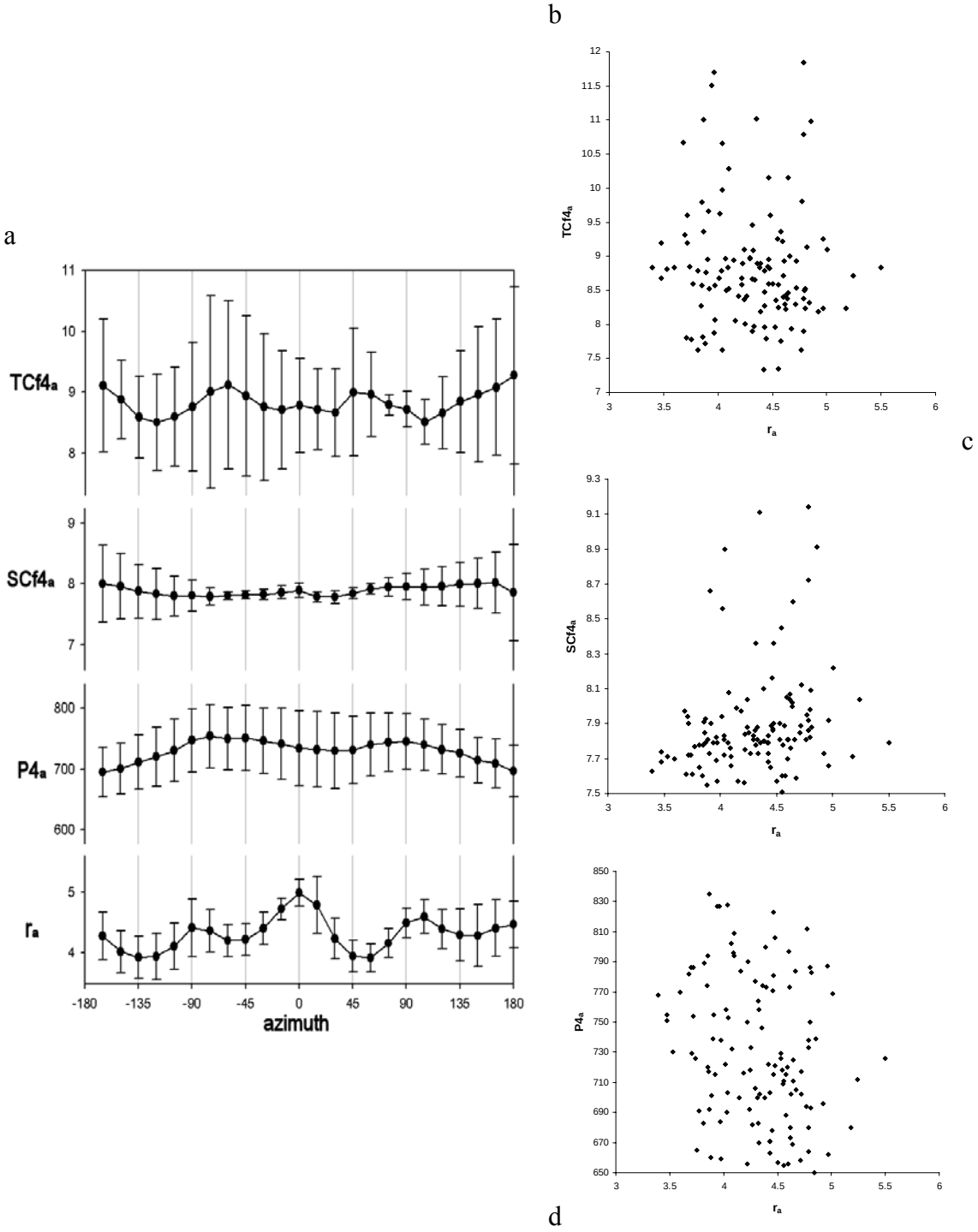

Figure 10.8 Comparison of r_a with 4mm radius pachymetry and corneal curvatures (mean ±sd)

(a) Mean (±sd) r_a relative to horizontal corneal radius; mean (±sd) pachymetry ($P4_a$, μm), anterior sagittal curvature ($SCf4_a$, mm) and anterior tangential curvature ($TCf4_a$, mm) at a radius of 4mm from the geometric corneal centre. (b) r_a (horizontal) v $TCF4_a$ ($R^2 = 0.0072$); (c) r_a v $SCF4_a$ ($R^2 = 0.0353$); (d) r_a v $P4_a$ ($R^2 = 0.0533$). In each case there is no significant corellation.

10.3 Results 2: Birefringence

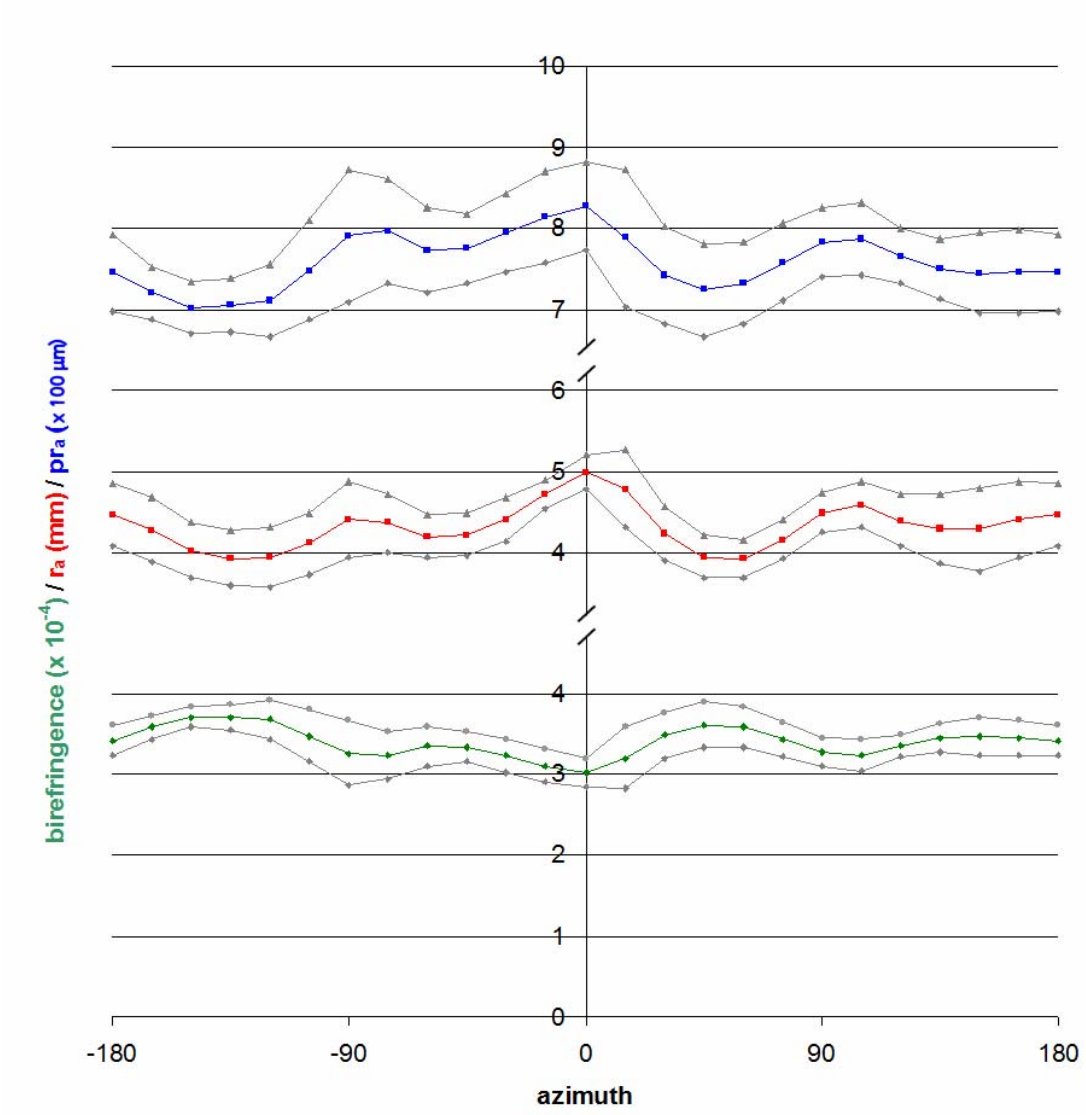

Figure 10.9 Graph of mean(±sd) r_a, mean(±sd) pr_a and calculated mean(±sd) birefringence

Mean r_a (upper blue ±sd grey: vertical scale mm), mean pr_a, (pachymetric thickness at r_a, red line ±sd grey: vertical scale x10^2 µm) and calculated birefringence (lower green line ±sd grey: vertical scale x10^{-4}) for meridians −180° to +180° in 15° increments

The relationship of r_a to meridian is shown in Figure 10.9 together with Pr_a the pachymetric thickness at that point. Note close correspondence between the two lines.

Bearing in mind that r_a is the distance from the corneal centre of the 280nm retardation isochrome, the association reflects the increasing corneal thickness with radius from the corneal centre. The locus of the 280nm retardation contour at corneal positions with different thicknesses implies that birefringence changes with meridian; furthermore, it is inversely proportional to r_a and there are four maxima and four minima.

Birefringence is calculated at the points of r_a according to the method previously outlined (§10.1.1) and results for the five individual eyes are given in Figure 10.10a where they are compared to r_a. Means ± sd are given in Figure 10.10b. Mean, maximum and minimum estimated birefringences and their azimuths are listed in Table 10.2 and vary from 3.00 (±0.11) × 10^{-4} to 3.68 (±0.30) × 10^{-4}. There is an approximate inverse proportionality such that birefringence minima occur at the meridians of the r_a maxima and *vice versa*. Once again there was no apparent relationship between calculated birefringence and the measured topographic parameters.

Table 10.2 Mean, maximum and minimum estimated birefringence

	magnitude (mm)		azimuth (degrees)		corneal thickness (μm)		Anterior sagittal (axial) curvature (mm)		birefringence × 10^{-4}	
	mean	sd	mean	sd	mean	sd	mean	sd	mean	sd
R_n	5.06	0.33	2.4	7.8	835	39	8.2	0.2	3.00	0.11
R_s	4.75	0.25	101.9	3.5	799	38	8.1	0.3	3.17	0.15
R_t	4.38	0.36	–32.3	193.1	750	45	8.0	0.9	3.43	0.22
R_i	4.66	0.32	–82.0	3.4	819	58	8.0	0.2	3.13	0.22
r_n	3.80	0.19	51.8	4.4	717	57	7.9	0.1	3.67	0.30
r_s	4.12	0.43	144.5	2.5	728	32	8.0	0.5	3.57	0.17
r_t	3.91	0.36	–124.3	7.2	716	27	7.8	0.4	3.64	0.15
r_i	4.20	0.48	–46.6	3.7	761	22	7.8	0.2	3.39	0.12

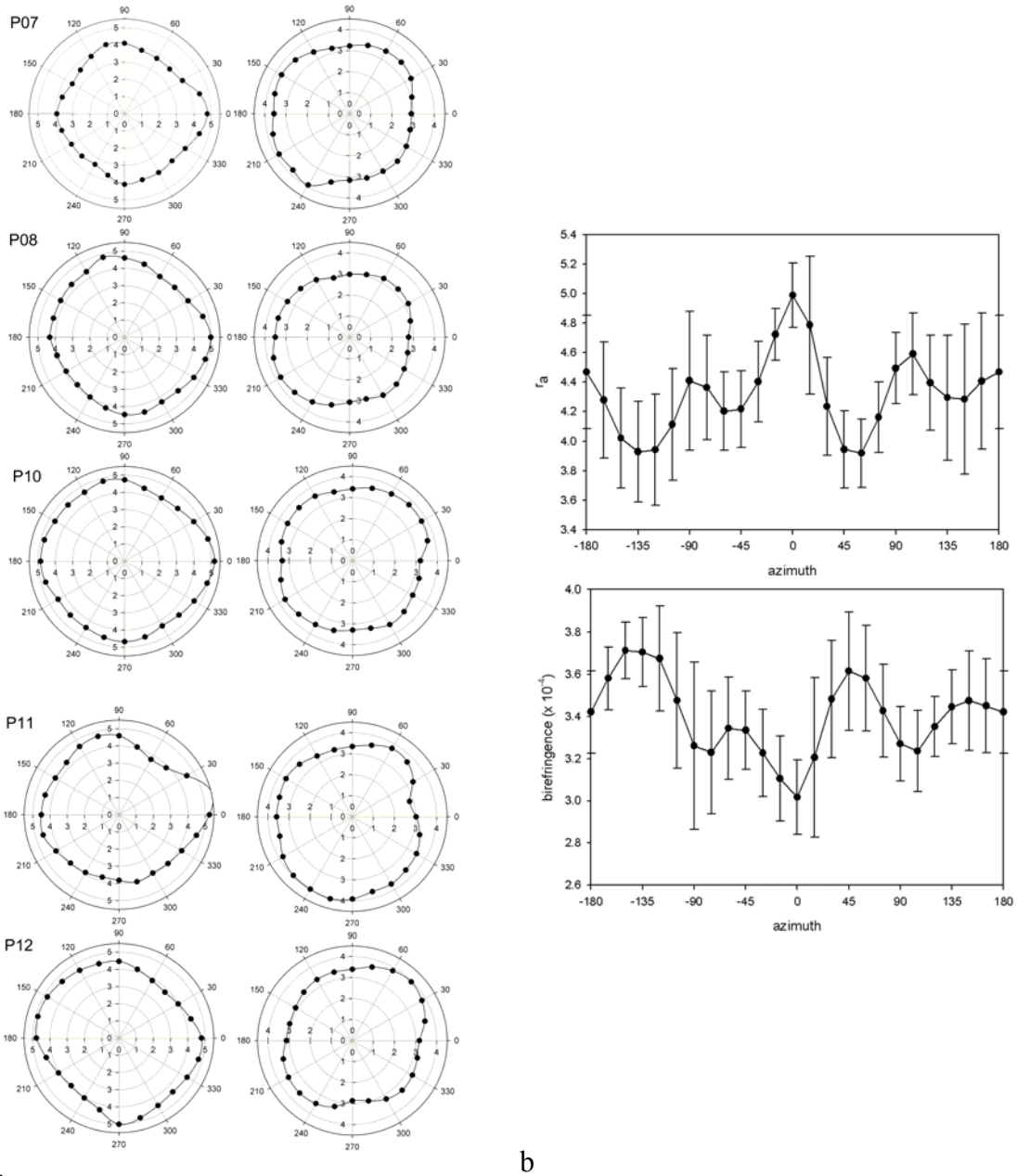

Figure 10.10 Graphs of r_a and calculated birefringence at r_a for right eyes of all five cases

(a) r_a (right), birefringence at r_a (left) eyes of all five cases. Radial units are fractions of horizontal corneal radius for r_a and $0 – 4.5 \times 10^{-4}$ for birefringence
(b) Mean ± sd of r_a (upper) calculated birefringence at r_a (lower)

10.4 Discussion

Regional/meridional variation in the 280nm isochrome indicates regional variation in peripheral corneal retardation. Such variation is due either to variation in light path distance in the peripheral corneal or to variation in birefringence.

The first part of this chapter looks at possible relationships between isochrome distribution and corneal thickness as measured by regional pachymetry. The thickness of the peripheral cornea in the five cases studied supports the accepted view that the cornea becomes progressively thicker towards the periphery (§2.1.2). The first conclusion of this chapter is that the meridional thickness variation is small, and insufficient to account for the observed variation in isochrome distribution.

The reliability of the Pentacam data has been the subject of many investigations and is generally considered to be high although dependent on subject cooperation (§15.5.1.3). Other methods of topographic pachymetry are reported to be of equivalent accuracy and include slit-scanning optical pachymetry (Orbscan; Bausch & Lomb, Rochester, New York, USA) and optical coherence tomography (OCT; Carl Zeiss Meditec, Inc., CA, USA) (Konstantopoulos, Kuo et al. 2008).

This is a detailed study of a small number of eyes. Great variation has already been seen in ocular parameters such as central corneal retardation, variation is also seen in the measured Pentacam parameters as indicated by the large standard deviations of data points demonstrated in the graphs. The possibility that the five cases studied are unrepresentative of normal eyes has to be considered, but the consistency of findings (e.g. the presence and shape of isochromes) suggests that the qualitative conclusions of this study are valid. Conclusions regarding association of corneal topographic data,

however, require greater numbers of subjects before the apparent non-correlations of topographic and polarimetric data can be confirmed (§14.1.2). Thus it is surprising not to see regional variations in topographic parameters such as peripheral corneal thickness and the isochrome maxima/minima, particularly as the vertical and horizontal isochrome maxima (corresponding to birefringence minima) are roughly aligned with the directions of action of the rectus muscles of ocular movement (see §2.2). To the author's knowledge, there are no described correlations between topographic parameters and extraocular muscle (EOM) data despite the commonly held belief that the action of the EOM have some influence on corneal astigmatism (Marin-Amat 1956; Löpping and Weale 1965). The lack of association between birefringent properties (magnitude and orientation of central corneal retardation) and other ocular parameters (corneal thickness, corneal curvature, refraction) has been noted in previous studies (Weinreb, Bowd et al. 2002).

The second set of results of this chapter attempts to calculate the absolute value of peripheral corneal birefringence. Several assumptions have been necessary, the most fundamental of which is of a simple relationship between path distance and birefringence. Path distance is a calculated value based on the angle of incidence of parallel rays at a given point from the centre of a spherical surface of a given radial thickness. Thus calculated path distance can only be an approximation, however, the physiological parameters from which the value is derived vary by relatively small amounts so the results, if not a precise measurement, give an indication of the real value and how it changes over the extent of the corneal surface. More direct measurement of corneal thickness / path distance may be possible with higher resolution

imaging of the peripheral cornea such as is now available with anterior segment optical coherence tomography (Prospero Ponce, Rocha et al. 2009).

Birefringence is precisely defined only for monochromatic light. Dispersion is a characteristic of the particular optical media in question and causes wavelength-dependent variation in refractive index, and hence birefringence. Dispersion is low for the cornea (Sivak and Mandelman 1982) and extremely small at the small angles and dimensions of the refractile structures in this study.

Published data of corneal retardation is confined to the pupillary area and does not exceed a radius of 3mm from the corneal centre (Bour and Lopes Cardozo 1981; Blokland and Verhelst 1987; Knighton, Huang et al. 2008). A subjective method of determining human corneal birefringence *in vivo* was used by Bour and Lopes Cardozo (1981) who also plotted quadrangular isoretardation contours within a 3mm radius of the corneal centre. Retardation minima were recorded in vertical and horizontal meridians as in the present study. The pattern was not confirmed by the other two groups although this may well represent the fact that the area of cornea studied was confined to that over the dilated pupil i.e. where biaxial behaviour is hypothesised and where isotropes (points of zero or near zero retardation) have been demonstrated.

The peripheral birefringence estimated in the present study varies from minima of 3.00×10^{-4} to maxima of 3.67×10^{-4}. No previous data exist regarding retardation/birefringence of the corneal periphery, however, these values are compatible with the value of central corneal birefringence of approximately 10^{-4} (§2.4.1). Furthermore, the theoretical analysis of Chapter 3 (see e.g. Figure 4.4) indicates that values in the range $2.5 – 5.0 \times 10^{-4}$ at equivalent corneal locations are not unreasonable. Birefringence variation will be detailed in Chapter11.

10.5 Chapter Summary

1) The distribution of peripheral corneal thickness does not correlate with the isochrome pattern.
2) Variations in isochrome distribution are due to regional changes in birefringence of the peripheral cornea.
3) Birefringence is inversely proportional to the distance of any given peripheral isochrome/isoretardation contour from the corneal centre.
4) Birefringence minima occur in the vertical and horizontal meridians at isochrome apices.
5) Birefringence maxima occur approximately mid-way between minima on any given isochrome.
6) Peripheral birefringence varies from $3.000 \times 10^{-4} - 3.674 \times 10^{-4}$
7) In this study there is no correlation between isochrome pattern and corneal sagittal/tangential radii.
8) This study was on five eyes only: larger studies are necessary to explore possible correlations of regional retardation/birefringence variations with corneal topographic parameters.
9) This study relies on the calculation of optical path length in the peripheral cornea. Alternative technologies (e.g. OCT) may allow more accurate and direct measurement of path length.

11 The biaxial model of corneal birefringence

This chapter examines further the question concerning the biaxial model and the observed pattern of peripheral corneal isochromes.

The first part of this chapter demonstrates qualitatively the similarities and differences of isochrome/isotrope pattern in a known negative biaxial crystal (aragonite, see § 4.6) and isochrome/isotrope pattern in the cornea. A quantitative approach highlights the differences using the theoretically predicted isochrome pattern of §4.5.

The second part develops the theoretical negative biaxial corneal model of finite thickness and defined curvatures (as introduced in §4.5) to determine the amount of regional thickness variation necessary to generate isochromes similar to those seen *in vivo*.

11.1 Comparison of birefringence: cornea v negative biaxial crystal

The negative biaxial properties of a thin section (plate) of crystalline aragonite observed under the petrological microscope with conoscopic illumination were introduced in §4.6. A modification of the microscopic technique allows a comparison to be made between the aragonite plate and the cornea as observed with 140P and 550P EPB. The optics of the petrological microscope are augmented with two accessory retarders such that one retarder is placed beneath the specimen with slow/fast axes 45° to the principle directions of the crossed polarizer/analyzer and an identical second retarder is placed above the specimen orientated perpendicular to the first (i.e. in a subtraction position: see e.g. §5.2.6). Such a configuration using quarter-wave retarders was first described by Benford (Craig 1961) as a method for identifying the extent of isochromes by

eliminating the isogyres of conoscopic interference patterns in petrological microscopy. The method allowed easy location of the positions of optic axes thereby facilitating the determination of 2V (§3.4). The method was subsequently used in biological polarization microscopy (Frohlich 1986). In this chapter, the optics of EPB with 150P and 550P will be emulated by using matched crossed paired 140nm and 550nm retarders. The theory is detailed in §5.2.5, 5.3.1 Eq. 5.21 and the experimental configuration is as described in §5.4.1, but with modifications as shown in Figure 11.1.

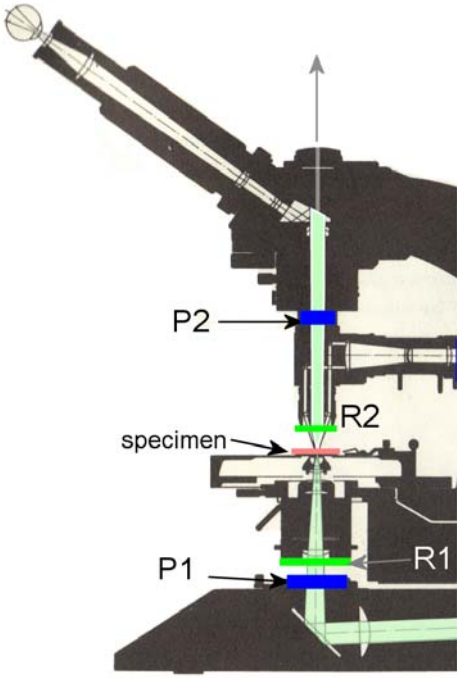

Figure 11.1 Experimental configuration

Modification of petrological microscope with matched retarders R1, R2. P1 is polarizer, P2 is analyzer

Images of the aragonite plate are presented on the left of Figure 11.2 where (a) is taken with paired 140nm retarders and (c) with paired 550nm retarders. The images are compared to a typical right cornea imaged by EPB with 140P (b) and 550P (d). This example graphically demonstrates the similarities and differences between the retardation patterns of the cornea and a geometrically equivalent negative biaxial crystal.

Note a superficial similarity between aragonite plate and cornea. With 140nm retarder/140P (Figure 11.2 a, b) two isotropes are present on either side of the centre of the image and peripheral isochromes are present. The aragonite and corneal isochrome colours are similar as is the colour change between adjacent isochromes. The smaller number of isochromes in the aragonite example is explained by the constant thickness of the aragonite plate as opposed to the progressively increasing corneal thickness. Summation phenomena are well defined in the lower 550nm/550P images where subtraction (lower order of colour) occurs in the NE and SW quadrants aligned with the slow axis of the upper retarder (R2), and addition (higher order colours) occurs in the SE and NW quadrants. This indicates that the slow axis of retardation follows the isochromes in the periphery of each image: a defining feature of negative optical sign (see e.g. § 3.4). An important difference, seen particularly in the upper 140P images, is the pattern of peripheral isochromes which are oval for the negative biaxial aragonite, but quadrangular for the cornea as previously established (§9.5).

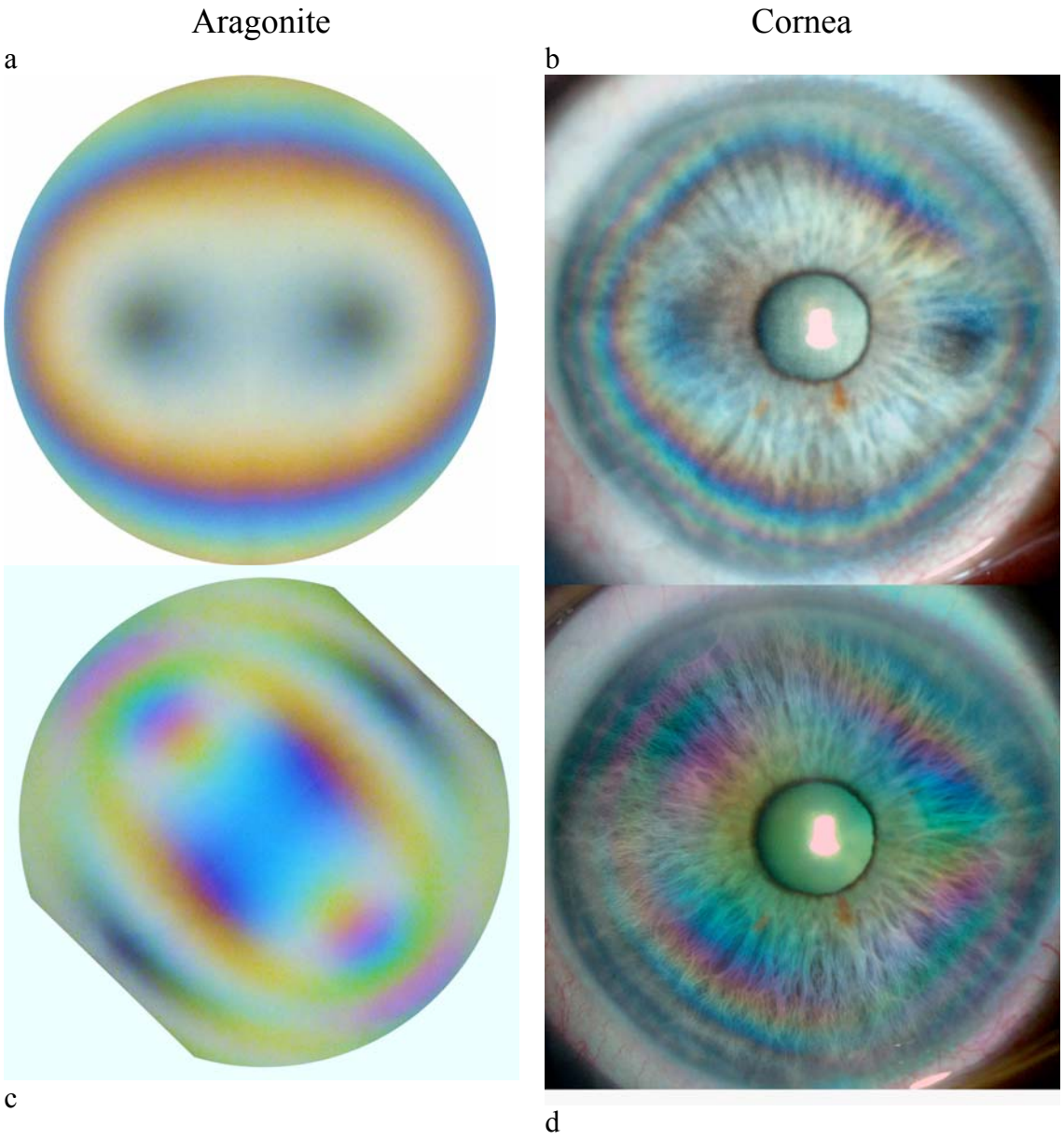

Figure 11.2 Aragonite plate and cornea

Aragonite plate (negative biaxial) under conoscopic illumination. Left column: (a) R1 = R2 = 140nm; (c) R1 = R2 = 550nm; see text for details).
Right column: EPB of cornea with 140P (b) and 550P (d) (Subject X04Ro). R2 and 550P slow is NE–SW.

11.1.1 Theoretically derived equirefringence contours.

Taking a negative biaxial model and typical corneal parameters as described in Chapter 3, a distribution of birefringence is derived as depicted in Figure 4.4 (§4.4). This distribution has been superimposed on the aragonite isochromes/isotropes (Figure 11.3a) and also a typical example of a right cornea (Figure 11.3b). Furthermore predicted equirefringence curves of typical values expected for the 280nm isochrome are presented in Figure 11.4 with the average (n = 25) right eye isochrome distribution data (see §9.3.2). The model proposed in Chapter 3 therefore predicts accurately the aragonite retardation pattern in its entirety, correlates well with the corneal isotropes, but shows no correlation with peripheral corneal isochromes. This is further supported by the birefringence data from the five Pentacam subjects (see §10.3, Figure 10.9). An unmodified biaxial model is therefore not appropriate for the peripheral cornea.

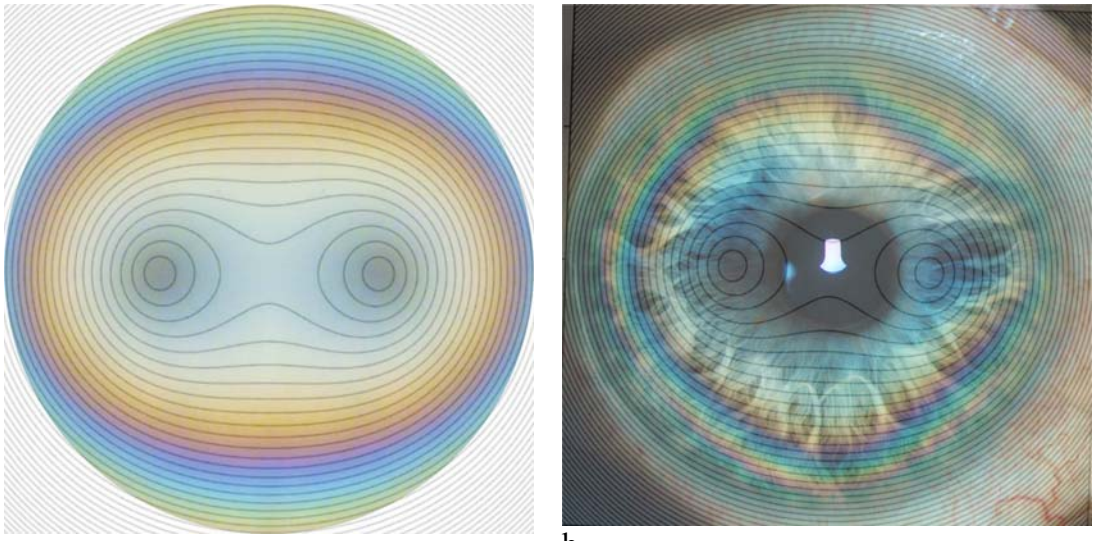

a b

Figure 11.3 Overlay of theoretically calculated biaxial equirefringence contours onto (a) aragonite model, (b) cornea

Note correspondence of equirefringence contours with isotropes/isochromes for aragonite (a) but not for cornea (b) particularly in vertical and nasal meridians. Aragonite image as in Figure 11.2a upper. Corneal image as in Figure 11.2b upper: 140P polariscopy, right eye, subject X04Ro.

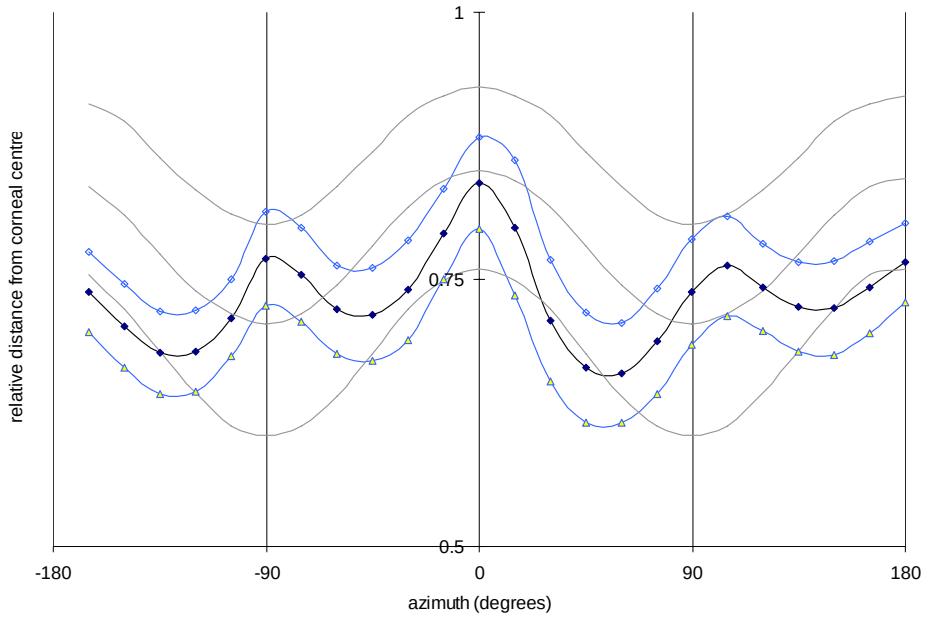

c

Figure 11.4 Corneal mean (±sd) 280nm isochrome distribution and calculated biaxial isochromes

Isochromes, mean r_a ± sd as in Figure 9.4; predicted biaxial isochromes, grey continuous lines. Vertical axis: distance from corneal centre relative to horizontal radius.

11.2 Transformation of the biaxial model

Isochromes correspond to contours of equal retardation, which are the product of light path distance through the cornea and birefringence along that path. The evidence of Chapters 9 and 10 favours regional changes in birefringence as the cause of the observed isochromes. The pattern of peripheral retardation/birefringence does not agree with the biaxial model whereas the central cornea is adequately explained by this model. If it is assumed that the biaxial model is valid throughout the extent of the cornea, then the question arises as to what conditions might cause the model biaxial cornea to generate quadrangular isochromes such as those observed *in vivo*. It was previously concluded (§9.5(14)) that variations in thickness within the physiological range were insufficient for the required isochrome pattern. This section investigates the extent to which a model cornea must be deformed to generate quadrangular isochromes.

11.2.1 Astigmatic model

Data from a recent study of 40 eyes (Fares, Otri et al. 2012) indicates that, for a point 7mm from the corneal apex, thicknesses are as follows: "temporal, 639.15μm (sd 34.59μm, range 553 – 730μm), inferior 664.21μm (sd 41.80μm range 586 – 763μm), superior 671.22μm (sd 44.28μm, range 571-766μm), nasal 676.78μm (sd 42.62μm range 582 – 761μm)". Furthermore, for circles centred at the point of least corneal thickness, mean thickness are stated as "700.88μm (sd 39.25μm) at a diameter of 8mm and 784.81μm (sd 47.73μm) at a diameter of 10mm". The precision of measurement is questionable and a discrepancy between 5mm radius and 7mm radius thickness ranges

is not explained. Furthermore, range data was not explicitly stated although it can be estimated from the regression graphs as approximately 675 - 900μm for the 10mm diameter circle. Despite its limitations, and in the absence of other data, it will be assumed here that the thickness at 7mm from the corneal apex ranges in different subjects from 553 – 766 μm and approximately 675 – 900μm at 5mm radius. In both cases the range is similar with an approximate difference of 200μm. Such a range is most unlikely to occur in a single eye, but it can be used as an upper bound for a 'physiological' value.

Turning to calculated birefringence using the section functions defined for the biaxial model (Eq. 3.12, Eq. 3.13) and previously defined parameters (Table 4.1), at 0.8 × corneal radius (5 – 6mm radius from apex) minimum and maximum birefringence are 0.88×10^{-3} and 1.07×10^{-3} respectively. This corresponds (Eq. 3.14) to differences in retardation of $0.88 \times 10^{-3} \times 0.20 \times 10^{6}$ nm = 176 nm and $1.07 \times 10^{-3} \times 0.35 \times 10^{6}$ nm = 214 nm i.e. 0.3 – 0.4 of a wavelength. In other words, a retardance difference of $< \lambda/2$ is caused by an orthogonal meridional peripheral thickness difference of 200μm. The mean difference between maximum and minimum thickness at 4mm radius from the cornea centre is 66μm *in vivo* (Table 15.1) so the value of 200μm is most unlikely to occur in either normal or abnormal human corneas.

11.2.2 Quadrangular isochromes

From the experimental data (Table 9.2) the ratio of vertical to horizontal maxima of the 280 isochrome Dh/Dv = 0.795/0.765 = 1.04. To simulate isochromes approaching this ratio, the retardation function $\Lambda(m, n) = b(m, n).\ \tau(m, n)$ (Eq. 3.14) is used and the τ-

function defined for the ellipsoidal model with parameters a, b, c, f, g, h (see Appendix 3; §15.2.4). Appropriate values, determined by numerical iteration, are a = 1, b = 1.468, c = 0.93, f = g = h = 0.86 (Figure 11.5) which define the model Ex (§4.5.1.2). The resultant isochrome/isoretardation pattern and thickness profile is presented in Figure 11.6. The section functions of maximum and minimum curvatures of Ex compared to a 'physiological' cornea (Model Ea) are shown in Figure 4.7.

The 4mm radius thickness contour for the quadrangular isochrome model (Ex) is compared with the equivalent Pentacam measured values (§15.6) in Figure 11.7.

These results show that, for a model cornea with biaxial birefringence, the thickness variation necessary to distort the isochromes to a pattern similar to that observed *in vivo* far exceeds that which is measured *in vivo* or is anatomically possible.

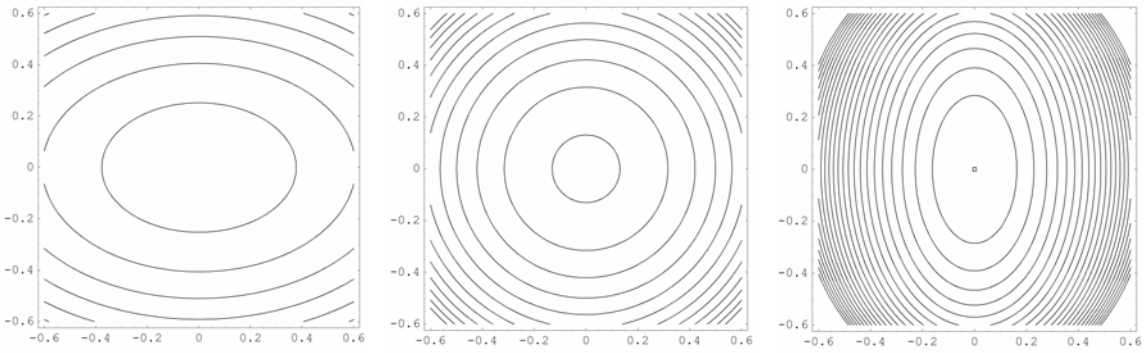

Figure 11.5 Height and thickness profiles of corneal model Ex

(a) Front surface height profile, central height 0.93; (b) back surface height profile, central height 0.86; (c) corneal thickness, central thickness 0.07; parameters a = 1, b = 1.468, c = 0.93, f = g = h = 0.86. Contour intervals and axes as in Figure 4.5

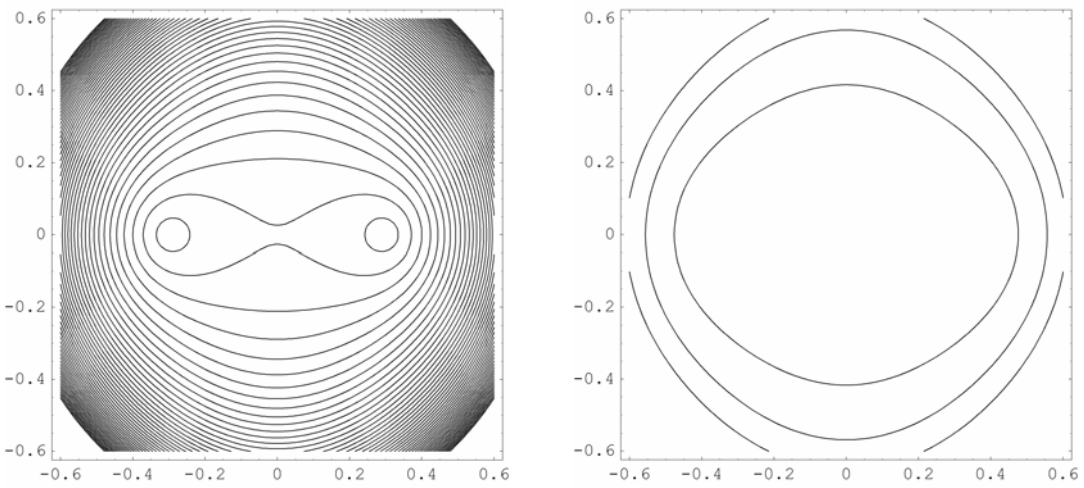

a b

Figure 11.6 Simulation of quadrangular isochromes

Distorted isochromes resulting from thinning cornea in the vertical meridian according to the parameters $\alpha = 1.376205$, $\beta = 1.376345$, $\gamma = 1.377795$; a = 1, b = 1.468, c = 0.93, f = g = h = 0.86.
(a) predicted isochromes/isoretardation contours (2% intervals)
(b) 0.5λ (inner), 1λ and 1.5λ (outer) isoretardation contours.

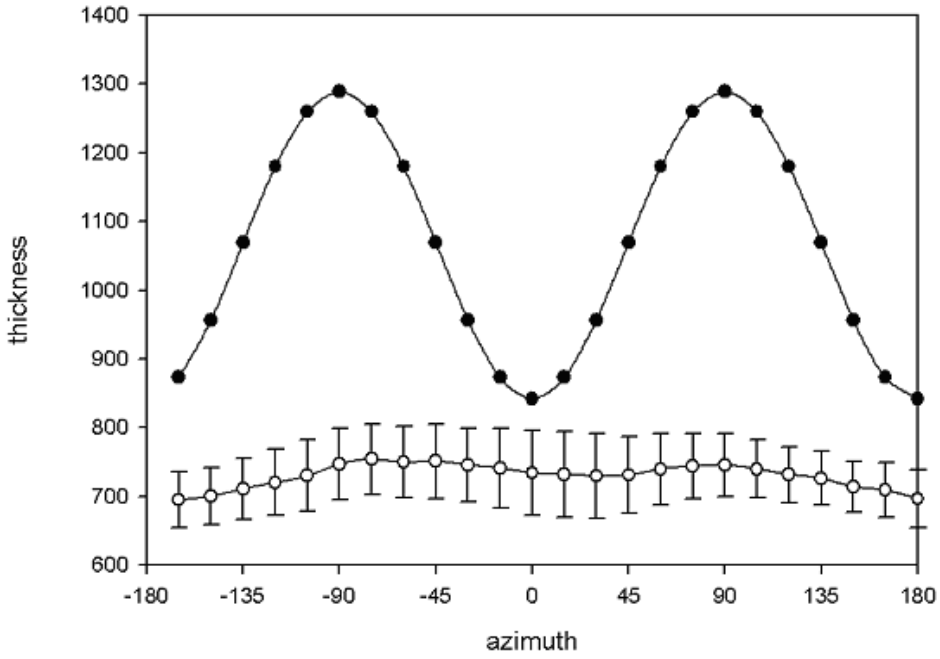

Figure 11.7 Thickness at 4mm radius from corneal centre of predicted (upper graph, filled circles) vs. mean (±sd) Pentacam values

11.3 Discussion

The disparity between the biaxial central cornea and non-biaxial periphery has been detailed in previous chapters. The first part of this chapter demonstrated the disparity by comparing the corneal isochromes/isotropes with those of aragonite, a known negative biaxial material. The second part of this chapter establishes that a biaxial model applied to a transformable geometric model of a cornea with finite thickness may be configured to produce a curved rhomboidal pattern of retardation similar to isochromes. The necessary transformations, however, result in geometry that is not possible for the human cornea. This supports the previous conclusion (§7.3) that the peripheral corneal birefringence is not that predicted by a strictly biaxial model.

Many assumptions are necessarily made in the mathematical modelling, not least that the corneal thickness and light path distance models are sufficiently representative of the *in vivo* cornea for the purposes of this study. Corneal values are taken that reflect the extrema of measured values although, as emphasised in the text, such values are unlikely to occur in the same eye *in vivo*. The rationale is that if extreme, but plausible, values are insufficient to explain the observed isochrome pattern, then more physiological values will also be insufficient. Taking points with extreme value parameters, the difference between maximum and minimum peripheral retardation is less than one half wavelength, a value similar to that observed *in vivo* in normal corneas with near-radially symmetric thickness (§10.4).

The distribution of isochromes is next modelled as described in §4.5, but with the parameters defining corneal geometry varied iteratively to generate quadrangular

isochrome patterns similar to those observed. The resultant parameters translate into corneal thickness values that exceeded any anatomically possible values.

Corneal birefringence is determined by regularity/symmetry of stromal structure (§4.2.1), therefore the incongruence between peripheral and central cornea with respect to the biaxial birefringence model suggests that the stromas of the peripheral and the central cornea are structurally distinct. In these regions, corneal birefringence is determined by regularity birefringence.

11.4 Chapter Summary

1) The isochromes/isotropes of the cornea *in vivo* are compared to those of a physical model of a negative biaxial crystal observed under conoscopic illumination.
2) Isotropes and isochromes of monocrystalline aragonite, a known negative biaxial material, agree with those predicted by the model of Chapter 3.
3) The isotropes of the central corneal zones are similar to those of the biaxial crystal and agree with theoretical prediction.
4) The quadrangular peripheral corneal isochromes differ from the elliptical isochromes of the biaxial crystal and disagree with theoretical prediction.
5) The observed variation may be due to peripheral path difference variation in a biaxial cornea or peripheral non-biaxial properties.
6) Physiologically realistic corneal thickness profiles can be modelled by the ellipsoidal corneal model Ea expresses as the thickness function τ given appropriate values of parameters a, b, c, f, g, h.
7) Peripheral isoretardation contours generated by the retardation function Λ are elliptical in a model astigmatic cornea within the range of physiological thickness parameters.
8) The retardation function Λ generates quadrangular isoretardation contours given appropriate parameters of the optical path distance function τ.

9) The parameters (a, b, c, f, g, h) of τ necessary to generate quadrangular isoretardation contours translate to corneal thickness variations that have no anatomical/physiological counterpart.

10) The *in vivo* variation of the isoretardation contours/ isochromes from a biaxial model are not due to physiological variations of light path distance through the cornea.

11) The *in vivo* variations of the isoretardation contours/ isochromes result from regional changes in birefringence.

12) The *in vivo* variations in peripheral isoretardation contours / isochromes do not follow the birefringence function b of a biaxial model.

13) The isoretardation contours / isochromes of the peripheral cornea do not conform to the biaxial model.

14) The peripheral corneal stroma is structurally distinct from the central corneal stroma.

15) The peripheral corneal stroma has sufficient regularity of structure to account for the observed birefringence/isochrome/retardation pattern.

12 Corneal Polarization Biomicroscopy of the abnormal cornea

A brief survey of miscellaneous cases demonstrates the application of EPB to the abnormal/post-surgical cornea and highlights several areas for further investigation. The original application using a 'circular' polarizing filter identified stress-induced birefringence associated with sutures in the post-operative peripheral cornea (Misson and Stevens 1990). This original study pre-dated advances in corneal surgery, particularly laser refractive techniques.

12.1.1 Corneal disease / trauma

Pathological processes can occur in any of the five anatomical corneal layers (Harry and Misson 2001). Epithelial disturbances have little effect on the EPB appearance.

12.1.1.1 Calcific band keratopathy

Calcific band keratopathy is an abnormal deposition of calcium salts in Bowman's membrane and anterior stroma. The abnormal areas are white, opaque, and if involving the visual axis, cause visual loss. The case shown (Figure 12.1) is photographed in plane light (a) and with EPB (b). The cornea is normal on the right side of the pupil where the elliptic/hyperbolic fibrils are easily seen under higher magnification (Figure 12.2): fibrils are obscured on the left by the calcium salts deposit.

a

b

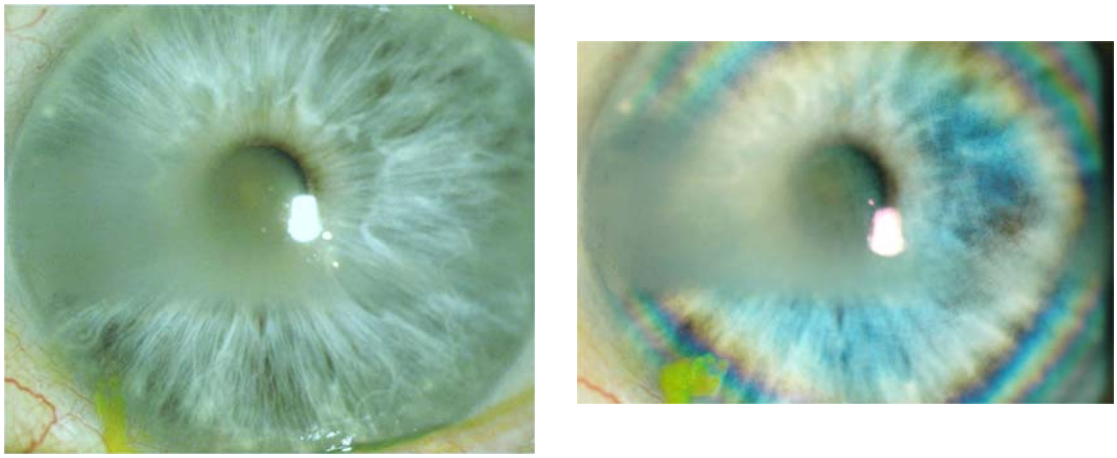

Figure 12.1 Calcific band keratopathy

(a) plane white light; (b) EPB

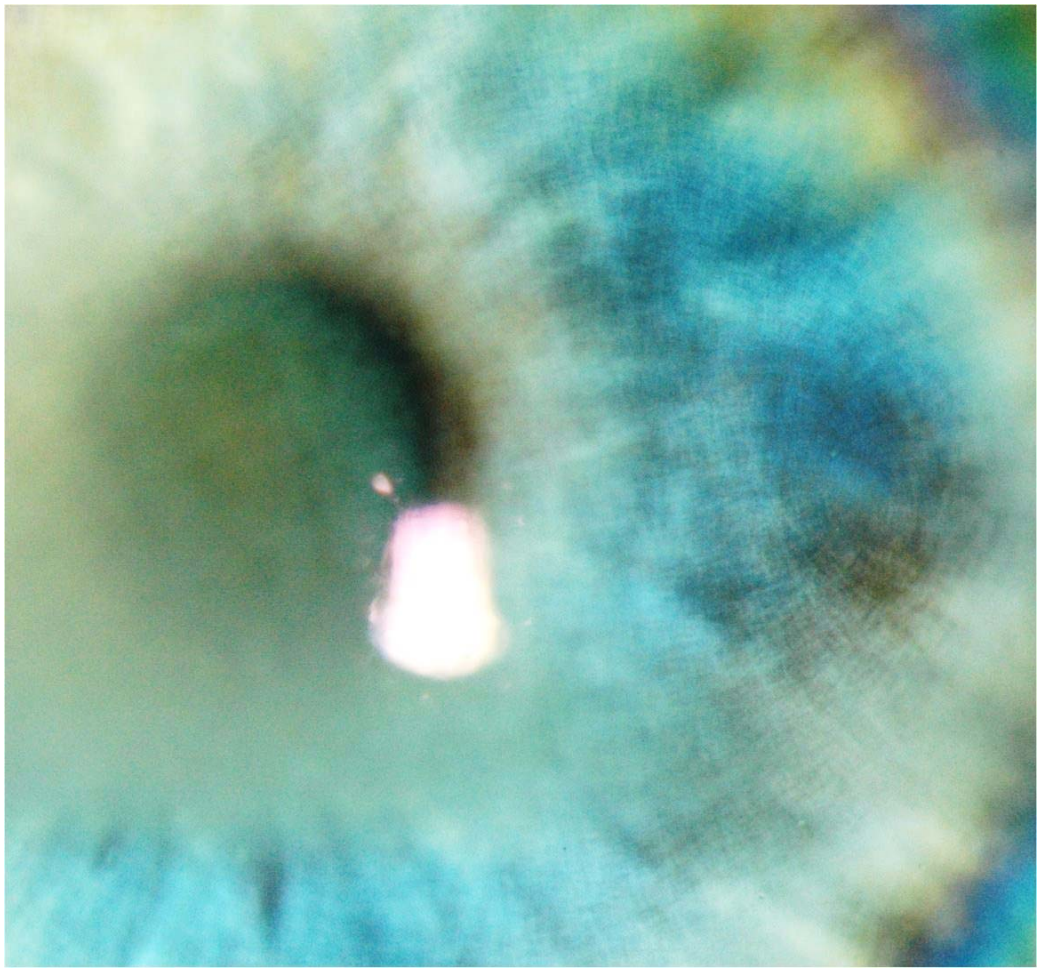

Figure 12.2 Calcific band keratopathy

High power EPB image showing elliptic/hyperbolic pattern (right) obscured by band keratopathy (left)

12.1.1.2 Corneal scarring

Corneal stromal trauma due to foreign bodies initially leave a visible scar which later fades and may become imperceptible (Figure 12.3a). Such foreign body scars are easily detected with EPB (Figure 12.3b). Similarly scarring due to other pathologies such as herpes simplex keratitis are seen in greater detail with EPB than with plane light examination.

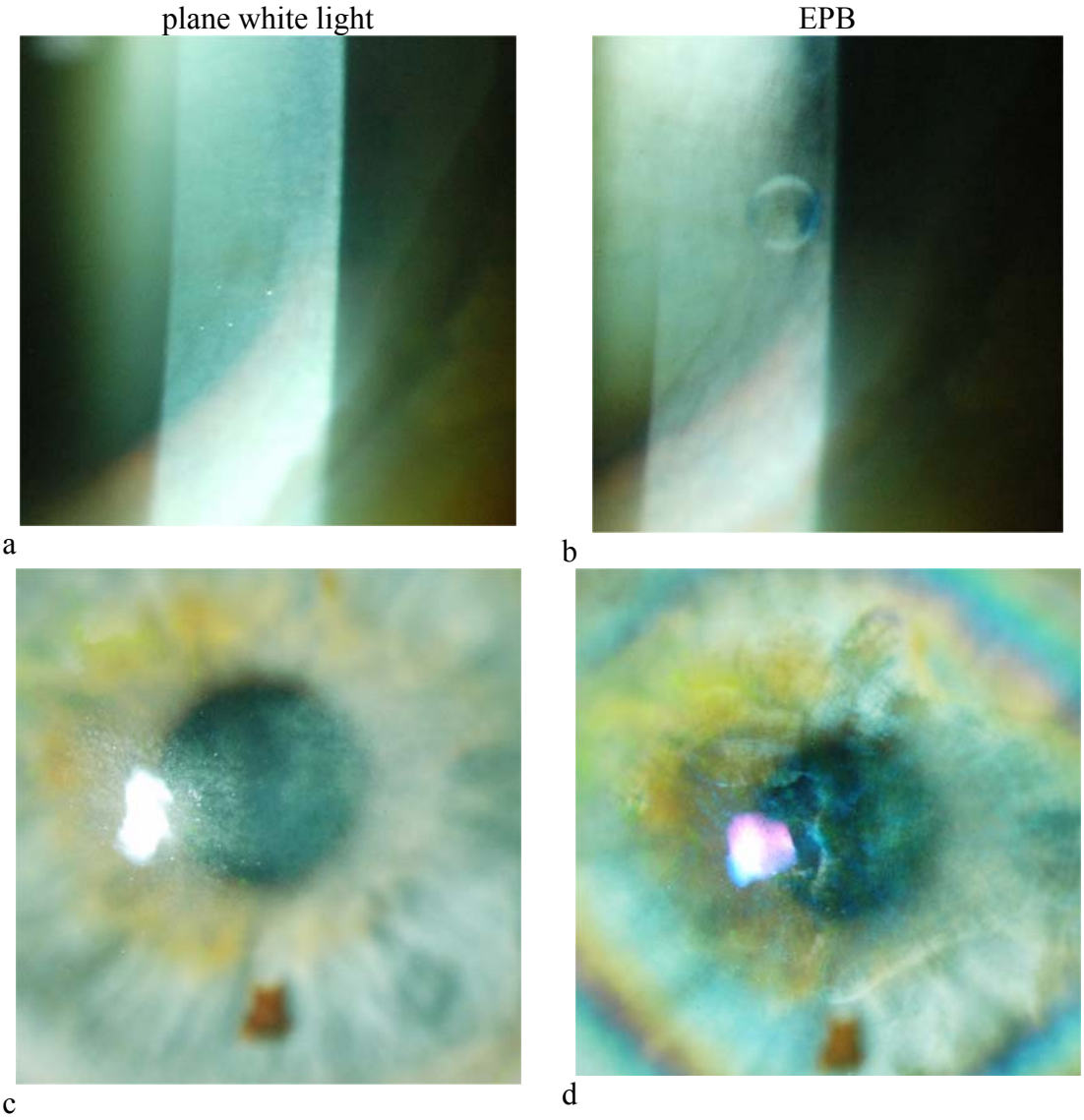

Figure 12.3 Corneal scarring

Foreign body scar (a) plane white light; (b) EPB; Herpes simple keratitis (c) plane white light (d) EPB

12.1.1.3 Keratoconus

Keratoconus has been mentioned on several occasions in the text as a disorder of tissue biomechanics whereby the cornea progressively thins and deforms into a irregular conic shape. The author has observed a number of cases and not found any distinguishing EPB features in early stages. In late cases there is progressive conic deformation of the central cornea and thinning of the corneal apex. This is seen as a distortion of the retardation pattern and linking of the two isotropes with an isotropic band. The band is probably a result of corneal thinning rather than any intrinsic change in birefringence bearing in mind the apparent normality of isochromes.

a b

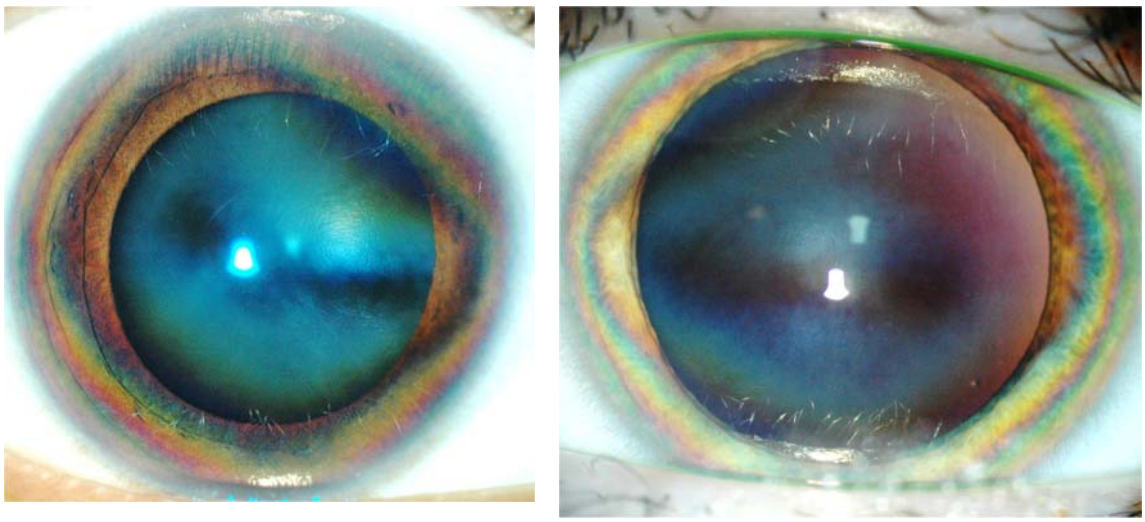

Figure 12.4 Keratoconus

EPB images showing interisotrope band. (Two subjects: (a) right eye KC05; (b) left eye KC06)

12.1.2 Corneal Surgery

Peripheral corneal incisions such as those made in cataract surgery are more visible with EPB, but do not obviously change the patterns of isochromes. Stress-induced changes in interference patterns are dealt with elsewhere (Misson and Stevens 1990). More

invasive surgical procedures such as corneal grafts (penetrating keratoplasty) and corneorefractive surgery change the normal EPB appearance significantly.

12.1.2.1 Penetrating keratoplasty

The current practice of penetrating keratoplasty (PK) it to remove a full thickness circular/cylindrical 'button' of diseased host cornea and to replace it with a similar sized, but healthy, viable donor button. The donor cornea is sutured in place and eventually integrates into the host by healing processes. The peculiar immune behaviour of the eye allows host/donor compatibility with donor material that has not been antigenically (tissue-type) matched with the host so makes it the most successful of any transplant procedure in terms of rejection risk. At present donor corneas are not matched for gender nor eye side. Furthermore, to date, there has been no efficient method of orientating the donor into the host. The latter may have biomechanical consequences as outlined in §14.3.3.3 and the problem may be solved polariscopically using the methods of Chapter 5.

The general appearance of PK with white light biomicroscopy and EPB is shown in Figure 12.5.

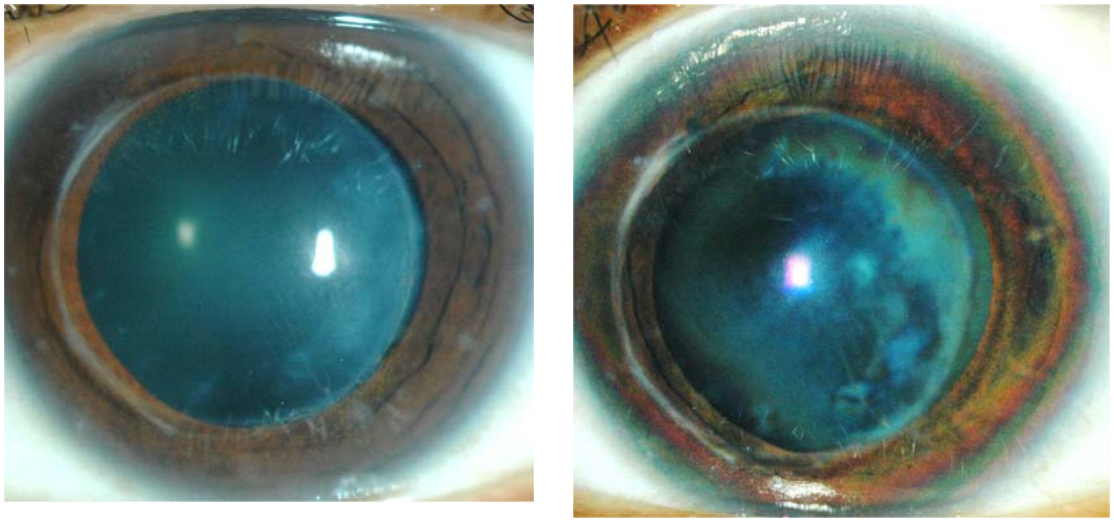

Figure 12.5 Penetrating keratoplasty

(a) Plane white light; (b) EPB: Left eye subject PK05.
Not isotropes orientated at approximately 45° superonasal/ inferotemporal

The random orientations of donor buttons are illustrated in Figure 12.6 where the isotope orientations do not conform to the superotemporal-inferonasal rule. In one case (a) the donor button appears to have been trephined eccentrically as the isotropes are 'off-axis'. The use of polarimetry in the preparation of the donor material may determine pre-existing scarring, assist with centration of the trephination as well as orientating the donor to match the host retardation pattern.

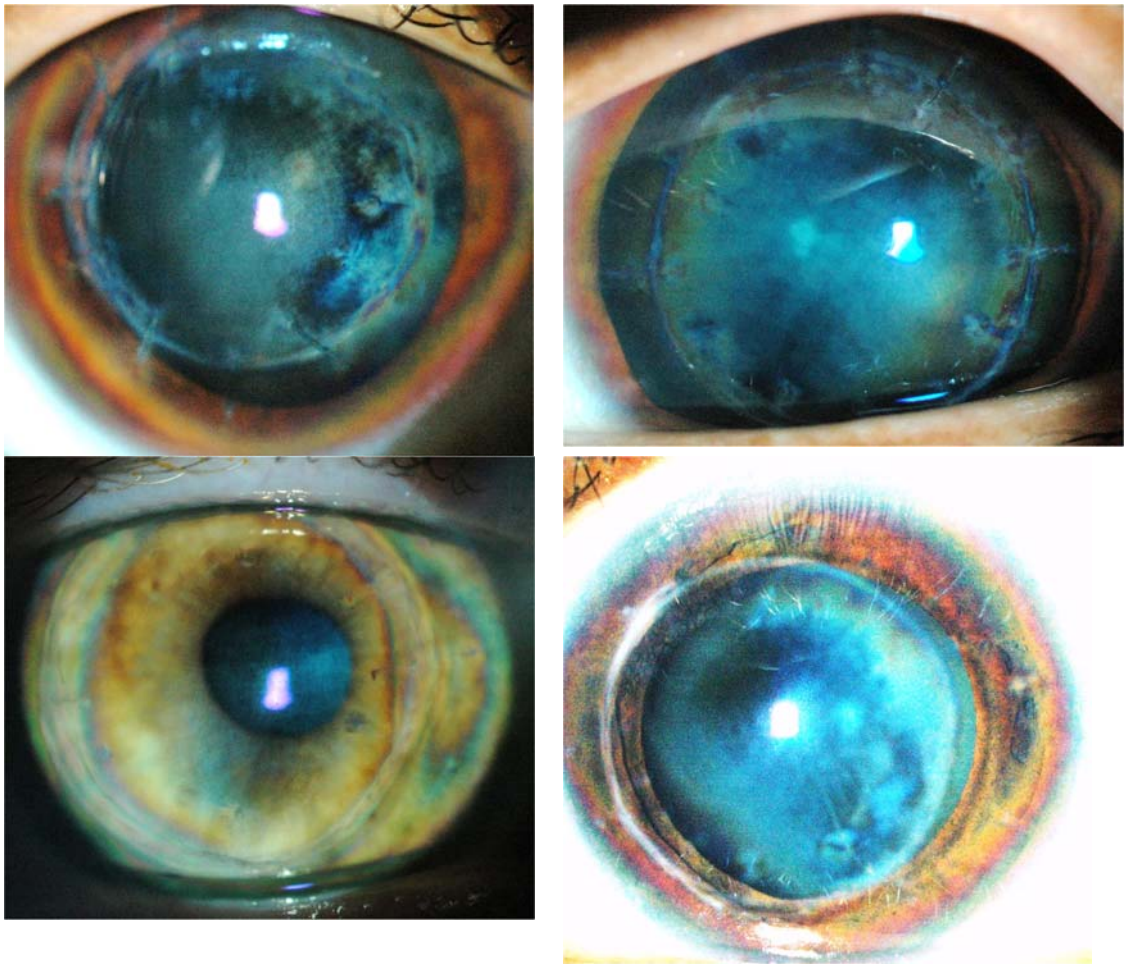

Figure 12.6 Penetrating keratoplasty

Four PK cases: note orientations of isotropes in donor buttons (a) Right eye: superotemporal-inferonasal 60° off-axis (PK01); (b) Right eye: superonasal-inferotemporal 60° (PK03); (c) Left eye: vertical (PK02); (d) Left eye PK05: superonasal-inferotemporal 45°.

12.1.2.2 Post-refractive surgical cornea

The curvature of the cornea, and hence its refractive properties, can be surgically altered indirectly by carefully placed peripheral incisions or directly by laser ablation (§2.3, Chapter14). The biomicroscopic appearance of radial keratotomy is shown in Figure 12.7 where the scars of the radial incisions are rendered more visible by EPB.

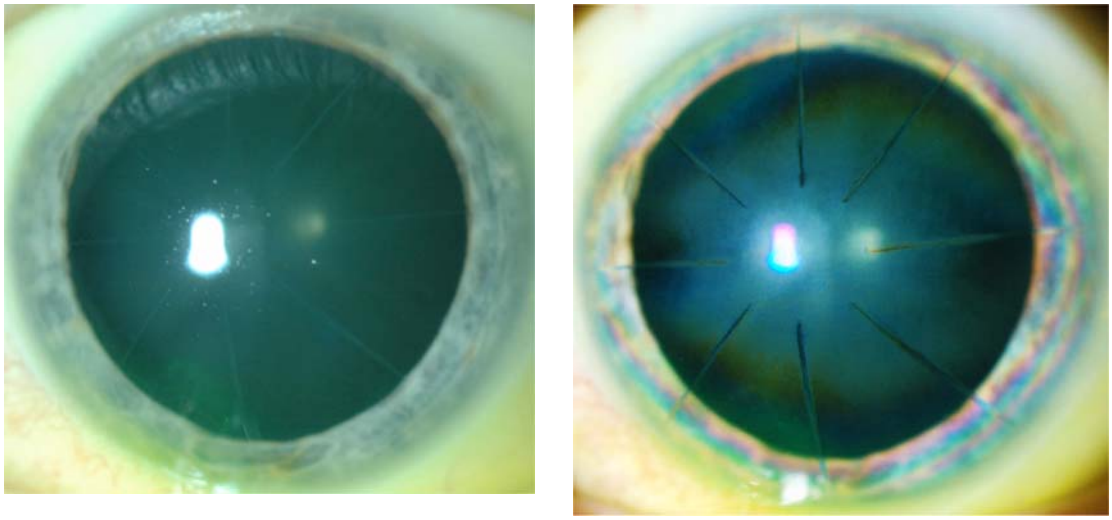

Figure 12.7 Radial keratotomy
(a) plane slit lamp image; (b) EPB. Case RS04 (left)

The EPB appearance of photorefractive keratectomy and laser-assisted sub-epithelial keratectomy (LASEK) are shown in Figure 12.8, and laser-assisted in situ keratomeliusis (LASIK) in Figure 12.9. The EPB findings are essentially similar in all cases of superficial laser ablations i.e. a loss of detail of fibrillar structure and a 'mottled' pattern of retardation in treated areas. Laser surgery is known to alter corneal birefringence (Centofanti, Oddone et al. 2005), but the significance of the findings of the present study has yet to be determined.

a b

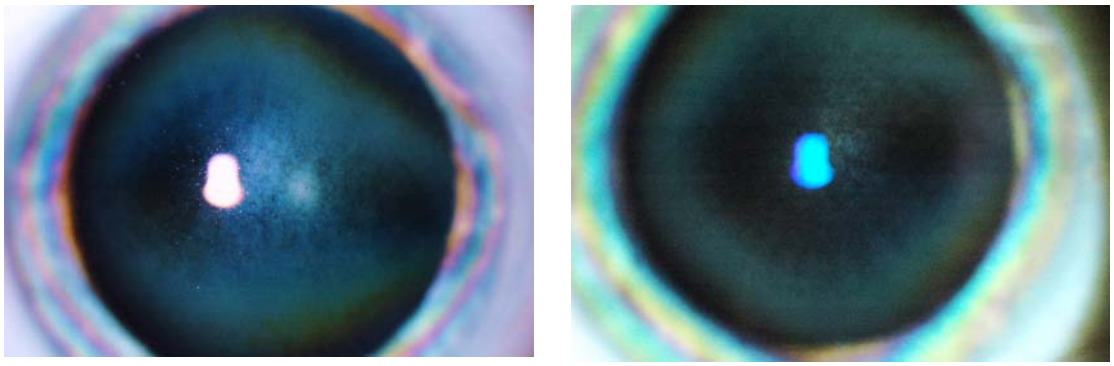

Figure 12.8 Subepithelial ablation
(a) PRK (RS04, right); (b) LASEK(RS05)

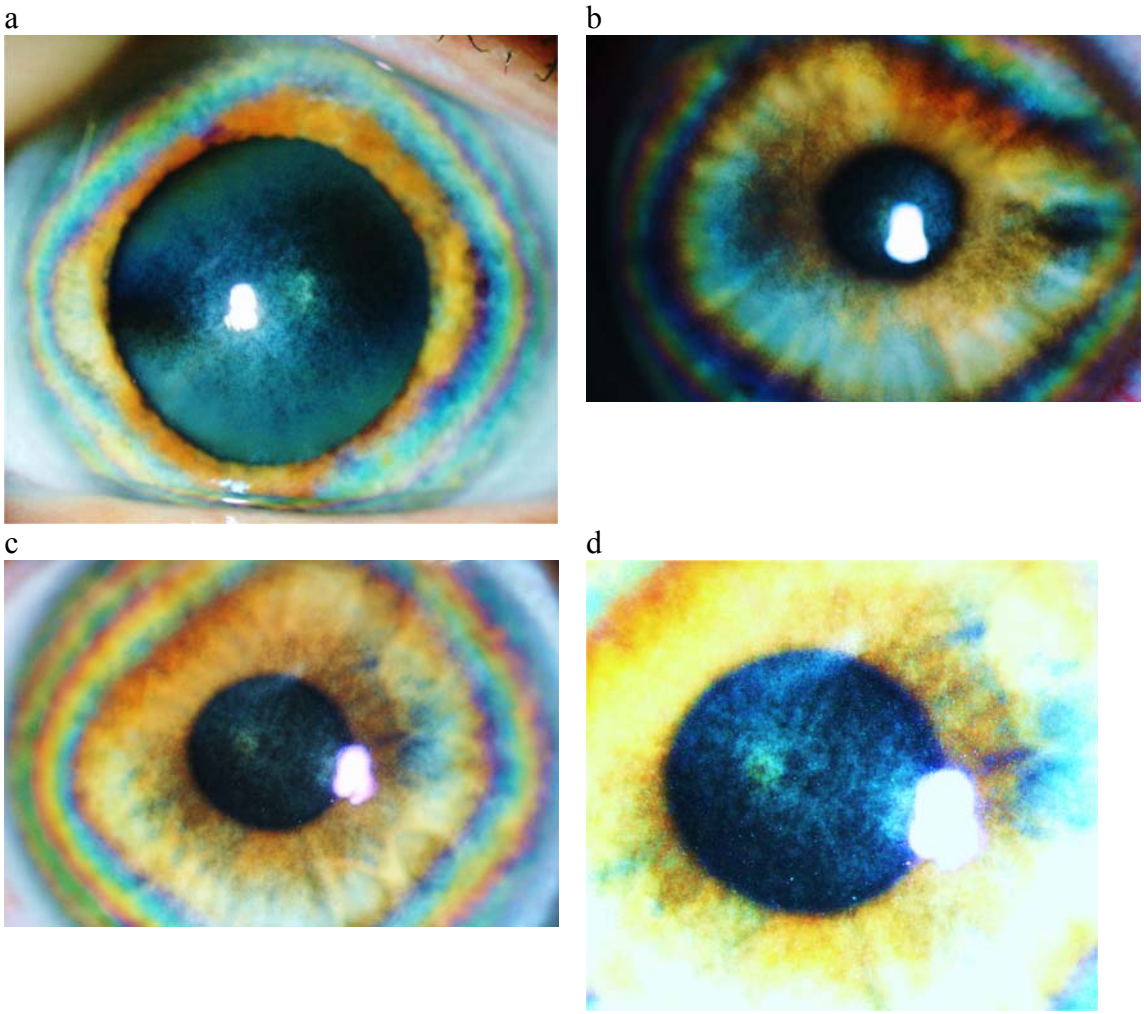

Figure 12.9 LASIK

(a) RS01; (b) RS02; (c) RS03; (d) RS03 magnified with enhanced contrast to demonstrate mottling

13 A model of corneal structure

The first part of this study (Chapters 3, 4) explored the theoretical aspects of the biaxial model of corneal birefringence. In particular the distribution of refractive index of a model cornea was plotted and it was predicted that two isotropes are symmetrically placed about the corneal centre where there was non-zero retardation. Contours of equal retardation became increasingly elliptic towards the corneal periphery. The experimental part of the study confirmed that the central corneal zones behave optically as a negative biaxial structure. However, the peripheral cornea, although also birefringent, does not behave in this way. As birefringence is determined by stromal structure, the implication is that the peripheral corneal stroma is structurally distinct from the central stroma.

The present chapter reviews the historical and current published corneal structural models and discusses their compatibility with the experimental data. Each model has its merits, but none fully accounts for the known properties of the cornea. A novel model of corneal structure is developed compatible with experimental data that is based on repeating units of similar geometric form.

13.1 Historical Review

The early work of His (1856) identified the lamellae as the principle birefringent components of the cornea and proposed that the lamellar distribution determined the birefringent behaviour of the cornea as a whole. The first comprehensive attempt to

relate observed birefringence to structure was that of Rollett (Rolett 1871 quoted in Stanworth and Naylor 1950) who assumed that the cornea behaved as a curved uniaxial crystal plate and proposed that the observed interference phenomena might result from a radial orientation of corneal lamellae. This model lacked anatomical support and did not consider the anatomical implications of convergent radial fibres at the corneal centre. A more feasible explanation for the characteristic biaxial-like interference pattern of the bovine cornea was proposed by Schiötz (Schiotz 1882). This comprises confocal elliptical fibre populations with decreasing ellipticity towards the periphery with superimposed arcuate fibres concentrated in the vertical and horizontal meridians (Figure 13.1). This model is discussed by Stanworth and Naylor (Stanworth and Naylor 1950) who concluded that it was inappropriate for human, cat, dog and rabbit cornea which they assumed had uniaxial behaviour.

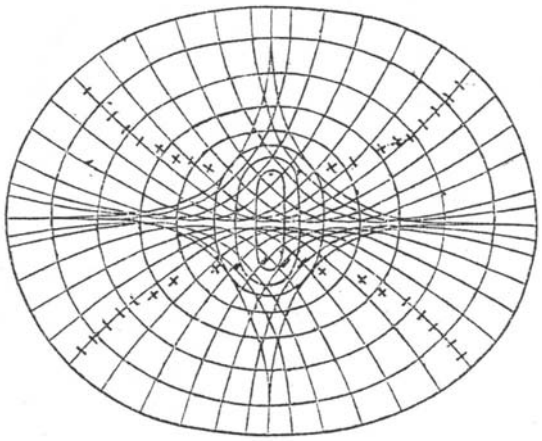

Figure 13.1 Schiötz model of lamellar distribution

Bovine eye (Schiotz 1882)

It was hypothesised by Stanworth and Naylor that a biaxial pattern for the human or other ‘uniaxial’ corneas might result from externally applied mechanical stress, surgically induced astigmatism or was the result of experimental artefact. It was noted however, that whatever the model of birefringence, it represented the summation of birefringence of many superimposed corneal lamellae. By analogy with similar phenomena in optical crystallography (and following the work of Valentin) Stanworth and Naylor described the corneal birefringence phenomena as isogyres and isochromatics. Furthermore, they proposed, the distributions of vibration direction for uniaxial and biaxial patterns of corneal birefringence (Figure 13.2).

The conclusion of Stanworth and Naylor (Stanworth and Naylor 1950; Stanworth and Naylor 1953) was that the human cornea exhibited uniaxial behaviour. Furthermore, they proposed that the cause of uniaxial behaviour was a random (i.e. structurally isotropic) distribution of overlapping optically anisotropic corneal lamellae. The overall effect of their model was for the intrinsic birefringence of individual lamella to cancel each other out.

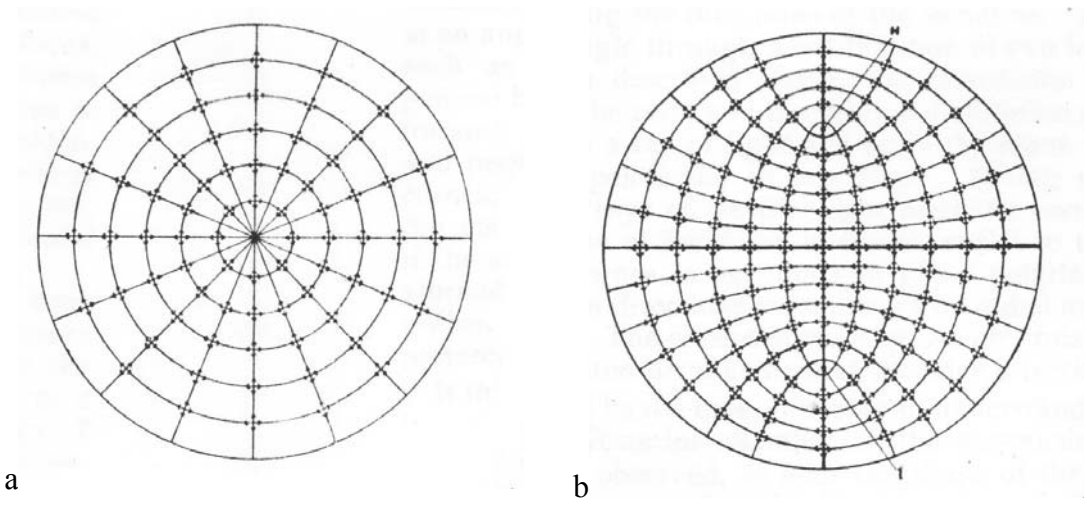

a b

Figure 13.2 Stanworth and Naylor's vibration directions. a uniaxial; b biaxial

(Stanworth and Naylor 1950)

A further radial/micelle model of cornea structure based on birefringence was proposed by Kikkawa (Kikkawa 1955), but lacked anatomical foundation. Both radial and random orientation models did not explain the finding that, in psychophysical experiments using Haidinger's brushes (Boehm 1940; Shute 1974), the central cornea behaved as a retarder. The slow direction was typically inclined in a superotemporal-inferonasal direction and magnitude of retardance was up to one eighth of a wavelength: a finding that was taken to imply a preferred orientation of central corneal lamellae (Shute 1974).

13.2 Current models

The current corneal structural models can be categorised into those based on x-ray scatter, theoretical models of stacked birefringent lamellae and the biaxial model as developed in the present study.

13.2.1 X-ray scatter models

X-ray scatter studies (see §2.2.3) suggest an orthogonal preference of vertical and horizontally disposed bundles on a 'background' of random orientations for central corneal regions, (Daxer and Fratzl 1997; Meek and Quantock 2001). In a recent review (Meek 2009) , Meek and Boote were sufficiently confident of their x-ray derived corneal structural model to state '... [their findings of a] *four-fold lobed intensity distribution,* [was] *indicative of collagen fibrils lying within two preferred orthogonal directions. This observation finally settled the argument about preferred lamellae directions in the cornea that had persisted since the work of Kokott (1938).*' This statement fails to take into account the birefringence data of many previous authors. The 'orthogonal preference' of the x-ray data implies equal dominance of vertical/horizontal bundles resulting in negation of birefringence and therefore, at most, uniaxial behaviour. The interpretations of x-ray data therefore offer no explanation of the consistent findings of the existence and orientation of the central corneal retardation: a conclusion acknowledged by the authors (Meek and Boote 2009).

The simplest interpretation of the central corneal retardation is that it is due to a preferential orientation of collagen bundles in a superotemporal to inferonasal direction following the slow axis of retardation. This does not exclude the possibility of an

orthogonal fibril configuration as hypothesised from x-ray data, but it requires one orthogonal population to have a greater retardation (e.g. a greater number of fibrils in that direction) allowing the superotemporal-inferonasal slow-axis of retardation to dominate. One x-ray study (Boote, Dennis et al. 2005) presents data that is compatible with such an orientation preference, although it is not developed further.

Data from x-ray studies of the corneal periphery (Aghamohammadzadeh, Newton et al. 2004) imply preferentially aligned collagen was shown in one cornea to follow a diamond-shaped contour. A later study modified this model to incorporate experimentally observed mirror symmetry between eyes (Boote, Hayes et al. 2006) and deformed the diamond-shaped distribution into a rhombus to explain the findings in one pair and 5 unpaired post mortem eyes. These data are compatible with the observed isochrome distribution and will be discussed in §13.3.3.

There are several possible explanations for the disagreement between retardation and x-ray data for the central cornea. Retardation/birefringence data has been substantiated many times by many different workers so can be accepted as repeatable. X-ray data is predominantly the output of one group examining a relatively small number of excised *ex vivo* corneas. A consistent finding of the birefringence studies, particularly with large subject numbers, is the variation in both the magnitude of retardation and slow-axis orientation between subjects. There are several reports of low or zero central corneal retardations (Knighton and Huang 2002; Weinreb, Bowd et al. 2002; Knighton, Huang et al. 2008). These are presumed to be due to either randomly orientated or horizontal / vertical orthogonal birefringent fibrils of equal dominance. It is possible that corneas with similar properties were used in the x-ray studies although one report (7 corneas) identifies variation in the proportion of horizontal vs. vertical orientations of

up to 25% (Boote, Dennis et al. 2005). Such variations are not incorporated into current x-ray-derived models of corneal structure (Meek 2009).

All x-ray studies are of cadaveric material under non-physiological conditions and subject to intense ionising radiation. Apart from imprecision of orientation, the cadaveric cornea is prone to histological artefacts even a short time after death thus suggesting caution when interpreting data. Furthermore there are no reports of the structural effect on the corneal tissue of the intense levels of x-irradiation necessary to observe scatter in measurable amounts.

Another unlikely possibility, and one that is contrary to the hypotheses associated with both birefringence and x-ray scatter, is that the structures causing birefringence and those detected by x-rays are different.

In the x-ray studies, all corneas were obtained from eye banks so it is implied that donor eyes were not specifically enucleated for the purpose of the study. Donor eyes are usually harvested in a mortuary and eye orientation is performed with unaided vision at the time of enucleation by placing a transconjunctival suture near the visually estimated upper (12 o'clock) point of the limbus. The suture is of finite width (typically 6/0 non-absorbable, diameter approx 0.1mm), the suture track is typically placed parallel to the limbus and is of the order of 1mm long. Suture placement is without microscopic control and even if microscopic suture placement were performed, the cadaveric eye position is most unlikely to represent the primary position in the living state. Thus caution must be exercised in interpreting the orientation of cadaveric corneas and errors of up to 20° of orientation might be expected i.e. errors consistent with the known azimuth of orientation above horizontal for central corneal birefringence recorded *in vivo*. Thus ocular orientation related x-ray data may be subject to error particularly

when claiming that there is horizontal/vertical preferred orientation. Their data supports an orthogonal structure, but not necessarily with a preferred horizontal/vertical orientation.

13.2.2 Stacked lamellar models

A large number of randomly orientated superimposed lamellae have a resultant retardation of zero for perpendicular light rays, but exhibit a uniaxial pattern with nonnormal incidence (§4.2.1). The total normal incidence retardance of two superimposed orthogonal birefringent lamellae, each of equal and small retardance, is zero. A non-zero retardance results from a stack of otherwise identical lamellae if one orientation predominates in which case the slow axis is aligned with the dominating orientation. Theoretical studies (Farrell, Wharam et al. 1999) demonstrate that statistical variations of a finite number of lamellae cause a non-zero retardation possibly with a biaxial-like pattern of birefringence (Farrell, Rouseff et al. 2005). Furthermore, these studies predict that the two optical axes converge to a single axis normal to the plane of the stacks (i.e. uniaxial behaviour) if two layers of the 2- or 3-layeres stack are orthogonally orientated with respect to their slow-axes. Extrapolation to 200 layers generated two non-normal optic axes, but could not be configured for uniaxial behaviour.

The predictions of these models are quantitatively different from observed phenomena and, in particular, predict a wide distribution of slow-axes unlike the observed superotemporal-inferonasal orientation (Knighton and Huang 2002). Apart from generation of optic axes, it was not stated if the models conformed to the biaxial/uniaxial pattern of non-normal refractive index/birefringence as discussed in

Chapter 3. Furthermore this model was not applied to a curved surface nor was it used to model retardation and isochrome behaviour.

13.2.3 Biaxial model

The current view that the central cornea approximates to a curved biaxial crystal allows a theoretical model of to be derived that defines the distribution of refractive indices (equirefringence contours), birefringence and retardation in an idealised cornea (Chapters 3 and 4). The derived confocal elliptic/hyperbolic equirefringence contours have similar patterns to elements of the structural models of Schiotz (1882) and Stanworth and Naylor (1950) (§13.1). Furthermore, a structural correlate of the predicted equirefringence contours is found experimentally in Chapter 8. It is hypothesised (§4.7) that the equirefringence contours (Figure 4.2, Figure 4.3) indicate the paths of positive uniaxial filamentous structural units such as collagen fibril bundles. In the corneal periphery, the biaxial model predicts elliptical isochromes but quadrangular isochromes are observed experimentally (Chapters 7 and 9). The predicted elliptic isochromes have their major axes aligned with the isotropes, but no correlation is found between the observed isotrope orientation and measurable isochrome parameters. The present study demonstrates that the observed isochrome pattern is due to regional changes in birefringence and not due to variations in corneal thickness (Chapter 10). Whilst the biaxial model can be transformed to generate quadrangular isochromes, the necessary manipulations result in a ‘cornea’ that cannot exist in reality (§11.2). The peripheral corneal retardation cannot therefore be explained by the biaxial model alone. A summary of the differences between the biaxial model and experimental findings is given in Table 13.1.

Table 13.1 Biaxial model vs. Experimental findings

Parameter	Biaxial model	Experimental findings	Agreement
Isotropes	present	present	yes
Number/alignment of isotropes	2 on optic plane equidistant from optic axis	2 aligned superotemporal/inferonasal approx equidistant from corneal apex	yes
Optical sign	yes: negative	yes: negative	yes
Isochromes	present	present	yes
Isochrome shape	elliptic	quadrangular	no
Alignment of isotropes relative to isochromes	optic plane on major axis of elliptic isochromes	no correlation between isotropes and isochrome extrema	no
Variability	constant for any particular crystalline material	great intersubject variability, midline mirror symmetry	no

13.3 Synthesis

The three categories of structural/optical model each explain some component of corneal retardation but no single model is wholly compatible with experimental observations. A new unified model is required which is compatible with known anatomy, accounts for all forms of anisotropy (optical, x-ray scatter, mechanical, thermal etc), and able to predict biomechanics. The model must be compatible with and preferably explain the following:

1) central retardation– preferred orientation of collagen fibrils
2) two isotropes – areas of zero retardation i.e. negation of birefringence of corneal lamellae (precise orthogonality/ random orientations)
3) quadrangular peripheral isochrome distribution – organized structure

13.3.1 Central retardation:

The central cornea behaves optically as a fixed retarder (c 60 nm; i.e. approximately $^{1}/_{10}$ wavelength at 560nm) with slow axis aligned with the centres of the isotropes (superotemporal/inferonasal at about 20° from horizontal). The currently accepted structural interpretation is of a preferential orientation of collagen in this region as supported by the stacked lamellar models. The x-ray data is interpreted by Meek et al (e.g. Meek 2009) as an orthogonal mesh in this region with vertical/ horizontal preference. Therefore, according to the stacked lamellar models, Meek's model would have zero retardation and, even if one fibril orientation dominated over the other the vertical/horizontal orientation would not be compatible with the experimentally

observed superotemporal/inferonasal orientation of retardation. Within the region of the corneal apex, the biaxial model reduces to a stacked lamellar model and is consistent with experimental data.

The experimental findings of the present study can be interpreted as evidence for the preferred orientation required for the central corneal birefringence. The results of Chapter 7 expanded in Chapter 8 identify populations of fibrillar structures of appropriate orientation for the observed central birefringence. The findings reported in Chapter 8 identify near linear orthogonal fibrillar structures between the foci/isotropes of the polarimetric image. The interfocal/isotrope angle of approximately 15° from horizontal superotemporal/inferonasal is in agreement with the range of the previously reported slow axis of central retardation. The horizontal fibrillar structures are more evident than the vertical thus suggesting that horizontal or near horizontal fibrils dominate in the central regions. Furthermore, the fibrillar structures are compatible with the x-ray data if it is assumed that the differences in dominance of the orthogonal fibrils is beyond the resolution of the x-ray techniques.

13.3.2 Isotropes

Paired areas of low/zero retardation (isotropes) are approximately symmetric about the corneal centre and aligned with the slow axis of central retardation i.e. the configuration has approximately 1-fold rotational symmetry about the central cornea. The birefringent components of the cornea in the isotropic areas are therefore orientated so as to negate retardation and must be structurally different from non-isochrome corneal areas. The stacked lamellar model accounts for the presence of isotropes, but is only relevant to flat lamellae and is not in quantitative agreement with experimental data.

The x-ray diffraction model requires two orthogonal fibril populations throughout the central corneal regions (2-fold rotational symmetry about the corneal centre) and therefore implies one isotrope along a normal to the corneal surface. The negative biaxial model, as developed in this study, accounts quantitatively for two isotropes at the spheroconic foci, the alignment of isotropes with the slow axis of central retardation, and the magnitude of central retardation. The required elliptic/hyperbolic configuration of birefringent fibrils is demonstrated experimentally in Chapter 8 where the isotropes occur at the hyperbolic/elliptic foci.

13.3.3 Isochromes

The biaxial model is applicable to central corneal regions and predicts the existence of circumferential and orthogonal radial refractile structures/fibrils in the peripheral/limbal cornea. Circumferentially orientated collagen bundles exist in the corneal periphery (Maurice 1988), but do not necessarily form a continuous band (See §2.2.3). Furthermore, Maurice suggests that fibrils could take a curved course between different, and possibly widely placed, positions on the limbus (scleral-anchored fibrils). X-ray scatter studies support the model of a circumcorneal annulus of collagen (Newton and Meek 1998) which is also compatible with the biaxial model as developed in Chapter 3. The presence of bands of fibrils of scleral origin and associated with the insertions of the four rectus muscles is supported by embryological evidence. During early development the collagen fibril bands that comprise the insertions of the muscles extend from the equator of the eye to the limbus where they merge with the developing sclerocornea. They reach their adult location 6 to 8mm behind the limbus only between the post-natal ages of 18 months and 2 years (Sevel 1986).

Corneal peripheral isochromes have a quadrangular pattern that does not conform to the elliptical pattern required by the biaxial model. The biaxial model is therefore not valid in the peripheral/limbal zones. The corneal stroma is known to be composed of a mesh of collagen fibrils parallel within bundles, but with bundles crossing at all orientations (see §2.2). Thus, in the corneal periphery, there is a superposition of presumed annular, or at least pseudoannular, and non-annular collagen bundles each with its own birefringence. The observed birefringence is the sum of all birefringent elements (e.g. §4.2.1 and Maurice (1988)). The isochrome 'maxima' (Chapters 7 and 9) in the horizontal and off-vertical positions represent birefringence minima and conversely the positions of isochromes closest to the pupil centre are birefringence maxima. A possible structural explanation for where the peripheral corneal birefringence is relatively low (the isochrome 'maxima') is that there is a greater amount of orthogonal collagen bundle crossing and hence subtraction of birefringence (e.g. Eq. 5.7) in accordance with the findings of Farrell, Wharam et al. (1999). Conversely there is less orthogonality in the isochrome 'minima' where birefringence is higher. In other words there is greater orthogonality of collagen fibrils in the horizontal and off-vertical meridians of the peripheral cornea. This explanation is supported by the work of Aghamohammadzadeh, Newton et al. (2004) using X-ray scatter to map collagen distribution in the human cornea and limbus *ex vivo*.

X-ray scatter from preferentially aligned collagen was shown in one cornea to follow a diamond-shaped contour similar to the distribution of isochromes demonstrated in this study. It was concluded that populations of 'anchoring' lamellae (a term first used by Maurice (1988)) enter the limbus from the sclera and arc within the peripheral cornea between adjacent principle (superior, nasal, inferior, temporal) meridians to form a

diamond-shaped configuration. The meridional concentration of collagen bands are thought to originate from the insertions of the rectus muscles which is in keeping with known embryology and the pioneering work of Kokott (1938) who related this configuration to mechanical functions such as eye movement. A later study modified this model to incorporate experimentally observed mirror symmetry between eyes (Boote, Hayes et al. 2006) and deformed the diamond-shaped distribution into a rhombus to explain the findings in one pair and 5 unpaired post mortem eyes (Figure 2.4). Such symmetry is also observed in the isochromes of the present study. The similarity between patterns of peripheral orientated collagen predicted by x-ray scatter study and isochromes is demonstrated in Figure 13.3.

The collagen fibrils associated with the insertions of the rectus muscles are thought to advance into the peripheral cornea in keeping with the known embryology of the region. The fibres enter the limbus orthogonal to the circumcorneal annulus thereby cancelling the birefringence of an underlying biaxial pattern to produce isochrome maxima.

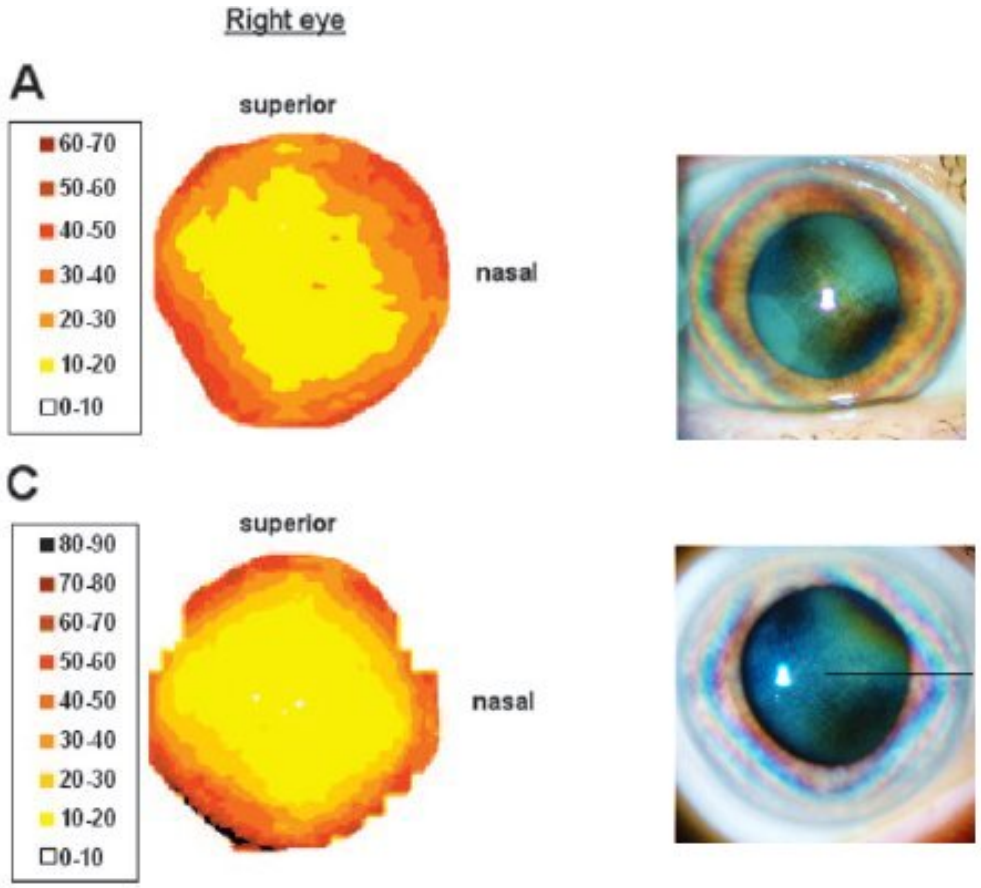

Figure 13.3 Comparison of aligned collagen scatter maps with isochromes

X-ray scatter maps from Boote Figure 6 (Boote, Hayes et al. 2006) ; colour scale is scatter expressed in arbitrary units. Isochromes (right eyes) of subjects IK16 (upper right) and IK24 (lower right). Note similarity in distribution of isochromes with scatter contours. See text for discussion.

13.4 The spherical elliptic model of corneal structure

From the previous discussion, it is hypothesised that the basis for the observed corneal birefringence is an organization of birefringent elements with a basic geometry derived from the negative biaxial birefringence model. The model is modified towards the corneal periphery with arcuate elements aligned with the horizontal and vertical meridians.

The fundamental structural/birefringent unit of the corneal stroma is the collagen fibril bundle ('lamella') which has positive uniaxial birefringence (i.e. length slow) due to both intrinsic crystalline and form birefringence (§4.2.1.). The pattern of corneal birefringence results from a summation of the fibril bundle orientations throughout the whole corneal thickness (Maurice 1988). Large proportions of bundles are randomly orientated, but with a superimposed directional component.

A common feature identified in both the theoretical and experimental findings of the present study is the existence of collagenous bands/ribbons/ arcs / lamellae which are described in terms of part or complete spherical elliptic structures. It is proposed that the basic structural unit of the corneal stroma is a spherical-elliptical band of optically positive biaxial birefringent elements either wholly or partly within the corneal stroma.

The stroma consists of an overlapping meshwork of the spherical elliptical structural units which need not all be confocal nor concentric, but are of varying ellipticities. Some units are regularly arranged within central corneal regions where they form the confocal elliptic/hyperbolic configurations identified in Chapter 8 and hence exhibit biaxial-like behaviour. Complete confocal spherical ellipses with progressively

increasing ellipticity form the x-ellipse populations. Sections of orthogonal spherical ellipses (z-ellipses, see §4.3) pass from limbus-to-limbus, but are confocal with the x-ellipse systems. The configuration of populations of confocal spherical elliptic units results in a central orientation preference, isotropes and the circumcorneal annulus. Additional non-confocal (or confocal about a different locus from the central bands) and purely peripheral spherical elliptic arcuate bands related to the insertions of the extraocular muscles curve through the peripheral/limbal corneal zones. The variation in density and crossing angles of the superimposed bands account for the observed distribution of isochromes: there being a greater density of scleral origin associated with the insertions of the rectus muscles. This greater orthogonality in the vertical and horizontal meridians explains the relatively low retardations compared to intermediate positions on the corneal circumference thereby accounting for the observed isochrome maxima and minima.

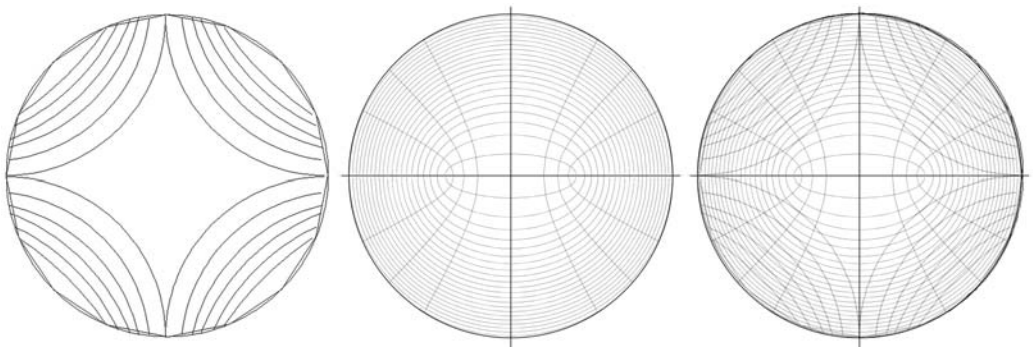

a b c

Figure 13.4 The spherical elliptic model of corneal stromal organization

a) peripheral arcuate fibrils associated with the insertions of the extraocular muscles as inferred from x-ray data; b) confocal conic (spherical elliptic) fibrils as inferred from biaxial model; c) composite of a and b.

Figure 13.4 (a) represents the peripheral extraocular muscle (EOM)-related fibrils similar to those hypothesised from both isochrome and x-ray data (Newton and Meek

1998; Boote, Hayes et al. 2006), Figure 13.4(b) represents the confocal conic/spherical elliptic central fibrils and Figure 13.4(c) is a composite of the two.

A more realistic model takes into consideration the lower order symmetry of the isochromes and the oblique superonasal-inferotemporal inclination of the major axes of the central ellipses. This variant of the simple model is presented in Figure 13.5 which represents a typical right eye.

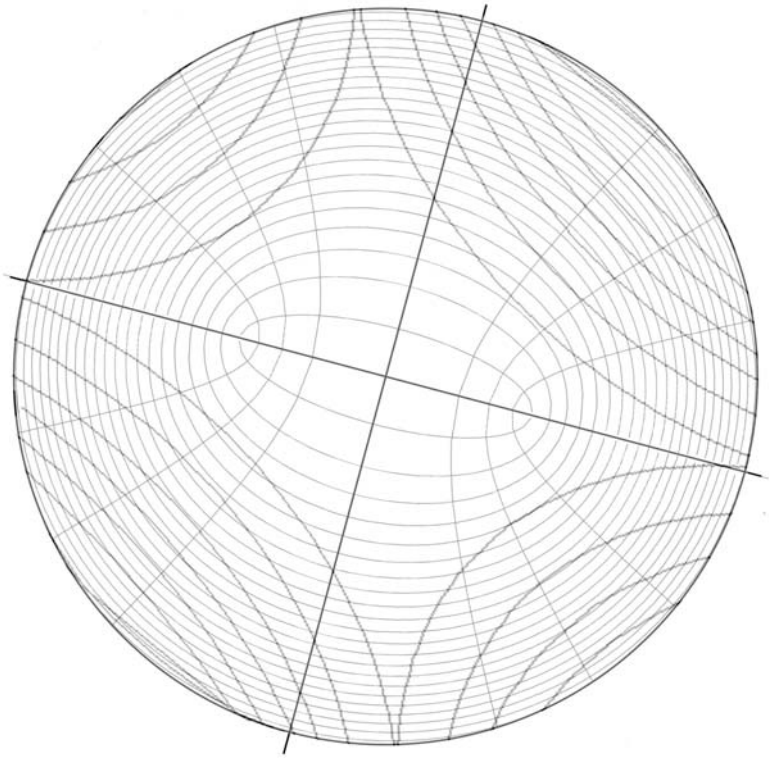

Figure 13.5 Transformed spherical elliptic model of corneal stromal structure

Model as in Figure 13.4 but transformed to include non-radially symmetric peripheral EOM-related fibre arcs and superotemporal-inferonasal inclination of ellipse major axes. (right eye)

13.4.1 Composite structures

Three possible configurations of collagen bundles might account for the proposed fundamental spherical elliptic birefringent units.

The first and simplest is that the collagen bundles of the stromal lamellae directly form the spherical elliptic units. That this is an oversimplification is suggested in the uniaxial case and outlined in §2.2.3, Figure 2.4. The findings of Radner and Mallinger (2002) indicate that there is interlacing between lamellae. This raises the possibility that the apparent biaxial behaviour of the whole cornea result from summation of the birefringence of composite collagenous assemblies rather than from the distribution of discrete collagenous bands. The individual bands do not necessarily conform to spheroconic geometry, but the composite effect of interlaced bundles/lamellae results in the observed birefringence: this argument (Radner, Zehetmayer et al. 1998) has been used to explain the apparent circular disposition of fibrils towards the limbus (circumlimbal annulus) (Maurice 1988; Newton and Meek 1998). The assembly of collagen fibrils necessary to produce the required spheroconic/spherical elliptic structures may therefore be equivalent to the parabolic segments (conic arcs = Bézier curves, See §15.7) created by plotting a curve through adjacent intersections of sequential line segments (repeated linear interpolation) as illustrated in Figure 13.6.

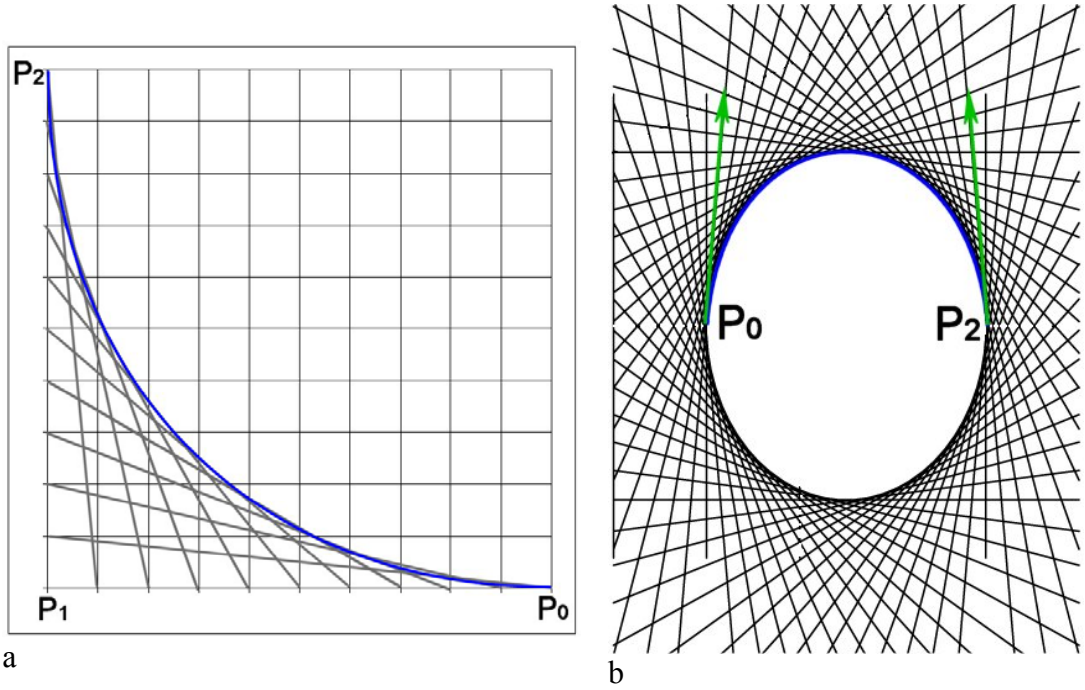

Figure 13.6 Bézier curves

Quadratic (second-order) Bézier curves (blue) defined by control points P_0, P_1, P_2 (a) P_0P_1 and P_1P_2 are orthogonal; (b) P_0P_1 and P_1P_2 (green arrowed lines) are at an acute angle with P_1 out of range of page. Construction lines demonstrate generation of elliptic curve comprising two quadratic Bézier curves (see §15.7). Note that in both cases, the Bézier curve results from repeated linear interpolation.

A third possibility relates to the fact that lamellae are formed of repeated elements, typically running parallel, and overlay adjacent lamellae at varying angles up to orthogonal. These conditions are appropriate for the moiré phenomenon (e.g. Amidror 2009) in which the superposition of repeated geometric elements results in patterns that can vary from a magnified version of the original elements or a pattern bearing no resemblance to them as demonstrated in Figure 13.7. The resultant pattern depends on the parameters of period, orientation and shape of the generating elements.

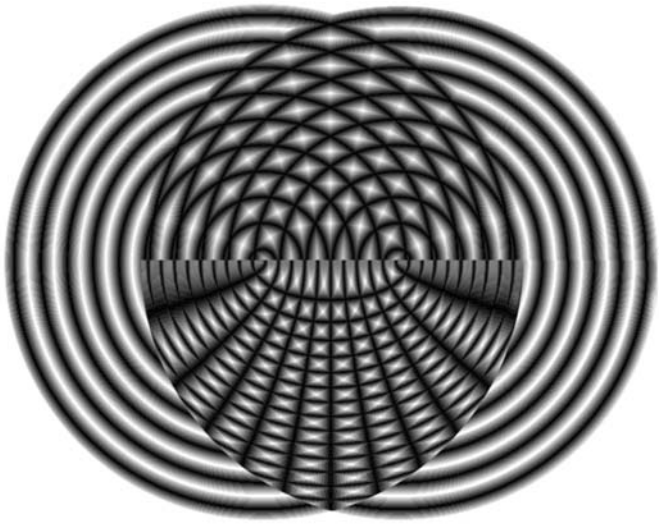

Figure 13.7 Hyperbolic and elliptic moiré fringes

Fringes generated by intersection of concentric circles with cosinusoidal intensity profiles. Multiplicative (upper half) and difference (lower half) superposition. For further details see text and Amidror (2009).

The three possible assemblies (discrete orientated fibril bands, fibril composite Bézier curves, moiré due to fibril mesh superposition) are not mutually exclusive bearing in mind the known characteristics of collagen bundles/lamellae and the multilaminar nature of the corneal stroma.

Whatever the nature of the fibrillar organization, the composite result of that organization is the formation of the spherical elliptic structural units necessary to produce the retardation patterns observed in the cornea. The close link between birefringence and mechanical properties is well known (§2.3) so it is further proposed that spherical elliptic geometry also underlies the mechanical properties of the cornea as a whole.

13.5 Discussion

It was stated by Meek and Boote (2009) that the model presented here and previously published (Misson 2007; Misson 2010) is incompatible with the x-ray findings. The present study demonstrates the opposite: the orthogonal elliptic/hyperbolic fibre pattern predicted theoretically (Chapter 3; Misson 2010) and identified experimentally (Chapters 7, 8; Misson, Timmerman et al. 2007) is compatible with the x-ray data for central corneal regions.

It is proposed that the central orthogonal spherical elliptic fibril populations of the present study are the 'vertical and horizontal' fibrils identified by x-ray scatter. The x-ray technique, or its application, has insufficient precision to accurately orientate the fibrils in space or to determine the dominance of one fibril population over the other. The spherical elliptic fibres become more circular as they near the corneal periphery. This is compatible with histological (Kokott 1938), electron microscopic (Radner, Zehetmayer et al. 1998) and x-ray scatter investigations which identify a circumcorneal annulus of collagen fibrils at the limbus (Newton and Meek 1998).

Meek and Boote (2004) have questioned how the central orthogonal fibrils might integrate with peripheral circumferential fibrils. This is answered in the present study by the observed centrifugal progression of fibril pattern from near linear in the central cornea, elliptic in the intermediate zones and circular in the corneal periphery. The less dense hyperbolic (z-ellipse) populations cross the elliptic (x-ellipse) fibril structures at or nearly at right angles, cross the limbus as radial fibrils and continue into the sclera. At all times the x-elliptic structures dominate the hyperbolic z-elliptic thereby giving rise to the observed pattern of birefringence. The superposition of orthogonal

populations of structural elements may account for the x-ray scatter observations of some populations of fibrils apparently abruptly changing direction just before the limbus (Meek and Boote 2004). Furthermore, the spherical elliptic model proposed in this study has been supported by visually demonstrable and appropriately orientated stromal fibril alignments (Chapter 8). Whilst the biaxial model appears to break down towards the limbus, the model proposed in the present study offers an explanation in terms of bundles of scleral origin overlapping a basic biaxial pattern.

Integration of peripheral fibrils into the circumcorneal annulus is therefore implicit in the spherical elliptic model. In contrast this requires the contrivance of acute changes in fibril direction for the x-ray derived model.

The spherical elliptic model accounts for the peripheral increase in corneal thickness as increasing numbers of confocal concentric spherical elliptic bands augmented with scleral-anchored arcs. Finally, the x-ray derived model requires different populations of fibrils with varying geometry whereas the spheroconic and biaxial models, as detailed in the present study, require a single geometric construct, the spherical ellipse, as the unit from which the whole stromal structure can be derived.

The spherical elliptic model is compared to three other structural/optical models in Table 13.2. The uniaxial and biaxial models are as previously described (§13.1). The most recent model derived from x-ray data (Meek 2009) incorporates peripheral extraocular muscle ‘anchoring’ fibrils.

Table 13.2 Comparison of corneal models

√ = agree; × = disagree

	Model			
	uniaxial	biaxial	Meek	Misson
Compatible with existence central retardance	×	√	×	√
Compatible with orientation of central retardance	×	√	×	√
Compatible with biaxial model	×	√	×	√
Orthogonal lamellae	×	√	√	√
Preferred orientation	×	√	√	√
Mirror symmetry	√	√	√	√
Compatible with isochrome distribution	×	×	√	√
Compatible with EOM-related asymmetry	×	×	√	√
Fibre integration into 'circumcorneal annulus'	√	√	√ (complex)	√ (implicit)
Supporting evidence for preferred orientations	×	√ (central zones)	×	√ (central zones)
Compatible with increasing peripheral corneal thickness	√ (implicit)	√ (implicit)	√ (assumes sclera-anchored fibrils)	√ (implicit)
Geometric units	circumferential or random	spherical elliptic	multiple undefined arcs	spherical elliptic

13.6 Chapter Summary

1) The biaxial model is compatible with published experimental data of central corneal retardation and the presence of isotropes.
2) The fibrillar structures identified in Chapter 8 are the necessary configuration to account for the biaxial patterns observed experimentally.
3) The biaxial model/behaviour cannot be explained by the current x-ray derived structural models.
4) Resolution and interpretation of the x-ray data is questioned.
5) The quadrangular isochromes are similar to x-ray findings interpreted as representing peripheral arcuate fibres.
6) The biaxial model and quadrangular isochromes are not necessarily mutually exclusive.
7) A model of corneal structure is proposed that is composed of spherical elliptic structural units.
8) The central stromal structure comprises confocal orthogonal spherical elliptic structure conforming to the geometry of equirefringence contours of the biaxial model.
9) The peripheral stroma comprises
    a. circumferential elements that belong to the same population as the central spherical ellipses
    b. overlapping spherical elliptic arcs passing from limbus-to-limbus into the peripheral stroma. The limbal components are concentrated in the meridians of the insertions of the rectus muscles.

10) The shape of peripheral isochromes is determined by the degree of orthogonality of the two overlapping peripheral spherical elliptic populations.
11) All structural models must be compatible with the symmetries implied in the biaxial model.
12) The spherical elliptic structures may be composites of fibrils the path of each not necessarily conforming to the spherical elliptic geometry.

14 Summary, Implications and Future Study

This chapter summarises the principle findings of this study. Implications and areas for future study are discussed with respect to EPB and the spherical elliptic model. Additional areas of further study are listed in Appendix §15.8

The results of the study can be summarised as:

1) The development and interpretation of a theoretical model of negative biaxial birefringence relating to the cornea. A confocal orthogonal spherical elliptic pattern of refractive indices and characteristic patterns of vibration direction and birefringence are predicted.
2) The development of the technique of elliptic polarization biomicroscopy (EPB) for the *in vivo* determination of corneal retardation and visualisation of birefringent fine-structure. The principle results of the application of EPB to the living human cornea are:
    a. The large-scale retardation properties: the central cornea behaves as expected of a biaxial structure as previously predicted, but the peripheral cornea does not.
    b. At a smaller scale, EPB reveals fibrillar structures within the central cornea compatible with the geometry predicted from the theoretical analysis of the biaxial model.
3) The development of a novel model of corneal stromal structure that is based on both birefringence theory and *in vivo* measurement. The model is constructed

from spherical elliptic units. It accounts for phenomena observed in both central and peripheral birefringence as well as the x-ray measurements.

14.1 EPB and its interpretation

The technique of elliptic polarization biomicroscopy is readily implemented and interpreted by a simple adaptation of existing equipment. Results may be used for qualitative purposes or quantified for detailed study. The ease of both application and interpretation allows EPB to be used in the clinical setting.

14.1.1 EPB technique

The EPB technique is based on back reflection through the birefringent cornea of initially elliptically polarized light generated by a linear polarizer and fixed retarder. The combined effect of reflection from intraocular structures and double pass through the cornea results in a change in the ellipticity of emergent polarized light. This is resolved by a second-pass through the retarder-polarizer combination into an interference colour that relates to the magnitude and orientation of retardation for a given point on the cornea.

EPB as developed in the present study can be applied *in vivo*. It is essentially qualitative with the potential for quantification of image data.

The use of polychromatic light (§5.3) overcomes some of the difficulties in phase stepping techniques (e.g. processing of multiple images, software-based data manipulation including phase unwrapping, §5.1.1). Chromatic analysis of interference patterns allows for quantitative determination of magnitude of retardation.

14.1.2 EPB results, interpretation and application

EBP reveals visible patterns of retardation in individual corneas *in vivo*. The observed patterns of retardation are two isotropes, a non-zero central corneal retardation, and coloured fringes of equal retardation (isochromes). At higher magnifications EPB reveals a fibrillar fine structure in non-limbal areas. It is proposed that the origins of the patterns are due to a specific arrangement of birefringent fibrillar elements.

Findings using second-harmonic generation microscopy (Stoller, Reiser et al. 2002) confirm the small-scale organization of collagen fibrils in the porcine eye (Teng, Tan et al. 2006), a concentric orientation of stromal collagen in the GFP mouse (Lo, Teng et al. 2006) and structural differences between the anterior and posterior stroma in mouse, rabbit and human corneas (Morishige, Petroll et al. 2006). Whilst this is a promising technique, it has yet to be applied to the human eye *in vivo*.

The current study has not determined the depth variation of the observed phenomena. x-ray scatter studies of microkeratome / femtosecond laser cut sections of cornea have shown (Abahussin, Hayes et al. 2009; Winkler, Chai et al. 2011) depth variation of scatter patterns suggesting structural differences in different layers of the stroma. The technique developed in the thesis could be used to examine retardation is such specimens to complement the x-ray data, and identify planar variations in structure as well as linear depth-related changes.

Relating the measurable retardation to the fundamental physical property of birefringence requires quantification of path distance of light rays transmitted through the cornea. The present study uses an approximate mathematical model which makes

assumptions about corneal surface geometry, thickness variation, and refractive index. Improvements can be made by using patient-specific measurements e.g. corneal thickness as obtained by the Pentacam or other techniques such as OCT.

14.2 The unified model of corneal structure

The proposed unified model consists of two populations of spherical elliptic structural units. The first population comprises complete spherical elliptic units concentric about the geometric corneal centre and confocal about the loci of the optic axes. The second population comprises spherical elliptic arcs extending limbus-to-limbus and entering the peripheral cornea where they over lap the circumferential units. The arcuate units are concentrated in the horizontal and vertical meridians possibly in association with the insertions of the rectus muscles.

The present study predicts differences in density and/or orientation of collagen in different regions of the corneal stroma. Such changes should be detectable with conventional histological techniques utilising 3-D image reconstruction and/or morphometric analysis. Furthermore techniques of lamellar keratectomy (e.g. using an applanating microkeratome, femtosecond laser) developed for corneorefractive laser surgery may be adapted for such anatomical investigations.

Optical verification may be possible with OCT based techniques (§5.1.1) but, as with the anatomical techniques, requires 3-D reconstruction and large area surveys.

Two related anatomical phenomena have been previously unexplained: the observation that no collagen terminations are evident in the stroma (Bron, Tripathi et al. 1997) (fibrils are either in) and increase in thickness of stroma from centre to periphery without an apparent change in stromal morphology (Ruberti, Sinha Roy et al. 2011).

Both may be explained by the spherical elliptic model. The absence of terminations arises as bundles are organized as continuous bands or form arcs originate from the sclera. The increase in peripheral thickness results from the increasing number of peripheral spherical elliptic units with decreasing ellipticity towards the periphery.

The work of Kokott (1938) demonstrated both radially and circumferentially orientated collagen fibrils. The presence of a circumcorneal annulus, implicit in the biaxial model, has anatomical support (Tripathi and Tripathi 1984; Maurice 1988; Radner, Zehetmayer et al. 1998) although the 'reinforcing' fibres associated with the rectus muscles have not been identified anatomically.

Models incorporating the circumcorneal annulus and the fibrillar model derived from x-ray data (Pinsky, van der Heide et al. 2005; Li and Tighe 2006; Pandolfi and Manganiello 2006) have been proposed. There is no adequate biomechanical model of the cornea as highlighted by Ruberti, Sinha Roy et al. (2011) who conclude that more experimentally-derived structural data is required. The incorporation of the spherical elliptic geometry as described in the present study requires investigation. Furthermore, any proposed biomechanical model should be compatible with the anisotropies implied by the spherical elliptical model and the observed optical anisotropy.

14.3 Clinical application

The technique of EPB has potential as a clinical diagnostic tool. The spherical elliptic model furthers the understanding of the rationale, methods, outcomes and optimization of both clinical diagnosis and treatments.

14.3.1 EPB as a diagnostic instrument

The present study shows how EPB reveals novel structural features of corneal stromal anatomy. Preliminary clinical findings of EPB are presented in Chapter 12 in corneas where stromal structure is disrupted by disease, trauma or surgical intervention. Results show features that are invisible by conventional examination techniques such as corneal scars (§12.1.1.2, §12.1.2). The abnormal retardation patterns following laser corneorefractive surgery are clearly defined and present in all cases of PRK and LASIK examined (§12.1.2.2). Cases of keratoconus are sometimes difficult to diagnose with conventional methods. Using EPB, keratoconus cases (§12.1.1.3) showed distortion of isochromes in keeping with the distorted cornea and a band of low/zero retardation connecting isotropes. These preliminary findings require further study particularly with respect to the mechanisms and clinical significance of observed changes.

A further application of EPB is as a screening method for identifying patients who have had prior corneorefractive surgery, but may not volunteer this information. This has significant implications in cataract surgery where previous corneorefractive surgery significantly influences the accuracy of pre-operative biometric investigations necessary for the correct choice of intraocular lens implant (Lee, Qazi et al. 2008).

Additional clinical use may be in the diagnosis of corneal dystrophies, some of which are known to cause changes in the birefringent properties of the cornea at least in histological preparations (e.g. lattice corneal dystrophy).

14.3.2 Understanding biomechanical pathology: Keratoconus and iatrogenic ectasia

Keratoconus and iatrogenic corneal ectasia are two disorders of biomechanics leading to progressive corneal distortion due to a weakened stroma.

Keratoconus is a relatively common disorder resulting in a characteristic cone-like distortion of corneal topography with consequent irregular astigmatism. Keratoconus has been shown in this study to cause abnormal retardation patterns (§14.3, §12.1.1.3). Most cases are treated with contact lenses, but some require more invasive treatments such as deep lamellar or penetrating keratoplasty, intrastromal ring implants or the relatively new treatment of chemical collagen cross-linking. The characteristic histological features in advanced cases are central corneal thinning, and loss and disorganization of lamellae as mirrored by x-ray diffraction studies (Daxer and Fratzl 1997; Meek, Tuft et al. 2005). Early cases are difficult to detect and no detailed structural information using conventional *ex vivo* methods is available due to the scarcity of material. The current view of pathogenesis is that there is a physico-chemical structural defect allowing degeneration (Kenney, Brown et al. 2000) or slippage (Frank, 1976) of collagen bundles or a combination of both (Daxer and Fratzl 1997) under the effect of the intraocular pressure. The characteristic deformation results from mechanical failure of the stroma: the stromal structure is therefore key to the development, progression and clinical features of the disorder.

Surgically-induced (iatrogenic) corneal ectasia is progressive thinning and steepening of the cornea following refractive surgery. It is rare and is thought to occur as a consequence of mechanical decompensation following over-treatment of a pre-existing thin cornea or inadvertent treatment of previously undiagnosed keratoconus. Pre-

operative detection of at-risk corneas is imprecise and a method for such detection is required.

The keratoconic and ectatic cornea remains transparent until late stages of progression suggesting that the pathophysiology occurs at a scale greater than that of the transparency mechanisms i.e. at the level of the stromal bands/lamellae. Thus the cornea may remain birefringent but disruption of fibril bundles may alter its magnitude and pattern: this may be detectable as changes in retardation determined by EPB.

No useful models of keratoconus/corneal ectasia have yet been identified that explain all the features of the conditions including its prognosis. Incorporation of the findings of the present study regarding normal stromal architecture and the application of EPB require further investigation.

14.3.3 Biomechanical intervention: predicting surgery

Surgery in general may be defined as the deliberate infliction of trauma with the intention of a beneficial outcome. Undesirable and unintended outcomes are inevitable when complex biological systems are interfered with, so it is of great importance to be able to predict any adverse effects of well-intentioned interventions. Corneal surgery is no exception to the above general rule although, unlike many tissue systems, its physical parameters can be quantified.

14.3.3.1 Corneorefractive surgery

Various techniques have been devised to alter the surface curvature of the human cornea with the intention of correcting refractive errors. Controlled modification of corneal

curvature is achieved by selective ablation of the stroma, by altering mechanical forces within the stroma by carefully placed incisions, thermocoagulation or other controlled trauma. Other methods include integrating an exogenous refractive component (e.g. modified cadaveric stroma) to the host cornea (keratomelieusis) or implantation of plastic components into the stroma that have a direct effect on refraction (corneal inlay) or alter the shape of the central cornea (corneal stromal ring implant). Predicting the results of the procedure has been predominantly empirical although various biomechanical models have been proposed (Roberts 2000).

The inadequacy of biomechanical models has been outlined previously despite some incorporated published data of presumed collagen distribution (Pinsky, van der Heide et al. 2005; Li and Tighe 2006; Pandolfi and Manganiello 2006). No models, to date, have considered the correlation of mechanical anisotropy with biaxial optical anisotropy. Such considerations, including the concept of spherical elliptic corneal structural units, if incorporated into computational models, might well increase the accuracy of simulating the response of the cornea to real-world applications including surgery. Furthermore, these may advance the understanding of the later complications of keratoplasty and corneorefractive surgery such as post-operative astigmatism and ectasia. A pre- and post- treatment EPB measurement and documentation would provide a history of permanent laser-induced changes.

14.3.3.2 Surgically induced refractive errors and astigmatism

Radial incisions change central corneal curvature and were used extensively in the refractive surgical technique of radial keratotomy (see 12.2 and Fig 12.2.1). Whilst

empirical nomograms exist that relate incision parameters (e.g. depth and length) with induced astigmatism, the corrective effect is often imprecise.

Circumferential incision into the peripheral cornea/limbus results in flattening (i.e. increase in radius of curvature/ decrease in diopteric power) of the central cornea along the axis of the centre of the incision. This effect is used to reduce astigmatism particularly during cataract surgery (limbal/corneal relaxing incisions; astigmatic targeting). Conversely, cataract incisions into the peripheral cornea of previously non-astigmatic corneas may sometimes induce unacceptable degrees of central corneal astigmatism. Predicting those patients at risk is not yet possible but may be facilitated by EPB.

The amount of astigmatism induced by radial limbal (e.g. cataract) incisions may be meridian-dependent. Upper temporal incisions of right eyes are reported to induce less astigmatism than similar incisions in the upper nasal quadrant of left eyes (Altan-Yaycioglu, Pelit et al. 2007) although these findings are not supported in a similar but smaller study (Jacobs, Gaynes et al. 1999) and there is no difference between superior and temporal incisions (Oshika, Sugita et al. 2000). Such differences have been ascribed to meridional-dependent structural differences in the peripheral cornea and the known right-left structural enantiomorphism (Smolek, Klyce et al. 2002; Boote, Hayes et al. 2006). The relationship of incision site and induced astigmatism requires clarification.

Variations between individuals make general rules approximate, so information concerning the peripheral corneal structure in individual patients may be of value in incision planning. Isochrome distribution relates to the degree of orthogonality of superimposed fibrils, thus at the isochrome maxima (birefringence minima) radial fibrils

are at their highest concentration so circumferential incisions in these regions might be expected to have maximum effect on astigmatism. EPB may prove to be a simple method of identifying optimal sites of incision location e.g. to minimise post operative astigmatism. Correlation of the pre-operative EPB findings, particularly isochromes, with post-operative outcomes is therefore required.

14.3.3.3 Keratoplasty

The replacement of diseased corneal tissue with healthy cadaveric donor material (corneal grafting, keratoplasty) has been practiced for at least a century and remains a standard treatment for severely diseased or injured corneas. Apart from full thickness grafting (penetrating keratoplasty) numerous other related procedures have evolved such that currently the demand for donor material exceeds availability. The techniques themselves are subject to potential biomechanical-related complications such as mismatching of the biomechanical properties of the graft with the host bed resulting in astigmatism. Aligning donor to host was considered by the author in 1990 (Misson 1990) although the idea was independently published several years later (Rapuano, Dana et al. 1995; Meek and Newton 1999). The difficulty in aligning donor corneas with the host bed may now be overcome by using EPB.

An emerging problem for keratoplasty is integrity of donor corneas. In particular it is necessary to identify and discard donor corneas that have undergone corneorefractive surgery, have keratoconus or other occult pathology. Polariscopy, (including EPB, but also other methods described in Chapter 5) have potential use in screening of donor corneas for imperfections (see below §12.1.2.1) that might adversely affect surgical outcome.

14.3.3.4 Artificial corneas

There is a finite and limited supply of human cadaveric donor corneas suitable for transplantation. The scarcity of donor material and problems arising from rejection may be overcome by the development of artificial corneal prostheses. Synthetic collagen-based lamellar corneal replacements are being investigated (Ruberti, Sinha Roy et al. 2011), but their success depends on integration into the host which requires them to mimic or replicate natural corneal structure. Ideally the artificial cornea should replicate the optical and biomechanical properties of the natural cornea as closely as possible. Furthermore, prostheses must be biocompatible locally with the host bed and systemically with the host's immune system. Thus furthering the understanding of corneal structure such as presented in this study may contribute significantly to the development of corneal prosthetics.

14.3.4 Clinical polarimetry

The accuracy of scanning laser polarimetry and other retardation-sensitive techniques (§5.1.1) require adequate compensation of corneal retardation. For devices relying on light passing through a small area of corneal apex, a linear retarder of variable orientation and magnitude is sufficient and superior to a retarder of fixed magnitude and orientation. Greater accuracy of corneal compensation is required with off-axis measurements as inferred in the work of Knighton, Huang et al. (2008): this could be facilitated by the assumption of a biaxial model as detailed in Chapter 3.

15 Appendices

15.1 The Eye

The ability of living organisms to respond to light (light sensitivity) is widespread throughout all life forms, offers considerable survival advantage and has been a driving force in evolution. Only in the Animal Kingdom have light sensitive cells (photoreceptors) become organised into functional structures (organs) with spatial vision i.e. the ability to compare and make sense of the amount of light coming from different directions. The eye is the organ of spatial vision. Two broad categories of eye exist: single chamber and compound. Single chamber ('simple' or camera) eyes comprise a single focussing apparatus and a light-sensitive retina. Compound eyes are composed of multiple components (lenses or reflectors) focussing an image either onto a sentient structure specific for that lens/mirror facet (apposition compound eye) or a continuous retina receiving input from numerous adjacent focussing facets (superposition compound eye). Eight, or possibly nine, basic designs of eye (four compound, 4 or 5 single-chamber) have evolved independently and probably on many occasions since the Cambrian 'explosion' of life forms approximately 530 million years ago (Land, 1981; Wagner, 2009). One type, the terrestrial single chamber corneal lens eye of vertebrates (animals with backbones) and specifically the human eye (which is a typical terrestrial vertebrate eye), is the subject of the present study.

Life began in the sea and terrestrial vertebrates evolved from aquatic vertebrates. The single chamber aquatic vertebrate (e.g. fish) eye is a roughly spherical structure

comprising a tough opaque white outer coat (the sclera) with is specialised in one part to form a transparent window (cornea) with an overall refractive index similar to the adjacent sea water. The sclerocorneal envelope protects the internal structures that are precisely arranged to produce a real inverted image on the light sensitive retina diametrically opposite the cornea (Figure 15.1a). The principle refracting component, the crystalline lens, is an almost spherical structure composed of transparent protein that acts as a gradient-index lens suspended within a fluid/gel-filled chamber precisely at its focal point from the retina. As vertebrates evolved from an aquatic to a terrestrial environment, the water-cornea interface changed to the air-tear-cornea interface thereby requiring a change in ocular optics. In order to see on land the eye would have to increase significantly in length, the lens increase in power or the cornea-tear-air interface evolve refractive properties. In most terrestrial vertebrate eyes the cornea has evolved a precise curvature that, together with the lens, acts as a positive double-lens system that forms a real image on a sentient retina.

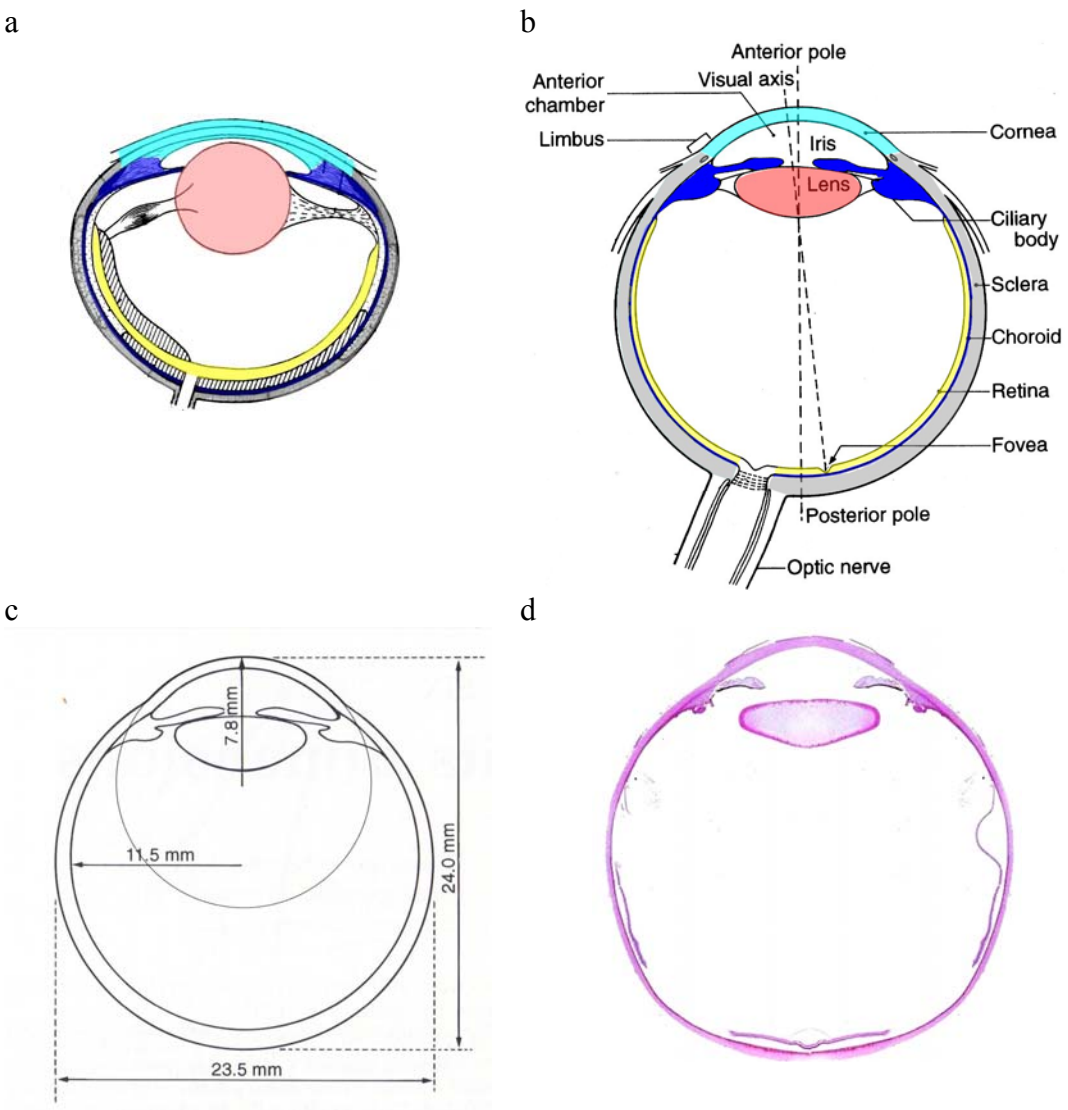

Figure 15.1 The Eye

(a) A typical aquatic (trout) eye. Principle structures are cornea (light blue), sclera (grey), choroid (dark blue), retina (yellow). (b) A typical terrestrial eye (human). (c) Approximate geometry and dimensions of the human eye. (d) Transverse histological section through human eye x1.5 (haematoxylin & eosin preparation). (a) (b) and (c) adapted from Duke-Elder (1958) and Bron, Tripathi et al. (1997).

The human eyeball or globe (Figure 15.1 b, c and d) is not spherical but approximates, at the macroscopic level, to two fused modified spheres. The smaller (radius 7.8mm) anteriorly (front) forms the cornea and is fused to the larger posterior (back) sphere (radius 12mm) of the sclera at a junction knows as the limbus (Figure 15.1b). A typical eye has an anteroposterior (front to back) dimension ('length') of about 24mm, and has

vertical and horizontal diameters respectively or 23mm and 23.5 mm (all ocular dimensions henceforth will refer to an 'average' eye and are taken from Bron, et al (1997) and Bron, Tripathi et al. (1997) which is also the principle source for this summary). The corneoscleral envelope forms the tough inelastic outer layer and completely encloses the uvea, the highly vascular second layer. The uvea is specialised from anterior to posterior into the iris, ciliary body and choroid. The iris is a muscular diaphragm with a central perforation (pupil) that both regulates light entry into the eye and acts as an aperture stop to change depth of focus. The ciliary body contains muscles which act via collagenous tendons to change the shape of the crystalline lens. The ciliary body also actively secretes the aqueous humour, a watery fluid that generates a constant hydrostatic pressure within the eye (intraocular pressure) thereby maintaining its rigid structure including the optically precise corneal curvature. The choroid is a layer rich in blood vessels and lies between the sclera and retina, the third layer of the eye. The retina is a highly complex neural tissue derived embryologically from the brain to which it is connected by the optic nerve. It contains populations of light sensitive cells (photoreceptors) that are sensitive to different wavelengths (cone photoreceptors) but also to low levels of illumination (rod photoreceptors). The retina contains a complex network of nerve cells (neurons) that process visual information generated by the photoreceptors and then encodes it into a binary frequency modulated signal for transmission to the brain via the optic nerve. The optic nerve contains approximately 1.2 million nerve fibres which exit the eye through the retina and channels in the sclera at the optic nerve head. In humans the retina is specialised at the optical focal point into the macula lutea (yellow spot) so called because of the yellow pigment lutein present within nerve fibres radially arranged around the fovea, a

depression at the centre of the macula. The macula is an area of high cone density and has the high spatial resolution which determines central visual acuity. The lens is a biconvex transparent structure suspended from the ciliary body by suspensory ligaments (zonule) and centred behind the pupil. The lens is a living structure and continues to grow throughout life with a typical adult thickness of 5mm and a diameter of 10mm. It is composed of fibre-like cells with a high concentration of transparent proteins (crystallins) that are flexible and have high refractive indices. The front and back curvatures are aspheric with approximate central curvatures respectively 9 – 10mm and 5.5 – 6mm. As in the aquatic eye, the refractive index varies throughout the lens which is a gradient index optical system. The lens divides the eye anatomically into two segments. The anterior segment comprises all structure anterior to the anterior surfaces of the lens and zonule and containing aqueous humour. The posterior segment contains all structures posterior to the posterior surfaces of the lens and zonule and comprises a cavity (vitreous cavity) lined by the retina. The vitreous cavity is filled with the vitreous humour (vitreous) which forms over two thirds of the ocular volume. The vitreous is a composite inanimate material comprising a hydrated gel (98% water derived from the aqueous) containing hyaluronic acid into which is embedded a loose meshwork of fine collagen fibrils. In man, eyes are paired forward-looking structures enclosed and protected by the orbits (eye-sockets) of the skull. Each eye is capable of a wide range of directional movement resulting from the action of six muscles with their origins in the bony orbit and insertions into the sclera. The position and coordinated action of the extraocular muscles allows for stereoscopic vision. The human eye is sensitive over a wide range of light intensities, is contrast-sensitive, has high resolution and is wavelength sensitive: it is also sensitive to polarization.

15.2 Geometric models: corneal topography and peripheral thickness

15.2.1 Mathematical models of corneal shape

An accurate model of the shape of the entire cornea has yet to be developed although there exist useful geometric models of curvature for the optically important central zones.

Figure 15.2 Simple models of corneal curvature

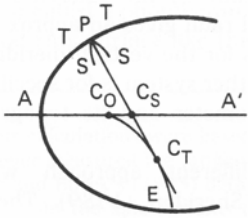

Elliptic profile of an astigmatic cornea. From (Rabbetts 1998)

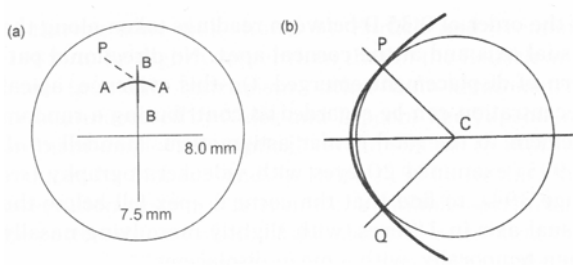

Frontal (observer's view of a toric cornea with central radii of 8.00mm along 180 deg and 7.50mm along 90 deg. At point p the sagittal (axial) curvature is AA' and tangential (continuous) curvature is BB'.
Cross section through spherical and ellipsoidal surfaces touching at P and Q with common normal PC and QC. The radius of the sphere is the sagittal radius at P and Q of the ellipsoid

At its simplest the corneal profile in any meridian is assumed to be a conic section with the curvature varying continuously from the centre outwards. More specifically, we assume an elliptical profile so a revolution about its axis of symmetry from vertex (apex) A to a point A' (Figure 15.2) results in an ellipsoid. The centre of curvature of the surface at A is Co and the distance ACo is the vertex radius ro. The curve Co E is one branch of the evolute of the ellipse i.e. the locus of all centres of curvature of the surface or, equivalently, the envelope of the normals to the curve. All normals meet the evolute tangentially. The surface has two orthogonal principle radii of curvature (i.e. is astigmatic) at any point P(x, y) excluding the vertex. The tangential curvature is in the

plane of the diagram and has a centre of curvature at Ct where the normal (P Cs Ct) meets the evolute. The sagittal section is orthogonal to the tangential and contains the normal. The centre of sagittal curvature is at Cs where the normal intersects the axis of symmetry AA'.

The equation, in Cartesian coordinates, of any conic section symmetrically placed about the x-axis and with its vertex at 0 (Baker 1943) and with a radius at 0 of r_o is:

$$y^2 = 2r_o x - px^2$$

Eq. 15.1

where p is a parameter defining the conic such that $p < 0$ are hyperbolas, $p = 0$ is a parabola, $0<p<1$ are ellipses and $p = 1$ is a circle.

The sagittal radius of curvature r_s (PCs) is given by:

$$r_s = \sqrt{r_o^{\,2} + (1-p)y^2}$$

Eq. 15.2

and the tangential radius r_t (PCt) by:

$$r_t = \frac{r_s^3}{r_o^2}$$

Eq. 15.3

The above is the simple case of an ellipsoid of revolution which is not typically the case of most corneas which approximate to triaxial (scalene) ellipsoids. The construction of Fig 2.4 applies in principle although analysis requires differential geometry to determine r_s and r_t. The terms tangential and sagittal are here less appropriate and are better designated as instantaneous and axial (relating to the distance along the normal to the axis of symmetry) curvatures (radii) respectively (Klein and Mandell 1995).

Despite their inaccuracy, tangential and sagittal remain terms that are used in clinical practice with respect to corneal topographical measurements as outlined in the next section.

There is also some variation (and confusion) in the literature with respect to the parameter (and hence versions of Eq. 15.1) determining the conic form. Thus Q = (p-1), 'eccentricity' $e = \sqrt{(1-p)}$ and 'shape factor' $SF = e^2 = (1-p)$ have all been used by various authors.

15.2.2 Models of corneal thickness

The anatomically-determined axial thickness of the cornea ranges from 0.52mm centrally to 0.67mm at the periphery (Maurice 1969; Bron, Tripathi et al. 1997) with up to 1.2mm at the limbus according to topographic measurements (§2.1.2).

We require a mathematical description of radial thickness as a function of position on the corneal surface i.e. distance between anterior and posterior surfaces along a normal to the anterior surface at a point f (see Figure 15.3). From this it is possible to calculate the optical path distance (τ) travelled by a ray of light parallel to the normal to the geometric centre of the corneal surface incident at f and subject to the mean refractive index of the cornea n = 1.376 (Figure 15.4).

15.2.3 Spherical model

If we consider a general case where the anterior and posterior surfaces are two spherical or ellipsoidal shells then relevant parameters are as presented in Figure 15.3

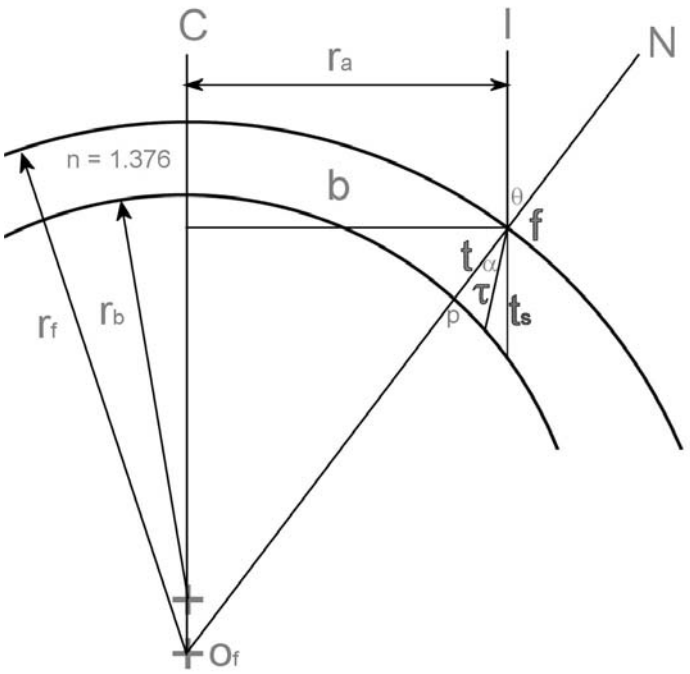

Figure 15.3 Schematic of corneal thickness models

Point f is at planar coordinated (m, n). Radial thickness (t) is along a normal to the anterior surface (NOf). Sagittal thickness (ts) is the distance between anterior and posterior corneal surfaces at point f along a line of incidence If parallel to the central geometric axis COf. The optical path distance (τ) of an incident beam If is determined by Snell's law.

The simple difference between the 'heights' (sagittal thickness, t_s) of the anterior and posterior surfaces at a particular coordinate (m,n) in the y-z plane of the model of Chapter 3. It is sometimes more relevant to determine the radial thickness (t) i.e. the distance between anterior and posterior surfaces along a normal to the anterior surface at a particular point (m,n). An analytic solution to this is difficult, but the distance can be assumed to be less than t_s. Furthermore a light ray parallel to the normal at the centre of the anterior surface incident at a point (m,n) will follow a path (τ) determined by Snell's law and the angle at the point of incidence (θ).

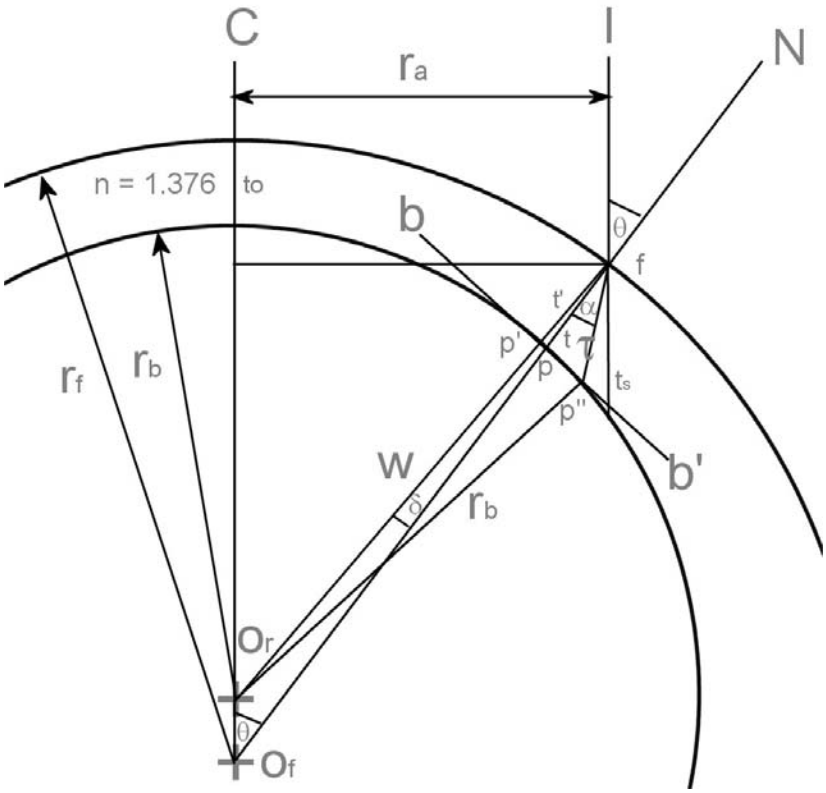

Figure 15.4 Calculation of path distance: simplified model

Simplified geometric corneal model comprising two hemispheric shells (front radius rf, back radius rb) used in derivation for approximate values of path distance (τ) of light incident at point f of the corneal surface.

To do this we assume that the anterior and posterior surfaces are caps of spheres with radii/origins r_f/o_f, r_b/o_b for the front and back surfaces respectively (Figure 15.4). Furthermore the central thickness along a line normal to the surface and passing through both o_f and o_b, $t_0 = r_f - r_b$.

A light ray *I* parallel to the central axis C of o_r is incident at a point *f* on the corneal surface that is a distance r_a from the geometric centre of the cornea and makes an angle θ with the normal *N f* at that point and therefore also at *N of C*. The distance of $o_r = (r_f - (r_b+t_0))$ thus by the cosine rule, the distance

$$o_r\, p'\, f = w = \sqrt{[(r_f^2+(r_f - (r_b+t_0))^2 - 2(r_f\,(r_f - (r_b+t_0)))\cos\theta]}$$

now $\sin\theta = r_a/r_f$ so $\cos\theta = \sqrt{(1-r_a^2/r_f^2)}$ and $w = = \sqrt{((r_b+t_0)^2\sqrt{(1-r_a^2/r_f^2)}}$

Let the angle o_r f $o_f = \delta$ then by the sine rule: $(r_f - (r_b + t_0))/\sin\delta = w/\sin\theta$,

so $\sin\delta = (r_f - (r_b + t_0))\sin\theta/w = (r_f - (r_b + t_0))r_a/w.r_f$

and by the cosine rule, $r_b^2 = \tau^2 + w^2 - 2\tau.w.\cos(\alpha + \delta)$

where, by Snell's law, $\sin\alpha = \sin\theta/n = r_a/r_f.n$ and where n is the average corneal refractive index. Thus the approximate path distance

$\tau = w.\cos(\alpha + \delta) - \sqrt{(w^2\cos^2(\alpha + \delta) + r_b^2 - w^2)}$, taking the negative square root.

Furthermore the perpendicular (radial) thickness at f i.e. thickness of cornea along a linear continuation of the normal at f,

$t = r_f (r_a - (r_b \cos a)/r_a)$

and the sagittal thickness (i.e. the physical distance from front to back corneal surface along the line of incidence I f at f,

$t_s = \sqrt{(r_f^2 - r_a^2)} - (\sqrt{(r_b^2 - r_a^2)} + (r_f - (r_b + t_0)))$

The relationship between the three values τ, t and t_s is shown in Figure 15.5 for a hypothetical cornea front radius (rf) 7.7, back radius (rb) 6.8 and central corneal thickness (t0) 0.5mm. This gives a thickness t = 0.66 at a distance 6mm form the corneal centre in approximate agreement with published data.

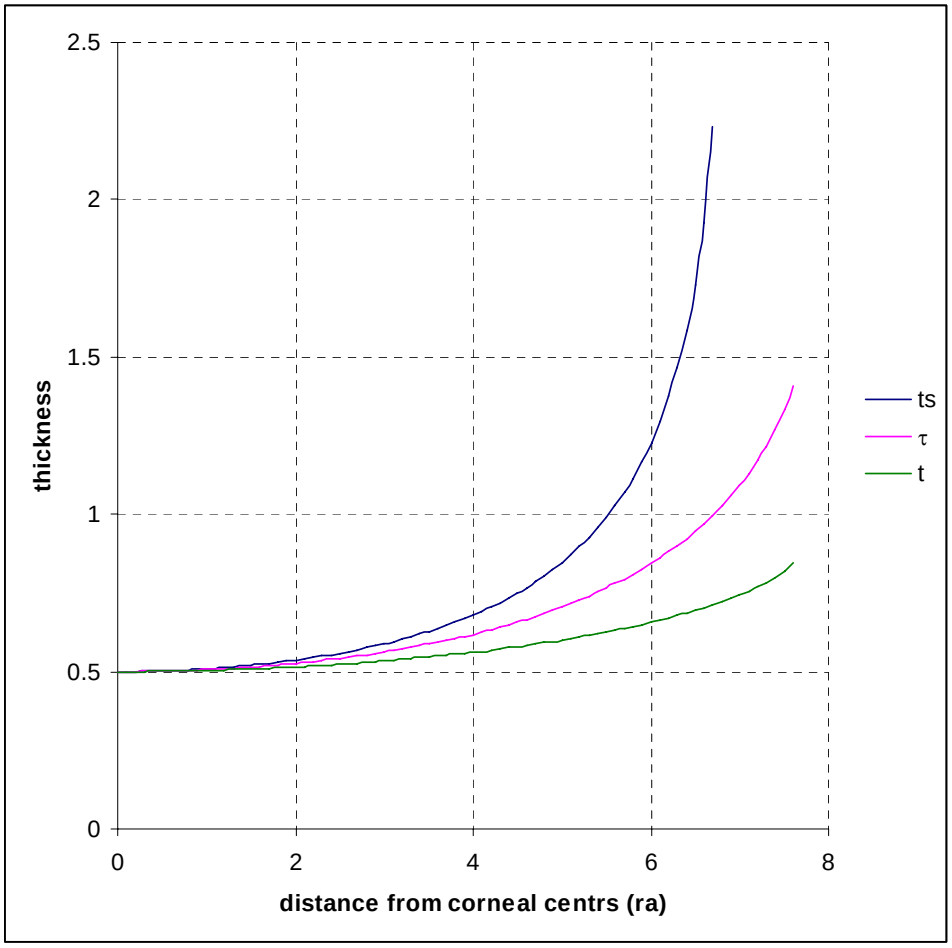

Figure 15.5 Corneal thickness (t and t_s) and path difference (τ)

Expressed as a function of distance from the geometric corneal centre.

15.2.4 Conic model

The corneal surfaces, in reality, are not spherical but are better approximated as conic surfaces (see chapter 2). To model a conic shell of finite thickness we return to the discussion of surfaces began in §4.5.1.

The equation in of an ellipsoid in Cartesian 3-space is: $\frac{x^2}{a^2}+\frac{y^2}{b^2}+\frac{z^2}{c^2}=1$

where a b c are distances of intersection of the surface respectively along the x, y and z-axes. If we define the normal to the centre of the cornea as the x-axis, with y horizontal

and z-vertical (this is in keeping with the coordinates used in the biaxial model) then the height of the surface above the y-z plane is:

$$\mathrm{x} = x = \pm\sqrt{a^2 - \frac{a^2 y^2}{b^2} - \frac{a^2 z^2}{c^2}}$$

Eq. 15.4

All measurements are normalised relative to the unit sphere which is here taken to be equivalent to a sphere with an average corneal radius of 7.7mm. Appropriate conversion is therefore necessary when relating models to real data.

We assume that the cornea has an outer and inner ellipsoidal surface and that the sagittal thickness is the difference between the surfaces at the point (y, z). Thus, taking the positive solutions to Eq. 15.4:

$$\mathrm{t_s} = \sqrt{a^2 - \frac{a^2 y^2}{b^2} - \frac{a^2 z^2}{c^2}} - \sqrt{f^2 - \frac{f^2 y^2}{g^2} - \frac{f^2 z^2}{h^2}}$$

Eq. 15.5

where a, b, c as defined above relate to the outer (front) surface and f, g, h are distances of intersection of the surface respectively along the x, y and z-axes for the inner (back) surface. By varying the parameters a, b, c, f, g, h it is possible to create astigmatic ellipsoidal surfaces that may be used as approximate corneal thickness models.

Three cases will be considered in which, for simplicity, the posterior surface is spherical (i.e. has a circular height contour profile) but the ellipsoidal anterior surface is: anastigmatic, astigmatic within the known range for humans, astigmatic to an extent that could not occur *in vivo*.

15.2.4.1 Anastigmatic (E0)

The contour profile is circular with no meridional change

An accepted value of $p = c^2/a^2 = 0.87$ for the front corneal surface.

15.2.4.2 'Physiological' astigmatic (Ea).

Assuming that the corneal apex approximates to the geometric corneal centre then, at a radius of 7mm from the centre, average corneal thickness varies from 640mm temporally to 678mm nasally with a range from 553 to 761mm (extrapolated from (Fares, Otri et al. 2012)). Thus physiologically reasonable variations in corneal thickness at 7mm are 678 – 640 = 38mm with an extreme and probably unphysiological difference of 761 – 553 = 208mm or, expressed as fraction of the mean, 0.06 and 0.32 respectively.

A 'physiological' astigmatic cornea is modelled with parameter values a = 0.94, b = 0.964, c = 0.93, f = g = h = 0.86 which give a central thickness of 539μm. The correspondence of values calculated using these parameters with measured values for five right eyes (Pentacam, see Chapter10) is presented in Table 15.1.

Table 15.1 Comparison of thickness models Ea and Ex with measured data

			cct	t sag (μm)					
			(μm)	4mm max	4mm min	diff	5mm max	5mm min	diff
Ea (physiological astigmatic)	a b c f = g = h	0.94 0.964 0.93 0.86	539	755	691	64	952	837	115
Measured	Pentacam (n=5)		571	812	746	66			
Ex (extreme astigmatic)	a b c f = g = h	1 1.468 0.93 0.86	539	1422	842	580	1106	2085	979

The model is further modified such that the meridians of maximum and minimum curvatures/thickness can be orientated at any angle Θ from horizontal. This allows the effect of meridional changes in thickness on retardation to be determined.

15.2.4.3 Extreme astigmatic (Ex)

This model is as for Ea, but with parameters a = 1, b = 1.468, c = 0.93, f = g= h= 0.86 resulting in meridional curvature/thickness differences exceeding those possible *in vivo*. Maximum/minimum curvature/thickness profiles are given in Table 15.1, Figure 15.6 and represented in 2- and 3-dimensions in Figure 4.6. The reason for this model is for the generation of isochromes detailed in §11.2.2 and exemplified in, Figure 11.6.

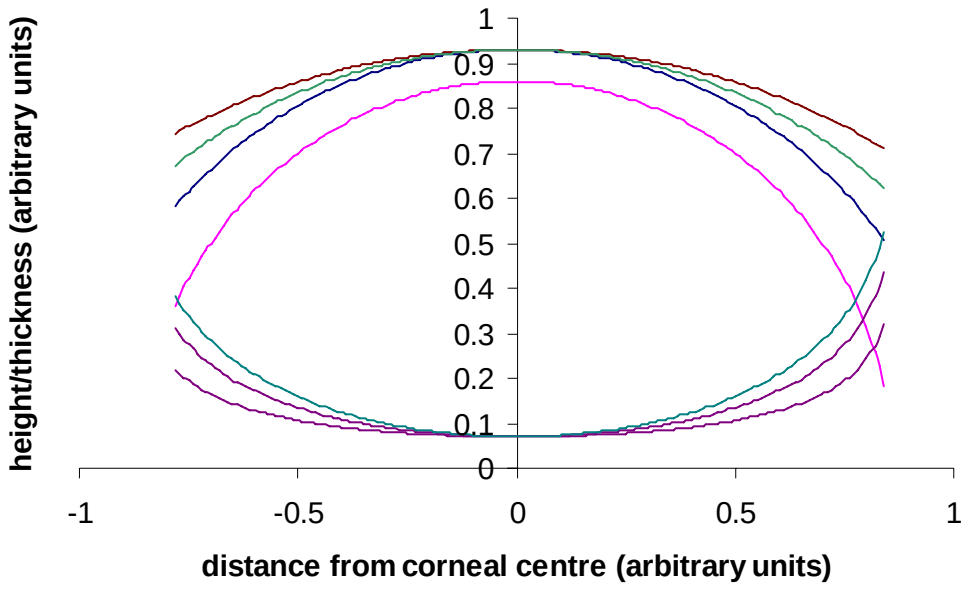

Figure 15.6 Extreme astigmatic model: section profiles.

Upper maximum (blue) and minimum (brown and green) front curvatures. Back curvature (purple). Sagittal thicknesses (lower three curves) corresponding to the three front curvatures.

15.3 Light, polarization and birefringence

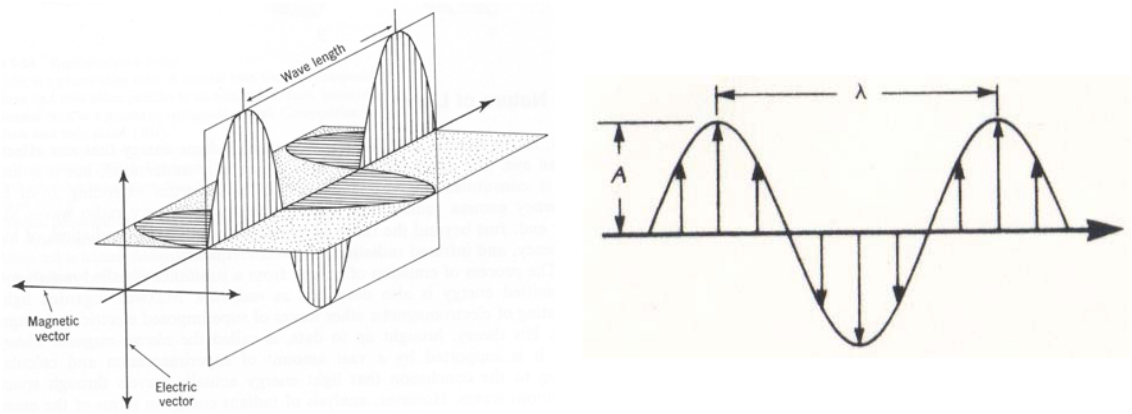

Figure 15.7 Conventional representation of a plane polarized light wave
(a) Orthogonal electric (**E**) and magnetic (**B**) vectors.
(b) Parameters of sinusoidal oscillation: amplitude (A), wavelength (λ)

Visible light is the radiant energy detected by the eye and may be modelled as rays, waves or particles (photons). Rays are lines that are straight in a vacuum, but which can be reflected or refracted respectively by mirrors or prisms/lenses according to precisely defined rules. Maxwell regarded light as superimposed waves of electric and magnetic fields, yet quantum theory requires that light travels through space as discontinuous indivisible particles. All theories are supported experimentally and it is now accepted that they are complementary. Ultimately the photon description subsumes the ray and wave models, although each has its place in simplifying and understanding optical phenomena.

An electromagnetic wave can be depicted in terms of its electric (**E**) and magnetic (**B**) vectors (Figure 15.7 (a)) vibrating sinusoidally at right angles to themselves and to the direction of propagation. Forces derived from **B** are generally very small and not be considered further. Light waves are generally analyzed in terms of **E** as this is the

dominant force interacting with matter and accounts for the optical phenomena relevant to this study. As with any other wave phenomena oscillating in simple harmonic motion (Figure 15.7 (b)), a light wave can be described in terms of the fundamental properties of amplitude (A), wavelength (λ), frequency (f), phase (ϕ), polarization and direction of propagation. The speed of a wave (v) is related to frequency and wavelength by $v = f\lambda$ and depends on the nature of the material through which it travels. The speed of all electromagnetic radiation, including light, *in vacuo* (c) is a fundamental constant of nature ($c \approx 3.0 \times 10^8$ ms^{-1}). Optical media other than a vacuum slow light down such that its speed in a particular medium depends on the optical density or refractive index (n) of that medium where $n = v/c$. Two adjacent waves of the same wavelength are said to be in phase if their peaks and troughs coincide or out of phase otherwise. The distance between similar parts of adjacent waves (e.g. peaks or troughs) is the phase difference.

Light passing through a medium consists of innumerable waves which may conveniently be considered *en mass*. A wave front is a surface connecting similar points (i.e. same phase) on adjacent waves travelling along a line perpendicular to that surface (the wave normal). A light ray is the direction of propagation of light energy and coincides with the wave normal in isotropic materials (light velocity equal in all directions) but not necessarily in anisotropic (light velocity different in different directions) materials (see Chapter 3).

15.3.1 Polarized light

Ordinary light, such as that generated by the sun or a light bulb, travelling through isotropic media (e.g. air) vibrates in all directions perpendicular to the propagation

direction. If the light waves are constrained such that the **E** vector vibrates in a systematic way around the direction of propagation then the light is said to be polarized. The three basic types of polarization are plane, circular and elliptical. In plane (linear) polarized light **E** vibrates in a single plane at some angle (α) usually measured anti-clockwise from horizontal. Circular polarized light can be thought of as being composed of two orthogonal waves of plane polarized light with equal amplitude, but out of phase by one quarter of a wavelength ($\lambda/4$). The sum of the **E** vectors sweeps out a helical surface with a circular cross-section when viewed along the direction of propagation. The spiral is right-handed (right circular polarization) if the phase difference is an odd number of quarter wavelengths and left-handed if the phase difference is an even number of quarter wavelengths (left circular polarization). The more general case of elliptical polarization arises when the phase difference is other than a whole number of wavelengths, half-wavelengths (this results in linear polarized light) or quarter wavelengths in which case the right- or left-handed helix has an elliptical cross-section.

Linear polarized light may be generated by reflection, double refraction (birefringence) or scattering, but is most conveniently produced by selective absorption in which ordinary light passes through a material that strongly absorbs light vibrating in one direction (pleochroism). A familiar example of the latter is polarizing film such as '*Polaroid*'. Generation of elliptical/circular polarized light will be discussed below.

A complete description of polarized monochromatic light can be defined according to parameters introduced by Stokes (Stokes (1852) reviewed in Collett (1993)). Formally, the behaviour of **E** can be described by two components: a vector in the OX direction $\mathbf{E_x}$ with amplitude a_x and an orthogonal vector $\mathbf{E_y}$ in the OY direction with amplitude a_y.

The phase difference between $\mathbf{E_x}$ and $\mathbf{E_y}$ is ϕ which also defines the handedness of polarization such that if $\pi>\phi>0$ polarization is right handed and left handed if $0>\phi>-\pi$. The Stokes parameters have units of intensity and are defined as:

$$S_0 = \langle a_x^2 + a_y^2 \rangle$$

$$S_1 = \langle a_x^2 - a_y^2 \rangle$$

$$S_2 = \langle a_x a_y \cos \phi \rangle$$

$$S_3 = \langle a_x a_y \sin \phi \rangle$$

Where the angular brackets indicate time averages as opposed to instantaneous intensities. Thus S_0 is overall intensity of the light ray, and the parameters S_1, S_2 and S_3 respectively relate to preference for horizontal linear polarization, preference for linear polarization at 45° ($+\pi/4$) and preference for right-circular polarization. Stokes parameters are readily measured using a detector and appropriately orientated linear and circular polarizing filters.

An important property of the Stokes parameters is that they can be presented as a column vector (Stokes vector) $\mathbf{S} = [S_0, S_1, S_2, S_3]^T$ and manipulated with conventional linear algebraic techniques. Transformations using 4×4 matrices representing optical components (Mueller matrices) will be described later and used extensively in Chapter 5.

Alternative descriptions of polarized light including the Poincaré sphere and Jones calculus are detailed elsewhere (e.g. Shurcliff 1962; Collett 1993) and will be omitted here as they are not used in this study. The Jones calculus has been used by the author in a study complementary to the present one (Misson, Timmerman et al. 2007).

15.3.2 Polarization Theory: retardation, retardance and birefringence

If a light wave passes through any optically anisotropic material in a direction other than along an optic axis it can be decomposed into two orthogonal plane polarized waves. Each wave has a different speed which is determined by the two refractive indices for that direction, as can be seen by examining the appropriate index ellipsoid. Each wave is therefore subject to one of two refractive indices and the material is said to be birefringent (doubly refracting): the wave with the lower refractive index is termed the fast wave and that with the higher refractive index, the slow wave. On emerging from an anisotropic material into air (or any isotropic material), the slow wave lags behind the fast wave by a distance termed the optical path length difference or retardation (Λ). The magnitude of retardation depends on the difference in fast (V_f) and slow (V_s) wave velocities, and the thickness of the material (d). The time (t_s) taken for the slow wave to travel through the material is

$$t_s = d/ V_s$$

Eq. 15.6

However, during this time, the fast wave passed through the material and travelled an extra distance equal to the retardation thus:

$$t_s = d/ V_f + \Lambda/V$$

Eq. 15.7

Equating Eq. 15.6 and Eq. 15.7 and rearranging gives:

$$\Lambda = d((V/V_s) - (V/V_f))$$

or

$$\Lambda = d(n_s - n_f)$$

Eq. 15.8

where n_s and n_f are respectively the slow and fast wave refractive indices and the difference ($n_s - n_f$) is the birefringence (b). Retardation (optical path difference) is expressed as a distance in nm.

The corresponding phase difference or retardance (δ, units in radians, degrees or wavelength fractions/multiples) for a given wavelength (λ) is

$$\delta = 2\pi\Lambda / \lambda \qquad \text{Eq. 5.34}$$

The important distinction between retardation and retardance should be noted as these terms will be used throughout the text without further definition.

A plate of birefringent material specifically made to produce a known retardation/retardance is termed a retarder and is characterised by Λ or δ and the orthogonal axes of direction of vibration of the fast and slow waves (fast and slow privileged directions, henceforth abbreviated to fast- and slow-directions). Plates of either uniaxial and biaxial materials may be cut along any plane parallel to the z-axis of the index ellipsoid for uniaxial materials, and in the x–y, x–z or y–z planes for biaxial materials. Retarders are used in the generation of circular and elliptical polarized light, and in the analysis of polarized light as outlined below.

Some birefringent materials show absorption of different wavelengths in one or more preferred directions sometimes associated with a distinct direction-dependent colour change. Such a phenomenon is termed dichroism for uniaxial materials and, more generally, pleochroism which includes biaxial materials some of which may be trichroic (e.g. the minerals andalusite (green, red, yellow) and tanzanite (purple, blue, yellow)). Strongly pleochroic materials are utilised in the fabrication of the now ubiquitous sheet polarizing filters.

15.3.2.1 Interference

Coherent waves (light of a single wavelength in which every ray oscillates in phase or with a precisely defined phase difference) vibrating in the same plane and travelling the same path interfere to produce a resultant motion.

As stated above, a polarized light wave entering a retarder is decomposed into two quasi-coherent orthogonally polarized waves, one retarded with respect to the other and aligned with the fast/slow privileged directions. These waves can be made to interfere by passage through a linear polarizer which constrains them to vibrate in the same plane as that polarizer: the emergent wave is the vector sum of the two waves projected onto the plane of polarization.

If the retarder retards by one half (or an odd number of half) wavelength/s, the waves resolved by the second polarizer will be in the same direction, constructively interferes and thus will be transmitted. The vector sum of waves emerging from the half wave retarder results in a plane polarized wave vibrating perpendicular to the incident waves: the overall effect being to rotate the plane of polarization by 90°. For all other retardances the wave emergent from the retarding plate has either circular (quarter-wave retardance) or elliptical polarization with some component being allowed to pass the second polarizer.

The transmission of monochromatic light through a retarder between two polarizers was analyzed geometrically many years ago (see e.g. Johannsen 1914) and can be summarised as:

$$I = I_0\left[\cos^2\alpha - \sin 2(\theta-\alpha)\sin 2\theta \sin^2\left(\frac{\delta}{2}\right)\right]$$

Eq. 15.9

where I is intensity of light emergent from the second polarizer (analyzer), I_0 is the intensity of light incident on the retarder (i.e. emergent from the first polarizer); α is the angle between polarizer and analyzer; θ is the angle made by a privileged direction of the retarder with the polarizer; δ is the retardance (relative phase difference) as defined by Eq. 5.34. The derivation of this equation is detailed elsewhere (Misson 1993). Calculations of retardance, transmission and other optical characteristics of light waves passing through multiple retarders using the above methods become progressively cumbersome as the number of optical elements in a system increases. Alternative linear algebraic methods are available that greatly simplify calculation.

15.3.3 Mueller Matrices

The effect of filters, total and partial polarizers and depolarizers, rotators and retarders on polarized, partially polarized or unpolarized light may be modelled by a series of linear transformations represented by 4x4 matrices **M** with m_{ij} (i, j = 0, 1, 2, 3) real-valued elements (Mueller matrices). The general form (Shurcliff 1962; Collett 1993) of the Mueller matrix, **Mr,** of an homogenous linear retarder with retardance δ and fast axis azimuth θ is:

$$\mathbf{Mr}_{\delta,\theta} = \begin{bmatrix} 1 & 0 & 0 & 0 \\ 0 & \cos^2 2\theta + \sin^2 2\theta.\cos\delta & \sin 2\theta.\cos 2\theta(1-\cos\delta) & -\sin 2\theta.\sin\delta \\ 0 & \sin 2\theta.\cos 2\theta(1-\cos\delta) & \sin^2 2\theta + \cos^2 2\theta.\cos\delta & \cos 2\theta.\sin\delta \\ 0 & \sin 2\theta.\sin\delta & -\cos 2\theta.\sin\delta & \cos\delta \end{bmatrix}$$

The general form of the Mueller matrix for an ideal polarizer, **Mp,** of azimuth α is:

$$\mathbf{Mp}_{\alpha} = \frac{1}{2}\begin{bmatrix} 1 & \cos 2\alpha & \sin 2\alpha & 0 \\ \cos 2\alpha & \cos^2 2\alpha & \sin 2\alpha \cos 2\alpha & 0 \\ \sin 2\alpha & \sin 2\alpha \cos 2\alpha & \sin^2 2\alpha & 0 \\ 0 & 0 & 0 & 0 \end{bmatrix}$$

The effect of an optical element on a beam of light is given by $\mathbf{S_{out}} = \mathbf{M}.\mathbf{S_{in}}$ where $\mathbf{S_{in}}$ is the Stokes vector of incident light and $\mathbf{S_{out}}$ is the resultant Stokes vector. For more than one optical element, the Mueller matrix for the system is obtained by multiplying the respective Mueller matrices for each element in sequence. The method is outline further and used extensively in Chapter 5.

15.4 Retarders and their calibration

Retarders are quantified by two parameters: the direction of fast/slow axis and the magnitude of retardation/retardance.

The fast slow direction is obtained by placing the retarder between crossed polarizers and rotating the retarder until extinction (i.e. zero light transmission) occurs. The fast/slow axes will be ±45° to the extinction direction.

The magnitude of retardation is determined by compensation, i.e. use of a calibrated variable known retarder orientated in such a way and of sufficient magnitude that it negates the retardation of the unknown by subtraction (see §5.2.2). The quantifiable variable retarder is known as a compensator and numerous types are available.

15.4.1 The Berek compensator

An Olympus Berek compensator (U-CBE, measuring range 0 – 20λ, (Olympus 2012)) was used in conjunction with the polarizing microscope. Measurements were taken using Hg e-line (546.1 nm) generated from a low pressure mercury vapour source and 546nm narrow band (FWHM 10nm) interference filter. Technique followed the manufacturer's instructions and results were obtained using appropriate manufacturer's tables. For the purposes of the present study, retardations were recorded to the nearest 5nm.

15.4.2 The quartz wedge

The quartz wedge was introduced in §6.1.1 as a graded retarder used in the experimental testing of polarimetric theory. The design of the wedge is such that there is a linear increase in retardation from the thin end of 100nm to a maximum of about 2200nm. The wedge is calibrated (Figure 15.8) by determining the linear position of dark extinction bands when the wedge is positioned at 45° between crossed polarizers (bands correspond to integer multiples of the incident wavelength) and between parallel polarizers (bands correspond to odd-integer multiples of half-wavelengths). The incident wavelength was 560nm generated by interference filter (FWHM 10nm) and incandescent light source. The reasons for the choice of this wavelength are given in §5.3.

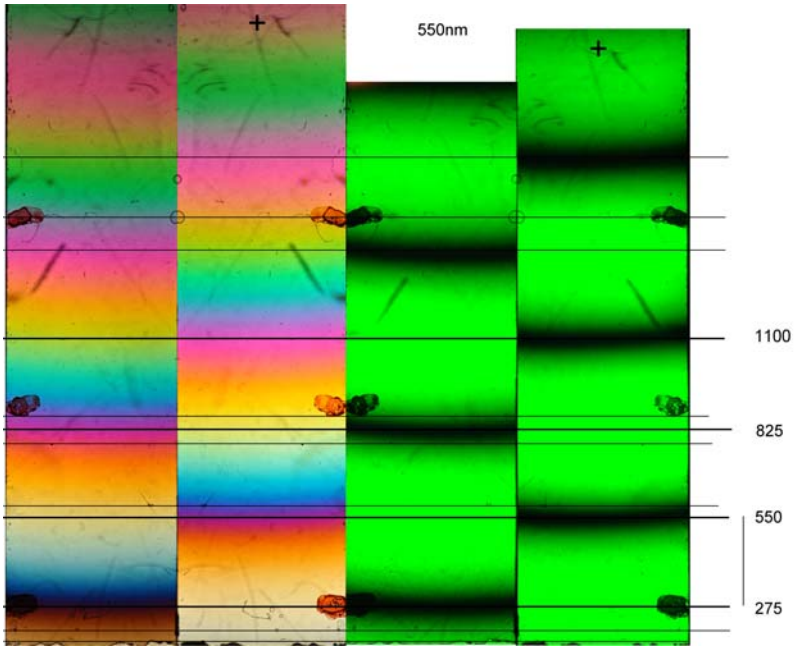

Figure 15.8 Calibration of quartz wedge

560nm (right columns) and white light (left columns); parallel polarizers (left column of each pair), crossed polarizers (right column of each pair marked with +). Note horizontal lines corresponding to half-wavelength (560/2 = 280nm) intervals and corresponding interference colours with white light and parallel/crossed polarizers (cf Figure 6.3)

15.4.3 Graduated wedge calibration

Towards the end of the study a graduated quartz wedge became available allowing a quantitative approach for characterization of 140P and 550P as detailed in §6.2. Calibration was performed as described above at 560nm and the calibration curve is given in Figure 15.9.

The wedge calibration equation is:

$\Delta_w = 0.52d + 0.24$ where Δ_w is wedge retardance i.e. retardance of the wedge in wavelength multiples of the calibrating wavelength (560nm in this case), d is the wedge scale reading. The calculated retardance of 0.24λ at d = 0 relates to the minimum thickness (c. 15 μm) to which the wedge can be reliably ground.

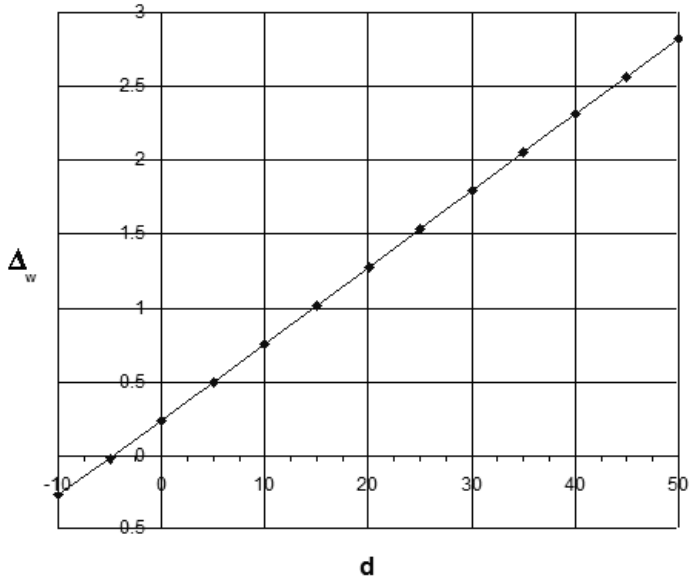

Figure 15.9 Graduated wedge calibration curve at 560nm

15.5 Examining and Measuring the Cornea

15.5.1 Topographic measurements

The cornea is a critical structure in determining the quality of the retinal image and hence vision. Thus small changes or irregularities in curvature, smoothness, thickness and transparency can degrade the retinal image. Measuring such changes is an essential component in the study of normal corneas and in the diagnosis and treatment of corneal disease. Furthermore measurements of curvature and thickness are mandatory in the assessment and treatment planning of corneorefractive surgery for correction of refractive errors and in cataract surgery.

Several technologies have evolved to determine quantitatively the topographic characteristics of the cornea and include keratometry, keratoscopy, photokeratography, interferometry, computer assisted videokeratography, and rasterstereography. They may be subdivided into those allowing discrete measurement at particular positions of the cornea and mapping techniques in which data is gathered over the whole, or a larger part, of the cornea.

15.5.1.1 Discrete measurements

Techniques for the measurement of corneal curvature and thickness at discrete points on the cornea date to the late 19th Century when Helmholtz and others developed the first keratometers (Helmholtz 1924).

15.5.1.1.1 Keratometry

A keratometer is an instrument that measures curvature of a single point near or at the geometric centre of the cornea and was originally intended to give a quantitative measure of astigmatism. Astigmatism is a state of refraction of a surface characterised by unequal curvatures in mutually perpendicular meridians. Light refracted through such a surface cannot be brought to a point focus. Whilst more accurate methods of determining astigmatism have evolved, keratometry remains an important instrument in contact lens practice and in ophthalmology where it is an essential measurement in cataract surgery. There are various different instrument designs including automated versions although all rely on measuring the image of a target object of know proportions after reflection from the convex mirror-like corneal surface. Keratometers measure the radius of curvature along a particular meridian. The optical power of the cornea along that meridian may be estimated from assumptions made about the cornea refractive index and geometry. In this way the maximum and minimum radii and their meridians give a measure of refractive power; corneal astigmatism being the differences in maximum and minimum powers. Keratometry measures only radii of curvature of the central optic (3mm diameter) zone and assumes that maximum and minimum radii are orthogonal (i.e. regular astigmatism). Keratometers give no information concerning radii of curvature of peripheral zones of the anterior cornea, posterior corneal curvature, corneal relief or irregular astigmatism.

15.5.1.1.2 Pachymetry

The thickness of the central cornea and at other points on the corneal surface may be measured in a number of ways including ultrasonic pachymetry, optical slit lamp pachymetry(Salz, Azen et al. 1983), specular microscopy(Argus 1995), confocal

microscopy (Lemp, Dilly et al. 1985), and partial coherence interferometry (for review see Swartz, Marten et al. (2007)). Each method has both advantages and disadvantages although it is generally accepted that large inter-observer and inter-instrument discrepancies can arise in the older methods of optical pachymetry (Marsich and Bullimore 2000). Ultrasonic pachymetry is the most commonly used in clinical practice because of its accuracy, relative low cost and ease of use although it has the disadvantages of requiring corneal contact and it is difficult to precisely locate the same points of measurement in serial examinations.

More recent developments allow the corneal thickness to be mapped throughout a large extent particularly the central and paracentral areas although in some cases it is possible to map thickness as far as the limbus. Topographic pachymeters including Orbscan, Pentacam, high-resolution ultrasonography and optical coherence tomography will be discussed below.

15.5.1.2 Mapping Techniques: Corneal Topography

Imaging techniques of the cornea have developed in parallel with advances in refractive surgery which require accurate continuous data of curvature, relief and thickness over large areas of the cornea (see Wang and Wang (2006) and Konstantopoulos, Hossain et al. (2007) for comprehensive reviews).

15.5.1.3 Pentacam (Oculus, Berlin)

The Pentacam uses a rotating Scheimpflug camera to derive true 3-dimensional topographic data for both the anterior and posterior corneal surfaces. A complete examination of an eye takes several seconds during which time the camera rotates through 180° taking 25 meridional Scheimpflug cross-section images with 500

measurement points through the cornea, anterior chamber and lens. Propriety software uses the elevation data to calculate corneal thickness (pachymetry) maps together with anterior and posterior surface topography, including axial and meridional curvature maps (Maus, Kröber et al. 2006). The advantages of the Pentacam over other methods include: high resolution, mapping the entire cornea, ability to measure irregular corneas (e.g. keratoconus), limbus-to-limbus pachymetry.

The Pentacam has been shown to have excellent repeatability for measurements of central corneal thickness (Lackner, Schmidinger et al. 2005), peripheral corneal thickness, anterior and posterior corneal curvature (Chen and Lam 2007; Shankar, Taranath et al. 2008). The instrument has also been found to provide measurements of corneal thickness from normal subjects that are in reasonable agreement with previously validated clinical instruments (Barkana, Gerber et al. 2005; Lackner, Schmidinger et al. 2005).

15.5.2 Slit-lamp biomicroscopy and photography

The slit-lamp biomicroscope is a versatile instrument essential to routine ophthalmic practice. It allows examination of the anterior segment of the eye and, with suitable lenses, much of the posterior segment at magnifications of 10 – 60×. Quantitative measurement of intraocular pressure, endothelial cell counting, corneal thickness, anterior chamber depth and other parameters are possible by the addition of auxiliary devices.

Slit lamp biomicroscopy derives its name from the adjustable vertical slit beam that is projected into the eye typically at a variable oblique angle. The light scattered/reflected from the beam by ocular structures is then observed through a horizontally positioned microscope with a long working distance of approximately 10cm. The third component

of the biomicroscope is a mechanical arrangement that allows illumination and observation of a subjects eye such that the subject is comfortably but firmly positioned in a stable upright sitting posture.

Figure 15.10 Modes of slit-lamp examination

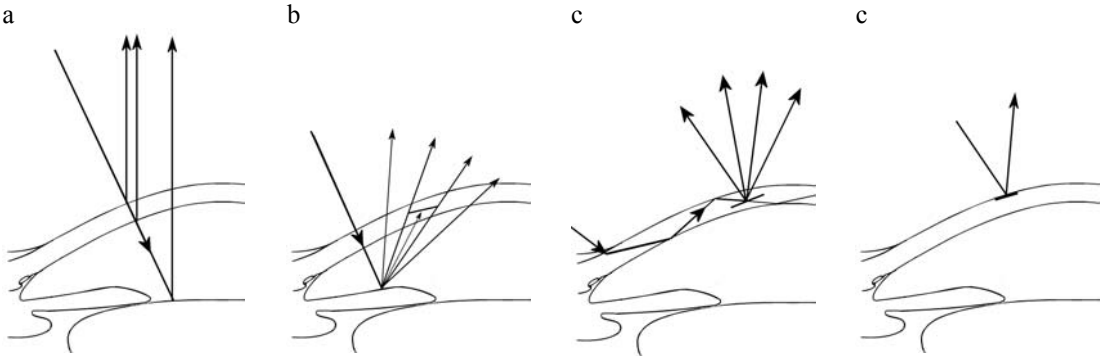

By carefully positioning the slit-beam relative to the cornea several complimentary views of the eye may be obtained often simultaneously (Figure 15.10):

1. Optical sectioning: with a narrow beam at approximately 45° to the focal point of the biomicroscope, an anatomical section can be observed through the transparent ocular components such as the tear film, cornea, anterior chamber and lens.
2. Tangential illumination: oblique illumination >45°cast shadows that highlight texture of ocular structures.
3. Pinpoint illumination: a narrow, high intensity beam obliquely through the anterior chamber allows individual cells to be seen as pin-points of light against the dark background of the iris.
4. Specular reflection: coaxial illumination/observation utilises light reflected particularly from the anterior and posterior corneal surfaces.

5. Proximal indirect illumination: a moderately wide beam is directed to an area adjacent to that of interest. Back scatter from deeper structures obliquely illuminates the area of interest against a darker background.
6. Sclerotic scatter: High intensity oblique illumination at the limbus is transmitted by total internal reflection (cf fibre optics) thought the cornea highlighting any stromal opacities against a darker background.
7. Retroillumination: Near coaxial illumination through a dilated pupil allows light to be reflected back from the fundus (cf 'red eye' of flash photography) through the transparent ocular structures. This allows detection of opacities in the vitreous, lens and cornea together with transparent defects in the iris.

Photographic modification of the slit lamp (flash, beam-splitters, camera-backs with associated mechanics, electronic and software) allow digital imaging for documentation, archiving and image analysis.

15.6 Miscellaneous Experimental Results

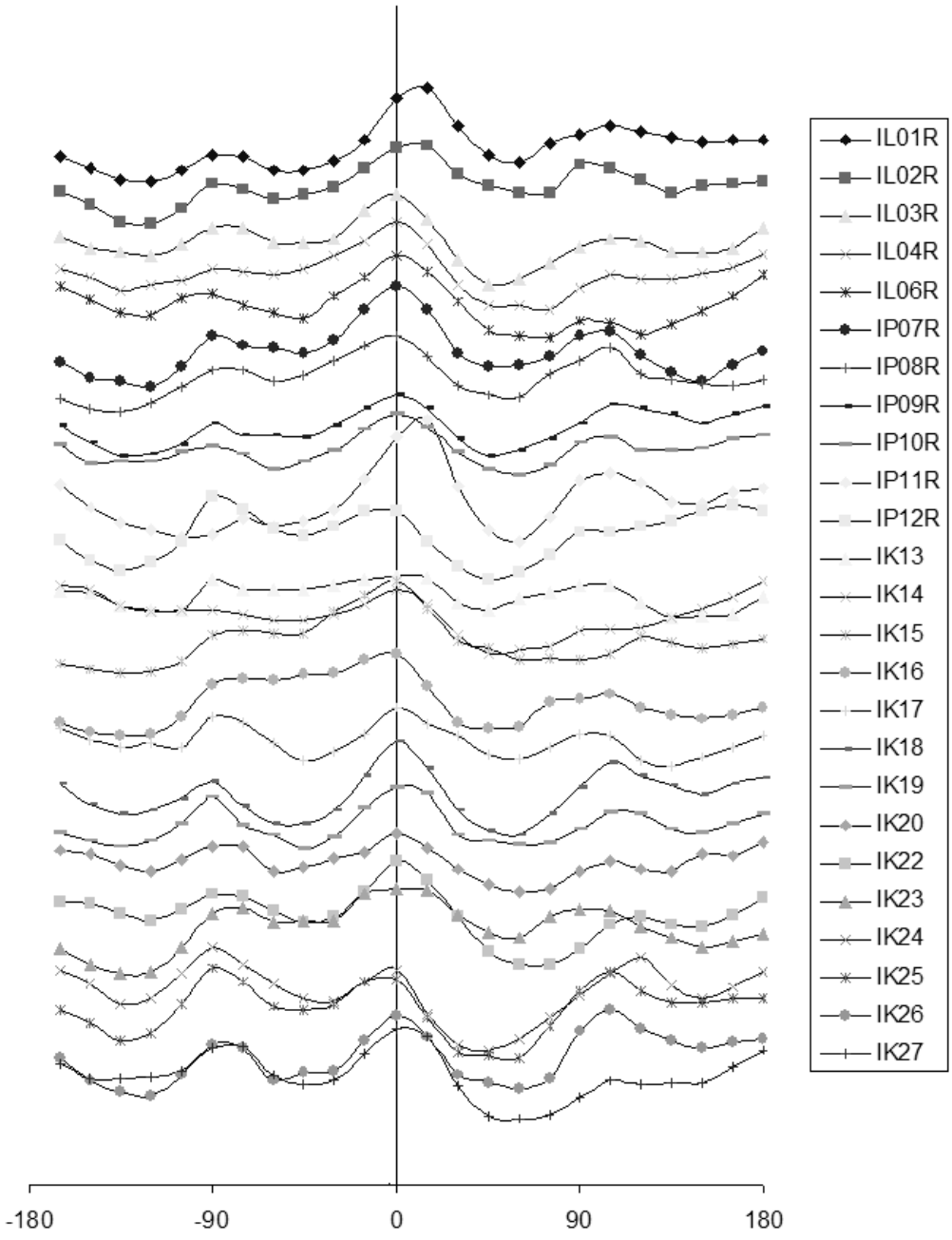

Figure 15.11 Raw 280nm isochrome data (b)

Distance from corneal centre of 280nm isochrome vs. azimuth as in Figure 9.3. Graphs separated to show form.

Variable	Correlations (Sheet1 in Correlations.stw) Marked correlations are significant at p < .05000 N=25 (Casewise deletion of missing data) age	sex	k1	k2	k mean	k diff	Rn	Rs	Rt	Ri	hl	vl	lfd	hl/vl	k1/k2	a2	Arn	Ars	Art	Ari	haz	vaz	lfaz
age	1.00	-0.29	-0.00	0.11	0.05	0.30	-0.24	-0.35	-0.08	-0.37	-0.23	-0.43	-0.27	0.17	-0.29	0.28	0.19	0.34	0.33	-0.07	0.12	0.25	-0.24
sex	-0.29	1.00	0.40	0.38	0.40	-0.09	0.11	0.31	0.30	0.19	0.32	0.31	0.19	0.01	0.11	0.08	-0.25	0.08	-0.14	0.01	-0.16	-0.05	0.20
k1	-0.00	0.40	1.00	0.93	0.98	-0.26	-0.25	0.06	0.59	0.40	0.30	0.17	-0.06	0.11	0.32	-0.06	-0.42	0.40	-0.03	-0.30	-0.21	-0.09	-0.19
k2	0.11	0.38	0.93	1.00	0.98	0.11	-0.24	-0.01	0.58	0.31	0.32	0.06	-0.02	0.22	-0.05	0.05	-0.24	0.53	0.08	-0.25	-0.14	0.01	-0.19
k mean	0.05	0.40	0.98	0.98	1.00	-0.08	-0.25	0.03	0.60	0.36	0.32	0.12	-0.04	0.17	0.14	-0.00	-0.33	0.47	0.02	-0.28	-0.18	-0.04	-0.19
k diff	0.30	-0.09	-0.26	0.11	-0.08	1.00	0.06	-0.20	-0.06	-0.29	0.03	-0.29	0.10	0.28	-1.00	0.31	0.52	0.33	0.30	0.16	0.20	0.27	0.00
Rn	-0.24	0.11	-0.25	-0.24	-0.25	0.06	1.00	0.16	-0.12	-0.17	0.51	0.14	0.16	0.32	-0.07	0.15	0.27	-0.57	-0.17	0.06	0.15	-0.16	0.38
Rs	-0.35	0.31	0.06	-0.01	0.03	-0.20	0.16	1.00	0.12	0.26	0.24	0.75	0.20	-0.44	0.19	0.29	-0.13	-0.16	-0.37	0.07	-0.25	-0.23	-0.28
Rt	-0.08	0.30	0.59	0.58	0.60	-0.06	-0.12	0.12	1.00	0.36	0.74	0.21	0.31	0.46	0.09	0.07	0.05	0.30	0.33	-0.08	0.32	0.06	0.13
Ri	-0.37	0.19	0.40	0.31	0.36	-0.29	-0.17	0.26	0.36	1.00	0.25	0.74	-0.15	-0.48	0.31	0.02	-0.46	-0.01	-0.05	-0.07	-0.21	-0.35	-0.27
hl	-0.23	0.32	0.30	0.32	0.32	0.03	0.51	0.24	0.74	0.25	1.00	0.34	0.40	0.57	-0.02	0.27	0.28	-0.11	0.16	0.08	0.41	-0.03	0.35
vl	-0.43	0.31	0.17	0.06	0.12	-0.29	0.14	0.75	0.21	0.74	0.34	1.00	0.04	-0.68	0.30	0.31	-0.31	-0.25	-0.24	0.09	-0.30	-0.35	-0.31
lfd	-0.27	0.19	-0.06	-0.02	-0.04	0.10	0.16	0.20	0.31	-0.15	0.40	0.04	1.00	0.32	-0.11	0.16	0.15	-0.07	-0.05	-0.04	0.17	0.08	0.37
hl/vl	0.17	0.01	0.11	0.22	0.17	0.28	0.32	-0.44	0.46	-0.42	0.57	-0.58	0.32	1.00	-0.27	-0.05	0.50	0.11	0.35	-0.01	0.62	0.28	0.59
k1/k2	-0.29	0.11	0.32	-0.05	0.14	-1.00	-0.07	0.19	0.09	0.31	-0.02	0.30	-0.11	-0.27	1.00	-0.31	-0.54	-0.29	-0.30	-0.18	-0.22	-0.27	-0.01
a2	0.28	0.08	-0.06	0.05	-0.00	0.31	0.15	0.29	0.07	0.02	0.27	0.31	0.16	-0.05	-0.31	1.00	0.28	0.01	-0.01	0.18	0.02	0.07	-0.35
Arn	0.19	-0.25	-0.42	-0.24	-0.33	0.52	0.27	-0.13	0.05	-0.46	0.28	-0.31	0.15	0.50	-0.54	0.28	1.00	0.02	0.49	0.28	0.76	0.38	0.42
Ars	0.34	0.08	0.40	0.53	0.47	0.33	-0.57	-0.16	0.30	-0.01	-0.11	-0.25	-0.07	0.11	-0.29	0.01	0.02	1.00	0.23	-0.08	0.01	0.40	-0.23
Art	0.33	-0.14	-0.03	0.08	0.02	0.30	-0.17	-0.37	0.33	-0.05	0.16	-0.24	-0.05	0.35	-0.30	-0.01	0.49	0.23	1.00	0.34	0.67	0.63	0.19
Ari	-0.07	0.01	-0.30	-0.25	-0.28	0.16	0.06	0.07	-0.08	-0.07	0.08	0.09	-0.04	-0.01	-0.18	0.18	0.28	-0.08	0.34	1.00	0.22	0.62	0.10
haz	0.12	-0.16	-0.21	-0.14	-0.18	0.20	0.15	-0.25	0.32	-0.21	0.41	-0.30	0.17	0.62	-0.22	0.02	0.76	0.01	0.67	0.22	1.00	0.42	0.57
vaz	0.25	-0.05	-0.09	0.01	-0.04	0.27	-0.16	-0.23	0.06	-0.35	-0.03	-0.35	0.08	0.28	-0.27	0.07	0.38	0.40	0.53	0.62	0.42	1.00	0.13
lfaz	-0.24	0.20	-0.19	-0.19	-0.19	0.00	0.38	-0.28	0.13	-0.27	0.35	-0.31	0.37	0.59	-0.01	-0.35	0.42	-0.23	0.19	0.10	0.57	0.13	1.00

Table 15.2 Correlation data for all parameters

Data outlined is significant at $p<0.05$. There are no non-trivial correlations.

15.7 Bézier curves

Bézier curves (Farin 2002) are parametric curves defined by:

$$B(t) = \sum_{i=0}^{n} b_{i,n}(t) P_i \qquad t \in [0,1]$$

where the polynomials (Bernstein basis polynomials of degree n)

$$b_{i,n}(t) = \binom{n}{i} t^i (1-t)^{n-i}, \qquad i = 0,...n$$

and $\binom{n}{i} = \frac{n!}{i!(n-i)!}$ is the binomial coefficient.

The points $P_0 \ldots P_i \ldots P_n$ ($n \in \mathbb{Z}$, $n \geq 0$) are defined as 'control points' for the Bézier curve which starts at P_0 and ends at P_n. The points $P_{0\ldots n}$ form a polygon (Bézier or control polygon) the convex hull of which contains the Bézier curve. The order of the Bézier curve is defined by n. First to fourth orders (n = 1…4) are termed linear, quadratic, cubic and quartic respectively. First order Bézier curves are straight lines between P_0 and P_n; second order Bézier curve are parabolic segments i.e. conic arcs. More complex lines can be approximated by higher order Bézier curves which have found great use in computer graphics. The generation of second-order Bézier curves and their relationship to repeated line segments is illustrated in Figure 13.6.

Of relevance to the present study is that segments of conic sections can be exactly defined by the rational Bézier function

$$B(t) = \frac{\sum_{i=0}^{n} b_{i,n}(t) P_i w_i}{\sum_{i=0}^{n} b_{i,n}(t) w_i}$$ where w_i are parameters termed weights

Thus it is not surprising to find conic geometric structures defined by linear components as is hypothesised in the present study with respect to corneal anatomy.

15.8 Miscellaneous areas of further study

Areas for further study arising from the study and literature review not detailed elsewhere include:

1. Accurate determination of peripheral corneal thickness and limbal geometry (§2.1.2).
2. Correlation of peripheral corneal thickness and astigmatism/ refractive errors (§2.1.2).
3. Construction of 3-d models of corneal thickness (§4.5.1).
4. Effect of high intensity/ long exposure x-rays on tissue architecture (§2.2.3).
5. Use phase/Fourier x-ray techniques rather than intensity data to investigate cornea x-ray scatter.
6. Observe peripheral cornea with EPB: look for extraocular muscle (EOM)-related fibrils.
7. Correlate EOM anatomy (e.g. insertion biometrics) with isochromes.
8. Compare x-ray diffraction patterns of cornea and aragonite.
9. Species survey of corneal birefringence.
10. Determine effect of altering corneal birefringence on visual function.
11. Investigate the theoretical link between Bézier curves, conic sections and the biaxial model.

16 References

Abahussin, M., S. Hayes, et al. (2009). "3D Collagen Orientation Study of the Human Cornea Using X-ray Diffraction and Femtosecond Laser Technology." Investigative Ophthalmology & Visual Science **50**(11): 5159-5164.

Aghamohammadzadeh, H., R. H. Newton, et al. (2004). "X-ray scattering used to map the preferred collagen orientation in the human cornea and limbus." Structure **12**(2): 249-256.

Altan-Yaycioglu, R., A. Pelit, et al. (2007). "Astigmatism induced by oblique clear corneal incision: right vs. left eyes." Canadian journal of ophthalmology. Journal canadien d'ophtalmologie **42**(4): 557-561.

Ameen, D. B., M. F. Bishop, et al. (1998). "A Lattice Model for Computing the Transmissivity of the Cornea and Sclera." Biophysical Journal **75**(5): 2520-2531.

Amidror, I. (2009). The Theory of the Moiré Phenomenon. London, Springer.

Argus, W. A. (1995). "Ocular hypertension and central corneal thickness." Ophthalmology **102**(12): 1810-1812.

Bailey, A. J. (1987). "Structure, function and ageing of the collagens of the eye." Eye **1 (Pt 2)**: 175-183.

Baker, T. Y. (1943). "Ray tracing through non-spherical surfaces." Proceedings of the Physical Society **55**(5): 361.

Barkana, Y., Y. Gerber, et al. (2005). "Central corneal thickness measurement with the Pentacam Scheimpflug system, optical low-coherence reflectometry pachymeter, and ultrasound pachymetry." J Cataract Refract Surg **31**(9): 1729-1735.

Benedek, G. B. (1971). "Theory of Transparency of the Eye." Appl. Opt. **10**(3): 459-473.

Blokland, G. J. v. (1985). "Ellipsometry of the human retina in vivo: preservation of polarization." J Opt Soc Am A **2**(1): 72-75.

Blokland, G. J. v. (1986). The optics of the human eye studies with respect to polarized light. Utrecht, Rijksuniversiteit. **PhD**.

Blokland, G. J. v. and S. C. Verhelst (1987). "Corneal polarization in the living human eye explained with a biaxial model." J Opt Soc Am A **4**(1): 82-90.

Boehm, G. (1940). "Über maculare (Haidinger'sche) Polarizationsbüschel und über eine polarizationsoptischen Fehler der Auges." Acta Ophthalmol **18**: 109-142.

Boettner, E. A. and J. R. Wolter (1962). "Transmission of the Ocular Media." Investigative Ophthalmology & Visual Science **1**(6): 776-783.

Bone, R. A. (1980). "The role of the macular pigment in the detection of polarized light." Vision Res **20**(3): 213-220.

Bone, R. A. and G. Draper (2007). "Optical anisotropy of the human cornea determined with a polarizing microscope." Appl Opt **46**(34): 8351-8357.

Boote, C., S. Dennis, et al. (2005). "Lamellar orientation in human cornea in relation to mechanical properties." J Struct Biol **149**(1): 1-6.

Boote, C., S. Hayes, et al. (2006). "Mapping collagen organization in the human cornea: left and right eyes are structurally distinct." Invest Ophthalmol Vis Sci **47**(3): 901-908.

Born, M. and E. Wolf (2005). Principles of Optics. Cambridge, Cambridge University Press.
Bour, L. J. (1991). Polarized light and the eye. Visual Optics and Instrumentation. W. N. Charman. New York, Macmillan Press. **1:** 310-325.
Bour, L. J. and N. J. Lopes Cardozo (1981). "On the birefringence of the living human eye." Vision Res **21**(9): 1413-1421.
Brewster, D. (1815). "Experiments on the de-polarization of light as exhibited by various mineral, animal and vegetable bodies with a reference to the general principles of polarization." Philosophical Transactions of the Royal Society of London **105**: 21-53.
Brink, H. B. k. (1991). "Birefringence of the human crystalline lens in vivo." J Opt Soc Am A **8**: 1788-1793.
Brink, H. B. k. and G. J. van Blokland (1988). "Birefringence of the human foveal area assessed in vivo with Mueller-matrix ellipsometry." J Opt Soc Am A **5**(1): 49-57.
Bron, A. J. (2001). "The architecture of the corneal stroma." Br J Ophthalmol **85**(4): 379-381.
Bron, A. J., R. Tripathi, C., et al. (1997). Wolff's Anatomy of the Eye and Orbit. London, Chapman and Hall Medical.
Bueno, J. M. (2000). "Measurement of parameters of polarization in the living human eye using imaging polarimetry." Vision Res **40**(28): 3791-3799.
Bueno, J. M. and M. C. W. Cambell (2001). "Polarization properties for in vitro human lenses." Invest Ophthalmol Vis Sci **42 (Suppl)**: S161.
Bueno, J. M. and J. Jaronski (2001). "Spatially resolved polarization properties for in vitro corneas." Ophthalmic Physiol Opt **21**(5): 384-392.
Centofanti, M., F. Oddone, et al. (2005). "Corneal birefringence changes after laser assisted in situ keratomileusis and their influence on retinal nerve fibre layer thickness measurement by means of scanning laser polarimetry." Br J Ophthalmol **89**(6): 689-693.
Charman, W. N. (1980). "Reflection of plane-polarized light by the retina." Br J Physiol Opt **34**: 34-49.
Chen, D. and A. K. Lam (2007). "Intrasession and intersession repeatability of the Pentacam system on posterior corneal assessment in the normal human eye." J Cataract Refract Surg **33**(3): 448-454.
Clarke, D. and J. F. Grainger (1971). Polarized Light and Optical Measurement. Oxford, Pergamon Press.
Cogan, D. G. (1941). "Some Ocular Phenomena Produced with Polarized Light." Arch.Ophthal **25**: 391-400.
Collett, E. (1993). Polarized Light. Fundamentals and Applications. New York, Marcel Dekker.
Cox, J., R. Farrell, et al. (1970). "The transparency of the mammalian cornea." J. Physiol. **210**(3): 601-616.
Craig, D. (1961). "The Benford plate." Amer Mineral **46**: 757-758.
Daxer, A. and P. Fratzl (1997). "Collagen fibril orientation in the human corneal stroma and its implication in keratoconus." Invest Ophthalmol Vis Sci **38**(1): 121-129.
Dingeldein, S. A. and S. D. Klyce (1989). "The topography of normal corneas." Arch Ophthalmol **107**(4): 512-518.

Dreher, A. W. and K. Reiter (1992). "Retinal laser ellipsometry: a new method for measuring the retinal nerve fiber layer thickness distribution? ,." Clin Vision Sci **7**: 481-488.
Dreher, A. W., K. Reiter, et al. (1992). "Spatially resolved birefringence of the retinal nerve fiber layer assessed with a retinal laser ellipsometer." Appl Opt **31**: 3730-3735.
Duke-Elder, S. (1958). System of Ophthalmology. London, Henry Kimpton.
Elsheikh, A., M. Brown, et al. (2008). "Experimental assessment of corneal anisotropy." Journal of refractive surgery (Thorofare, N.J. : 1995) **24**(2): 178-187.
Fares, U., A. M. Otri, et al. (2012). "Correlation of central and peripheral corneal thickness in healthy corneas." Contact lens & anterior eye : the journal of the British Contact Lens Association **35**(1): 39-45.
Farin, G. E. (2002). Curves and surfaces for CAGD: a practical guide, Morgan Kaufmann.
Farrell, R., R. McCally, et al. (1973). "Wave-length dependencies of light scattering in normal and cold swollen rabbit corneas and their structural implications." J. Physiol. **233**(3): 589-612.
Farrell, R. A., D. Rouseff, et al. (2005). "Propagation of polarized light through two- and three-layer anisotropic stacks." J Opt Soc Am A Opt Image Sci Vis **22**(9): 1981-1992.
Farrell, R. A., J. F. Wharam, et al. (1999). "Polarized light propagation in corneal lamellae." J Refract Surg **15**(6): 700-705.
Fletcher, L. (1892). The Optical Indicatrix and the Transmission of Light in Crystals. London, Henry Frowde.
Frank M, P. (1976). "Contributions of electron microscopy to the study of corneal pathology." Survey of Ophthalmology **20**(6): 375-414.
Fratzl, P. and A. Daxer (1993). "Structural transformation of collagen fibrils in corneal stroma during drying. An x-ray scattering study." Biophysical Journal **64**(4): 1210-1214.
Freund, D. E., R. L. McCally, et al. (1995). "Ultrastructure in anterior and posterior stroma of perfused human and rabbit corneas. Relation to transparency." Invest Ophthalmol Vis Sci **36**(8): 1508-1523.
Frohlich, M. W. (1986). Birefringent Objects Visualized by Circular Polarization Microscopy, Informa Healthcare. **61:** 139 - 143.
Garway-Heath, D. F., M. J. Greaney, et al. (2002). "Correction for the erroneous compensation of anterior segment birefringence with the scanning laser polarimeter for glaucoma diagnosis." Invest Ophthalmol Vis Sci **43**(5): 1465-1474.
Harry, J. and G. P. Misson (2001). Clinical Ophthalmic Pathology. Oxford, Butterworth Heinemann.
Hart, R. W. and R. A. Farrell (1969). "Light scattering in the cornea." J Opt Soc Am **59**(6): 766-774.
Helmholtz, H. (1924). Treatise on Physiological Optics, Optical Society of America.
His, W. (1856). Beitrage zur normalen und pathologischen Histologie der Cornea. Basel, Schweighauser.
Hjortdal, J. O. (1996). "Regional elastic performance of the human cornea." J Biomech **29**(7): 931-942.

Huang, D., E. A. Swanson, et al. (1991). "Optical coherence tomography." Science **254**(5035): 1178-1181.
Hunter, D. G., J. C. Sandruck, et al. (1999). "Mathematical modeling of retinal birefringence scanning." J Opt Soc Am A Opt Image Sci Vis **16**(9): 2103-2111.
Ichihashi, Y., M. H. Khin, et al. (1995). "Birefringence effect of the in vivo cornea." Optical Engineering **34**(3): 693-700.
Irsch, K. and A. A. Shah (2012). "Birefringence of the central cornea in children assessed with scanning laser polarimetry." Journal of Biomedical Optics **17**(8): 086001-086001.
Jacobs, B. J., B. I. Gaynes, et al. (1999). "Refractive astigmatism after oblique clear corneal phacoemulsification cataract incision." Journal of cataract and refractive surgery **25**(7): 949-952.
Jaronski, J. W. and H. T. Kasprzak (1998). New polarimetric method for in-vivo measurement of corneal birefringence. Tenth Polish-Czech-Slovak Optical Conference: Wave and Quantum Aspects of Contemporary Optics, SPIE.
Jaronski, J. W. and H. T. Kasprzak (2003). "Linear birefringence measurements of the in vitro human cornea." Ophthalmic Physiol Opt **23**(4): 361-369.
Jester, J. V. (2008). "Corneal crystallins and the development of cellular transparency." Seminars in Cell & Developmental Biology **19**(2): 82-93.
Johannsen, A. (1914). Manual of Petrographic Methods. New York, McGraw-Hill.
Johannsen, A. (1918). Manual of Petrographic Methods. New York, McGraw-Hill.
Kadler, K. E., C. Baldock, et al. (2007). "Collagens at a glance." J Cell Sci **120**(Pt 12): 1955-1958.
Kenney, C. M., D. J. Brown, et al. (2000). "The Elusive Causes of Keratoconus: A Working Hypothesis." Eye & Contact Lens **26**(1).
Kikkawa, Y. (1955). "Submicroscopic Structure of Rabbit Cornea Studied by Polarization Optics and Thermoelasticity." Jap.J.Physiol. **5**: 167-182.
Kikkawa, Y. (1957). "Fibrous Structure and Polarization Optics of the Rabbit Cornea." Jap.J.Ophthalmol. **1**: 35-42.
Klein, S. A. and R. B. Mandell (1995). "Axial and instantaneous power conversion in corneal topography." Invest Ophthalmol Vis Sci **36**(10): 2155-2159.
Knighton, R. W. and X. R. Huang (2002). "Linear birefringence of the central human cornea." Invest Ophthalmol Vis Sci **43**(1): 82-86.
Knighton, R. W., X. R. Huang, et al. (2008). "Corneal birefringence mapped by scanning laser polarimetry." Opt Express **16**(18): 13738-13751.
Koeppe, L. (1921). Die ultra und polarizationsmikroskopische Erforschung des Lebenden Auges und Ihre Ergebnisse. Leibzig, Ernst Bircher.
Kokott, W. (1938). "Uber mechanisch-funktionelle Strukturen des Auges." Albrecht Von Graefes Arch Ophthalmol **138**: 424-485.
Komai, Y. and T. Ushiki (1991). "The three-dimensional organization of collagen fibrils in the human cornea and sclera." Invest. Ophthalmol. Vis. Sci. **32**(8): 2244-2258.
Konstantopoulos, A., P. Hossain, et al. (2007). "Recent advances in ophthalmic anterior segment imaging: a new era for ophthalmic diagnosis?" Br J Ophthalmol **91**(4): 551-557.
Konstantopoulos, A., J. Kuo, et al. (2008). "Assessment of the use of anterior segment optical coherence tomography in microbial keratitis." Am J Ophthalmol **146**(4): 534-542.

Lackner, B., G. Schmidinger, et al. (2005). "Repeatability and reproducibility of central corneal thickness measurement with Pentacam, Orbscan, and ultrasound." Optom Vis Sci **82**(10): 892-899.
Lee, A. C., M. A. Qazi, et al. (2008). "Biometry and intraocular lens power calculation." Current Opinion in Ophthalmology **19**(1): 13-17 10.1097/ICU.1090b1013e3282f1091c1095ad.
Lemp, M. A., P. N. Dilly, et al. (1985). "Tandem-scanning (confocal) microscopy of the full-thickness cornea." Cornea **4**(4): 205-209.
Leonard, D. W. and K. M. Meek (1997). "Refractive indices of the collagen fibrils and extrafibrillar material of the corneal stroma." Biophys J **72**(3): 1382-1387.
Li, L. Y. and B. Tighe (2006). "The anisotropic material constitutive models for the human cornea." J Struct Biol **153**(3): 223-230.
Lo, W., S. W. Teng, et al. (2006). "Intact corneal stroma visualization of GFP mouse revealed by multiphoton imaging." Microsc Res Tech **69**(12): 973-975.
Löpping, B. and R. A. Weale (1965). "Changes in corneal curvature following ocular convergence." Vision Research **5**(4–5): 207-215.
Makita, S., F. Jaillon, et al. (2010). "Comprehensive in vivo micro-vascular imaging of the human eye by dual-beam-scan Doppler optical coherence angiography." Opt Express **19**(2): 1271-1283.
Malik, B. H. (2009). "Modeling the corneal birefringence of the eye toward the development of a polarimetric glucose sensor." J. Biomed. Opt. **15**(3): 037012.
Marin-Amat, M. (1956). "[Physiological variations of corneal curvature during life time; their importance and transcendence into ocular refraction]." Bull Soc Belge Ophtalmol **113**: 251-293.
Marsich, M. W. and M. A. Bullimore (2000). "The repeatability of corneal thickness measures." Cornea **19**(6): 792-795.
Maurice, D. M. (1957). "The structure and transparency of the cornea." J Physiol **136**(2): 263-286.
Maurice, D. M. (1969). The cornea and sclera. The Eye. H. Davson. New York, London, Academic Press. **1:** 489 - 600.
Maurice, D. M. (1984). The Cornea and Sclera. The Eye. H. Davson. London, Academic Press. **1b:** 1-158.
Maurice, D. M. (1988). Mechanics of the cornea. The Cornea: Transactions of the World Congress on the Cornea III. H. D. Cavanagh. New York, Raven Press Ltd**:** 187-193.
Maus, M., S. Kröber, et al. (2006). Pentacam. Corneal tomography in the wavefront era: a guide for clinical application. M. Wang. NJ, Slack**:** 281-293.
McCally, R. L. and R. A. Farrell (1990). Light scattering from cornea and corneal transparency. Noninvasive diagnostic techniques in ophthalmology. M. BR. New York, Springer-Verlag**:** 189 - 210.
Meek, K. (2009). "Corneal collagen—its role in maintaining corneal shape and transparency." Biophysical Reviews **1**(2): 83-93.
Meek, K. M. and C. Boote (2004). "The organization of collagen in the corneal stroma." Exp Eye Res **78**(3): 503-512.
Meek, K. M. and C. Boote (2009). "The use of X-ray scattering techniques to quantify the orientation and distribution of collagen in the corneal stroma." Progress in Retinal and Eye Research **28**(5): 369-392.

Meek, K. M., S. Dennis, et al. (2003). "Changes in the refractive index of the stroma and its extrafibrillar matrix when the cornea swells." Biophys J **85**(4): 2205-2212.
Meek, K. M. and R. H. Newton (1999). "Organization of collagen fibrils in the corneal stroma in relation to mechanical properties and surgical practice." J Refract Surg **15**(6): 695-699.
Meek, K. M. and A. J. Quantock (2001). "The use of X-ray scattering techniques to determine corneal ultrastructure." Prog Retin Eye Res **20**(1): 95-137.
Meek, K. M., S. J. Tuft, et al. (2005). "Changes in collagen orientation and distribution in keratoconus corneas." Invest Ophthalmol Vis Sci **46**(6): 1948-1956.
Mishima, S. (1958). "The Biomicroscopy of the Human eye using Polarized Light: Findings in Normal cornea." Jap.J.Ophthalmol. **2**(3): 183-187.
Mishima, S. (1960). "The use of polarized light in the biomicroscopy of the eye. Report I." Bibl Ophthalmol **55**: 1-20.
Mishima, S. (1960). "The use of polarized light in the biomicroscopy of the eye. Report II. The use of sensitive tint plate." Bibl Ophthalmol **55**: 21-31.
Misson, G. (1990). The birefringence of the human cornea and its structural implications. Midland Ophthalmological Society Annual Meeting. Birmingham and Midland Eye Hospital, unpublished.
Misson, G. P. (1993). "Form and behaviour of Haidinger's brushes." Ophthal Physiol Opt **13**(4): 392-396.
Misson, G. P. (2007). "Circular polarization biomicroscopy: a method for determining human corneal stromal lamellar organization in vivo." Ophthalmic Physiol Opt **27**(3): 256-264.
Misson, G. P. (2010). "The theory and implications of the biaxial model of corneal birefringence." Ophthalmic Physiol Opt **30**(6): 834-846.
Misson, G. P. and J. D. Stevens (1990). "Stress birefringence in the human cornea." Eye **4 (Pt 6)**: 830-834.
Misson, G. P., B. H. Timmerman, et al. (2007). "Human corneal stromal lamellar organization: a polarized light study in pseudophakic eyes." J Mod Optics **55**(4-5): 625-638.
Morishige, N., W. M. Petroll, et al. (2006). "Noninvasive corneal stromal collagen imaging using two-photon-generated second-harmonic signals." J Cataract Refract Surg **32**(11): 1784-1791.
Morishige, N., Y. Takagi, et al. (2011). "Three-Dimensional Analysis of Collagen Lamellae in the Anterior Stroma of the Human Cornea Visualized by Second Harmonic Generation Imaging Microscopy." Investigative Ophthalmology & Visual Science **52**(2): 911-915.
Morishige, N., A. J. Wahlert, et al. (2007). "Second-harmonic imaging microscopy of normal human and keratoconus cornea." Invest Ophthalmol Vis Sci **48**(3): 1087-1094.
Mountford, J. (1982). "Polarized Biomicroscopy." International Contact Lens Clinic **9**(9): 373-384.
Naylor, E. J. and A. Stanworth (1954). "Retinal pigment and the Haidinger effect." J Physiol **124**: 543-552.
Newton, R. H. and K. M. Meek (1998). "Circumcorneal annulus of collagen fibrils in the human limbus." Invest Ophthalmol Vis Sci **39**(7): 1125-1134.

Newton, R. H. and K. M. Meek (1998). "The integration of the corneal and limbal fibrils in the human eye." Biophys J **75**(5): 2508-2512.
Nyquist, G. W. (1968). "Stress-induced birefringence of the cornea." Am J Ophthalmol **65**(3): 398-404.
Nyquist, G. W. and G. L. Cloud (1970). "Stress-dependent dispersion of corneal birefringence: a proposed optical technique for intraocular pressure measurement." J Biomech **3**(3): 249-253.
O'Donnell, C. and C. Maldonado-Codina (2005). "Agreement and repeatability of central thickness measurement in normal corneas using ultrasound pachymetry and the OCULUS Pentacam." Cornea **24**(8): 920-924.
OceanOptics. Retrieved 03/07/2012, from http://www.oceanoptics.com/technical.asp.
Olympus. (2012). "The Berek Compensator." Microscopy resource center Retrieved 03/07/2012, from http://www.olympusmicro.com/primer/techniques/polarized/berekcompensator.html.
Oshika, T., G. Sugita, et al. (2000). "Regular and irregular astigmatism after superior versus temporal scleral incision cataract surgery." Ophthalmology **107**(11): 2049-2053.
Pandolfi, A. and F. Manganiello (2006). "A model for the human cornea: constitutive formulation and numerical analysis." Biomech Model Mechanobiol **5**(4): 237-246.
Patel, S., J. Marshall, et al. (1993). "Shape and radius of posterior corneal surface." Refract Corneal Surg **9**(3): 173-181.
Pinsky, P. M., D. van der Heide, et al. (2005). "Computational modeling of mechanical anisotropy in the cornea and sclera." J Cataract Refract Surg **31**(1): 136-145.
Pircher, M., C. K. Hitzenberger, et al. (2011). "Polarization sensitive optical coherence tomography in the human eye." Progress in Retinal and Eye Research **30**(6): 431-451.
Prospero Ponce, C. M., K. M. Rocha, et al. (2009). "Central and peripheral corneal thickness measured with optical coherence tomography, Scheimpflug imaging, and ultrasound pachymetry in normal, keratoconus-suspect, and post–laser in situ keratomileusis eyes." Journal of Cataract & Refractive Surgery **35**(6): 1055-1062.
Rabbetts, R. B. (1998). Bennett and Rabbetts' Clinical Visual Optics. Oxford, Butterworth Heinemann.
Rabinovitch, B., W. F. March, et al. (1982). "Noninvasive glucose monitoring of the aqueous humor of the eye: Part I. Measurement of very small optical rotations." Diabetes Care **5**(3): 254-258.
Radner, W. and R. Mallinger (2002). "Interlacing of collagen lamellae in the midstroma of the human cornea." Cornea **21**(6): 598-601.
Radner, W., M. Zehetmayer, et al. (1998). "Interlacing and cross-angle distribution of collagen lamellae in the human cornea." Cornea **17**(5): 537-543.
Randleman, J. B., D. G. Dawson, et al. (2008). "Depth-dependent cohesive tensile strength in human donor corneas: implications for refractive surgery." J Refract Surg **24**(1): S85-89.
Rapuano, C. J., M. R. Dana, et al. (1995). "Astigmatic effect of graft alignment in penetrating keratoplasty." Invest Ophthalmol Vis Sci **36**(suppl): S653.

Rasband, W. S. (1997-2012). ImageJ. Bethesda, Maryland, USA, U. S. National Institutes of Health.
Roberts, C. (2000). "The cornea is not a piece of plastic." J Refract Surg **16**(4): 407-413.
Ruberti, J. W., A. Sinha Roy, et al. (2011). "Corneal Biomechanics and Biomaterials." Annual Review of Biomedical Engineering **13**(1): 269-295.
Salz, J. J., S. P. Azen, et al. (1983). "Evaluation and comparison of sources of variability in the measurement of corneal thickness with ultrasonic and optical pachymeters." Ophthalmic Surg **14**(9): 750-754.
Sayers, Z., M. H. Koch, et al. (1982). "Synchrotron x-ray diffraction study of corneal stroma." J Mol Biol **160**(4): 593-607.
Schiotz, H. (1882). "Om nogle optiske egenskaber ved cornea." Nord Med Ark **14**(28): 1-47.
Sevel, D. (1986). "The origins and insertions of the extraocular muscles: development, histologic features, and clinical significance." Trans Am Ophthalmol Soc **84**: 488-526.
Shankar, H., D. Taranath, et al. (2008). "Anterior segment biometry with the Pentacam: comprehensive assessment of repeatability of automated measurements." J Cataract Refract Surg **34**(1): 103-113.
Shurcliff, W. A. (1962). Polarized Light: Production and Use. Cambridge, Massachusetts, Harvard University Press.
Shute, C. C. (1974). "Haidinger's brushes and predominant orientation of collagen in corneal stroma." Nature **250**(462): 163-164.
Sivak, J. G. and T. Mandelman (1982). "Chromatic dispersion of the ocular media." Vision Research **22**(8): 997-1003.
Smolek, M. K. (1993). "Interlamellar cohesive strength in the vertical meridian of human eye bank corneas." Invest Ophthalmol Vis Sci **34**(10): 2962-2969.
Smolek, M. K., S. D. Klyce, et al. (2002). "Inattention to nonsuperimposable midline symmetry causes wavefront analysis error." Arch Ophthalmol **120**(4): 439-447.
Stanworth, A. and E. J. Naylor (1950). "The polarization optics of the isolated cornea." Br.J.Ophthal. **34**: 201-211.
Stanworth, A. and E. J. Naylor (1953). "Polarized Light Studies of the Cornea. I.The Isolated Cornea." J.Exp.Biol. **30**: 160-163.
Stoller, P., K. M. Reiser, et al. (2002). "Polarization-modulated second harmonic generation in collagen." Biophys J **82**(6): 3330-3342.
Swartz, T., L. Marten, et al. (2007). "Measuring the cornea: the latest developments in corneal topography." Curr Opin Ophthalmol **18**(4): 325-333.
Tannenbaum, D. P., D. Hoffman, et al. (2004). "Variable corneal compensation improves discrimination between normal and glaucomatous eyes with the scanning laser polarimeter." Ophthalmology **111**(2): 259-264.
Teng, S.-W., H.-Y. Tan, et al. (2006). "Multiphoton Autofluorescence and Second-Harmonic Generation Imaging of the Ex Vivo Porcine Eye." Invest. Ophthalmol. Vis. Sci. **47**(3): 1216-1224.
Tripathi, R., C. and B. Tripathi, J (1984). Anatomy, Orbit and Adnexa of the Human Eye. The Eye. H. Davson. London, Academic Press. **1a:** 1-268.
Twerskyt, V. (1975). "Transparency of pair-correlated, random distributions of small scatterers, with applications to the cornea." J. Opt. Soc. Am. **65**(5): 524-530.

Volkov, V. V., L. K. Malyshev, et al. (1990). "[The current status and prospects for using the method of photoelasticity in ophthalmology]." Oftalmol Zh(8): 479-482.
Vukusic, P. and J. R. Sambles (2003). "Photonic structures in biology." Nature **424**(6950): 852.
Wahlstrom, E., E. (1979). Optical Crystallography. New York, John Wiley and Sons.
Wang, M. and M. Wang (2006). Corneal topography in the wavefront era: a guide for clinical application, SLACK Inc.
Weale, R. A. (1979). "Sex, age and the birefringence of the human crystalline lens." Exp Eye Res **29**: 449-461.
Weinreb, R. N., C. Bowd, et al. (2002). "Measurement of the magnitude and axis of corneal polarization with scanning laser polarimetry." Arch Ophthalmol **120**(7): 901-906.
Winkler, M., D. Chai, et al. (2011). "Nonlinear Optical Macroscopic Assessment of 3-D Corneal Collagen Organization and Axial Biomechanics." Investigative Ophthalmology & Visual Science **52**(12): 8818-8827.
Wolman, M. and F. H. Kasten (1986). "Polarized light microscopy in the study of the molecular structure of collagen and reticulin." Histochemistry **85**(1): 41-49.
Wright, F. E. (1923). "The formation of interference figures. A study of the phenomenon exhibited by transparent inactive crystal plates in convergent light." J Opt Soc Am **7**: 779 - 817.
Yamanari, M., S. Makita, et al. (2011). "Full-range polarization-sensitive swept-source optical coherence tomography by simultaneous transversal and spectral modulation." Opt Express **18**(13): 13964-13980.
Zhou, Q. and R. N. Weinreb (2002). "Individualized compensation of anterior segment birefringence during scanning laser polarimetry." Invest Ophthalmol Vis Sci **43**(7): 2221-2228.